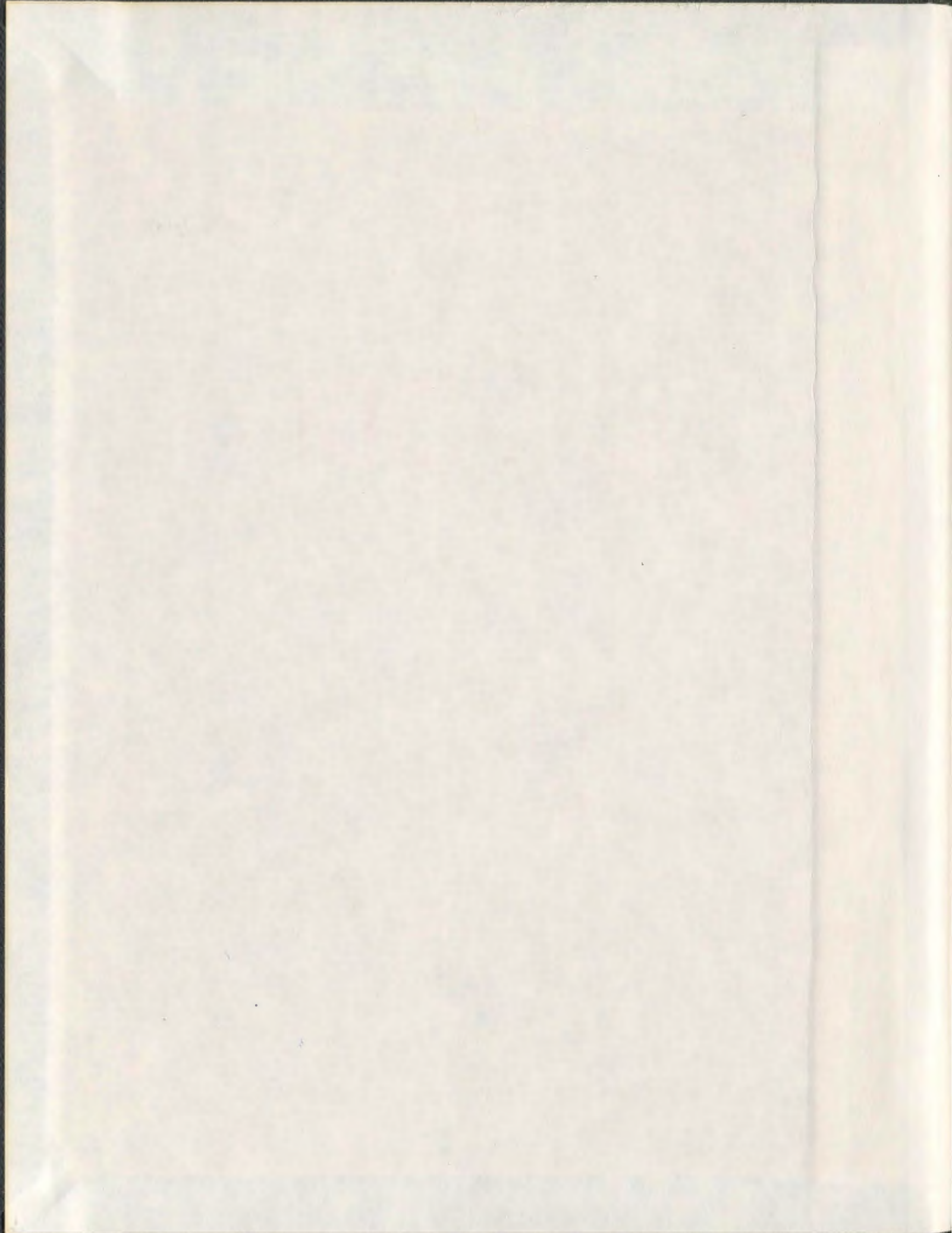


PALEOCEANOGRAPHIC AND PALEOCLIMATIC
EVOLUTION OF THE AEGEAN SEA SINCE THE
LAST INTERGLACIAL (~130 ka BP)
WITH SPECIAL EMPHASIS ON SAPROPEL FORMATION

E. BURSIN ISLER



001311



PALEOCEANOGRAPHIC AND PALEOCLIMATIC
EVOLUTION OF THE AEGEAN SEA
SINCE THE LAST INTERGLACIAL (~130 ka BP)
WITH SPECIAL EMPHASIS ON
SAPROPEL FORMATION

by
©E. Bursin İşler

A thesis submitted to the
School of Graduate Studies
in partial fulfillment of the
requirements for the degree of
Doctor of Philosophy
Department of Earth Sciences
Memorial University of Newfoundland
August 2012

St. John's Newfoundland

Abstract

Five long piston cores collected from different subbasins of the Aegean Sea constitute the primary source of data for this PhD thesis. This study is the first to document a continuous paleoceanographic and paleoclimatic record of the Aegean Sea since the last interglacial.

The chronostratigraphic reconstructions of the cored sediments based on organic carbon contents, stratigraphic position of known ash layers and oxygen isotopic curve matching collectively demonstrate the presence of sapropel S1 and MIS5 sapropels S3, S4 and S5 in the Aegean Sea subbasins. Generally, the organic carbon (TOC wt%) contents in sapropels range between 0.8% and 2% with highest concentrations of 9–13% in sapropels S4 and S5.

Average sedimentation rates range between 4.7 and 11.8 cm/ka with highest rates being observed in Euboea and North Ikaria basins (9.8 and 11.8 cm/ka, respectively). The timing of the onset of sapropels S4 and S5 mostly predate those in the eastern Mediterranean with ages ranging from 106.4–105.6 and 128.6–128.4 ka BP, respectively. On the other hand, the initiation of the onset of sapropel S3 (i.e., 83.2–80.4 ka BP) seems to agree with its Mediterranean counterparts, which highlights the heterogeneity of the Aegean Sea subbasins in terms of rapid vs. lagged response to changing climatic conditions. The sapropel initiations appear to be synchronous across the Aegean Sea; whereas, the terminations display a wider temporal variability implying that the cessation of sapropels is controlled both by the amplitude of paleoclimatic changes and the physiography/location of the subbasins.

Quantitative variations in the planktonic faunal assemblages exhibit a sequence of bioevents during the last ~130,000 years which allow identification of four major biozones. The distributional patterns of the most significant taxa demonstrate similar trends among all core localities suggesting that the major changes in the planktonic foraminifera assemblages have taken place rather synchronously in the Aegean Sea. Sapropels S3, S4 and S5 were deposited under similar hydrographic conditions during which a distinct deep chlorophyll maximum (DCM) layer was established. This situation points to a stratified water column and increased export productivity during times of sapropel formation. On the other hand, the faunal contrast between S1 and older sapropels indicates that the former was developed in the absence of a DCM layer, lacking a deep phytoplankton assemblage. Under such conditions, oxygen advection via intermediate water flow must have been significantly reduced which implies significant stagnation.

Sapropels are interpreted to have been deposited under normal marine conditions with temporary establishment of semi-euxinic bottom water conditions. Both marine and terrestrial organic matter contributed equally to MIS5 sapropels. In addition, organic carbon isotopic values across sapropels are more depleted than those in the eastern Mediterranean which, in turn, suggests enhanced riverine input during their deposition. Primary productivity calculations show that, particularly for sapropels with very high TOC values, both preservation and increased productivity are imperative in order to deposit sapropels with very high organic carbon contents (i.e., up to 13%).

Acknowledgments

Completing a Ph.D. is truly a marathon event, and I would not have been able to complete this journey without the aid and support of several people over the past seven years. First of all, I would like to express my deepest sense of gratitude to my supervisors Drs. Ali E. Aksu and Richard N. Hiscott for their patience, encouragement and excellent advice throughout this study. The broad knowledge, editorial guidance and assistance that they provided at all levels of this research project have added considerably to my graduate experience. I must acknowledge Mike Tubrett and Alison Pye for their assistance, suggestions and helpful perspectives during geochemical analyses.

A very special thanks goes out to the Aksu family (Gertrude, Ali, Niki and Bruiser) for their invaluable companionship that provided motivational, spiritual and moral support through my graduate years. It would have been immeasurably difficult to attain this level without their mind-refreshing discussions and very-much-enjoyed meals.

Dr. Aksu provided me with friendship, direction, intellectual/technical support and became more of a mentor and friend, than a professor. It was through his persistence, understanding and kindness that I completed my degree. I doubt that I will ever be able to convey my appreciation fully, but I owe him my eternal gratitude.

My final, and most heartfelt, acknowledgment must go to my family. Their support and eternal love have turned my journey through graduate school into a pleasure. I am forever indebted to my father (Rıdvan), my mom (Güzide), my sister (İştar) and to my grandparents (Nuran-EkremAtabay) for their understanding, endless patience, support and encouragement when it was most required.

Table of Contents

Abstract	iii
Acknowledgments	v
Table of Contents	vi
List of Tables	ix
List of Figures	ix
List of Appendices	xi
Co-authorship Statement	xii

Chapter 1. Introduction.....	1
1.1. Mediterranean Sea Oceanography and Climate.....	1
1.2. Study Area.....	4
1.3. Seabed Morphology.....	4
1.4. Oceanography and Regional Climate.....	7
1.5. Quaternary sapropels.....	11
1.6. Proxies/Methods.....	20
1.6.1. Micropaleontology.....	20
1.6.2. Inorganic Geochemistry.....	27
1.6.2.1. Oxygen Isotopes ($\delta^{18}\text{O}$).....	27
1.6.2.2. Carbon Isotopes ($\delta^{13}\text{C}$).....	32
1.6.3. Organic Geochemistry.....	33
1.6.3.1. Organic Carbon (TOC).....	33
1.6.3.2. Sulfur (TS).....	33
1.6.3.3. Sulfur Isotopes ($\delta^{34}\text{S}$).....	34
1.6.3.4. Organic Carbon Isotopes($\delta^{13}\text{C}_{\text{org}}$).....	35
1.6.4. Transfer Function.....	38
1.6.5. Magnesium.....	39
1.7. Scope of this study.....	42
1.8. Objectives.....	43
References.....	45

Chapter 2. Late Quaternary chronostratigraphy of the Aegean Sea with special reference to the ages of the sapropels S1–S5.....	62
Abstract.....	62
2.1. Introduction.....	63
2.1.1. Earth's Orbital Parameters.....	68
2.1.2. Physiography of the Aegean Sea.....	69
2.1.3. Hydrography of the Aegean Sea.....	74
2.2. Source of Data and Methods.....	75
2.2.1. Core Collection and Sample Preparation.....	75
2.2.2. Laboratory Methods.....	77
2.3. Results.....	81
2.3.1. Lithologic Units.....	81

2.3.1.1. Unit A.....	85
2.3.1.2. Unit B.....	85
2.3.1.3. Unit C.....	90
2.3.1.4. Unit D.....	91
2.3.1.5. Unit E.....	91
2.3.1.6. Unit F.....	92
2.3.1.7. Unit G.....	93
2.3.1.8. Unit H.....	93
2.3.1.9. Unit I.....	94
2.3.2. Oxygen Isotopes.....	94
2.4. Depth-to-Age Conversion.....	96
2.5. Discussion.....	104
2.5.1. Sedimentation Rates.....	104
2.5.2. Chronology.....	114
2.5.2.1. Tephra Chronology Below Y5 (Nisyros and X1 Tephras).....	126
2.6. Conclusions.....	128
References.....	130

Chapter 3. Late Quaternary Paleoceanographic Evolution of the Aegean Sea: a planktonic foraminiferal approach.....138

Abstract.....	138
3.1. Introduction.....	139
3.2. Seabed Morphology and Hydrography of the Aegean Sea.....	140
3.3. Data and Methods.....	144
3.4. Lithostratigraphy.....	149
3.5. Age Models.....	155
3.6. Planktonic Foraminifera.....	158
3.6.1. Integrity of the Faunal Assemblage in the cores.....	158
3.6.2. Downcore Distribution of Planktonic Faunal Assemblages -Ecozones.....	160
3.7. Oxygen Isotopes.....	173
3.8. Carbon Isotopes.....	178
3.9. Sea Surface Temperature (SST) and Sea Surface Salinity (SSS).....	182
3.10. Interpretation.....	187
3.10.1. Reliability of SST Derived from Transfer Functions.....	187
3.10.2. Significance of Downcore Distribution of <i>G. bulloides</i>	190
3.10.3. Significance of Downcore Distribution of <i>N. pachyderma</i> (d).....	192
3.10.4. Stable Carbon Isotopes ($\delta^{13}\text{C}$).....	193
3.11. Discussion.....	194
3.12. Conclusions.....	205
References.....	207

Chapter 4. Geochemistry of the Aegean Sea sediments: implications for surface/bottom water conditions during times of sapropel formation since the last interglacial.....	217
Abstract.....	217
4.1. Introduction.....	218
4.1.1. Seabed Morphology and Hydrography of the Aegean Sea.....	220
4.2. Data and Methods.....	223
4.2.1. Core Collection and Sample Preparation.....	223
4.2.2. Laboratory Methods.....	225
4.3. Lithostratigraphy.....	227
4.4. Age Models.....	233
4.5. Data Presentation.....	235
4.5.1. Oxygen Isotopes.....	235
4.5.2. Elemental Carbon and Sulfur (TC, TS).....	239
4.5.3. Carbon and Sulfur Isotopes ($\delta^{13}\text{C}_{\text{org}}$ and $\delta^{34}\text{S}$).....	239
4.6. Discussion.....	241
4.6.1. Bottom water conditions.....	241
4.6.1.1. C/S.....	242
4.6.1.2. $\delta^{34}\text{S}$	246
4.6.2. Source of organic matter.....	247
4.6.3. Paleoproductivity.....	250
4.6.4. Role of terrestrial carbon.....	266
4.7. Conclusions.....	266
References.....	269
Chapter 5. Summary.....	278

List of Tables

Table 1.1. Depth preference of planktonic foraminifera.....	23
Table 1.2. Species classification of the planktonic foraminifera in five hydrographic provinces.....	24
Table 1.3. Planktonic foraminifera species and latitudinal ranges in the five major faunal provinces.....	25
Table 2.1. Core locations, lengths and water depths.....	76
Table 2.2. Depth of the samples containing glass shards and number of counted shards in each sample.....	88
Table 2.3. Age control points and their depths within the cores used in Age-to-Depth conversion.....	101
Table 2.4. Age of the most recent sapropel S1 deduced from literature.....	102
Table 2.5. Sedimentation rates calculated for each successive age control point and mean sedimentation rates of the cores.....	107
Table 2.6. Calculated ages of sapropels S3, S4, S5 and Nisyros and X1 ash layers.....	119
Table 3.1. Core locations, lengths, and water depths.....	145
Table 3.2. Calculated ages of sapropels S3, S4, S5.....	157
Table 3.3. Calculated biozone boundary ages and durations.....	165
Table 4.1. Core locations, lengths and water depths.....	224
Table 4.2. Calculated ages of sapropels.....	237

List of Figures

Figure 1.1. Mediterranean Sea surface water circulation patterns.....	2
Figure 1.2. Location and seabed morphology of the Aegean Sea.....	5
Figure 1.3. Aegean Sea surface water circulation.....	9
Figure 1.4. Bottom water migration throughout the Aegean Sea.....	12
Figure 1.5. Global oxygen isotopic curve.....	31
Figure 1.6. Carbon isotopic composition of autotrophic marine and terrestrial organisms.....	36
Figure 1.7. Mg/Ca calibration for planktonic foraminifera.....	41
Figure 2.1. Correlation of the insolation monsoon index and the geological record of the eastern Mediterranean Sea sapropels during the last 465 ka.....	66
Figure 2.2. Simplified map of the Aegean Sea and surroundings.....	71
Figure 2.3a. Sapropel and nonsapropel units in the five cores and their assignment to one of nine lithologic units.....	81
Figure 2.3b. Sapropel and nonsapropel units in the five cores and their assignment to one of ten lithologic units.....	82

Figure 2.3c. Sapropel and nonsapropel units in the five cores and their assignment to one of ten lithologic units.....	83
Figure 2.4. Correlation of ash layers (red) ten lithologic units among the five cores.....	84
Figure 2.5a. Lithologic attributes of the cores.....	86
Figure 2.5b. Lithologic attributes of the cores.....	87
Figure 2.6a. Age control points throughout the cores.....	98
Figure 2.6b. Age control points throughout the cores.....	99
Figure 2.6c. Age control points throughout the cores.....	100
Figure 2.7a. Downcore variations of calculated sedimentation rates between successive age control points and average sedimentation rates of each core.....	105
Figure 2.7b. Downcore variations of calculated sedimentation rates between successive age control points and average sedimentation rates of each core.....	106
Figure 2.8. Age vs. sedimentation rate plots of the five cores.....	108
Figure 2.9a. Age-converted lithostratigraphic columns and their corresponding oxygen isotope measurements for the five cores.....	115
Figure 2.9b. Age-converted lithostratigraphic columns and their corresponding oxygen isotope measurements for the five cores.....	116
Figure 2.9c. Age-converted lithostratigraphic columns and their corresponding oxygen isotope measurements for the five cores.....	117
Figure 2.10a. Calculated onset/termination age ranges of sapropels S3, S4 and S5....	121
Figure 2.10b. Enlarged demonstration of calculated sapropel onset/termination age ranges.....	122
Figure 2.11. Calculated ages of the Nisyros and X1 tephras and their comparison with previously published ages.....	127
Figure 3.1. Simplified map of the Aegean Sea and surroundings showing core locations, major rivers, subbasins and circulation pattern.....	141
Figure 3.2a. Sapropel and non-sapropel units in the five cores and their assignment to one of nine lithologic units.....	150
Figure 3.2b. Sapropel and non-sapropel units in the five cores and their assignment to one of nine lithologic units.....	151
Figure 3.2c. Sapropel and non-sapropel units in the six cores and their assignment to one of nine lithologic units.....	152
Figure 3.3. Correlation of ash layers and lithological units.....	153
Figure 3.4a. Downcore assemblage distributions of planktonic foraminifera and identified biozones.....	162
Figure 3.4b. Downcore assemblage distributions of planktonic foraminifera and identified biozones.....	163
Figure 3.4c. Downcore assemblage distributions of planktonic foraminifera and identified biozones.....	164
Figure 3.5. Generalized downcore variations of planktonic and benthic oxygen isotopic compositions in the Aegean Sea since MIS5.....	174
Figure 3.6. Age-converted lithostratigraphic columns and their corresponding oxygen isotope measurements for five cores.....	176

Figure 3.7. Downcore variations in carbon isotopes of five cores.....	179
Figure 3.8a. Sea surface temperature (SST) and sea surface salinity (SSS) variations of five cores.....	183
Figure 3.8b. Sea surface temperature (SST) and sea surface salinity (SSS) variations of five cores.....	184
Figure 3.9. Comparison of the calculated sea surface temperatures obtained both from transfer functions and Mg/Ca.....	188
Figure 3.10. Dendrograms resulting from R-mode hierarchical cluster analysis.....	191
Figure 3.11. Schematic demonstration of water column hydrographic conditions during the formation of sapropels.....	196
Figure 3.12. Comparison of stacked $\delta^{13}\text{C}$ and $\delta^{18}\text{O}$ curves from this study with pollen records from NE Greece and the eastern Mediterranean.....	199
Figure 3.13. Comparison of the across-sapropel $\delta^{18}\text{O}_p$ variations from the eastern Mediterranean and the Aegean seas.....	201
Figure 4.1. Simplified map of the Aegean Sea and surroundings showing the core locations, major rivers, subbasins and circulation pattern.....	221
Figure 4.2. Sapropel and non-sapropel units and corresponding downcore variations of TOC and oxygen isotope values.....	228
Figure 4.3. Correlation of ash layers and lithologic units.....	230
Figure 4.4. Lithologic attributes of the cores.....	231
Figure 4.5. Age control points throughout the cores.....	234
Figure 4.6. Age-converted lithostratigraphic columns and their corresponding oxygen isotope measurements.....	236
Figure 4.7. Downcore changes in elemental and isotopic carbon and sulfur compositions among the five studied cores.....	240
Figure 4.8. C/S plots and C_{org} vs. sedimentation rate plots across sapropels S1, S3, S4 and S5.....	244
Figure 4.9. $\delta^{13}\text{C}_{\text{org}}$ values and terrestrial fraction across sapropels S1, S3, S4 and S5.....	249
Figure 4.10. Marine and terrestrial organic carbon fractions derived from $\delta^{13}\text{C}_{\text{org}}$ values.....	253
Figure 4.11. Age vs. sedimentation rate plots of the five cores.....	255
Figure 4.12. Downcore preservation factors.....	256
Figure 4.13. Measured and calculated OC_{mar} contents.....	259
Figure 4.14. Primary productivity variations.....	260
Figure 4.15. Calculated primary productivity values.....	262

List of Appendices

Appendix A

Co-authorship Statement

This PhD thesis is a manuscript-base thesis, hence composed of internally separate chapters constituting individual manuscripts written in paper-format. Each manuscript will be submitted to an international scientific journal upon the completion of thesis defence. Although the work was performed predominantly by me — both analytical and writing tasks — there have been contributions from co-authors to the manuscripts (i.e., A.E. Aksu and R.N. Hiscott) in terms of guidance and editorial advice and from lab technicians in terms of supplying laboratory materials, showing me the procedures, standard/sample calibrations. Ergo, each chapter/manuscript could not have been prepared without the contributions of others. That said, I am the first author of all chapters and did >90% of the work.

The data set that has been used to construct each paper is derived from five long piston cores and simultaneously-collected gravity cores. All cores were collected during the Marmara Sea Gateway Project in 2003 scientific cruises undertaken in the Aegean and Marmara seas. The cores were collected by the co-authors, A.E. Aksu and R.N. Hiscott, and me with the help of onboard seamen.

Visual descriptions of all cores were performed by R.N. Hiscott after they arrived to the department. Sampling of the cores was done by me.

For inorganic oxygen and carbon analyses, the sample preparation procedure was done by me, including sieving, drying, hand-picking pristine foraminifera (planktonic, benthic) tests, preparing standards in the isotope laboratory. I ran the samples myself, however, calibration of the results were performed by Alison Pye.

For organic geochemical analyses, samples were prepared by me in the palynology laboratory under Helen Gillespie's supervision. The procedure involves

sample acidification, purification, drying, pulverizing, placing in glass vials in the palynology laboratory followed by preparation of the tin capsules that involved weighing the samples and standards for the analyser in the isotope laboratory. The samples were run by me under Alison Pye's supervision. The results were calibrated by Alison Pye.

For the micropaleontological study, I was trained by A.E. Aksu. Sample preparation involved halving the sieved and dried samples into a number of aliquots until each aliquot included ~300 planktonic foraminifera tests. The species identification was done by me.

For the trace element analyses, the preparation of the glass slides was done by me, including picking and mounting pristine planktonic/benthic foraminifera tests on glass slides using double-sided sticky tapes. The analyses were performed at Memorial University's INCO center. Except for the initial trial runs, the analyses were run by me under Mike Tubrett's supervision. The calibration was done by Mike Tubrett and the results were extracted by me.

Chapter 1. Introduction and Overview

Following the Swedish Deep Sea Expedition in 1947-1948, the discovery of Mediterranean Sea Quaternary sediments containing high organic carbon called 'sapropels' have intrigued many researchers and numerous studies have been undertaken since then in order to understand the causative factors leading to such carbon-rich conditions in today's most oligotrophic waters including the Adriatic and the Aegean seas. Together with technological advances and growing interest, many long piston cores have been collected throughout the western and eastern Mediterranean in an attempt to unravel the sapropel mystery.

In the Aegean Sea, organic rich layers were first described by Ninkovich and Heezen (1965) from cores taken from the central and southern Aegean Sea. Since then, more than 250 gravity and piston cores were collected mostly from the hemipelagic basins of northern and southern Aegean. However, many of these cores were either not examined or the results were never been published. Previous studies have predominantly focussed on the uppermost portions of the Aegean Sea sediments encompassing a time interval from last glacial (~20 ka BP) to Present. As a result, very little is known with regards to the past hydrographic and climatic history of the Aegean Sea.

1.1. Mediterranean Sea Oceanography and Climate

The Mediterranean Sea is a mid-latitude, semi-enclosed marginal sea connected to the Atlantic Ocean via the Strait of Gibraltar (Fig. 1.1). There are two principal physiographic components of the Mediterranean Sea, western and eastern, which are connected by the shallow Strait of Sicily. The main oceanographic characteristic of the

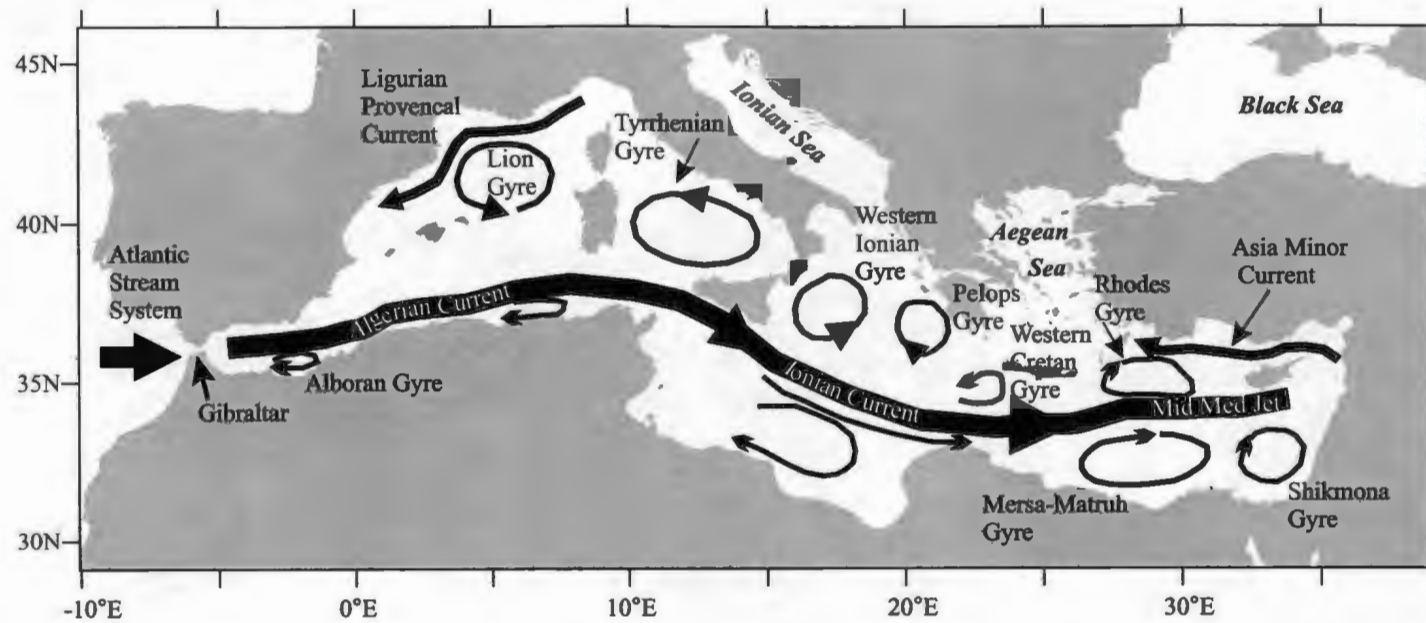


Figure 1.1. Mediterranean Sea surface water circulation patterns (modified from Roussenov et al., 1995).

Mediterranean Sea as a whole is that it is an evaporative basin (evaporation exceeds precipitation), and the deficit of water is supplied by the inflow of Atlantic waters from the Strait of Gibraltar (Fig. 1.1). This is considered to be the main forcing mechanism of the Mediterranean circulation. In a schematic view of the surface circulation Atlantic surface waters coming from the Strait of Gibraltar flow eastward along the North African coast, forming the so-called Algerian current (Millot, 1987, 1999). When this current reaches the Strait of Sicily, it bifurcates: one branch follows a cyclonic (anticlockwise) path around the Western Mediterranean Basin, while the other branch crosses the Channel of Sicily into the eastern basin where it also follows a general cyclonic path. The longer the Atlantic watermass stays in the Mediterranean, the saltier it becomes due to mixing with adjacent water masses and to evaporation.

The Eastern and Western Mediterranean basins themselves can be further divided into several subbasins, which are separated by topographic features (straits or channels) and are characterized by different water masses, patterns of circulation and characteristic forcing mechanisms (e.g. heat fluxes, wind stress, river discharge, etc).

The Mediterranean Sea is situated in between the high- to mid-latitude and the subtropical atmospheric systems, hence its climate relies in the latitudinal shift of these climate systems with the seasons and varies between mild wet winters and hot dry summers (Rohling et al., 2008). The mild and wet winter regime is related to the southward spreading of the temperate westerlies from central and northern Europe with occasional outbreaks of cold continental air masses funnelled through the valleys of the northern Mediterranean margin (Maheras et al., 1999). In summer, warm and dry conditions dominate as a result of the northward shift of the subtropical high-pressure

belt over the basin (Saaroni et al., 2003).

1.2. Study Area

The Aegean Sea is a semi-enclosed elongate basin situated in the northeastern Mediterranean Sea between mainland Turkey in the east and Greece in the west (Fig. 1.2). In the north, it is connected to the Black Sea via the Straits of Dardanelles and Bosphorus and the small land-locked Marmara Sea; whereas in the south it is connected with the open Mediterranean Sea through the eastern (Kasos, Karpathos, Rhodes) and western (Kithira, Andikithira, Crete) straits of the Cretan Arc (Fig. 1.2). The Aegean Sea has a surface area of $\sim 2 \times 10^5$ km² and a total volume of $\sim 74,104$ km³, comprising $\sim 10\%$ of the Mediterranean Sea. Approximately 33.6% of the Aegean Sea is shallower than 200 m, and the mean water depth is ~ 362 m.

1.3. Seabed morphology

The Aegean Sea is an archipelago where its bottom topography is controlled by the distribution of numerous islands, and shallow basins and intervening relatively deep basins. It is naturally divided into three physiographic regions (Fig. 1.2). The northern Aegean Sea includes the North Aegean Trough, which forms a narrow and arcuate, 800–1000 m-deep bathymetric depression extending WSW from the Gelibolu Peninsula, swinging to a more southwesterly trend and widening toward the west. The North Aegean Trough comprises a number of interconnected deep depocentres, including the Saros and Sporades basins. The central Aegean Sea is characterized by a series of plateaux and basins. The basins consist of relatively shallow (400–600 m) NE-trending

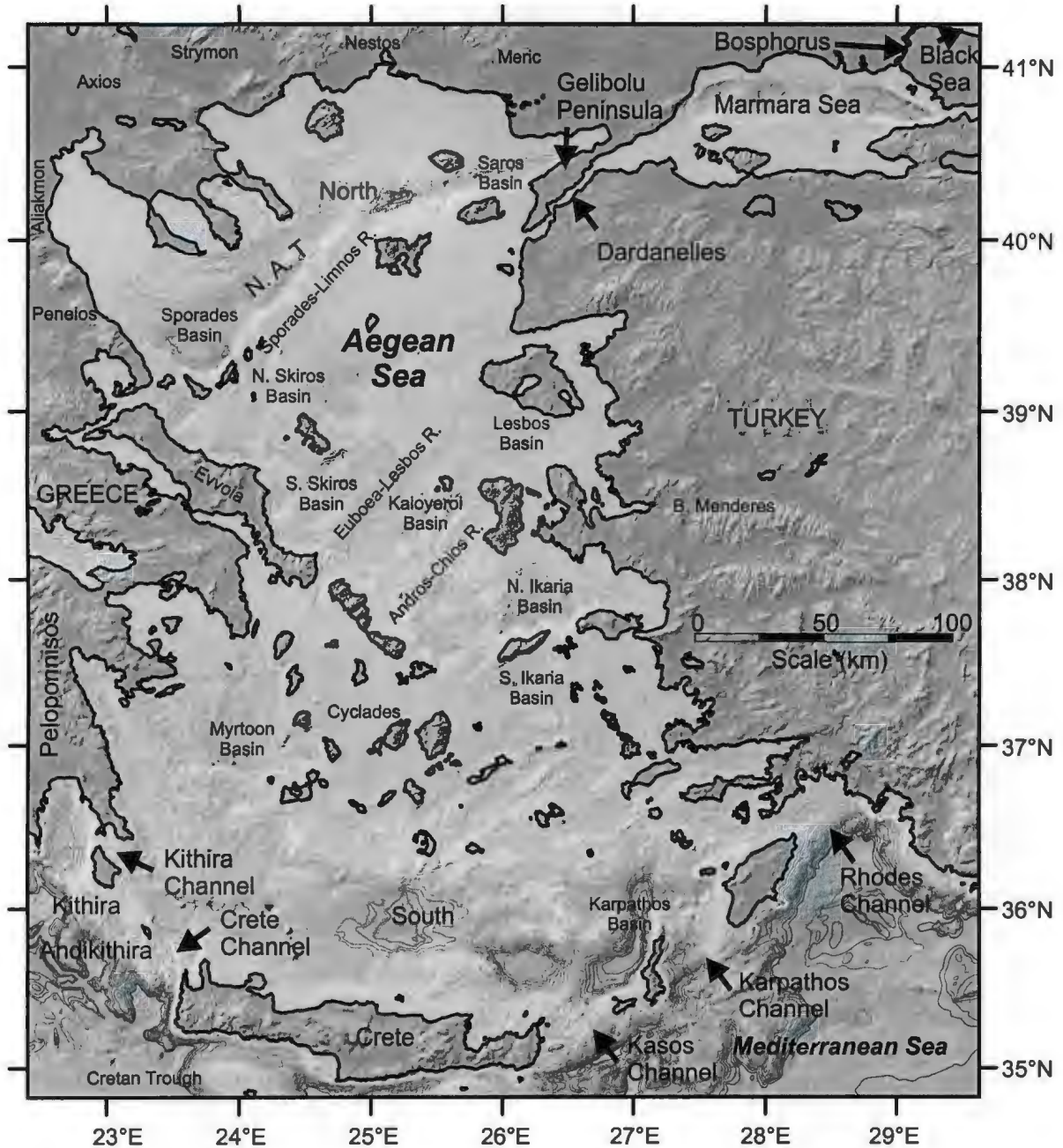


Figure 1.2. Location and seabed morphology of the Aegean Sea and its connection paths with the Black Sea and the Mediterranean Sea. bathymetric contours at 100 m intervals. NAT : North Aegean Trough

broad depressions including the North and South Skiros, Lesbos, Kaloyeroi, North and South Ikaria basins. They are separated by intervening 100–200 m-deep shoals and banks, including Sporades-Limnos, Euboea-Lesbos, Andros-Chios Ridges and associated islands (Fig. 1.2). The southern Aegean Sea is separated from the central Aegean Sea by the arcuate Cyclades, a convex-southward shallow volcanic arc dotted by numerous islands and shoals extending from the southern tip of Evia Island to southwestern Turkey. A large, and 1000–2000 m-deep, generally E–W-trending depression, the Cretan Trough, occupies the southernmost portion of the Aegean Sea immediately north of Crete. Two smaller Myrtoon and Karpathos basins occur in the northwestern and northeastern portions of the Cretan Trough, respectively (Fig. 1.2).

Although the shelves surrounding the Aegean Sea are generally 5–25 km wide, they widen considerably to ~ 65–75 km off the mouths of major rivers such as the B. Menderes, Meriç, Nestos, Strymon, Axios, Aliakmon and Peneios rivers. Here, the shelf-to-slope transitions are marked by the topset-to-foreset transitions of drowned deltas which last prograded during the sea-level lowstand of the last glacial maximum (e.g., Aksu et al., 1987; Lykousis, 2009).

The Aegean Sea has experienced considerable sea-level fluctuations through glacial–interglacial cycles. During the last glacial maximum (LGM), ca. 20,000 cal yr BP (calendar years before present), the sea level stood at ~ –115 m (e.g., Aksu et al., 1987; Lykousis, 2009) and both the straits of Bosphorus and Dardanelles were subaerially exposed disrupting the water exchange between the Black Sea and the Aegean Sea (Yaltrak et al., 2002). In addition, most of the continental shelves and shallow channels in the Aegean Volcanic Arc (Cyclades) were also subaerially exposed,

so the water exchange between the open Mediterranean Sea and the Aegean Sea was considerably reduced.

1.4. Oceanography and Regional Climate

The water exchange between the Black Sea and the eastern Mediterranean occurs through the Straits of Bosphorus and Dardanelles and the Marmara Sea as a two-layer flow (Latif et al., 1992; Özsoy et al., 1995; Polat and Tuğrul, 1996). The cooler (5° – 15°C) and lower salinity (17–20psu) surface water leaves the Black Sea, then flows south and southwest through the straits with velocities of 10–30 cm s^{-1} . It has an annual outflow of $\sim 300 \text{ km}^3$ across the Strait of Dardanelles into the northeast Aegean Sea, mostly occurring in late spring and summer as the result of maximum discharge of large rivers entering the Black Sea, such as the Dnieper, Dniester, Don, Danube and Bug (Özsoy et al., 1995). This water mass forms a 25–100 m-thick surface layer in the Black Sea and Marmara Sea as well as the northeasternmost segment of the Aegean Sea. In the northern Aegean Sea, this lower-salinity and relatively cold surface water forms a cyclonic gyre which is affected by the bottom topography, shoreline configurations, and the prevailing winds in the region (Yüce, 1991). The warmer (15° – 20°C) and higher salinity (38–39psu) Mediterranean water flows along the eastern side of the Aegean Sea, enters the Strait of Dardanelles and moves northeast beneath the Black Sea surface water with velocities of 5–25 cm s^{-1} . The prevailing winds in the region show notable seasonal variability and alter the flow path of the surface waters. During the winters, the northeasterly gales (Bora type) are the most frequent winds in the northern Aegean Sea. These gales occur with outbreaks of continental polar or arctic air from the Black Sea and

bring cold-dry winds into the area (Yüce, 1991). In summers, the persistent winds of the northern Aegean are known as the Etesians. These winds are primarily northeasterly monsoon-type winds, and result in upwelling and downwelling along the Turkish and Greek coasts, respectively.

The physical oceanography of the Aegean Sea is controlled mainly by the regional climate, the fresh-water discharge from major rivers draining southeastern Europe, and the seasonal variations in the Black Sea surface-water outflow through the Strait of Dardanelles. Based on the analysis of CTD data collected throughout the Aegean Sea during the summer, autumn, winter and spring, Yaşar (1994) distinguished three distinct water masses: surface, intermediate and bottom.

The Aegean Sea surface water forms a 40–50 m-thick layer, with summer and winter temperatures of 21°–26°C and 10°–16°C, and salinities of 30.0–39.5psu and 36.1–39.5psu, respectively. The steepest salinity gradient is observed in the northern Aegean Sea immediately west of the Strait of Dardanelles. Previous studies concerning the hydrographic conditions reveal that the general surface water mass circulation of the Aegean Sea forms a cyclonic gyre (Fig.1.3; Aksu et al., 1995; Lykousis et al., 2002).

A branch of the westward flowing Asia Minor current deviates toward the north, leaves the eastern Mediterranean basin and enters the Aegean Sea through the eastern straits (i.e., Rhodes, Karpathos, Kasos). This current carries the warm (16-25°C) and highly saline (39.2-39.5 psu) Levantine Surface Water (LSW) and Levantine Intermediate Water (LIW) masses along the Turkish western coast and occupies the first 400 m of the water column. Further north, over the Lesvos shelf, this water mass encounters the Black Sea Water (BSW) outflow through the Dardanelles Strait and

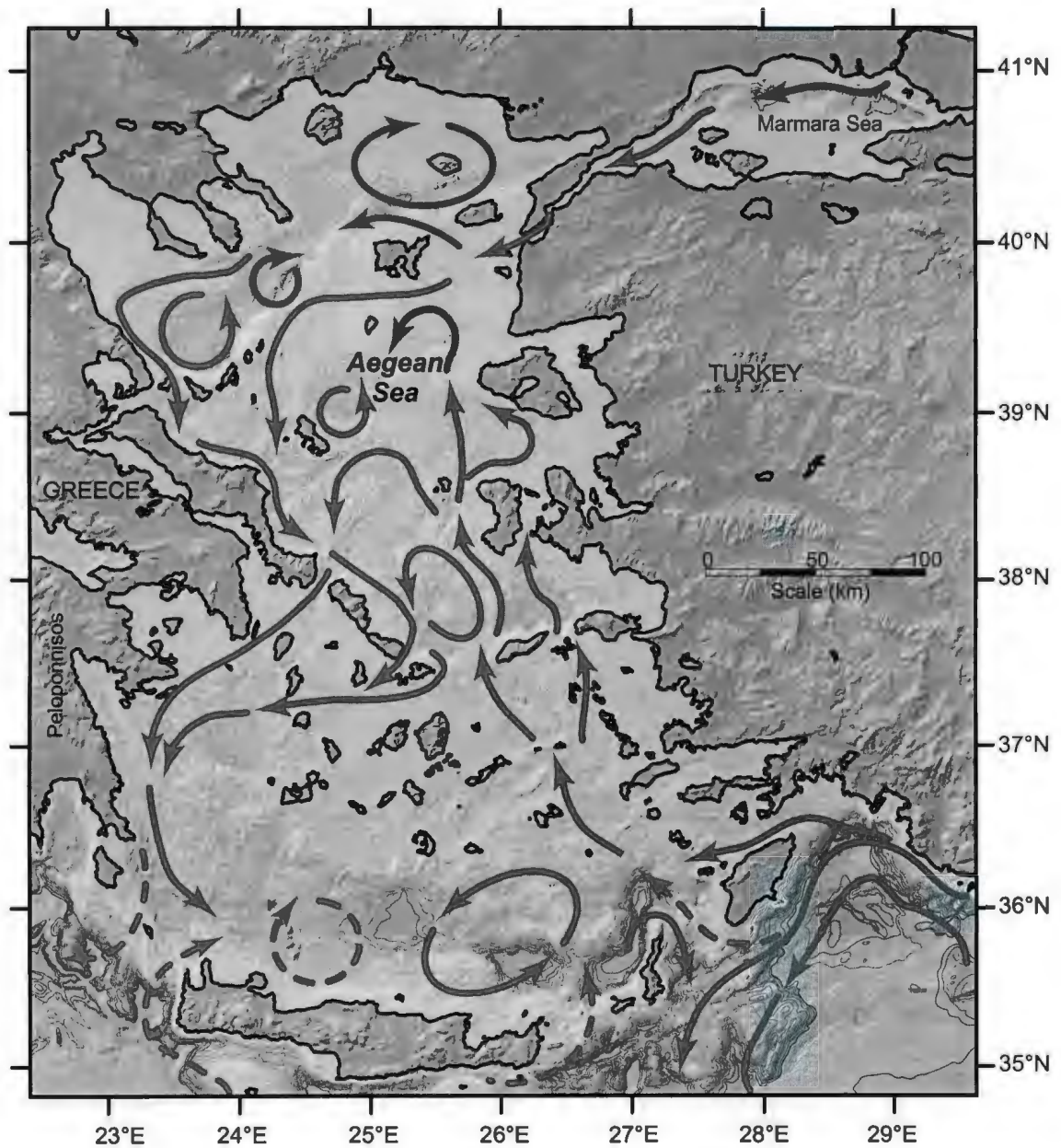


Figure 1.3. Aegean Sea surface water circulation (dashed and solid red arrows; modified from Lykousis et al., 2002).

generates a strong thermohaline front, along which the saline Levantine waters descend beneath the more buoyant, relatively cool (9–22°C) and less saline (22–23psu) thin layer of BSW. Hence, the water column structure in the northern and central Aegean Sea is characterized by a 20–70 m-thick veneer of modified Black Sea Water with mean summer and winter temperature and salinity values ranging between 23–13°C and 34.7–37.7 psu, respectively.

The Aegean Sea intermediate water consists mostly of Levantine Intermediate Water and extends from 100 m down to 400 m. It exhibits small variations in salinity (39.0–39.1psu) and temperature (15°–18° to 11°–16°C) during summers and winters, respectively. The surface and intermediate waters follow the general counter-clockwise circulation around the Aegean Sea, and progressively mix together as they flow southwards. As they reach the south Aegean Sea, these waters become significantly less saline than the northward-flowing Levantine waters. These waters exit the Aegean Sea through the western Cretan Arc Straits. Hence, in the southern Aegean Sea, the surface layers are comprised mostly of high salinity Levantine-origin waters and to a lesser extent contain lower salinity Atlantic Water and/or Black Sea Water. Intermediate waters occupy depths down to ~300 m and are made up of relatively high salinity (38.8–39.3 psu) Cretan Intermediate Water. Below the Cretan Intermediate Water layer there is a core of Transition Mediterranean Water (TMW, down to ~600–700 m), originating in the Levantine and Ionian basins, which is a mixture of LIW and Eastern Mediterranean Deep Water (Balopoulos et al., 1999; Theocharis et al., 1999a; Lykousis et al., 2002; Zervakis et al., 2004). Finally, the deeper parts of the Cretan Sea are replaced dense Cretan Deep Water.

The water column below 400 m in the Aegean Sea is occupied by a deep-bottom layer of locally formed North Aegean Deep Water with uniform temperature (13–14°C) and salinity (39.1–39.2 psu) displaying distinct characteristics in each basin (Aksu et al., 1995a; Zervakis et al., 2000; Zervakis et al., 2004; Velaoras and Lascaratos, 2005). Previous studies showed that there is a significant density contrast between the deep waters of the northern-central and southern Aegean basins. The density values in the north are the densest in the eastern Mediterranean (1029.64 kg m⁻³ in 1993; Zervakis et al., 2000). The presence of such high density bottom waters together with the limited exchange depth (down to ~400 m) suggest that deep water formation in these basins is a local phenomenon which, in turn, leads to the inference that the Aegean Sea, at least north of the Cyclades, behaves as a concentration basin (Fig. 1.4). Deep water formation is ascribed primarily to salinity increase in the intermediate waters (and to a lesser extent heat loss) with the highly saline Levantine Intermediate Water playing an important role (Velaoras and Lascaratos, 2005). Other researchers have suggested that, although the Black Sea Water inflow into the Aegean Sea increases the freshwater content, overall there is a buoyancy loss due to high rates of net heat loss and evaporation (Poulos et al., 1997; Drakopoulos et al., 1998). The rate of deep water formation and residency time are closely related to the size of each basin and the water mass characteristics and circulation of the overlying intermediate layers. The deep water exchange among these basins occurs through density currents. The old dense waters are uplifted to intermediate levels by newly formed bottom waters and flow towards the southern Aegean, gaining buoyancy on the way through mixing (Wu et al., 2000; Georgopoulos, 2002; Stratford and Haines, 2002; Zervakis et al., 2004).

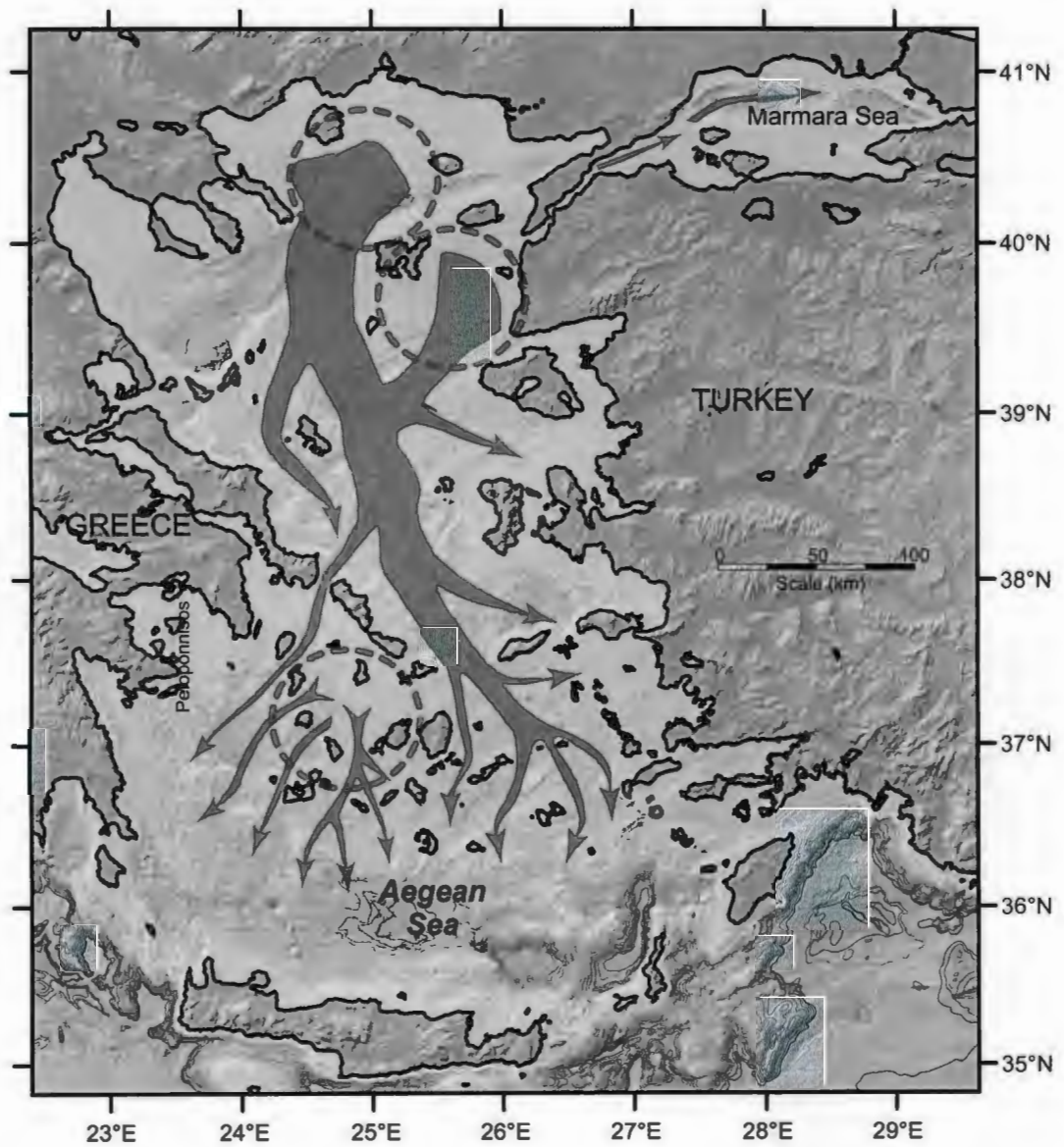


Figure 1.4. Bottom water migration throughout the Aegean Sea. Dashed circles show areas of bottom water formation (modified from Gertman et al., 2006).

The Quaternary-Holocene sediments of the Mediterranean Sea consist of two dramatically different lithologies: hemipelagic sediments and dark-coloured, organic-carbon-rich muds called “sapropels”.

In the eastern Mediterranean, although not calling them ‘sapropel’, the existence of sapropels was first predicted by Bradley (1938). He hypothesized that thin laminae of sediment, rich in organic matter, would have accumulated in the eastern Mediterranean due to changes in climate and sea-level fall during which the bottom waters became stagnant and “poisoned” with hydrogen sulphide.

The term sapropel remained mostly qualitative until the late 1970's when Kidd et al. (1978) first proposed a quantitative definition for sapropel as “a discrete layer, greater than 1 cm in thickness, set in open marine pelagic sediments containing greater than 2% organic carbon by weight”. They further defined sedimentary deposits containing organic carbon between 0.5 and 2% by weight as sapropelic layers.

Since ~1980 the paleoclimatic and paleoceanographic information stored in Mediterranean sapropels has intrigued many workers and much effort has been devoted to unravelling the mechanism(s) responsible for enhanced organic carbon accumulation leading to sapropel formation.

Based on published geochemical, micropaleontological, and sedimentological studies, Quaternary sapropel layers of the eastern Mediterranean Basin have the following general characteristics:

- They contain high levels of organic carbon – sapropels are known to have organic carbon values as high as 30% in a Pliocene sapropel (Sigl et al., 1978);

- They are usually laminated and underlain by a gray protosapropel zone and overlain by an oxidized layer (Maldonado and Stanley, 1976);
- They mostly lack benthic microfossils (except for occasional benthic foraminifera Parker, 1958; Cita and Podenzani, 1980; Mullineaux and Lohmann, 1981; Aksu et al., 1995), and evidence of bioturbation so that individual lamina and sharp contacts of sapropel layers are preserved;
- They contain an unusual planktonic foraminiferal assemblage usually dominated by *Neogloboquadrina dutertrei* (Kullenberg, 1951; Parker, 1958; Olausson, 1961; Cita et al., 1977, 1982; Thunell et al., 1977), a low salinity species (Ruddiman, 1971; Thunell, 1987a; Loubere, 1981);
- There is no appreciable change in total calcium carbonate content relative to surrounding sediments (Sigl et al., 1978; Cita et al., 1982);
- There is notable depletion of $\delta^{18}\text{O}$ values in tests of planktonic foraminifera during sapropel formation, an indication of either a salinity decrease (e.g. Aksu et al., 1995 a,b) or temperature increase in surface waters (Cita et al., 1977; Vergnaud-Grazzini et al., 1977; Williams and Thunell, 1979; Thunell and Williams, 1984; Rossignol-Strick et al., 1982; Thunell et al., 1984);
- There is increased mineral alteration in clays resulting from the greater organic content so that clays tend to be degraded toward mixed-layer types or chlorite or are completely destroyed, and the abundances of certain major compounds such as SiO_2 , Al_2O_3 , TiO_2 , and K_2O are lower than in nonsapropel marls and oozes in the same cores (Cita et al., 1977, 1982);

- Abundant pyrite occurs mainly within the sapropel layers while marcasite occurs below and sometimes near the top of the layers, where reducing conditions were less intense (Cita et al., 1977; Aksu et al., 1995b);
- Nine sapropels were deposited during the last 250,000 years (Ryan, 1972) with most occurring during interglacial episodes. Sapropels have been recognized in sediments as old as the Middle Miocene in deeply drilled sections (Kidd et al., 1978). The thicknesses of the layers indicate that each stagnation event lasted a few thousand years.

Two main theories have been proposed for the development of sapropels. Both theories take large influxes of water to the Mediterranean as a starting point at the beginning of an interglacial period, but diverge when explaining how this could have led to deposition of organic-rich sediments.

Anoxia theory

The 'Anoxia theory' generally invokes increased fresh or less-saline water input to the eastern Mediterranean and emphasizes water-column stratification. The widespread, low-salinity surface water would act as a low-density, thus more buoyant, layer inducing a freshwater cap or lens that floats above the more saline (high-density) intermediate and deep waters. The presence of this freshwater lens would result in a strong and stable density stratification in the water column inhibiting vertical mixing and renewal of bottom waters by oxygenated surface waters. This situation is commonly referred to as "stagnation". Through time the bottom waters would progressively become anoxic because of respiration of biota and consumption of oxygen by the decay of

organic matter. Evidence for a low-salinity layer is supported by depletions in $\delta^{18}\text{O}$ profiles obtained from planktonic foraminifera shells within sapropels, which is ascribed to the $\delta^{18}\text{O}$ signature of freshwater input (e.g. Vergnaud-Grazzini et al., 1986; Tang and Stott, 1993; Aksu et al., 1995b) and by faunal studies (Thunell et al., 1984).

Several scenarios have been postulated to account for the occurrence of a freshwater layer or lens:

- The increased fluvial and glacial meltwater influxes from the Black Sea and the Adriatic Sea at transitions from glacial to interglacial stages (Olausson, 1961; Ryan, 1972; Thunell et al., 1977; Vergnaud-Grazzini et al., 1977; Stanley and Blanpied, 1980; Aksu et al., 1995 a,b);
- Increased precipitation over the ocean itself due to global climatic changes during glacial-interglacial transitions from arid to pluvial conditions (Bradley, 1938; Kullenberg, 1952);
- Increased fluvial input from the Nile River following increased monsoonal summer precipitation along the mid latitudes in tropical eastern Africa (Rossignol-Strick et al., 1982; Rossignol-Strick, 1983, 1985; Freydier et al., 2001; Ducassou et al., 2008; Revel et al., 2010);
- Inflow of less saline Atlantic surface water during global sea-level rises associated with glacial-interglacial transitions (Müller, 1973).

Other researchers aligned with the "Anoxia theory" have presented scenarios that they believe would lead to stagnation and stratification without the requirement for fresh/brackish surface waters. These proposals include:

- Rapid rise of winter surface water temperatures during glacial-interglacial warming to create a density stratification in the water column due to differential heating (Van Straaten, 1972; Nesteroff, 1973);
- Intensification of the Indian Ocean summer monsoon and associated Mediterranean atmospheric depressions leading to a reduction, not a complete reversal, in the anti-estuarine circulation pattern (e.g., Zahn et al., 1987) that would promote nutrient preservation (Rohling, 1994);
- Radical weakening of the density difference between Mediterranean outflow and Atlantic intermediate waters proximal to the Strait of Gibraltar so that water exchange across the Sicily-Tunisia Strait would diminish, inhibiting the aeration of the eastern Mediterranean deep waters (Bethoux, 1984, 1993).

Primary productivity theory

The 'Primary productivity theory', originally suggested by Berger (1977), invokes enhanced biological productivity associated with a rise in the flux of nutrients to the sediments as the main control on sapropel development. Under this scenario, increased surface-water eutrophication leads to the formation of reducing conditions, and enhanced organic matter preservation is the result of oxygen consumption rates exceeding renewal rates. Many authors have advocated that enhanced productivity is the primary cause of sapropel formation (e.g., Schrader and Matherne, 1981; Thunell and Willimas, 1984; Ganssen and Trolestra, 1987; Parisi, 1987; Fontugne et al., 1989). Other proponents of the primary productivity theory, generally based on geochemical evidence, do not refute the presence of anoxia, but they indicate that the prerequisite for the formation of

sapropel is enhanced productivity (according increased export production) and anoxia by itself is not the primary causal mechanism. This relegates anoxia to being a symptom of sapropel development rather than a fundamental underlying cause.

Taking into account average sedimentation rates, sediment density, porosity, and the empirical relations presented by Müller and Suess (1979), Calvert (1983) pointed out that the formation of such organic-carbon-rich layers requires that primary productivity exceeds $500 \text{ g C m}^{-2} \text{ yr}^{-1}$, a rate observed in modern upwelling systems. He concluded that those Mediterranean sapropels containing very high amounts of organic carbon (up to 30%) cannot be explained by present-day productivity levels even if stagnant bottom water conditions prevailed. Moreover, the present anti-estuarine circulation of the Mediterranean Sea is not capable of inducing hydrographic conditions favorable to this level of high productivity.

For example, in the Tyro and Bannock basins, where hypersaline and anoxic bottom waters dominate, the enhanced organic carbon preservation is higher (at 1.3% C_{org}) than elsewhere in the Mediterranean (basinal average 0.3% C_{org} ; Jongsma et al., 1983; De Lange and ten Haven, 1983; Cita et al., 1985; Parisi et al., 1987). However, the present-day values are still lower than typical sapropel values (3–17% C_{org}). In order to create such conditions, Calvert (1983) suggested that increased Nile River outflow and an excess of precipitation over evaporation, instead of leading to stagnation, caused a reversal of the water circulation in the eastern Mediterranean Sea (Calvert, 1983; Sarmiento et al., 1988; Thunell and Williams, 1989) from anti-estuarine to estuarine which, in turn, made the eastern Mediterranean Sea a nutrient trap. In this situation, excess nutrient production in the photic zone would result in a "rain" of organic matter to

the seabed where oxygen consumption rates would exceed renewal rates, creating anoxic conditions at the sediment-water interface under relatively well oxygenated bottom waters (Schrader and Matherne, 1981; Calvert, 1983; Sarmiento et al., 1988; Pedersen and Calvert, 1990; Calvert and Pedersen, 1992). Some support for the productivity theory comes from modern upwelling areas where local hydrographic flow is not stagnant and bottom waters are not anoxic (Calvert and Price, 1983; Pedersen, 1983; Zahn and Pedersen, 1991).

Some authors did not think that the anoxia and primary productivity theories are mutually exclusive. For example, Rohling and Gieskes (1989) combined decreased deep water aeration with enhanced biological production and suggested that decreased excess evaporation and reduced inflow of western Mediterranean water caused shoaling of the pycnocline (and nutricline) into the euphotic zone. This phenomenon led to the development of a distinct deep chlorophyll maximum and enhanced marine biological activity. The shoaling of the pycnocline is also postulated by Rohling and Hilgen (1991) and received mathematical support from Rohling (1991). Sancetta (1994) proposed a mat-sedimentation model to explain 'pulses' in productivity in the Mediterranean invoking large fluxes of mat-forming diatoms responsible for high carbon fluxes which might represent the deep chlorophyll maximum. Her theory has recently been bolstered for a Pleistocene sapropel horizon by foraminiferal and nannofossil studies (Kemp et al., 1999). Canfield (1994) argued that the preservation and productivity theories are both essentially correct and that the C_{org} in the sediments is the resultant of a shifting balance between C_{org} flux and the diluting clastic input. He concluded that at lower deposition rates ($<0.04 \text{ g cm}^{-2} \text{ yr}^{-1}$), a high organic carbon flux will result in organic-rich sediments

regardless of the redox state of the water. His solution for organic matter preservation has received little support.

Opposing evidence comes from the NW Aegean Sea and the eastern Mediterranean where increased rates of terrigenous input during the deposition of the most recent sapropel or sapropelic layer have been postulated (Cramp et al., 1988; Shaw and Evans, 1984; Poulos, 2009; Roussakis et al., 2004; Hamann et al., 2008). Studies of Plio-Pleistocene carbonate cycles and sapropels have further shown that dilution with terrestrial material (Howell et al., 1990; Thunell et al., 1990) and diagenetic (dissolution) processes (Sprovieri et al., 1986) may have played an important role during their formation.

1.6. Proxies/Methods

1.6.1. Micropaleontology

The identification and quantification of the microorganisms (e.g., planktonic foraminifera) and their assemblages provide important and that definitive data that allow the unraveling of ecological responses to paleoceanographic and paleoclimatologic changes.

The distribution patterns and variations in diversity and abundance of the planktonic foraminifera are closely related to environmental conditions that are controlled by the intricate interaction of biological, chemical and physical factors (Bé and Hutson, 1977; Reiss et al., 1999; Rohling, 1993). Previous studies of living planktonic foraminifera show that members of this group display strong preferences for particular

ranges of sea surface temperature, salinity and nutrient supply (Hemleben et al., 1989). A comprehensive understanding of a planktonic foraminifera's ontogeny in relation to environmental factors is necessary to make reliable paleoecological interpretations.

Planktonic foraminifera are unicellular microorganisms that inhabit mostly the epipelagic zone and feed primarily upon phytoplankton (e.g. dinoflagellates, diatoms, and algae; Hemleben, 1989). Planktonic foraminifera tests are mostly formed within the upper 100 m in the oceans, with the highest concentrations occurring between subsurface depths of 10–50 m; although, species living at depths of ~500 m have also been documented (i.e., *Globigerina digitata*, *Globorotalia crassaformis*). Previous studies show that the life span of planktonic foraminifera is species-specific and ranges from 5 to 40 days (Berger, 1970; Hemleben et al., 1989).

The abundance variations of the planktonic foraminifera are closely related to seasonal hydrographic changes (Rohling et al., 2004). During periods of cold weather, the cooling of the surface waters will weaken the thermocline gradient, resulting in the downwelling and upwelling of the surface and nutrient-rich bottom waters, respectively. Weather-dependent nutrient enrichment in the epipelagic zone occurs at different times of the year depending on latitude (Hemleben et al., 1989). The maximum abundance of planktonic foraminifera is observed between December and March in northern mid-latitude regions, whereas the planktonic foraminifera productivity peaks between May and October in subarctic waters.

Planktonic foraminifera species exhibit a broad depth preference (Table 1.1; Bé, 1977) delineated by correlating their quantitative abundances with the physical and chemical parameters of the ambient water, such as temperature, salinity, oxygen,

phosphate. Data of this type enable the specification of the most favourable environmental conditions for each species. As caveats, the vertical range of depths inhabited by planktonic foraminifera is extremely wide and varies both regionally and seasonally. In addition, some species descend to deeper habitats as they proceed through their ontogeny.

The spatial distribution of the planktonic foraminifera has been studied by several authors and their latitudinal occurrences, in relation to surface water temperatures, are recognized. The biogeographic distribution patterns of planktonic foraminifera within the epipelagic zone of the world oceans is established and five distinct faunal provinces are defined corresponding to climatic belts: tropical, subtropical, transitional, subpolar, polar. Tables 1.2 and 1.3 list the planktonic foraminifera associated with these five climatic zones. Species diversity decreases from low to high latitudes. Moreover, latitudinal distribution of the species demonstrates that the evolutionary diversification has proceeded more rapidly in warm-water regions as the ratio of indigenous species to total species gradually increase toward the polar regions.

Immediately after a planktonic foraminifera dies, the test is subjected to a number of processes which determine its preservation and abundance in the sediments. Hence, it is important to understand these after-death processes in order to achieve an accurate paleoecological interpretation.

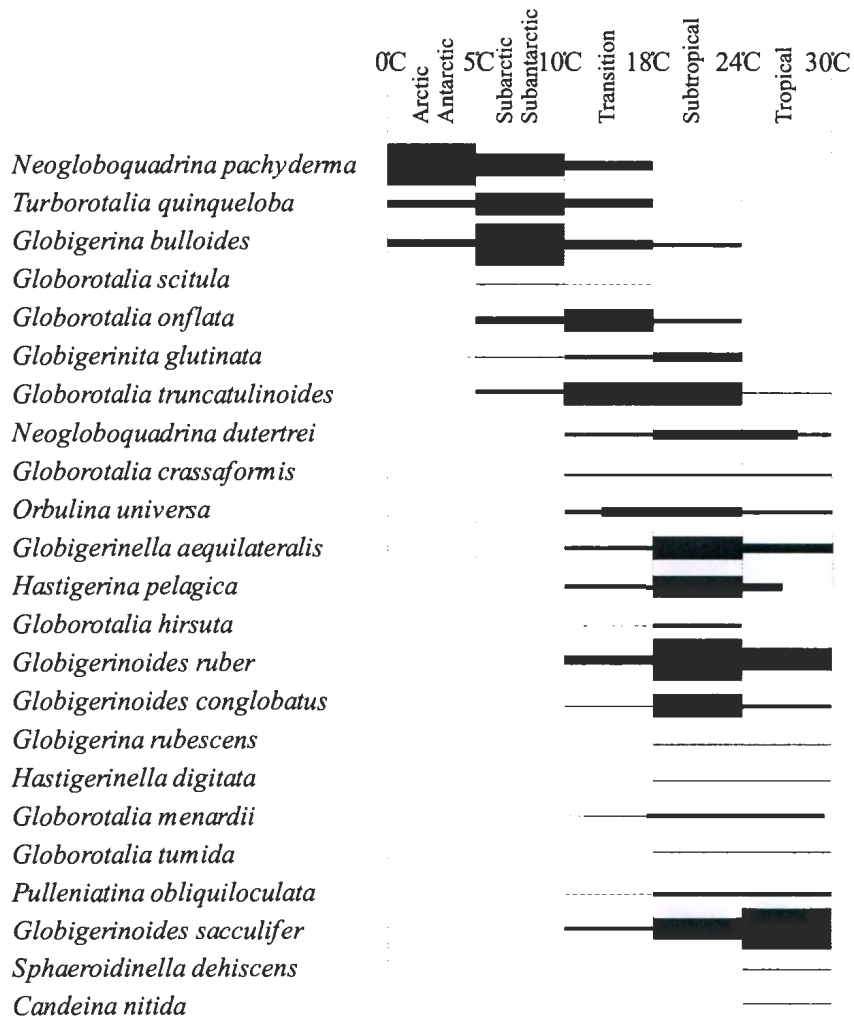
Dissolution of calcareous tests occurs in waters that are undersaturated with calcium carbonate. Dissolution is selective with regard to test size, wall thickness and test porosity of the planktonic foraminifera species. Several authors have studied dissolution of planktonic foraminifera tests and have concluded that the solution-susceptible species

Shallow water	Intermediate water	Deep water
<i>Globigerinoides ruber</i>	<i>Globigerina bulloides</i>	<i>Neogloboquadrina pachyderma</i>
<i>Globigerinoides sacculifer</i>	<i>Hastigerina pelagica</i>	<i>Sphaeroidinella dehiscens</i>
<i>Globigerinoides conglobatus</i>	<i>Pulleniatina obliquiloculata</i>	<i>Hastigerinella digitata</i>
<i>Globigerina quinqueloba</i>	<i>Neogloboquadrina dutertrei</i>	<i>Globorotalia truncatulinoides</i>
<i>Globigerina rubescens</i>	<i>Orbulina universa</i>	<i>Globorotalia scitula</i>
	<i>Candeina nitida</i>	<i>Globorotalia menardii</i>
	<i>Globigerinellaequilateralis</i>	<i>Globorotalia tumida</i>
	<i>Globigerinalla calida</i>	<i>Globorotalia inflata</i>
	<i>Globigerinita glutinata</i>	<i>Globorotalia hirsuta</i>
		<i>Globorotalia crassaformis</i>

Table 1.1: Depth stratification of planktonic foraminifera inhabiting the epipelagic zone (Bé, 1977).

Polar	Subpolar	Transition	Subtropical	Tropical
<i>N. pachyderma(s)</i>	<i>G. bulloides</i> <i>N. pachyderma(d)</i> <i>T. quinqueloba</i> <i>Ga. bradyi</i>	<i>Gr. inflata</i>	<i>Gs. ruber</i> <i>Gr. truncatulinoides</i> <i>Gr. hirsuta</i> <i>Ge. aequilateralis</i> <i>G. falconensis</i> <i>H. pelagica</i> <i>Gs. conglobatus</i> <i>Ga. glutinata</i> <i>G. humilis</i> <i>O. universa</i> <i>Gr. crassaformis</i>	<i>Gs. sacculifer</i> <i>P. obliquiloculata</i> <i>Gr. menardii menardii</i> <i>Gr. tumida</i> <i>G. rubescens</i> <i>C. nitida</i> <i>N dutertrei</i> <i>H. digitata</i> <i>"S. dehiscens"</i>

Table 1.2: Species distribution of the planktonic foraminifera among five climatic zones (Bé, 1977).



Number of species indigenous to each zone	1	4	1	12	10
Total number of species occurring in each zone	5	8	18	19	20

Table 1.3. Planktonic foraminifera species and latitudinal ranges in the five major faunal provinces redrawn from Bé, 1977).

the less resistant species, thus diminishing their abundance in the dead assemblage. There are other factors that influence the degree of dissolution of a foraminifera shell, such as the degree of undersaturation of ocean water with respect to CaCO_3 , the rate of bottom water oxygenation, the rate of oxidation of organic matter, and the rate of calcareous test supply. Therefore, it is crucial to look for evidence of dissolution during microscopic examination of samples. Strong evidence comes from the presence or absence of pteropoda, which are made up of aragonite which is highly soluble. These processes include ingestion by scavengers, settling, current transport, scouring and redeposition, bioturbational mixing, and dissolution.

The settling rate of a foraminifera shell is controlled by the rate of decomposition of the protoplasmic envelope. An organic-free calcite shell will settle at 0.3 cm s^{-1} to 2.3 cm s^{-1} for tests between $62\text{-}125 \mu\text{m}$ and $>250 \mu\text{m}$ in size, respectively. In a water depth of 1000 m, the minimum deposition time for tests of $62\text{-}125 \mu\text{m}$ size will be ~ 12 days. In regions of strong subsurface currents, the empty tests can be carried over significant distances from their original habitat, and arrival at a 1000 m-deep seabed can take much longer than 12 days as the tests are periodically swept upward by large-scale eddies. Post-depositional transportation of death assemblages by bottom currents and turbidity currents can occur, causing redeposition of the assemblages away from a position vertically beneath their original surface water habitats. Bioturbation is the displacement and mixing of sediment particles during faunal activities (e.g. burrowing) by benthic fauna (e.g. worms, bivalves, gastropods) and flora. Bioturbation depth ranges typically between $2\text{-}15 \text{ cm}$ and rarely exceeds depths more than 30 cm (Boudreau, 1994). The

principal effect is to mix foraminiferal tests upward and downward, thus blurring the temporal record. In some cases, fragile tests can be broken and/or crushed in the mouths or guts of sediment-injecting organisms. Bioturbational mixing can significantly contaminate the surface water assemblage with fossil assemblages representing a different time and different surface water mass. The amount of mixing is controlled by the bioturbation depth (i.e. type of benthic fauna) and the sedimentation rate.

1.6.2. Inorganic geochemistry

1.6.2.1. Oxygen isotopes

The $^{18}\text{O}/^{16}\text{O}$ variations in marine carbonates reflect the temperature and the oxygen isotopic composition of the water in which they precipitate which is, in turn, a function of water salinity. However, there are several other factors influencing the oxygen isotopic composition of foraminifera shells, given by Berger and Gardner (1975) as the equation:

$$\Delta\delta_f = \Delta\delta_T + \Delta\delta_G + \Delta\delta_{E,P} + \Delta\delta_V + \Delta\delta_D + \Delta\delta_R(1)$$

where $\Delta\delta$ is the difference in $\delta^{18}\text{O}$ between two samples. $\Delta\delta_f$ denotes the glacial-interglacial $\delta^{18}\text{O}$ variation of the two foraminiferal samples; $\Delta\delta_T$ represents the difference in $\delta^{18}\text{O}$ due to glacial-interglacial temperature change in the oceans; $\Delta\delta_G$ stands for the difference in the $\delta^{18}\text{O}$ of the foraminiferal shells caused by changes in the oxygen isotopic composition of the ocean water (controlled by the volume of continental ice sheets); $\Delta\delta_{E,P}$ is the $\delta^{18}\text{O}$ difference due to evaporation and precipitation alterations

during glacial and interglacial periods; $\Delta\delta_v$ denotes a change in the deviation of foraminifera from thermodynamic equilibrium; $\Delta\delta_D$ is the difference in the $\delta^{18}\text{O}$ composition of foraminifera due to an adjustment of the depth habitat from glacial to interglacial stages; $\Delta\delta_R$ represents the change in the isotopic composition due to preferential dissolution of the foraminifera shells.

Transfer function paleotemperature calculations using the oxygen isotopic composition of planktonic foraminifera return paleotemperatures much higher than the true water temperature. The reason for excessive temperatures is believed to be test secretion out of isotopic equilibrium (i.e. vital effect). Analyses of large populations of foraminifera reveal that the amount of disequilibrium is a species-dependant variable so that oxygen isotopic values of individual planktonic foraminifera species display relatively fixed offsets from equilibrium.

The mean difference in the $\delta^{18}\text{O}_w$ of the open oceans away from continental masses between a full glacial and full interglacial is known to be $\sim 1.5\text{‰}$, primarily resulting from global variations in water temperature and salinity from the equator to the poles. The maximum change in $\delta^{18}\text{O}_w$ from glacial to interglacial times at a single locality in the open ocean away from continental influence ranges from 0.5‰ to as high as 1.7‰ (Emiliani, 1955; Craig, 1965; Shackleton, 1967; Imbrie et al., 1973; Chapell and Shackleton, 1986; Fairbanks, 1989). Studies from semi-enclosed basins (e.g., Mediterranean Sea) show that oxygen isotopic shifts between glacial and interglacial stages are larger and range from 2.8‰ to a maximum of 4.0‰ (Emiliani, 1955; Vergnaud Grazzini et al., 1977; Kroon et al., 1998).

In order to compare oxygen isotopic records from one locality to another, steps must be taken to ensure that the measured values are proxies for a regional or, better, global parameter. This can be accomplished by eliminating or minimizing the contributions of the last four terms of Equation 1, so that only water temperature and global ice-sheet volume contribute to the isotopic signal through terms $\Delta\delta_T$ and $\Delta\delta_G$, respectively. Ideally, dependence on nothing but global ice volume would be ideal.

To isolate the temperature effect and to better understand the amplitude of the glacial ice volume effect, the oxygen isotopic variations of benthic foraminifera have been analysed (Kuhnt et al., 2008). Bottom waters occupying the deeper portions of the oceans lie well below the permanent thermocline where the temperature variations between glacial and interglacial maxima do not exceed 3°C. The variations in the oxygen isotopic ratios of benthic foraminifera collected from such depths in places like the Norwegian Sea can be attributed primarily to the glacial ice-volume effect. The isotopic signals of both benthic foraminifera from such deep basins and planktonic foraminifera show similar trends, indicating that the major portion of the oxygen isotopic signal of ocean water reflects changes in global ice volume rather than temperature. Previous studies have shown that glacial to interglacial swings in the $\delta^{18}\text{O}$ of benthic foraminifera are ~1.2 ‰, and this variation is accepted to be the approximate magnitude of the glacial ice-volume effect (Shackleton, 1965; Imbrie et al., 1973).

As shown above, the temperature effect ($\Delta\delta_T$) is of secondary importance in controlling variations in the $\delta^{18}\text{O}$ of benthic foraminifera shells, and in low- and mid-latitude seas like the Mediterranean Sea it can be ignored because water temperatures

likely changed little between glacial and interglacial times, particularly at depth. The evaporation-precipitation effect surely played a minor role because of changes in surface water circulation patterns during global climatic changes; however, it is difficult to quantify. The vital effect ($\Delta\delta_v$) is commonly assumed to be constant for a single species even across glacial-interglacial transitions, particularly if temperature and salinity changed little. Oxygen isotopic variations due to different depth habitats of a foraminifera species can be minimized by analysing a very narrow size range of planktonic foraminifera. The degree of preferential dissolution ($\Delta\delta_R$) may vary from glacial to interglacial times and depends on water depth at the sampling site. This effect can be ignored if examination of samples shows no evidence for test corrosion and pitting.

By selecting a single species for measurement, picked from a single size fraction, foraminiferal shells can provide an oxygen isotopic record primarily reflecting ice volume and to a lesser extent temperature changes associated with glacial-interglacial cycles. Mathematically, the general equation is therefore reduced to:

$$\Delta\delta_f \approx \Delta\delta_T + \Delta\delta_G \quad (2)$$

Downcore variations in $\delta^{18}\text{O}$ display a “saw tooth pattern” reflecting glacial-interglacial cyclicity. Lisiecki and Raymo (2005) have developed an oxygen isotopic time scale for the past 780,000 years by stacking $\delta^{18}\text{O}$ records from various locations and integrating this data with existing age constraints and the assumption that the Earth’s orbital variations cause changes in global climate (Fig. 1.5). Stacking eliminates local temperature and other effects. The resultant curve displays large excursions where

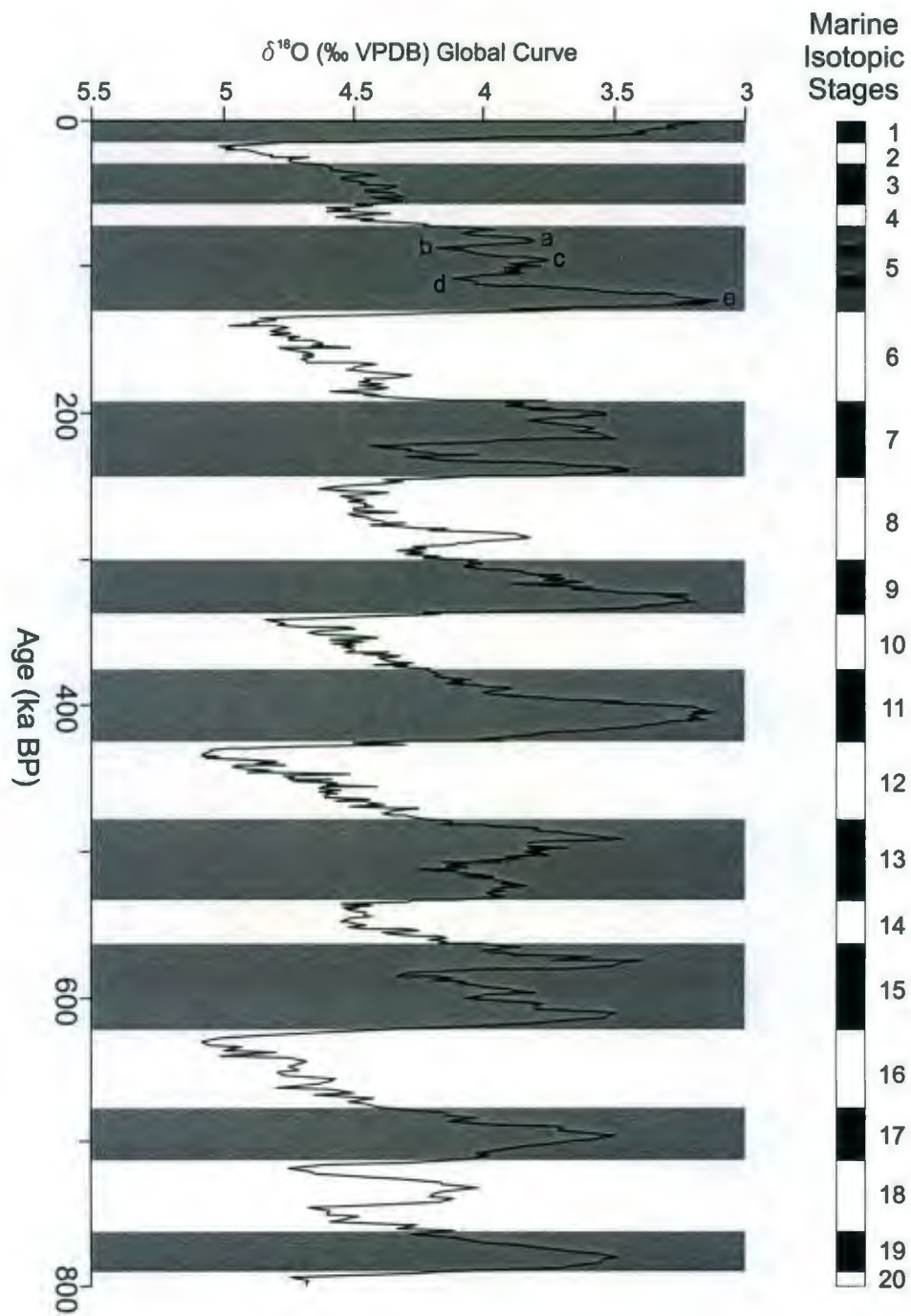


Figure 1.5. The oxygen isotopic curve on a geological time scale with glacial and interglacial periods assigned even and odd numbers, respectively (redrawn from Lisiecki and Raymo, 2005).

troughs and peaks represent the increasing and decreasing trends of the $\delta^{18}\text{O}$ values which are attributed to variations in the global volume of ice sheets related to the glacial and interglacial stages, respectively. The $\delta^{18}\text{O}$ geological time scale is a reliable tool that will play a crucial role during the construction of the chronostratigraphic framework for this study.

1.6.2.2. Carbon Isotopes ($\delta^{13}\text{C}$)

The carbon isotopic values of planktonic foraminifera are controlled by the $\delta^{13}\text{C}_{\text{DIC(Dissolved Inorganic Carbon)}}$ in seawater which is primarily influenced by biological processes (i.e. photosynthesis) and CO_2 exchange between seawater and the atmosphere. Dissolved inorganic carbon is the dissolved inorganic carbon available to organisms for construction of their hard parts, and resides in bicarbonate and carbonate complex anions.

The photosynthetic activity in the oceans results in a very strong enrichment of the surface waters in ^{13}C due to preferential ^{12}C uptake into the organic matter. Planktonic foraminifera inhabiting the photic zone secrete their tests from this isotopically heavy (enriched in ^{13}C) dissolved inorganic carbon (largely HCO_3^-). Common values recorded in the present oceans for planktonic foraminiferal tests range between +2 and +3‰ while the average whole ocean $\delta^{13}\text{C}$ value of total dissolved inorganic carbon is around zero. The $\delta^{13}\text{C}$ values of planktonic foraminiferal tests correlate inversely with nutrient concentrations where higher productivity will lead to isotopically heavier Total Dissolved Inorganic Carbon, thus, heavier CaCO_3 tests of planktonic foraminifera. As a result, the $\delta^{13}\text{C}$ of planktonic foraminifera reflects the

nutrient concentrations and ventilation of the surface water.

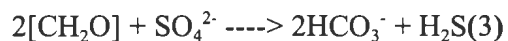
1.6.3. Organic geochemistry

1.6.3.1. Organic carbon (TOC)

The quality and quantity of organic matter contained in a sediment depend on environmental conditions and the source of the organic matter. Downcore total organic carbon measurements permit the identification of sapropel and/or sapropelic layers within cores and assessment of the paleoceanographic conditions during deposition. The amount of organic carbon is controlled by the productivity rate in the euphotic zone, bottom water conditions and the biological activities at the sediment/water interface. Evaluation of present productivity rates together with variations in thickness and organic carbon content of sapropel layers will be helpful during the assessment of conditions responsible for organic carbon preservation.

1.6.3.2. Sulfur (TS)

The sulfur in marine sediments is primarily deposited as pyrite and its precursor metastable minerals (e.g., FeS – hydrotroilite). Iron sulfides form during shallow burial, via the reaction of detrital iron minerals with H₂S. The H₂S is produced by the reduction of interstitial dissolved sulfate by bacteria using sedimentary organic matter as a reducing agent and energy source.



The major factors controlling how much pyrite can be deposited in a sediment are the

amounts of organic matter, presence/absence of reactive iron minerals and the availability of dissolved sulfate. Iron can be limiting in carbonate deposits and sulphate can become exhausted in rapidly accumulating organic-rich sediments (Berner, 1984; Pratt, 1984; Murray et al., 1987). In most marine sediments, the supply of reactive organic matter is very important because organic supply ultimately limits the rate of bacterial sulphate reduction. Hence, the concentration of pyrite in marine sediments is generally considered to be related in a simple way to the concentration of organic carbon. The organic carbon content of the sediment represents a somewhat fixed proportion of the organic matter remaining after microbial activity has removed the most easily metabolized fraction (Raiswell and Berner, 1985). Therefore, the relationship between total sulfur and organic carbon in marine sediments is a potential indicator for bottom water conditions.

1.6.3.3. Sulfur isotopes ($\delta^{34}\text{S}$)

Isotope fractionation during sulfate reduction by natural bacterial populations is of great importance for the interpretation of $\delta^{34}\text{S}$ values from both modern and ancient sedimentary sulfides (Passier et al., 1999). The sulfide produced is depleted in ^{34}S compared to the sulfate from which the sulfide is formed. Studies of isotope fractionation during dissimilatory reduction of sulfate by pure cultures have shown that the kinetic isotope effect produces sulfide depleted in ^{34}S by 5‰ to 46‰ compared to the isotopic composition of coexisting sulfate (Passier et al., 1999). Rates of sulfate reduction could therefore be useful in identification of the redox conditions of the bottom waters (Passier et al., 1999; Habicht and Canfield, 2001; Meyer and Kump, 2008).

1.6.3.4. Organic carbon isotopes ($\delta^{13}\text{C}_{\text{org}}$)

The organic matter in marine sediments is of terrestrial and marine origin. Allochthonous terrestrial organic material is delivered to the sea as dissolved organic compounds and suspended particulates in river water or as fine-grained particles via aeolian input (Menzel et al., 2003). Terrestrial plants derive their carbon from photosynthetic fixation of atmospheric CO_2 . Based on the adopted photosynthetic pathways, plants are classified into three types, C3, C4, and Crassulacean Acid Metabolism (CAM), with each having a distinct fractionation of carbon relative to atmospheric CO_2 . The C3 pathway (Calvin-Benson) is used by trees, shrubs, and cool-weather grasses found in high latitudes, cooler climates or regions with more arid summers (Nijenhuis and de Lange, 2000). The $\delta^{13}\text{C}$ values of C3 plants are -23 to -33‰, with an average of -26 to -27 ‰ (Fig. 1.6). The C4 photosynthetic pathway (Hatch-Slack or Kranz) consists of a two-step incorporation of CO_2 , where the $p(\text{CO}_2)$ is increased in the inner cell prior to incorporation by photosynthesis (CO_2). Tropical/warm-weather grasses (e.g., *Spartina*, a common marine salt marsh plant) use the C4 pathway. C4 plants display $\delta^{13}\text{C}$ values 10‰ higher than those of C3 plants, ranging from -9‰ to -16‰, averaging -12‰ to -13‰ (Fig. 1.6). The third type is the CAM plants which use both C3 and C4 mechanisms depending upon the external environment, using at any time the path which is more energetically favorable. CAM plants live predominantly in arid conditions (e.g. cactuses). The $\delta^{13}\text{C}$ values of crassulacean acid metabolism plants reflect both the C3 and C4 pathways and span the entire range of $\delta^{13}\text{C}$ values for plants.

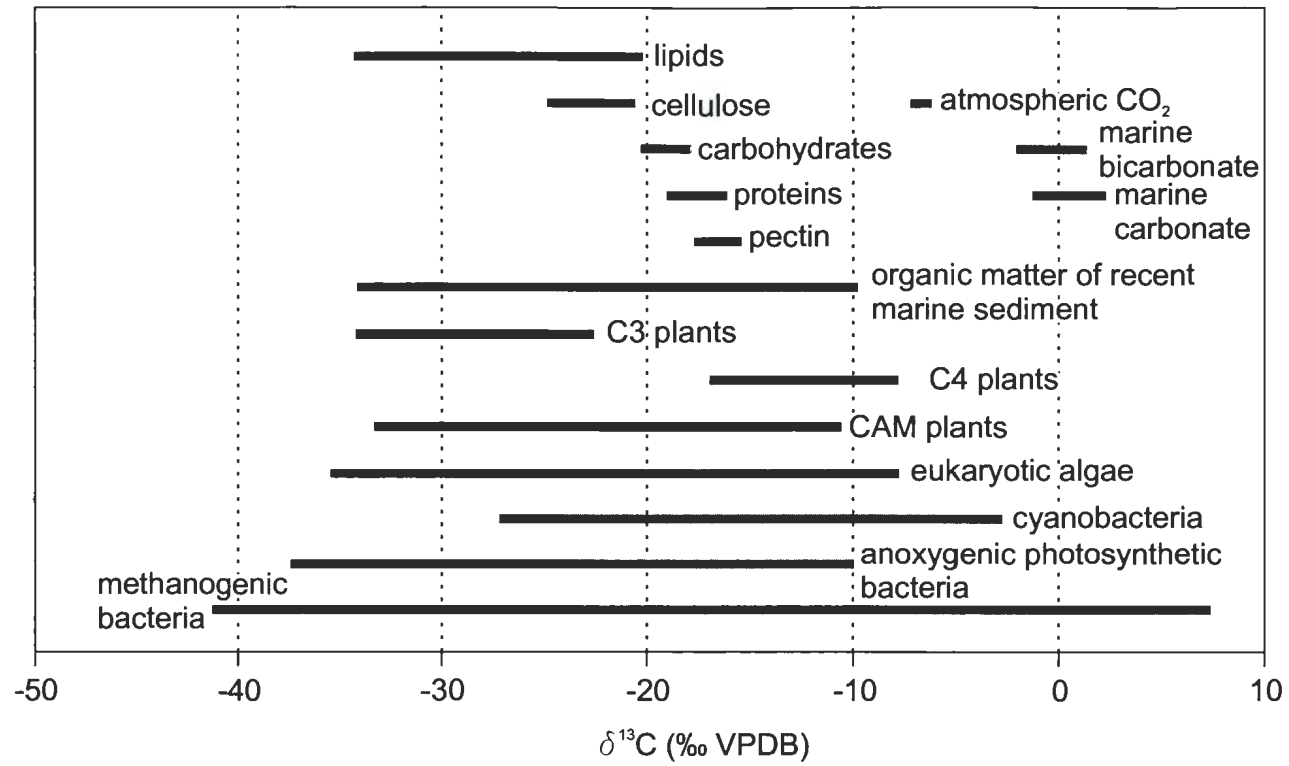


Figure 1.6. Carbon isotopic composition of autotrophic marine and terrestrial organisms (modified from Degens, 1969)

Marine organic matter is derived from marine microorganisms (e.g., phytoplankton, zooplankton, algae) which use dissolved CO₂ during photosynthesis (Fontugne and Calvert, 1992). There occurs a difference in fractionation during the formation of organic matter as a result of temperature variations of the surface waters. At high temperatures the solubility of CO₂ is low, resulting in isotopic values of organic matter as high as -13‰. Conversely, at low temperatures, the solubility of CO₂ and its availability to the microorganisms increases, resulting in much larger fractionation with values as low as -32‰. The concentration of dissolved CO₂ in surface seawater and the amount of fractionation during photosynthesis depends upon the concentration of CO₂ in the overlying air as well as on the temperature. In general the photosynthetic activity results in strong depletion of the total dissolved carbonate in the surface waters in ¹²C. Planktonic organisms living in the photic zone, and forming calcareous tests from dissolved inorganic carbon in these surface waters, use carbon that is enriched in ¹³C for the formation of their tests.

The carbon isotopic signature of marine and terrestrial organisms is usually preserved in the organic component of the sediment and their fractions can be calculated through the following equations generated by Calder and Parker (1968); Fontugne and Calvert (1992):

$$\delta^{13}\text{C} = (F_t \times \delta^{13}\text{C}_t) + (F_m \times \delta^{13}\text{C}_m) \quad (4)$$

$$\text{and } F_t + F_m = 1 \quad (5)$$

where F_t and F_m are the fractions of terrestrial and marine organic carbon, and $\delta^{13}\text{C}_t$ and $\delta^{13}\text{C}_m$ are the carbon isotopic compositions of terrestrial and marine source end-members.

In most situations, $\delta^{13}\text{C}_i$ is better constrained than $\delta^{13}\text{C}_m$, for reasons explained above.

1.6.4. Transfer functions

Downcore sea-surface salinity and temperature changes can be calculated by using the observed planktonic faunal assemblage. These calculations rely on studying modern assemblages and their environmental preferences and correlating the modern assemblages to fossil assemblages in order to estimate past environmental variables. For instance, a taxa assemblage “X” is always found in environmental conditions termed “Y”. If we find this same assemblage in the fossil record, we can deduce that the environmental conditions at that time in the past were similar to “Y”.

This concept has been used quantitatively as a method called paleoecological transfer functions. The first step to building a transfer function is to develop a training set. Training sets, which are used to build a transfer function, are composed of two sets of data: measurements of the environmental parameter (i.e. temperature, pH, salinity, etc.) and abundance of its associated taxa assemblage. These data are then developed into a set of equations (called transfer functions) that correlate the biological and environmental data. These equations often take the form:

$$T_m = XF_m \quad (6)$$

$$\text{and } T_p = Xf_p \quad (7)$$

where T is the estimated environmental parameter (m=modern, p=paleo), F is a matrix of modern and fossil data and X is a transfer coefficient or set of coefficients (Imbrie and Kipp, 1971; Hutson, 1977). Calibration is accomplished by solving this equation for X with a set of biological data (F) and observed values of the environmental parameter (T).

Once calibrated, the transfer function is applied to the fossil assemblage and the paleoenvironmental parameters can be estimated.

1.6.5. Magnesium

Mg^{2+} is one of several divalent cations which may readily substitute for Ca^{2+} during the formation of biogenic calcium carbonate. Its incorporation into foraminiferal calcite is influenced predominantly by temperature and, to a lesser extent, by pH and salinity of the ambient seawater during growth such that foraminiferal Mg/Ca ratios increase with increasing temperature (Lea et al., 1999). Several recent studies have demonstrated an increase in Mg/Ca in planktonic foraminiferal shells with increased temperature (Nuernberg et al., 1996a; Mashiotta et al., 1999; Lea et al., 1999; Elderfield and Ganssen, 2000; Lea et al., 2000; Dekens et al., 2002; Rosenthal and Lohmann, 2002). Culturing experiments as well as core top samples have confirmed that the relationship is exponential and expressed as:

$$Mg/Ca = B^{(A \times T)} \quad (8)$$

where T is the calcification temperature in °C, B and A are constants and are species-dependent.

The exponential temperature dependence (A) is documented to be relatively constant for all planktonic species and is within the range 0.09 ± 0.01 which reflects a temperature sensitivity in Mg/Ca of about 10% per °C increase in T. However, calibrations for different species are often characterized by significantly different values for the constant B (Anand et al., 2003). Empirically based calibrations are important since biological differences between species may cause significant offsets in Mg/Ca for a

given temperature. Anand et al. (2003) constructed a Mg/Ca equation by using calcification temperatures and concluded that the Mg/Ca ratios of 10 out of 12 planktonic species, inhabiting within a narrow temperature range, can be described by a single relation:

$$\text{Mg/Ca} = 0.38^{(0.09 \times T)} \quad (9)$$

On the other hand, Elderfield and Ganssen (2000) argued that linking Mg/Ca ratios with sea surface temperature is preferred to making a link to calcification temperatures because using sea surface temperature in the empirical relationships removes uncertainties about the depth and time of test calcification (Fig. 1.7).

Mg/Ca thermometry has distinct advantages over other temperature proxies. The oceanic residence times for Ca and Mg are relatively long (10^6 and 10^7 years, respectively); therefore, the Mg/Ca ratio of seawater may be considered to be constant over glacial/interglacial time scales. This assertion removes considerable uncertainty when reconstructing paleotemperatures using foraminiferal Mg/Ca ratios. In contrast, foraminiferal $\delta^{18}\text{O}$, which is also sensitive to changes in temperature, is strongly influenced by changes in the isotopic composition of seawater (Lea et al., 2000). Since δ_w varies both as a function of global ice volume and local salinity differences, the direct interpretation of foraminiferal $\delta^{18}\text{O}$ is not straightforward. By the integration of Mg/Ca values with ^{18}O measurements on the same medium (i.e. planktonic foraminiferal calcite), paleo-seawater $\delta^{18}\text{O}$ can be isolated from the temperature-dependent fractionation of $\delta^{18}\text{O}$ that occurs during test precipitation, and paleo-salinity (and seawater density) can be estimated from relationships between seawater $\delta^{18}\text{O}$, temperature and salinity (Anand

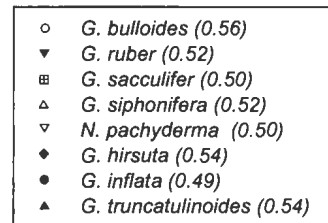
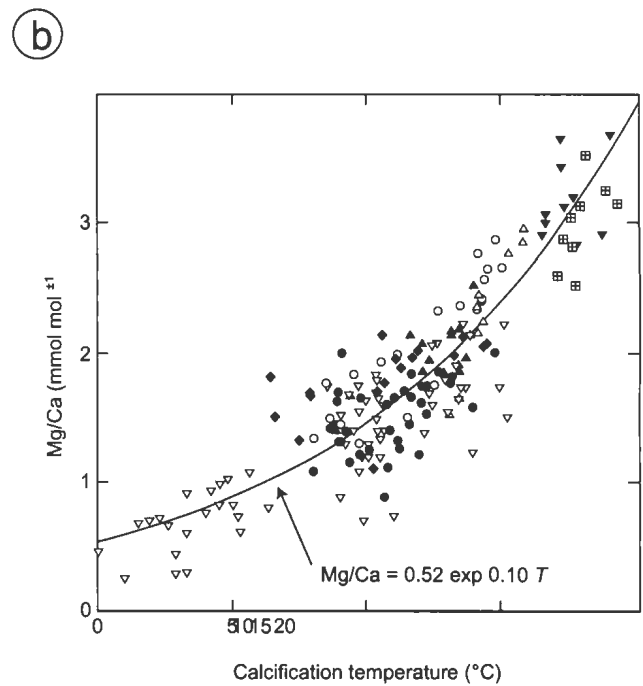
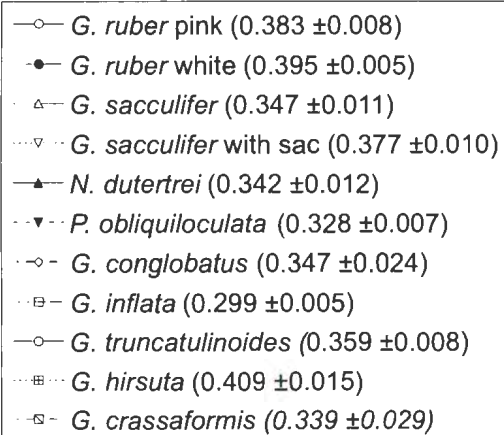
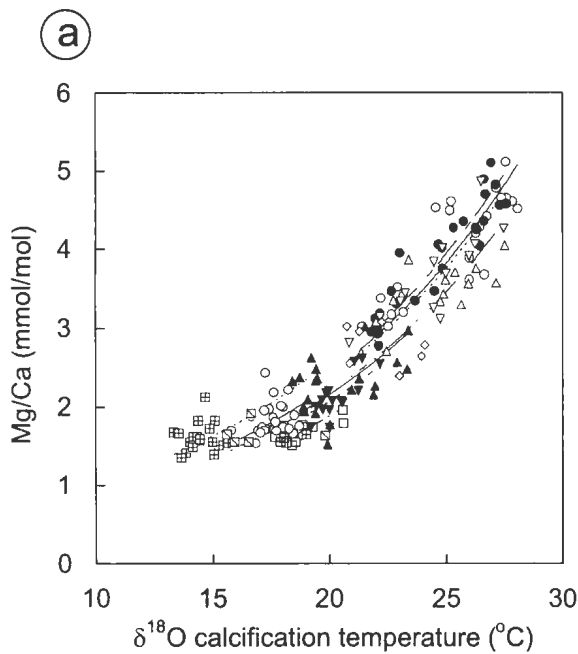


Figure 1.7. Mg/Ca calibration results for several species of planktonic foraminifera (a from Anand et al., 2003; b from Elderfield and Ganssen, 2000)

et al., 2003).

1.7. Scope of this study

Layers of sediment with dark color and high TOC content in the eastern Mediterranean Sea including the Adriatic Sea and the Aegean Sea have attracted interest since their first discovery in 1942. The interest originates from the fact that the eastern Mediterranean and adjacent marginal seas are among the most oligotrophic seas today with primary productivities of $\sim 30 \text{ g C m}^{-2} \text{ yr}^{-1}$ and average organic carbon content in surface sediments of $\sim 0.4\%$. Provided that the TOC content of sapropel layers mainly range between 1.5 and 3% to a maximum of $\sim 30\%$, fundamental paleoenvironmental changes modifying the surface/bottom waters, in relation to changes in climate and water column chemistry, must have occurred that lead to favourable conditions for increased organic carbon deposition in the sediments.

Previous studies conducted throughout the Aegean Sea focused on the uppermost sediments and paleoenvironmental conditions since the last glacial period ($\sim 25,000 \text{ yr BP}$). Hence, little is known concerning the earlier paleoenvironmental conditions associated with glacial and interglacial cycles.

By bringing together diverse but complementary tools of paleoceanographic investigation, such as micropaleontology, stable isotope and organic geochemistry, performed at ten centimetre resolution (millennial), the present thesis aims to provide detailed and integrated reconstructions of sea surface temperatures, salinities, productivity patterns and surface/bottom water chemistry during periods of increased organic carbon accumulations in the Aegean Sea since the last interglacial ($\sim 130,000 \text{ yr}$

BP to Present).

N.B. The chapters (i.e., 2, 3 and 4) of this thesis are written as individual manuscripts but they are internally related and constitute pieces of the larger project. The primary data set, introduced in Chapter 2, underpins the following manuscripts (Chapters 3, 4) and consists of cored sediments, lithologic information and corresponding oxygen isotope curves. Chapters 3 and 4 are constructed upon the primary data set by implementing additional methods/proxies. Therefore, repetition of introductory statements regarding the study area, lithology and oxygen isotope data cannot be avoided.

1.8. Objectives

Most previous studies conducted throughout the Aegean Sea focused on the uppermost organic-rich sediments and paleoenvironmental conditions since the last glacial period (~18,000 yr BP). However, little is known concerning earlier paleoenvironmental conditions associated with glacial and interglacial cycles since MIS 5. This PhD thesis will be the first to provide a comprehensive analysis of paleoceanographic and paleoclimatologic events during the late Quaternary in the Aegean Sea. The specific objectives of this thesis are as follows:

1. to construct a stratigraphic framework for the Aegean Sea sediments using lithostratigraphic descriptions, $\delta^{18}\text{O}$ curves obtained from planktonic foraminifera, ash layers and ^{14}C -U/Th dates;

2. to document the downcore faunal geochemical modifications caused by fundamental changes in the paleoenvironmental conditions associated with the transitions from glacial to interglacial periods during the late Quaternary;
3. to elucidate the bottom water conditions leading to favorable conditions for the formation of sapropel layers;
4. to test the validity of contradictory hypotheses and postulated theories for the development of the sapropel layers throughout the Aegean Sea.

Although, these objectives are local and are specifically directed to resolve issue in the Aegean Sea, they also have considerable global significance. For example, as the southern leg of a major gateway which connects the Black Sea to the eastern Mediterranean Sea the paleoclimatic and paleoceanographic evolution of the Aegean Sea have major impact and role on the watermass transport from polar latitudes to subtropical/tropical latitudes, via the Straits of Bosphorus and Dardanelles, and the intervening Marmara Sea. The PAGES (Past Global Changes) introduced within the framework of the International Geosphere-Biosphere Program – IGBP recommended the establishment of three Pole-Equator-Pole, PEP transect. The Marmara Sea Gateway is one such important transect which connects the northern Europe and northwestern Asia to the subtropical Mediterranean Sea. As such it serves as a major contributor to the Europe-Africa transect of PEP-III. Until the 2003 cruise, the political landscape and sporadic disputes regarding border issues in the Aegean Sea, prevented a consolidated and comprehensive investigation of the Aegean Sea segment of the gateway.

References

- Aksu, A. E., Piper, D. J. W. and Konuk, T., 1987. Late Quaternary tectonic and sedimentary history of outer İzmir and Çandarlı Bays, western Turkey. *Marine Geology*, 76, 89–104.
- Aksu, A.E., Yasar, D., Mudie, P.J., 1995a. Paleoclimatic and paleoceanographic conditions leading to development of sapropel layer S1 in the Aegean Sea basins. *Palaeoclimatology. Palaeogeography. Palaeoecology*. 116, 71–101.
- Aksu, A.E., Yasar, D., Mudie, P.J., Gillespie, H., 1995b. Late glacial-Holocene paleoclimatic and paleoceanographic evolution of the Aegean Sea: micropaleontological and stable isotopic evidence. *Marine Micropaleontology*, 25, 1–28.
- Anand, P., H. Elderfield, and M. H. Conte, 2003. Calibration of Mg/Ca thermometry in planktonic foraminifera from a sediment trap time series, *Paleoceanography*, 18(2), 1050, doi:10.1029/2002PA000846.
- Balopoulos E. T., Theocharis A, Kontoyiannis H, Varnavas S, Voutsinou-Taliadouri F, Iona A, Souvermezoglou A, Ignatiades L, Gotsis-Skretas O, Pavlidou A. 1999. Major advances in the oceanography of the southern Aegean Sea–Cretan Straits system (eastern Mediterranean). *Progress in Oceanography* 44: 109–130.
- Bé, A.W.H., 1977. An ecological, zoogeographic and taxonomic review of recent planktonic foraminifera. In *Oceanic Micropalaeontology*, Ed: A.T.S. Ramsay, v.1, 1–100.
- Bé, A.W.H. and Hutson, W.H., 1977. Ecology of planktonic foraminifera and biogeographic patterns of life and fossil assemblages in the Indian Ocean.

- Micropaleontology, 3, 369-414.
- Berger, W.H., 1970. Planktonic foraminifera: selective solution and the lysocline. *Marine Geology*, 8 (2), pp. 111-138.
- Berger, W.H., 1977. Deep-sea carbonate and the deglaciation preservation spike in pteropods and foraminifera. *Nature* 269, 301-304.
- Berger W.H. and Gardner, J.V., 1975. On the determination of Pleistocene temperatures from planktonic foraminifera. *Journal of Foraminiferal Research*, 5(2), 102-113.
- Berner, R.A., 1984. Sedimentary pyrite formation: An update. *Geochimica et Cosmochimica Acta*, 48, 605-615.
- Bethoux, J.P., 1984. Pale'o-hydrologie de la Me'diterrane'e au cours des derniers 20,000 ans. *Oceanol. Acta* 7 (1), 43-48.
- Bethoux, J.P., 1993. Mediterranean sapropel formation dynamic and climatic viewpoints. *Oceanologica Acta* 16 (2), 127-133.
- Bijma, J., Spero, H.J., and Lea, D.W., 1999. Reassessing foraminiferal stable isotope geochemistry: Impact of the oceanic carbonate system (experimental results), in *Use of Proxies in Paleoceanography: Examples from the South Atlantic*, edited by G. Fischer and G. Wefer, pp. 489-512, Springer-Verlag, New York.
- Bradley, W. H., 1938. Mediterranean sediments and Pleistocene sea levels. *Science*, 88: 376-379.
- Boudreau, B.P. 1994. Is burial velocity a master parameter for bioturbation. *Geochimica et Cosmochemica Acta* 58: 1243-1249
- Calvert, S.E., 1983. Geochemistry of Pleistocene sapropels and associated sediments from the eastern Mediterranean. *Oceanologica Acta* 6, 255-267.

- Calvert, S.E., Price, N.B., 1983. Geochemistry of Namibian Shelf sediments. In: Suess, E., Thiede, J. (Eds.), Coastal Upwelling; its Sedimentary Record, Part A. Plenum, New York, pp. 337–375.
- Calvert, S.E., Pedersen, T.F., 1992. Organic carbon accumulation and preservation in marine sediments: how important is anoxia? Productivity, Accumulation and Preservation of Organic Matter in Recent and Ancient Sediments. Columbia University Press, New York, pp. 231–263.
- Canfield, D. E., 1994. Factors influencing organic carbon preservation in marine sediments. *Chemical Geology*: 114, 315–329.
- Chapell, J. and Shackleton, N.J., 1986. Oxygen isotopes and sea level. *Nature*, 324, 137–140.
- Cita, M.B., Vergnaud-Grazzini, C., Robert, C., Chamley, H., Ciaranfi, N., and d'Onofrio, S. 1977. Paleoclimatic record of a long deep sea core from the eastern Mediterranean. *Quaternary Research* 8, 205–235.
- Cita, M.B., and D. Grignani, 1982. Nature and origin of Late Neogene Mediterranean sapropels. In: Schlanger, S.O., and M.B. Cita (Eds.), *Nature and Origin of Cretaceous Carbon rich Facies*, London (Academic Press), 165–196.
- Cita, M.B., Grignani, D., 1982. Nature and origin of Late Neogene Mediterranean sapropels. In: Schlanger, S.O., Cita, M.B. (Eds.), *The Nature and Origin of Cretaceous Carbon-Rich Facies*. Academic Press, London, pp. 165–196.
- Cita, M. B., Kastens, K. A., McCoy, F. W., Ahhib, F., Cambi, A., Camerlenghi, A., Corselli, C., Erba, E., Giambastani, M., Herbert, T., Leoni, C., Malinverno, P., Nosetto, A., and Parisi, E., 1985. Gypsum precipitation from cold brines in an

- anoxic basin in the eastern Mediterranean. *Nature*, 314: 152–154.
- Cramp, A., Collins, M. B., West, R., 1988. Late Pleistocene-Holocene sedimentation in the NW Aegean Sea: a paleoclimatic paleoceanographic reconstruction. *Palaeogeography, Palaeoclimatology, Palaeoecology*, 68: 61–77.
- Cramp, A., Collins, M.B., 1988. A late Pleistocene–Holocene sapropel layer in the NW Aegean Sea, eastern Mediterranean. *Geo-Marine Letters*, 8, 19–23.
- Degens, E.T., 1969. Biogeochemistry of stable carbon isotopes. In: Eglington, G., Murphy, M.T.J., (eds), *Organic geochemistry. Methods and results*. Springer, Berlin, pp 304–329.
- de Lange, G. J., and ten Haven, H. L., 1983. Recent sapropel formation in the eastern Mediterranean. *Nature*, 305: 797–798.
- Ducassou, E., Mulder, T., Migeon, S., Gonthier, E., Murat, A., Revel, M., Capotondi, L., Bernasconi, S.M., Mascle, J., Zaragosi, S., 2008. Nile floods recorded in deep Mediterranean sediments. *Quaternary Research* 70, 382–391.
- Dekens, P.S., Lea, D.W., Pak, D.K. and Spero, H.J., 2002. Core top calibration of Mg/Ca in tropical foraminifera: Refining paleotemperature estimation. *Geochemistry, Geophysics, Geosystems*, v.3, no.4.
- Drakopoulos PG, Poulos S, Lascaratos A. 1998. Buoyancy fluxes in the Aegean Sea. In *Rapport du 35e Congrès de la Commission Internationale pour l' Exploration Scientifique de la Mer Méditerranéenne*, 35. CIESM: Monaco; 35: 134–135.
- Elderfield, H., and G. Ganssen, 2000. Past temperature and $\delta^{18}\text{O}$ of surface ocean waters inferred from foraminiferal Mg/Ca ratios, *Nature*, 405, 442–445.

- Emiliani, C., 1955. Pleistocene temperatures. *Journal of Geology*, 63: 538–578.
- Fairbanks, R.G., 1989. 17,000-year glacio-eustatic sea level record: influence of glacial melting rates on the Younger Dryas event and deep-ocean circulation. *Nature*, 342, 637–642.
- Fontugne, M.R., Paterne, M., Calvert, S.E., Murat, A., Guischar, F., Arnold, M., 1989. Adriatic deep water formation during the Holocene; implications for the reoxygenation of the deep Mediterranean Sea. *Paleoceanography* 4, 199–206.
- Fontugne, M.R. and Calvert, S.E., 1992. Late Pleistocene variability of the carbon isotopic composition of organic matter in the eastern Mediterranean: Monitor of changes in carbon sources and atmospheric CO₂ concentrations.
- Freydier, R., Michard, A., De Lange, G., Thomson, J., 2001. Nd isotopic compositions of Eastern Mediterranean sediments: tracers of the Nile influence during sapropels formation? *Marine Geology* 177, 45–62.
- Ganssen, G., Troelstra, S.R., 1987. Paleoenvironmental change from stable isotopes in planktonic foraminifera from eastern Mediterranean sapropels. *Mar. Geol.* 75, 221–230.
- Georgopoulos D, Ignatiades L, Souvermezoglou A, Voutsinou Taliadouri F., 2002. Major outputs of the recent multidisciplinary biogeochemical researches undertaken in the Aegean Sea. *Journal of Marine Systems*, 33,(34):313-334.
- Gertman, I., Pinardi, N., Popov, Y., and Hecht, A., 2006. Aegean Sea Water Masses during the Early Stages of the Eastern Mediterranean Climatic Transient (1988–90). *Journal of Physical Oceanography*, 36: 1841-1859.

- Habicht, K.S. and Canfield, D.E., 2001. Isotope fractionation by sulfate-reducing natural populations and the isotopic composition of sulfide in marine sediments. *Geology*, v.29, no.6, 555–558.
- Hemleben, Ch., Spindler, M. and Anderson, O.R., 1989. *Modern planktonic foraminifera*. Springer-Verlag, New York, 335 pp.
- Howell, M. H., Rio, D. and Thunell, R., 1990, Laminated sediments from the Vrica section (Calabria, southern Italy): evidence for Plio-Pleistocene warming and cooling trends in the Mediterranean region: *Paleogeography, Paleoclimatology, Paleoecology*, v. 78, pp. 195–216.
- Hutson A.M., 1977. A revision of the families Synneuridae and Canthylloscelidae (Diptera)". *Bulletin of the British Museum (Natural History) Entomology* (London: British Museum (Natural History) 35 (3): 67–100.
- Imbrie, J. and Kipp, N.G., 1971. A new micropaleontological method for quantitative paleoclimatology.- application to a late Pleistocene Caribbean core. In Turekian, K.K. (ed.): *The late Cenozoic glacial ages*. Yale University Press, New Haven, 71-182.
- Imbrie, J., van Donk, J., and Kipp, N. G., 1973. Paleoclimatic investigation of a late Pleistocene deep-sea core: comparison of isotopic and faunal methods. *Quaternary Research.*, 3:10-38.
- Jongsma, D., Fortuin, A. R., Huson, W., Troeltra, S. R., Klaver, G. T., Peters, J. M., van Harten, D., de Lnage, G. J., and ten Haven, L., 1983. Discovery of an anoxic basin within the Strabo Trench, eastern Mediterranean. *Nature*, 305: 795–797.
- Kemp, A.E.S., Pearce, R.B., Koizomi, I., Pike, J. and rance, S.J., 1999. The role of mat-

forming diatoms in the formation of Mediterranean sapropels

- Kidd, R.B., Cita, M.B., Ryan, W.B.F., 1978. Stratigraphy of eastern Mediterranean sapropel sequences recovered during Leg 42A and their paleoenvironmental significance. *Init. Rep. DSDP 42A*, 421–443.
- Klinkhammer, G. P., Lambert, C. E., 1989. Preservation of organic matter during salinity excursions. *Nature*, 339: 271–274.
- Kroon, D., Alexander, I., Little, M., Lourens, L.J., Mattheewson, A., Robertson, A.H.F., and Sakamoto, T., 1998. Oxygen isotope and sapropel stratigraphy in the eastern Mediterranean during the last 3.2 million years. In Robertson, H.F., Emeis, K., Richter, C., Camerlenghi, A. (eds.), *Proceedings of the Ocean Drilling Program, Scientific Results*, v. 160, p. 181–190, College Station, TX (Ocean Drilling Program).
- Kullenberg, B., 1951. On the salinity of the water contained in marine sediments. *Medd. Oceanogr. Inst. Göteborg* 21, 1–38.
- Kuhnt, T., Schmiedl, G., Ehrmann, W., Hamann, Y., Andersen, N., 2008. Stable isotopic composition of Holocene benthic foraminifers from the Eastern Mediterranean Sea: Past changes in productivity and deep water oxygenation *Palaeogeography, Palaeoclimatology, Palaeoecology* 268, 106–115
- Kullenberg, B., 1952. On the salinity of the water contained in marine sediments, *Medd. Oceanogr. Inst. i Coteborx*, No. 21.
- Latif, M. L., Özsoy, E., Salihoğlu, İ., Gaines, A. F., Baştürk, Ö., Yılmaz, A., Tuğrul, S., 1992. Monitoring via Direct Measurements of the Modes of Mixing and Transport of Wastewater Discharges into the Bosphorus Underflow. Middle East Technical University, Institute of Marine Sciences, Technical Report No. 92-2, 98

pp.

- Lea, D. W., T. A. Mashiotta, and H. J. Spero, 1999. Controls on magnesium and strontium uptake in planktonic foraminifera determined by live culturing, *Geochimica et Cosmochimica Acta*, 63, 2369–2379.
- Lea, D.W., Pak, D.K. and Spero, H.J., 2000. Climate impact of late Quaternary equatorial Pacific Sea surface temperature variations. *Science*, v. 289.
- Loubere, P. (1981). Oceanographic parameters reflected in the seabed distribution of planktonic foraminifera from the North Atlantic and Mediterranean Sea, *Journal of Foraminiferal Research* 11, 137–158. Lykousis V, Chronis G, Tselepidis A, Price NB, Theocharis A, Sikou-Frangou I, Van Wambeke F, Danovaro R, Stavrakakis S, Duineveld G, Georgopoulos D, Ignatiades L, Souvermezoglou A, Voutsinou-Taliadour F. 2002. Major outputs of the recent multidisciplinary biogeochemical researches undertaken in the Aegean Sea. *Journal of Marine Systems* 33–34: 313–334.
- Lykousis, V., 2002. Circulation changes and nutrient concentrations in the late Quaternary Aegean Sea: a nonsteady state concept for sapropel formation. *Paleoceanography* 17, 1024-1034.
- Lykousis, V., 2009. Sea-level changes and shelf break prograding sequences during the last 400 ka in the Aegean margins: Subsidence rates and palaeogeographic implications. *Continental Shelf Research*, 29, 2037–2044.
- Maheras, P., Xoplaki, E., Davies, T., Martin-Vide, J., Bariendos, M., Alcoforado, M.J., 1999. Warm and cold monthly anomalies across the Mediterranean Basin and their relationship with circulation (1860–1990). *Int J Climatol* 19:1697–1715.

- Maldonado, A., Stanley, D.J., 1978. Nile Cone depositional processes and patterns in the Late Quaternary. In: Stanley, D.J., Kelling, G. (Eds.), *Sedimentation in Submarine Canyons, Fans and Trenches*. Dowden, Hutchinson and Ross, Stroudsburg, PA, 365 pp.
- Mashiotta, T. A., D. W. Lea, and H. J. Spero, 1999. Glacialinterglacial changes in subantarctic sea surface temperature and $\delta^{18}\text{O}$ -water using foraminiferal Mg/Ca, *Earth Planet. Sci. Lett.*, 170, 417-432.
- Menzel, D., van Bergen, P. F., Schouten, S. and Sinninghe Damste, J. S., 2003. Reconstruction of changes in export productivity during Pliocene sapropel deposition: a biomarker approach. *Palaeogeography, Palaeoclimatology, Palaeoecology* 190, 273–287.
- Meyer, K.M. and Kump, L.R., 2008. Oceanic Euxinia in Earth History: Causes and Consequences. *Annual Review of Earth and Planetary Science*, 36: 251–88.
- Millot, C., 1987. The circulation of the levantine intermediate water in the Algerian Basin. *Journal of Geophysical Research* 92(C8): doi: 10.1029/JGREA0000920000C8008265000001. issn: 0148-0227.
- Millot, C., 1999. Circulation in the Western Mediterranean sea. *Journal of Marine Systems* 20, 423–442.
- Muerdter, D.R., Kennett, J.P., Thunell, R.C., 1984. Late Quaternary sapropel sediments in the eastern Mediterranean Sea: faunal variations and chronology. *Quaternary Research*, 21, 385–403.
- Müller, C., 1973. Calcareous nannoplankton assemblages of Pleistocene–Recent sediments of the Mediterranean Sea. *Bulletin of Geological Society, Greece* 10,

133–144.

- Müller, P.J., Suess, E., 1979. Productivity, sedimentation rate and sedimentary organic matter in the oceans, I. Organic matation of eastern Mediterranean sapropels. Marine Geol. carbon preservation. Deep-Sea Res. 26A, 1347–1362.
- Murray, J.W., Grundmanis, V. and Smethie, W.J., 1987. Interstitial water chemistry in the sediments of Saanich Inlet. *Geochimica et Cosmochimica Acta*, 42, 1011–1026.
- Nesteroff, W.D., 1973. Petrography and mineralogy of sapropels. In: *Init. Repts. DSDP 13*. Washington, pp. 713–720.
- Nuernberg, D., J. Bijma, and C. Hemleben, 1996. Assessing the reliability of magnesium in foraminiferal calcite as a proxy for water mass temperatures, *Geochimica Cosmochimica Acta*, 60, 803- 814.
- Olausson, E., 1961. Studies in deep-sea cores. Rep. Swed. Deep-Sea Exped. 1947–1948, 8: 337–391.
- Özsoy, E., Latif, M. A., Tuğrul, S., Ünlüata, Ü., 1995. Exchanges with the Mediterranean, fluxes and boundary mixing processes in the Black Sea. In: Briand, F. (Ed.), *Mediterranean Tributary Seas*. Bulletin de l'Institut
- Parisi, E., Erba, E., and Cita, M., 1987. Stratigraphy and sedimentation in the anoxic Bannock Basin (Eastern Mediterranean). *Marine Geology*, 75: 93–117.
- Parker, F.L., 1958. Eastern Mediterranean foraminifera. Reports of the Swedish Deep-Sea Expedition, 1947-1948, 8(4), 353–391.
- Passier H., Bottcher, M. E., Delange, G. J., 1999. Sulphur Enrichment in Organic Matter of Eastern Mediterranean Sapropels: A Study of Sulphur Isotope Partitioning.

- Aquatic Geochemistry, 5, 99–118.
- Pedersen, T.F., 1983. Increased productivity in the eastern equatorial Pacific during the last glacial maximum (19,000 to 14,000 yr B.P.) *Geology* 11, 16–19.
- Pedersen, T.F., Calvert, S.E., 1990. Anoxia vs. productivity: What controls the formation of organic-carbon-rich sediments and sedimentary rocks?. *AAPG Bull.* 74, 454-466.
- Passier, H.F., Middelburg, J.J., de Lange, G.J. and Bottcher, M.E., 1999. Modes of sapropel formation in the eastern Mediterranean: some constraints based on pyrite properties. *Marine Geology*, 153, 199–219.
- Polat, Ç., Tuğrul, S., 1996. Chemical exchange between the Mediterranean and Black Sea via the Turkish Straits. In: Briand, F. (Ed.), *Dynamics of Mediterranean Straits and Channels*. Bulletin de l'Institut Océanographique, Monaco, Special No. 17, CIESME Science Series 2, pp. 167–186.
- Poulos SE, Drakopoulos PG, Collins MB., 1997. Seasonal variability in sea surface oceanographic conditions in the Aegean Sea (Eastern Mediterranean): an overview. *Journal of Marine Systems*, 13:225-244.
- Pratt, L.M., 1984. Influence of paleoenvironmental factors on preservation of organic matter in Middle Cretaceous Greenhorn Formation, Pueblo, Colorado. *American Association of Petroleum Geology Bulletin*, 78, 1146–1159.
- Raiswell, R. and Berner, R.A., 1985. Pyrite formation in euxinic and semi-euxinic sediments. *American Journal of Science*, 285, 710–724.
- Reiss, Z., Halicz, E. and Luz, B., 1999. Late-Holocene foraminifera from the SE Levantine Basin. *Isr. J. Earth Sci.*, 48, 1–17.

- Revel, M., Ducassou, E., Grousset, F. E., Bernasconi, S. M., Migeon, S., Revillon, S., Mascle, J., Murat, A., Zaragosi, S., Bosch, A., 2010. 100,000 Years of African monsoon variability recorded in sediments of the Nile margin. *Quaternary Science Reviews* 29, 1342–1362
- Rohling, E.J., Gieskes, W.W.C., 1989. Late Quaternary changes in Mediterranean intermediate water density and formation rate. *Paleoceanography* 4, 531–545.
- Rohling, E., 1991. A simple two layered model for shoaling of the eastern Mediterranean pycnocline due to glacio eustatic sea level lowering. *Paleoceanography*, 6, 537-541.
- Rohling, E.J., Hilgen, F.J., 1991. The eastern Mediterranean climate at times of sapropel formation: a review. *Geol. Mijn changes in the Mediterranean Sea: hydrographic and depositional effects. Nature* 338, 493-496.
- Rohling, E.J., Jorissen, F.J., Vergnaud Grazzini, C., Zachanasse, W.J. , 1993. Northern Levantine and Adriatic Quaternary planktic foraminifera; Reconstruction of paleoenvironmental gradients. *Marine Micropaleontology*, 21, 191–218.
- Rohling, E. J., 1994. Review and new aspects concerning the formation of eastern Mediterranean sapropels. *Marine Geology*, 122: 1–28.
- Rohling E.J., Grant K., Hemleben C., Siddall M., Hoogakker B.A.A., Bolshaw M. & Kucera M. 2008. High rates of sea-level rise during the last interglacial period. *Nature Geoscience* 1, 38–42.
- Rosenthal, Y. and Lohmann, G.P., 2002. Accurate estimation of sea surface temperatures using dissolution-corrected calibrations for Mg/Ca paleothermometry. *Paleoceanography*, v.17, no.3, 1044.

- Rossignol-Strick, M., Nesterov, W., Olive, P., Vergnaud-Grazzini, C., 1982. After the deluge: Mediterranean stagnation and sapropel formation. *Nature* 295, 105–110.
- Rossignol-Strick, M., 1983. African monsoons, an immediate response to orbital insolation. *Nature* 304, 46–49.
- Rossignol-Strick, M., 1985. Mediterranean Quaternary sapropels, an immediate response of the African monsoon to variation of insolation. *Palaeogeogr. Palaeoclimatol. Palaeoecol.* 49, 237–263.
- Ruddiman, W.F., 1971. Pleistocene sedimentation in the equatorial Atlantic: stratigraphy and faunal paleoclimatology. *Geol. Soc. Am. Bull.*, 82:283–302.
- Ryan, W.B.F., 1972. Stratigraphy of Late Quaternary sediments in the Eastern Mediterranean. In: Stanley, D.J. (Ed.), *The Mediterranean Sea*. Dowden, Hutchinson and Ross, Stroudsburg, PA, pp. 1–765.
- Saaroni, H., Ziv, B., Edelson, J. and Alpert, P., 2003. Long-term variations in summer temperatures over the Eastern Mediterranean. *Geophysical Research Letters*, 30(18), 1946.
- Sancetta, C., 1994. Mediterranean sapropels: seasonal stratification yields high production and carbon flux. *Paleoceanography*, 9: 195–196.
- Sarmiento, J., Herbert, T. and Toggweiler, J.R., 1988. Mediterranean nutrient balance and episodes of anoxia. *Global Biogeochemical Cycles* 2(4): doi: 10.1029/88GB03434. issn: 0886-6236.
- Shackleton, N. J., 1965. The High-Precision Isotopic Analysis of Oxygen and Carbon in Carbon Dioxide. *Journal of Scientific Instruments*, 42: 689-92.
- Schrader, H., Matherne, A., 1981. Sapropel formation in the eastern Mediterranean Sea:

- evidence from preserved opal assemblages. *Micropaleontology* 27, 191–203.
- Shaw, H. F., and Evans, G., 1984. The nature distribution and origin of a sapropelic layer in the sediments of the Cilicia Basin, north eastern Mediterranean. *Marine Geology*, 61: 1–12.
- Sigl, W., Chamley, H., Fabricius, F., Giroud d'Argoud, G., and Mueller, J., 1978. Sedimentology and environmental conditions of sapropels. *In* Hsü, K.J., Montadert, L., et al., *Init. Repts. DSDP, 42: Washington (U.S. Govt. Printing Office)*, 445–465.
- Sprovieri, R. Thunell, R. and Howell, M., 1986. Paleontological and geochemical analysis of three laminated sedimentary units of late Pliocene—early Pleistocene age from the Monte San Nicola section in Sicily Riv. Ital. *Paleontol.*, 92, pp. 401–434.
- Stanley, D. J. and Blanpied, C., 1980. Late Quaternary water exchange between the eastern Mediterranean and the Black Sea. *Nature*, 285, 537–541.
- Stratford, K. and Haines, K., 2002. Modelling nutrient cycling during the eastern Mediterranean transient event 1987–1995 and beyond. *Geophysical Research Letters*, VOL. 29, 1035, 4 PP., 2002
- Tang, C.M., Stott, L.D., 1993. Seasonal salinity changes during Mediterranean sapropel deposition 9000 years B.P.: evidence from isotopic analyses of individual planktonic foraminifera. *Paleoceanography* 8 (4), 473–493).
- Theocharis, A., E. Balopoulos, S. Kioroglou, H. Kontoyiannis, and A. Iona, 199a. A synthesis of the circulation and hydrography of the south Aegean Sea and the Straits of the Cretan Arc (March 1994-February 1995). *Progress in Oceanography*,

44 (4), 469–509.

- Thunell, R.C., Williams, S.D.F., Kennett, J.P., 1977. Late Quaternary paleoclimatology, stratigraphy and sapropel history in eastern Mediterranean deep-sea sediments. *Marine Micro pal.* 2, 371–388.
- Thunell, R.C., Williams, D.F., Belayea, P., 1984. Anoxic events in the Mediterranean Sea in relation to the evolution of late Neogene climates. *Marine Geol.* 59, 105–134.
- Thunell, R., Williams, D. and Howell, M., 1987a. Atlantic-Mediterranean water exchange during the late Neogene. *Paleoceanography*, 2: 661–678.
- Thunell, R.C., Williams, D.F., 1989. Glacial–Holocene salinity changes in the Mediterranean Sea: hydrographic and depositional effects. *Nature* 338, 493–496.
- Thunell, R., Williams, D., Tappa, E., Rio, D. and Raffi I., 1990, Pliocene-Pleistocene Stable Isotope Record for Ocean Drilling Program Site 653, Tyrrhenian Basin: Implication for the Paleoenvironmental History of the Mediterranean Sea, in Kastens, K.A., Mascle, J., et al., eds, *Proc. ODP Sc. Result.*, v. 107, pp. 387-399. College Station, TX (Ocean Drilling Program).
- Williams, D.F., Thunell, R.C., 1979. Faunal and oxygen isotopic evidence for surface water salinity changes during sapropel formation in the eastern Mediterranean. *Sediment. Geol.* 23, 81–93.
- Van Straaten, R.M.V.U., 1972. Holocene stages of oxygen depletion in waters of the Adriatic. In: Stanley, D.J. (Ed.), *The Mediterranean Sea: A Natural Sedimentation Laboratory*. Dowden, Hutchinson and Ross, Stroudsburg, PA, 631pp.
- Velaoras, D. and Lascaratos, A., 2005. Deep water mass characteristics and interannual variability in the North and Central Aegean Sea *Journal of Marine Systems* 53,

59–85.

Vergnaud Grazzini, C., Ryan, W.B.F., Cita, M.B., 1977. Stable isotope fractionation, climate change and episodic stagnation in the Eastern Mediterranean during the Late Quaternary. *Mar. Micropaleontol.* 2, 353–370.

Vergnaud Grazzini, C., 1985. Mediterranean late Cenozoic stable isotope record: Stratigraphic and paleoclimatic implications. In: Stanley, D.J., Wezel, F.C. (Eds.), *Geological Evolution of the Mediterranean Basin*. Springer, New York, pp.413–451.

Vergnaud Grazzini, C., Devaux, M., Znaidi, J., 1986. Stable isotope anomalies in Mediterranean Pleistocene records. *Marine Micropaleontology* 10, 35- 69.

Wu, D.J., Chao, J.K. and Lepping, R.P., 2000. Interaction between an interplanetary magnetic cloud and the Earth's magnetosphere: Motions of the bow shock. *Journal of Geophysical Research* 105(A6): doi: 10.1029/1999JA000265. issn: 0148-0227.

Yaltrak, C. and Alpar, B., 2002. Kinematics and evolution of the northern branch of the North Anatolian Fault (Ganos Fault) between the Sea of Marmara and the Gulf of Saros. *Marine Geology*, 190, 351–367.

Yaşar, D., 1994. Late glacial–Holocene evolution of the Aegean Sea. Ph.D. Thesis, Inst. Mar. Sci. Technol., Dokuz Eylül Univ., 329 pp. (Unpubl.)

Yüce, H., 1991. Water level variations in the northeastern Aegean Sea. *Doğa-Tr. J. of Engineering and Environmental Sciences, TÜBİTAK*, 15, 179–187.

Zahn, R., Sarthein, M. and Erlenkeuser, H., 1987. Benthic isotope evidence for changes

of the Mediterranean outflow during the late Quaternary. *Paleoceanography*, 2:
543–559.

Zahn, R., Pedersen, T.F., 1991. Late Pleistocene evolution of surface and mid-depth hydrography at the Oman Margin: planktonic and benthic isotope records at ODP Site 724. *Proc. ODP, Sci. Results* 117, 291–308.

Zervakis, V., Georgopoulos, D., Drakopoulos, P.G., 2000. The role of the North Aegean in triggering the recent Eastern Mediterranean climatic changes. *Journal Geophysical Research* 105 (C11), 26103-26116.

Zervakis, V., D. Georgopoulos, A.P. Karageorgis, and A. Theocharis, 2004. On the response of the Aegean sea to climatic variability: a review, *International Journal of Climatology*, 24, 1845-1858.

Chapter 2. LATE QUATERNARY CHRONOSTRATIGRAPHY OF THE AEGEAN SEA WITH SPECIAL REFERENCE TO THE AGES OF SAPROPELS S1-S5

Abstract

The chronostratigraphy of Aegean Sea sediments was determined using five long piston cores collected from different subbasins of the Aegean Sea. The penetration depths and organic carbon contents of the piston cores and chronostratigraphic reconstructions collectively demonstrate the presence of MIS5 sapropels S3, S4 and S5 in the Aegean Sea subbasins. The presence of sapropels S3 and S4 in all five cores and the consecutive presence of all three MIS5 sapropels at least in two cores (North Skiros and Mikonos basins) demonstrate the suitability of conditions in the Aegean Sea for sapropel deposition.

Calculated average sedimentation rates range between 4.7 and 11.8 cm/ka, with highest rates being observed in Euboea and North Ikaria basins (9.8 and 11.8 cm/ka, respectively). Throughout the Aegean Sea the initiation of sapropels S4 and S5 mostly predated those in the eastern Mediterranean, with S4 and S5 onset ranging from 106.4–105.6 and 128.6–128.4 ka BP, respectively. On the other hand, the 83.2–80.4 ka BP initiation of sapropel S3 agrees well with its eastern Mediterranean counterpart but also postdates by several thousand years in the northernmost cores, which highlights the heterogeneity of the Aegean Sea subbasins in terms of rapid vs. lagged response to changing climatic conditions. The sapropel initiations were abrupt; whereas, the timing

of sapropel terminations was apparently controlled both by the amplitude of paleoclimatic changes and the physiography/location of the subbasins. However, the impact of possible sapropel burndown-fronts cannot be ruled out, which could mask the true ages of sapropel terminations.

The calculated age of the Nisyros tephra does not agree with its previously published age and suggests that future refinement of its chronology might be required. The ash layer defined as X1 in core MAR03-2 requires detailed geochemical analysis in order to make an accurate identification and correlation to known eruptions.

2.1. Introduction

Pleistocene sediments of the eastern Mediterranean Sea contain multiple dark organic carbon-rich layers (sapropels) that have been extensively studied since their first discovery during the Swedish Deep Sea Expedition in 1947 (Kullenberg, 1952). A quantitative definition of a sapropel was first proposed by Kidd et al. (1978) as 'an individual layer that is at least 1 cm thick, deposited in an open marine environment containing >2% total organic carbon by weight'. Kidd et al. (1978) further defined sapropelic sequences as being similar marine deposits containing between 0.5 and 2 wt% total organic carbon. It is difficult in practice to apply such a quantitative classification because organic carbon content can vary in the same lithological layer from 1 to >5 wt%, hence a part of this layer fits the Kidd et al. (1978) definition of sapropel, while the rest does not. Fontugne and Calvert (1992) and Hilgen (1991) defined sapropels and sapropelic sediments as horizons where organic carbon content is higher than 1 wt% and 0.5 wt%, respectively. In a more recent paper, Murat and Got (2000) indicated that the

organic carbon content in eastern Mediterranean sediments generally ranges from 0.1 to 0.5 wt%, but the organic carbon content in sapropel is always higher than 1 wt%. They suggested that this 1 wt% value seems to be more appropriate for sapropel definition in the eastern Mediterranean basin than the value of 2 wt% proposed by Kidd et al. (1978). Furthermore, a study from Bannock Basin, a hypersaline anoxic deep basin in the eastern Mediterranean, shows that the organic carbon content of the most recent sapropel S1 is about 3–4 wt% higher than the overlying surficial sediments (Howell and Thunell, 1992). Murat and Got (2000) pointed out that this 3–4 wt% difference is also observed in other areas of the Eastern Mediterranean basin, where presently oxic bottom waters prevail. Calvert and Karlin (1998) studied sediment cores from the Black Sea and showed that sapropel and non-sapropel (marl) units contain 5–20 wt% and 2–6 wt% organic carbon, respectively. In addition, they indicated that the accumulation rate of organic carbon in a sapropel is not significantly different from that in non-sapropel units; instead, there is less dilution of the organic fraction in sapropels by the other detrital components. Rather than using an absolute value, considering the organic carbon content differences between sapropels and underlying and overlying sediments (i.e., background) seems to be a more reasonable strategy for the definition of a sapropel layer.

Sapropels and sapropelic sediments represent times when the input of organic carbon exceeded its removal by oxidation. This could happen if anoxic/dysoxic bottom-water conditions largely prevented oxidation of TOC on the sea floor and/or if increased surface-water productivity significantly increased the input of organic matter to the sea floor. Neither situation exists today in the eastern Mediterranean Sea.

Two main hypotheses (i.e., anoxia versus primary productivity) and several

models have been postulated for the formation of sapropel layers; however, the primary mechanisms leading to increased organic-carbon accumulations are still not entirely resolved despite the generally accepted facts that (1) sapropels coincide with times of astronomical precessional minima (Fig.2.1) and (2) modified hydrographic settings associated with enhanced precipitation and continental runoff generally took place during their formation (Fig. 2.1; Rossignol-Strick et al., 1982, 1985; Rohling and Hilgen, 1991).

Until relatively recently, chronostratigraphic reconstructions of late Quaternary marine sapropel-containing sequences were solely based upon radiometric dating techniques and graphic correlation with similar sequences elsewhere. Following the recognition of the importance of the astronomical time scale to pelagic and hemipelagic marine sedimentation, the deposition of successive sapropels in the eastern Mediterranean Sea has been related to astronomical forcing of the climate. Individual sapropels were correlated with times when perihelion falls in the boreal (Northern Hemisphere) summer (precessional minima) resulting in a summer insolation maximum in the Northern Hemisphere (NH) (Fig. 2.1; Rossignol-Strick, 1983; Hilgen, 1991a).

The Aegean Sea is one of the most intriguing areas for paleoceanographic and paleoclimatic studies due to its high sensitivity to global climatic changes that results from its confined geography, semi-isolation from the rest of the Mediterranean Sea, and abundance of local freshwater inputs particularly because of its location on the pathway of Black Sea–Mediterranean Sea water exchange (Aksu et al., 1995; Yalçırak et al., 2002). Following the first recognition of sapropel layers in the Aegean Sea (Ninkovich and Heezen, 1967), numerous gravity and piston cores were collected throughout the Aegean Sea, primarily to investigate the most recent sapropel layer S1, the age of which

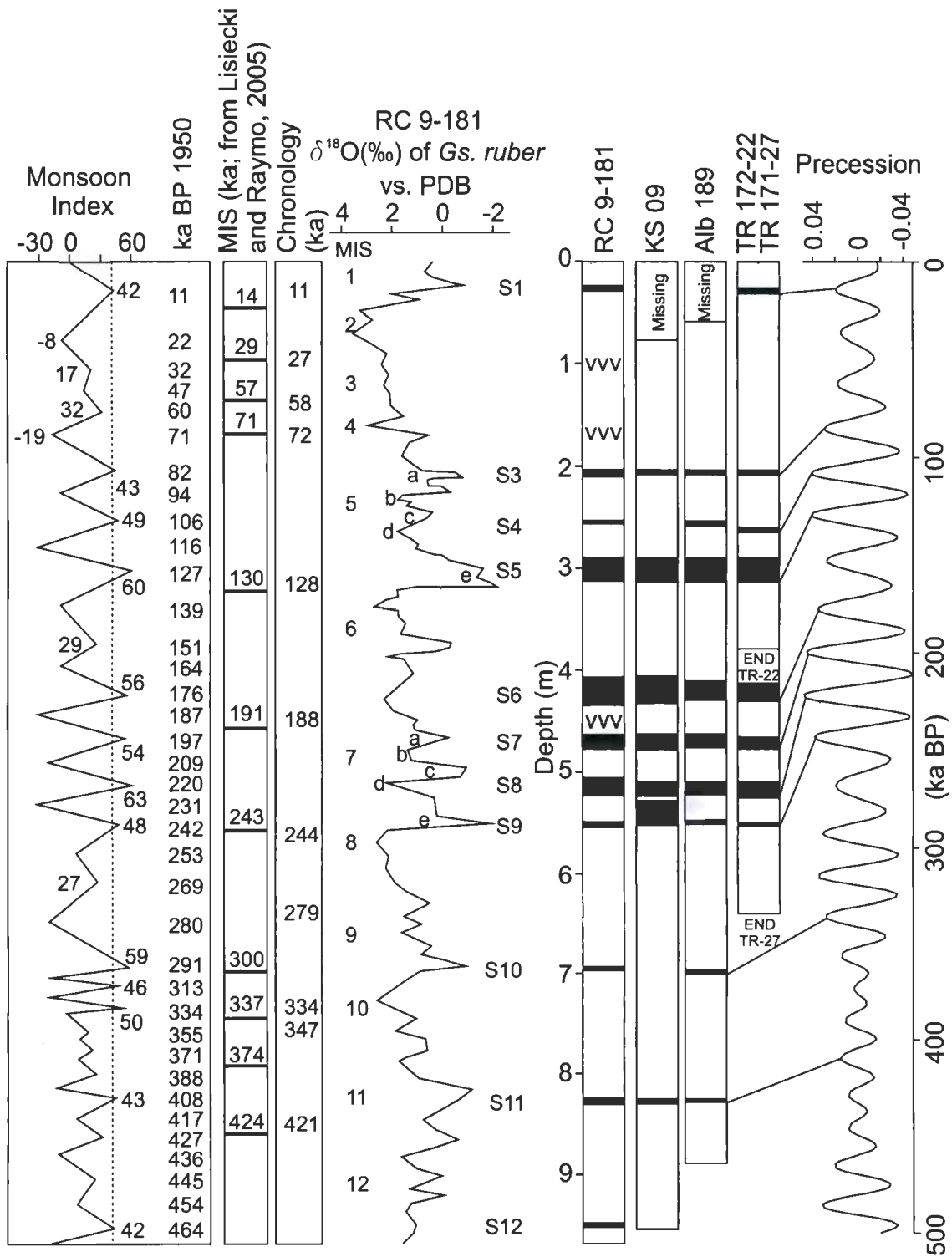


Figure 2.1. Correlation of the variation of the insolation monsoon index and the geological record of the eastern Mediterranean Sea sapropels during the last 465 ka (from Rossignol-Strick, 1983). First column: Monsoon index (sum of insolation at the Tropic of Cancer and gradient of insolation between the Tropic of Cancer (warm) and the Equator (cool)). Dashed line in monsoon index is the threshold value considered to be prerequisite for sapropel formation. Numbers right of the monsoon index are the astronomical chronology. Second column is the marine isotopic stages from Lisiecki and Raymo (2005). Third column is the chronology of the isotopic stage boundaries. Next is a plot of Oxygen isotope stratigraphy of core RC 9-181, based on *Globigerinoides ruber*. Fourth column show the correlation of sapropels S1 to S12 in RC 9-181 (true depth scale) with other eastern Mediterranean cores (no depth scales implied). Precession curve is from Peter Huybers (<http://www.people.fas.harvard.edu/~phuybers/Inso/index.html>)

is well constrained by radiocarbon dating (^{14}C). Notwithstanding the existence of a 13.5 m-long piston core (i.e. LC21 [water depth 1520 m]; 35°39.71' N, 26°34.96' E) collected in 1995 by RV *Marion Dufresne* from southern Aegean Sea (northeast of Crete), which includes sapropel S5, a continuous chronostratigraphy of the Aegean Sea sediments encompassing the time of deposition of sapropels S1 through S5 has not yet been published. The purpose of this chapter is to provide a chronology for sapropel layers S1–S5 in the Aegean Sea as a framework for future paleoceanographic and paleoclimatic studies.

2.1.1. Earth's Orbital Parameters

Climate is sensitive to both the total amount, and the latitudinal and seasonal distribution of solar radiation onto the surface of the planet. Three astronomical cycles are of relevance: the eccentricity cycle, the precession cycle and the obliquity cycle (Lascar et al., 1993).

The precessional cycle is caused by changes in the direction of the tilt of Earth's rotational axis relative to the plane of Earth's orbit around the sun. Precession causes the north pole, which today points towards Polaris, to point towards Vega (which then becomes the North Star) after half a precession cycle, and back towards Polaris again after a complete precessional cycle. A full cycle of precession takes 26,000 years; however, because of the rotation of Earth's orbit around the sun, the precessional cycle occurs at two dominant periodicities: 23,000 years and 19,000 years.

The eccentricity cycle derives from variations in the shape of Earth's orbit around the sun and is defined as the ratio of the focal length of the ellipse (the distance between

the foci) to the length of its major axis. The eccentricity of Earth's orbit about the sun changes in a cyclic fashion, with three main periods: 94,800 years, 123,800 years and 404,000 years (~100,000 and ~400,000 years) and has ranged from less than 0.01 (eccentricity minima) to more than 0.05 (eccentricity maxima) over the past 600 ka. Today Earth's orbit is slightly elliptical (eccentricity close to 0.02).

Obliquity is the change in the angle of Earth's rotation axis relative to a perpendicular to the plane of Earth's orbit around the sun. This angle changes from 22.5° to 24.5° (presently 23.5°) and back again over a period of 41,000 years.

Today, Earth is at perihelion (closest approach to the sun) around the time of the boreal (northern hemisphere) winter solstice and, accordingly, at aphelion around the time of the boreal summer solstice. This means that the solar radiation for the planet as a whole is more intense in boreal winter (austral – southern hemisphere – summer) than in the boreal summer (austral winter). Effectively, this weakens the seasonal contrast in the northern hemisphere, whereas in the southern hemisphere it is strengthened. About half a precession cycle ago (i.e., at ~11,000 yr BP), the orbital configuration would have been the reverse of the current geometry with perihelion near the boreal summer solstice and aphelion around the time of the boreal winter solstice (enhanced seasonal contrast on the northern hemisphere).

The precession and obliquity cycles govern the seasonal insolation contrast, but its impact depends on the degree of eccentricity of the orbit. For instance, in a circular orbit the precessional cycle has no impact, while in times of maximum eccentricity the precessional cycle reaches maximum impact.

2.1.2. Physiography of the Aegean Sea

The Aegean Sea is an ~610 km-long and ~300 km-wide shallow elongate embayment situated in the northeastern Mediterranean Sea between mainland Turkey in the east and Greece in the west. To the north, it is connected to the Black Sea through the straits of Dardanelles and Bosphorus and the small land-locked Marmara Sea. In the south, the Aegean Sea communicates with the eastern Mediterranean Sea through several broad and deep straits located between the Peloponnesus Peninsula, Kythira, Antikithyra and the western end of the island of Crete in the southwest, and between Turkey and the islands of Rhodes, Karpathos, Kasos and the eastern end of the island of Crete in the southeast (Fig. 2.2).

The bottom topography of the Aegean Sea is characterized by an alternation of shelves and sills with intervening basins. The Aegean Sea is divided into three physiographic regions (Fig. 2.2): the northern Aegean Sea, including the North Aegean Trough; the central Aegean plateaux and basins; and the southern Aegean Sea including the Cretan Trough.

The dominant bathymetric feature in the northern portion of the Aegean Sea is the North Aegean Trough (Fig. 2.2). It forms a narrow and arcuate, 800–1200 m-deep bathymetric depression which extends from Saros Bay with a WSW trend, swinging to a more southwesterly trend and widening toward the west. The North Aegean Trough comprises a number of interconnected depressions (Fig. 2.2).

The central Aegean Sea is characterized by a series of shallower (600–1100 m), generally NE-trending depressions, including the North and South Skiros, Lesbos, Psara, Euboea, Mikonos, and North and South Ikaria basins, and their intervening 100–300 m-

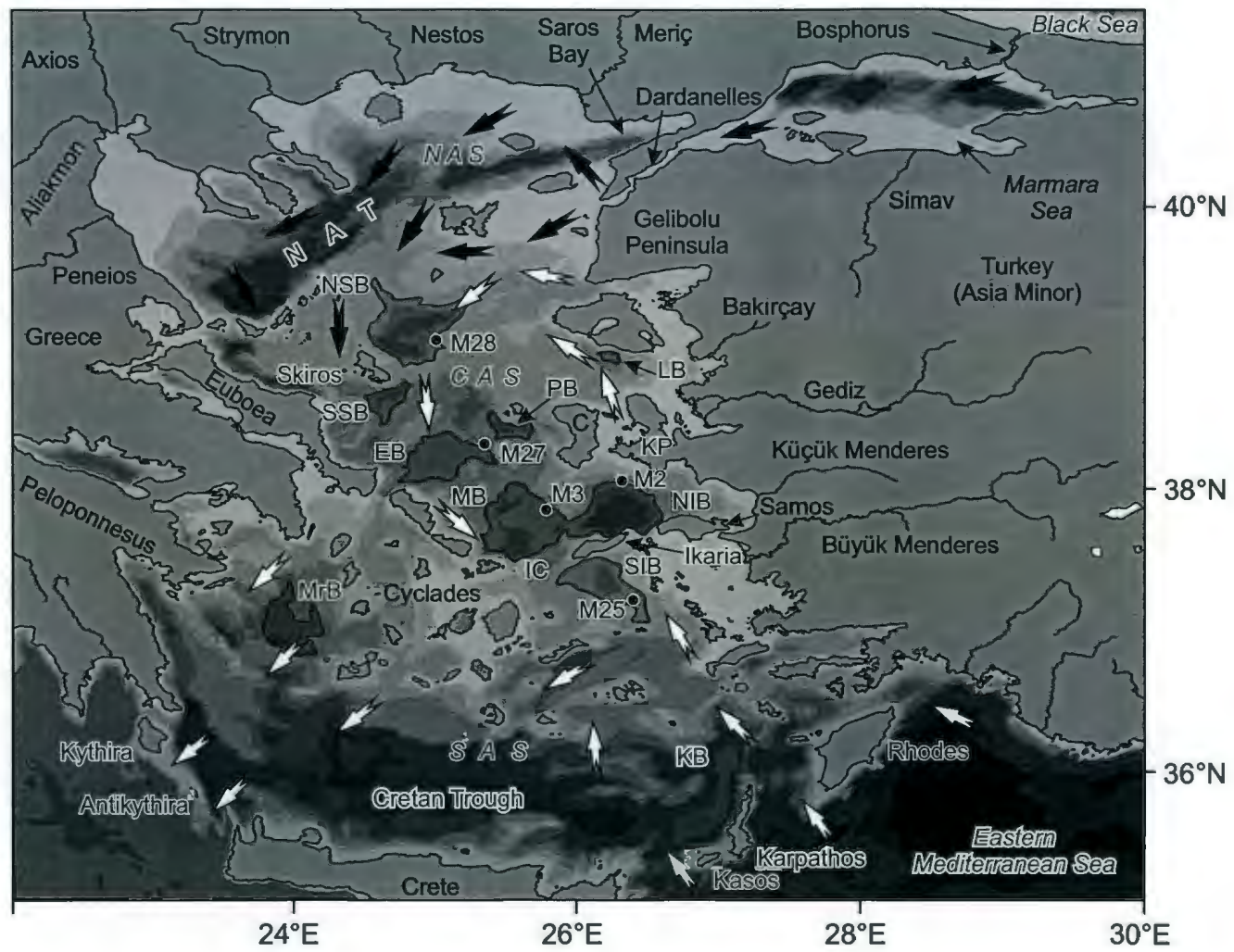


Figure 2.2. Simplified map of the Aegean Sea and surroundings showing the core locations, major rivers, subbasins and circulation pattern. Light to progressively darker grey tones represent <100 m and 200-1000 m depths (at 200 m intervals). The black zone in the southeast of the map is >1200m deep. Outlined contours highlight the limits of subbasins. NAS-North Aegean Sea, NAT-North Aegean Trough, NSB-North Skiros Basin, SSB-South Skiros Basin, CAS-Central Aegean Sea, LB-Lesbos basin, EB-Euboea Basin, MB-Mikonos Basin, PB-Psara Basin, NIB-North Ikaria Basin, IC-Ikaria Channel, SIB-South Ikaria Basin, SAS-South Aegean Sea, KP-Karaburun Peninsula, C-Chios Island. Black and white arrows illustrate the surface water circulation of the Black Sea and the Mediterranean Sea waters, respectively. Core names are abbreviated; e.g., 'M' stands for 'MAR03'.

deep shoals and associated islands (Fig. 2.2). South Ikaria Basin is a NW–SE-oriented, >600-m-deep elongate depression situated south of the island of Ikaria. Mikonos and North Ikaria basins occupy the southern part of the central Aegean Sea and have maximum depths of 800 and >1000 metres, respectively. Mikonos Basin is situated north of the Ikaria Channel and has a concave-eastward geometry with the deeper portions (>800 m) in its western part. It is linked in the east to North Ikaria Basin, which is a bowl-shaped depression reaching >1000 m depths. It is surrounded by the islands of Ikaria and Samos in the south and by the Chios Island and the Karaburun Peninsula in the north. The Mikonos Basin has a relatively steeper northern slope, whereas the North Ikaria Basin has a relatively steeper southern slope (Fig. 2.2). Euboea Basin is a comparatively shallow basin with maximum depths ranging between 600 and 700 m. Its western slope is notably steeper than the eastern side where a gently sloping floor extends toward the Psara Basin. The Euboea Basin is separated from the Mikonos and South Skiros basins by broadly NE–SW-trending shoals (Fig. 2.2). North Skiros Basin is a broadly NE–SW-oriented depression with a maximum depth of 1000 metres; it is situated at the northern edge of the central Aegean Sea and is separated from the North Aegean Trough and south Skiros Basin by 100–200 m-deep shoals (Fig. 2.2). Southwestern and eastern slopes of the North Skiros Basin are steeper than those in the northwest. The basin extends northeast toward the Gelibolu Peninsula.

The southern Aegean Sea is separated from the central Aegean Sea by the arcuate Cyclades, a convex-southward shallow volcanic arc dotted by numerous islands and shoals extending from the southern tip of Euboea Island to southwestern Turkey (Fig. 2.2). A large, 1000–2000 m-deep, generally E–W-trending depression, the Cretan

Trough, occupies the southernmost portion of the Aegean Sea immediately north of Crete. The two smaller Myrtoon and Karpathos basins occur in the northwestern and eastern portions of the Cretan Trough, respectively.

Although the shelves surrounding the Aegean Sea are generally 5–25 km wide, they widen considerably to ~ 65–75 km off the mouths of major rivers such as the Meriç, Nestos, Strymon, Axios, Aliakmon, Peneios, Büyük Menderes and Bakırçay rivers (Fig. 2.2).

2.1.3. Hydrography of the Aegean Sea

The physical oceanography of the Aegean Sea is controlled primarily by the regional climate, the freshwater discharge from major rivers draining southeastern Europe, and seasonal variations in the Black Sea surface-water outflow through the Strait of Dardanelles (Aksu et al., 1995). Previous studies concerning the hydrographic conditions reveal that the surface water of the Aegean Sea circulates in a cyclonic gyre (Fig. 2.2; Lykousis et al., 2002). A branch of the westward flowing Asia Minor current deviates toward the north out of the eastern Mediterranean basin and enters the Aegean Sea through the eastern straits in the vicinity of Rhodes. This current carries the warm (16–25°C) and highly saline (39.2–39.5psu) Levantine Surface Water (LSW) and Levantine Intermediate Water (LIW) masses along the Turkish western coast and occupies the uppermost 400 m of the water column. Farther north, over the Lesvos shelf, this water mass encounters the Black Sea Water (BSW) as it flows outward through the Dardanelles. They interact to form a strong thermohaline front where the LSW and LIW sink below the more buoyant relatively cool (9–22°C) and less saline (22–23psu) thin

layer of BSW (Aksu et al., 1995). Hence, the water column structure in the northern and central Aegean Sea is comprised of a 20–70 m-thick veneer of modified BSW with mean summer and winter temperature and salinity values ranging between 23–13°C and 34.7–37.7psu, respectively. Below it is an intermediate layer of Levantine waters (mostly LIW) extending down to 400 m. This water mass has relatively smaller temperature and salinity variations. Temperature ranges between 15–18°C and 11–16°C during summer and winter, respectively. Salinity ranges between 39.0 and 39.1psu. The water column below 400 m is occupied by the locally formed North Aegean Deep Water (NAeDW) with uniform temperature (13–14°C) and salinity (39.1–39.2psu) (Aksu et al., 1995; Zervakis et al., 2000; Zervakis et al., 2004; Velaoras and Lascaratos, 2005). The surface and intermediate waters follow the general counter-clockwise circulation of the Aegean Sea, and progressively mix together as they flow southwards along the east coast of Greece.

2.2. Source of Data and Methods

2.2.1. Core collection and sample preparation

The data set is derived from five long piston cores and their trigger-weight gravity cores collected during the 2003 cruise MAR-03 of the RV *Koca Piri Reis* of the Institute of Marine Sciences and Technology (Dokuz Eylül University, Izmir, Turkey). Piston cores were acquired with a 9–12 m-long Benthos piston corer with 300 kg head weight. The trigger corer was a 2 m-long gravity corer, and was deployed to allow quantification of the amount of missing section at the tops of the piston cores. Core locations are

Cores	Latitude	Longitude	PC length (cm)	TWC length (cm)	PC missing top (cm)	CC length (cm)	Water depth (m)
MAR03-2	38°03.97'N	26°22.30'E	776	86	37	813	398
MAR03-3	37°51.72'N	25°49.17'E	580	50	24	604	720
MAR03-25	37°10.36'N	26°26.55'E	604	25	25	629	494
MAR03-27	38°18.68'N	25°18.97'E	952	106	80	1032	651
MAR03-28	39°01.02'N	25°01.48'E	726	165	100	826	453

Table 2.1. Core locations, piston (PC), gravity (TWC), composite (CC) core lengths and water depths.

provided in Figure 2.2 and Table 2.1. Core locations were taken using an onboard GPS (Global Positioning System) receiver; water depths at the coring sites were calculated from 12 kHz echo-sounder data using an acoustic velocity of 1480 m s⁻¹.

Cores were recovered from different subbasins of the Aegean Sea to establish a comprehensive understanding of the past oceanographic and climatic changes that occurred during the late Pleistocene to Holocene. Three cores (MAR03-28, MAR03-25, MAR03-2) were collected from the slopes of the basins at a depth range of 400–500 metres. Cores MAR03-27 and MAR03-3 were collected from deeper basin centres at depths of 651 m and 720 m, respectively (Table 2.1).

Cores were shipped to Memorial University of Newfoundland, where they were split and described by R. N. Hiscott. Sediment colour was determined using the 'Rock-Color Chart' published by the Geological Society of America in 1984. Sample preparation involved collection of 2 cm-wide "half-round" samples (~20 cm³) at 10 cm intervals from each core, then subsampling of approximately 7 cm³ of sediment for organic geochemical/stable isotopic analyses, and 13 cm³ of sediment for inorganic stable isotope analyses and faunal studies.

For inorganic stable isotope analyses (i.e., $\delta^{18}\text{O}$, $\delta^{13}\text{C}$), samples are dried in a 40°C oven for 48 hours, weighed and subsequently put in glass beakers to be disaggregated in 100 cm³ of distilled water containing 15 cm³ of 1% Calgon (Na-hexametaphosphate) and 10 cm³ of 30% hydrogen peroxide. Samples were wet sieved through a 63 μm sieve to remove the mud fraction, dried, weighed again and placed in glass vials.

2.2.2. Laboratory Methods

For oxygen isotopic analyses, only clean and intact planktonic and benthic specimens of $>150\mu\text{m}$ *Globigerinoides ruber* and *Uvigerina mediterranea* were used. At a few intervals, where *Gs. ruber* was absent, *Globigerina bulloides* and *Neogloboquadrina pachyderma* were used instead. Calibration of the oxygen isotope values between these three species was determined in 30 samples containing both *Gs. ruber* and *G. bulloides* and 15 samples containing both *G. bulloides* and *N. pachyderma*. The downcore oxygen isotope variations of the six cores were obtained predominantly from carbonate tests of benthic foraminifera (except core MAR03-27) for a better correlation with the global oxygen isotope curve. Cores MAR03-27 and MAR03-28 were sampled in 2004 and oxygen isotope analyses were conducted on planktonic foraminifera. In cores MAR03-28 and MAR03-2, both benthic and planktonic oxygen isotope curves were obtained.

For each sampling interval, 16–20 (average 18) planktonic and 4–6 (average 5) benthic foraminifera specimens were hand-picked (~ 0.25 mg of CaCO_3), cleaned in distilled water, dried in an oven at 50°C and placed in 12 ml autoinjector reaction vessels. The vials were covered with Exetainer screw caps with pierceable septa, and were placed in a heated sample holder held at 70°C . Using a GC Pal™ autoinjector, the vials were flushed with He (Ultra High Purity grade) for 5 min using a double-holed needle connected by tubing to the He gas source. Sample vials were then manually injected with 0.1 ml of 100% H_3PO_4 using a syringe and needle. A minimum of 1 hour was allowed for carbonate samples to dissolve in the phosphoric acid. The samples were analysed using a triple-collector Thermo Electron Delta V Plus™ isotope ratio mass spectrometer.

The GC Pal™ autoinjector collects the headspace in each vial using a double-holed needle. The needle is flushed with a He carrier gas. The sample gas from the vial and the He are carried through the tubing and into a Thermo Electron Gas Bench II™. The Gas Bench II™ acts as an interface between the samples in the vials and the mass spectrometer. Using a sampling loop, portions of the sample gas are injected onto a 25 m x 0.32 mm Poraplot Q™ fused silica capillary gas chromatograph (GC) column in the Gas Bench II™ to isolate the CO₂ fraction. Nafion™ water traps remove water vapour from the gas stream. The CO₂ sample gas is then carried by the He carrier gas via an open slit tube into the source of the mass spectrometer. Eight injections of sample gas were taken for each sample analysis. Another open split tube allows the injection of a reference gas (CO₂) into the source. Reference gases were prepared from three different standards of known isotopic composition using the same methods employed for the unknown samples, and were used to calibrate each run. The $\delta^{18}\text{O}$ and $\delta^{13}\text{C}$ values are reported with respect to the Pee Dee Belemnite standard.

The amount of total organic carbon (TOC) was determined using a Carlo-Erba NA 1500 Elemental Analyzer coupled to a Finnegan MAT 252 isotope-ratio mass spectrometer (IRMS). Samples were acidified using 30% HCl, and carbonate-free residues were dried overnight in an oven at 40°C. A small amount of sample (15 mg) was transferred into 4–6 mm tin capsules which were then sealed in preparation for analysis. Total organic carbon in the samples was converted to CO₂, SO₂, H₂O and other oxidized gases in the oxidation chamber and then passed through a reduction reagent, a Mg(ClO₄)₂ water trap and a 1.2 m Poropak QS 50/80 chromatographic column at 70°C for final

isolation. TOC quantification from measurement of generated CO₂ was accomplished using an external standard (sulphanilamide, C₆H₈N₂O₂S) and a thermal conductivity detector (TCD). From the TCD, the CO₂ was carried by He to a ConFloII interface, which allows a portion of the He and combustion gases to enter directly into the ion source of the IRMS for carbon and sulfur isotopic measurements. The TOC concentrations in the samples are back-calculated as a percentage of the dry weight of the sediment.

2.3. Results

2.3.1. Lithologic units

Based on organic carbon content and colour, seven lithologic units in cores MAR03-2, MAR03-25 and MAR03-27, and nine lithologic units in cores MAR03-28 and MAR03-3 are identified (Fig. 2.3a, b, c). These units are labelled as 'A' through 'I' from top to bottom; units A–E are present in all cores. Using the oxygen isotope curves of the cores together with the stratigraphic positions of ash layers, it is possible to correlate the lithologic units among the cores (Fig. 2.4). The isotopic curves and ash layers provide synchronous markers, whereas the sapropels might be diachronous. Throughout the cores, sapropel units are distinguished by their comparatively darker colours and, accordingly, higher organic carbon contents. However, a quantitative threshold (>0.5%, >1% or >2% TOC content) is not considered as a prerequisite to identify the unit as a sapropel. Instead, the organic carbon content must be twice the background level measured in underlying and overlying units. Macroscopically, both sapropel and non-

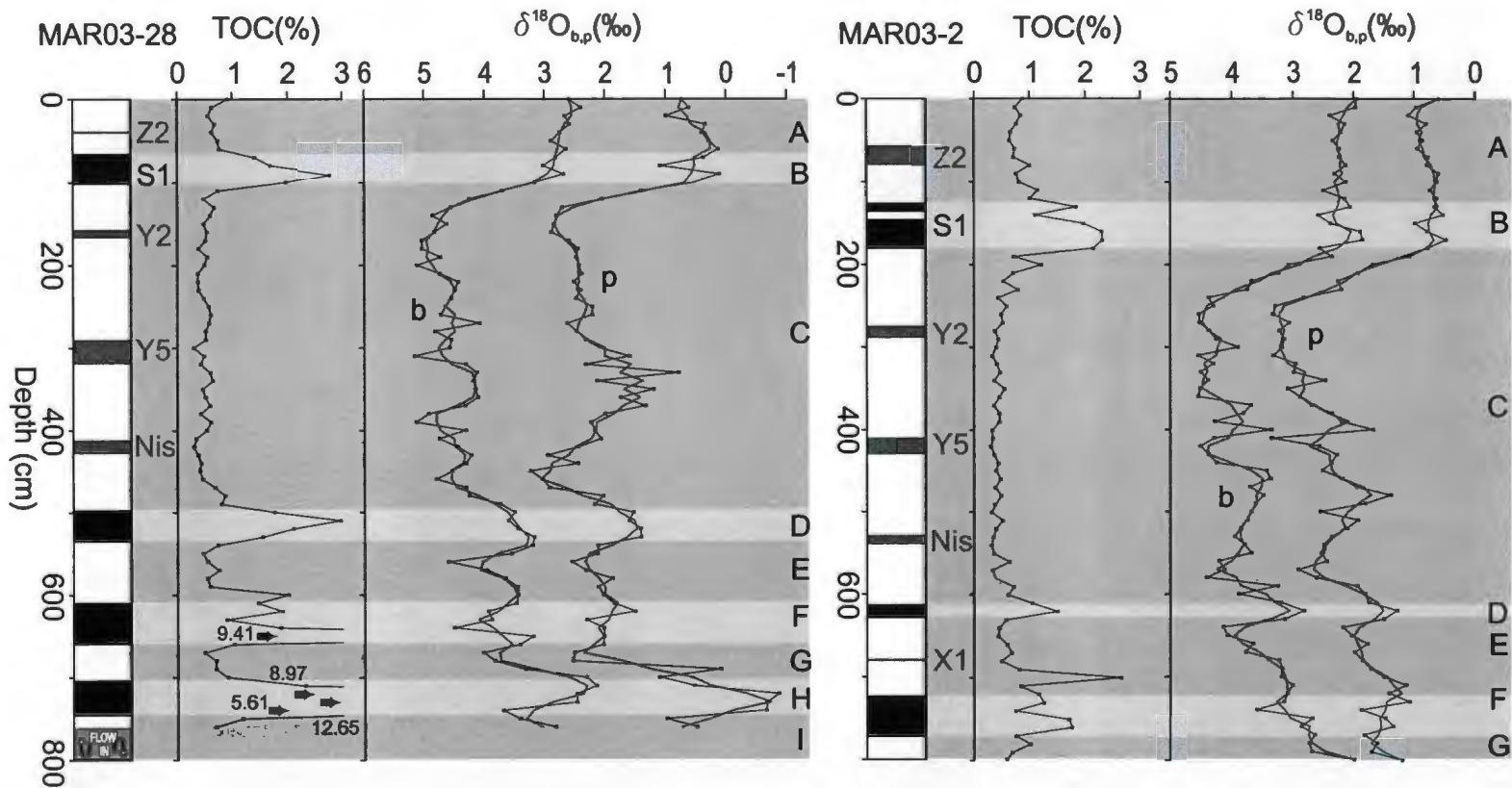


Figure 2.3a. Sapropel and nonsapropel units in the five cores and their assignment to one of ten lithologic units. Also shown are the downcore variations of TOC and oxygen isotope values. In all cores horizontal scales of TOC and $\delta^{18}O$ plots are the same. Red curves are 3-point moving averages. Grey area at the bottom of core MAR03-28 is flow-in. 'b' and 'p' stand for benthic and planktonic, respectively. Numbers in core MAR03-28 indicate maximum TOC contents.

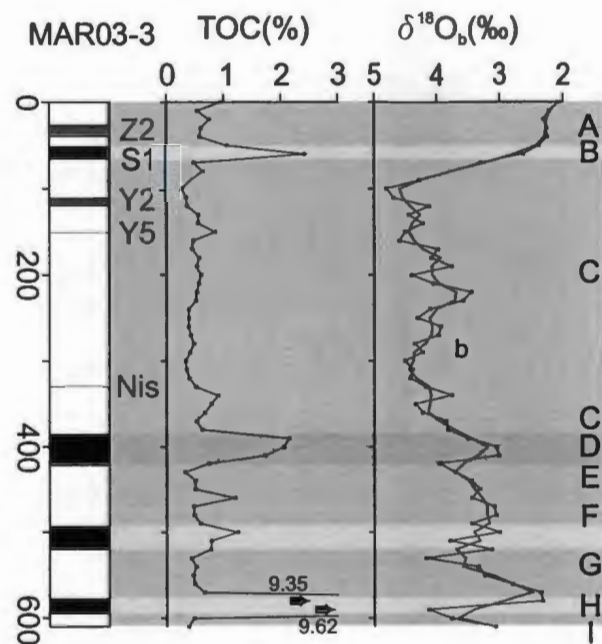


Figure 2.3b. Sapropel and nonsapropel units in the five cores and their assignment to one of ten lithologic units. Also shown are the downcore variations of TOC and oxygen isotope values. In all cores horizontal scales of TOC and $\delta^{18}\text{O}$ plots are the same. Red curves are 3-point moving averages. 'b' stands for benthic.

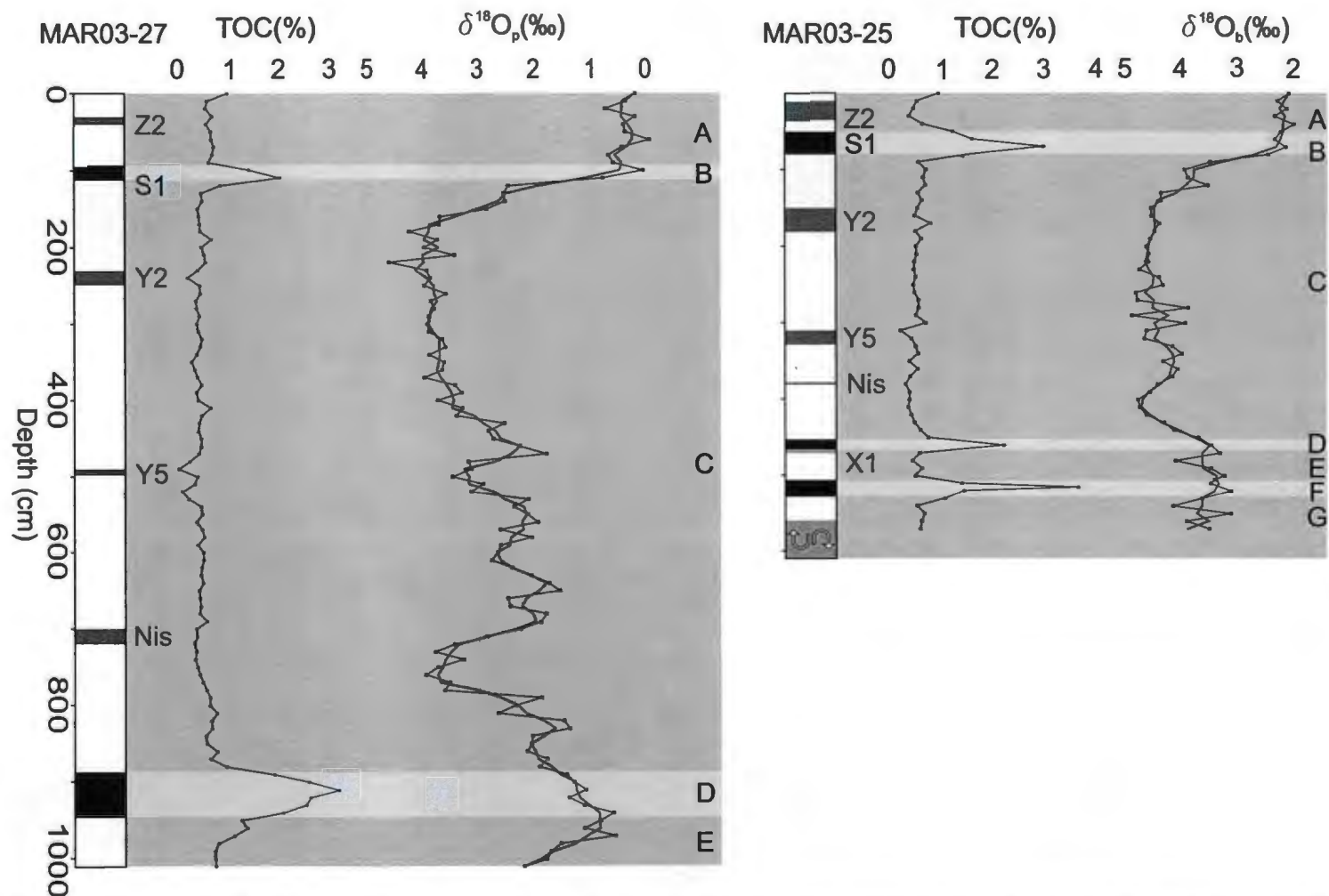


Figure 2.3c. Sapropel and nonsapropel units in the five cores and their assignment to one of ten lithologic units. Also shown are the downcore variations of TOC and oxygen isotope values. In all cores horizontal scales of TOC and $\delta^{18}O$ plots are the same. Red curves are 3-point moving averages. Grey area at the bottom of core MAR03-25 is flow-in.

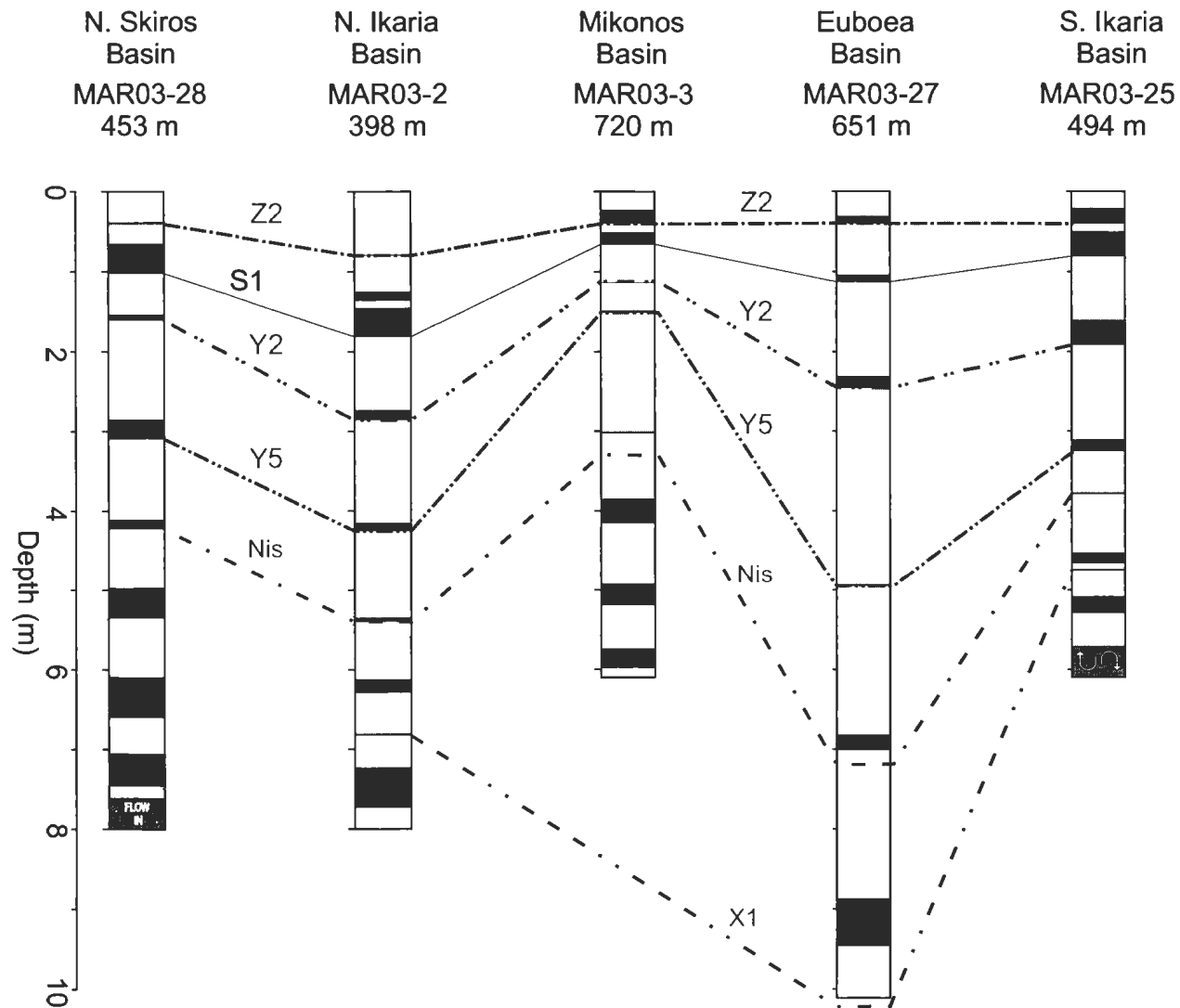


Figure 2.4. Correlation of ash layers (red) and ten lithologic units among the five cores. Ash correlations are from Aksu et al. (2008). Oxygen isotope curves were critical to the correct correlation of sapropel beds (black). Grey area at the bottom of cores MAR03-28 and MAR03-25 is flow-in.

sapropel sediments are slightly to moderately burrowed and are predominantly composed of clay/silt-sized particles. Moreover, there is a lack of evidence for re-sedimentation (e.g., lack of normally graded event beds), paucity of terrigenous sand-sized material, and continual presence of bioturbation throughout the cores, collectively suggesting accumulation through hemipelagic rain. The coarse fraction is predominantly made up of biogenic remains including foraminifera, pteropods, bivalve and gastropod shells. The sand fraction of many cores also includes variable amounts of volcanic ash.

2.3.1.1. Unit A

Unit A is composed of yellowish/dark yellowish brown (10YR5/4-10YR4/2) to light olive gray (5Y5/2) colour- and burrow-mottled foram-rich calcareous mud with an organic carbon content ranging from 0.39% in core MAR03-25 to 1.15% in core MAR03-2. The average TOC content of the unit ranges between 0.55% and 0.82% with a mean of 0.67%. Its thickness ranges from 51 cm in core MAR03-3 to 125 cm in core MAR03-2 (Fig. 2.3a, b, c; Fig. 2.5a, b). This unit contains an ash layer which is largely disseminated in fine mud. It is widespread throughout the Aegean Sea and part of the eastern Mediterranean Sea and has been identified by geochemical fingerprinting as the Z2 tephra from the Minoan eruption on Santorini Island (Aksu et al., 2008, and references therein). The thickness of the ash-bearing interval varies from 5 cm in core MAR03-28 to 45 cm in core MAR03-25 (Fig. 2.3a, b, c; Fig. 2.5a, b; Table 2.2).

2.3.1.2. Unit B

This unit is distinguished from overlying/underlying units by its peculiar darker

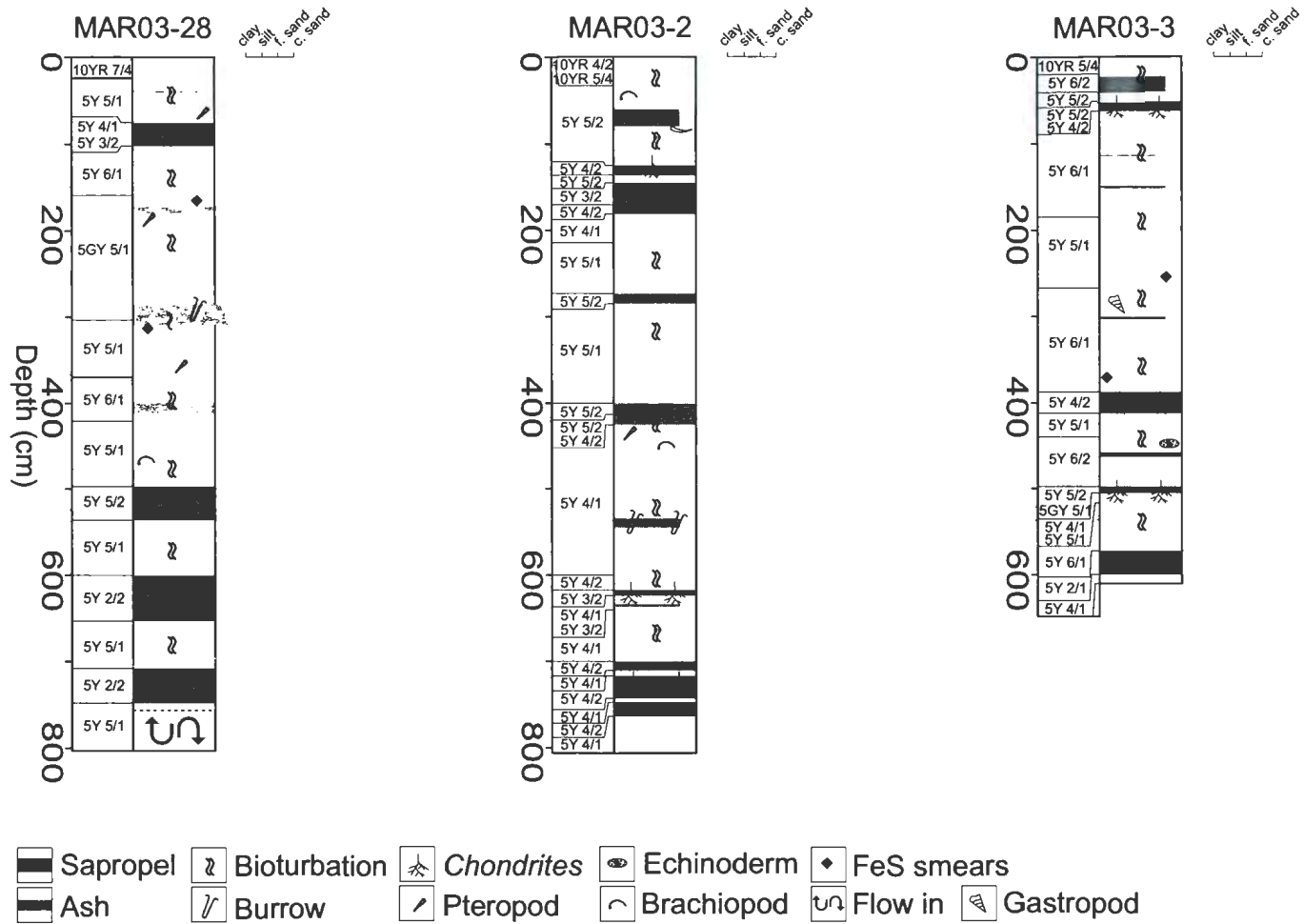


Figure 2.5a. Lithologic attributes of the cores MAR03-28, MAR03-2 and MAR03-3. Dashed line in core MAR03-28 indicates the beginning of flow-in.

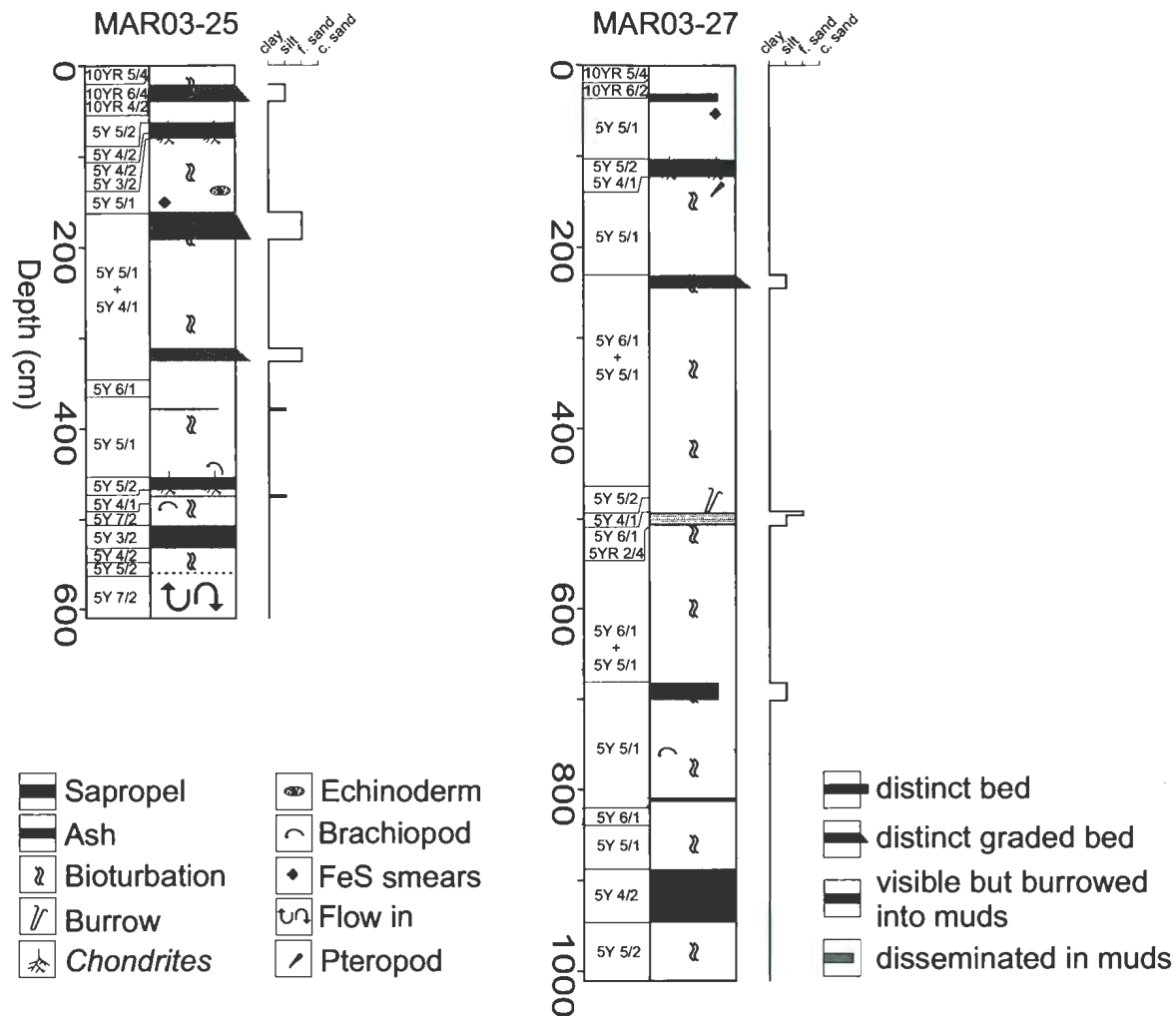


Figure 2.5b. Lithologic attributes of the cores MAR03-25 and MAR03-27. Dashed line in core MAR03-25 indicates the beginning of flow in.

Tephras	Z2		Y2		Y5		Nisyros		X1	
	Depth	shards	Depth	shards	Depth	shards	Depth	shards	Depth	shards
MAR03-2	60	31	280	97	410	285	530	12	680	45
	70	264	290	>7000	420	2453	540	398		
	80	590			430	1156				
	24		18		29		13		4	
MAR03-25	10	377	150	189	310	38	380	236	480	922
	20	275	160	3250	320	624				
	30	1250	170	324	330	141				
			180	49						
	27		32		23		8		5	
MAR03-28	40	89	160	1920	290	98	410	221		
			170	60	300	723	420	187		
					310	3061				
					320	433				
	3		16		34		19			
MAR03-3	30	192	110	158	150	352	330	121		
	40	50	120	237						
	15		12		6		5			
MAR03-27	30	92	230	102	490	248	700	224		
	40	326	240	234	500	162	710	153		
			250	20			720	32		
	13		22		7		28			

Table 2.2. Depth of the samples containing glass shards. Number of counted shards in each sample (13 cm³) is also given. Bold numbers are the actual thicknesses of the ash layers from visual core descriptions. Number of shards in tephra Y2 (>7000) in core MAR03-2 was calculated by dispersing the sample over a gridded micropaleontological slide (60 squares total) and counting the individual shards within three randomly-picked grids and multiplying by 20.

olive gray colour (5Y4/1 and 5Y3/2). It generally has a sharp base. Unit B is made up of dark, colour-banded clayey mud and includes small, sharp-walled and oval-shaped burrows identified as *Chondrites*. Unit B varies in thickness from 9–56 cm and is thickest in core MAR03-2. The organic carbon content of this unit varies from a minimum value of 1.1% in core MAR03-2 to a maximum of 2.98% in core MAR03-25. Organic carbon concentrations are generally higher within the lower portion of the unit and gradually decrease toward the top. Average TOC content of unit B ranges between 1.5% and 2%. Due to its consistent stratigraphic position throughout the cores, situated between the ash layers Z2 and Y2 (see Unit C), its deposition during interglacial stage 1, and its high organic carbon content, this unit is interpreted to be the most recent sapropel layer called S1 by other researchers. In core MAR03-2, the TOC content changes upward from 2.3% to 1.1% to 1.8%, suggesting two peaks of organic matter accumulation in the North Ikaria Basin. The intervening decline in organic-matter accumulation is not recognised among the other cores, either because it is not present or because it was not captured by the 10 cm sample spacing (Fig. 2.3a, b, c; Fig. 2.5a, b)

2.3.1.3. Unit C

Unit C is the thickest unit with a minimum thickness of 325 cm in core MAR03-03 and a maximum of 437 cm in core MAR03-2. The unit consists of burrow-mottled foram-bearing calcareous clayey mud and displays a colour variation from medium gray (5GY5/1) to light brown/neutral gray (5Y6/1, 5GY6/1). The TOC content mainly remains below 0.5% and rarely increases up to 0.7% in cores MAR03-3 and MAR03-28. Unit C contains three tephra layers which are described in detail by Aksu et al. (2008).

Equivalents of these tephra layers are observed all around the eastern Mediterranean Sea including the Aegean, Adriatic and the Ionian seas. From top to bottom they are identified by Aksu et al. (2008) as the Y2 tephra (the Cape Riva eruption on the Island of Santorini also known as the Akrotiri eruption), the Y5 tephra (Campanian Ignimbrite eruption of the Phlegran Fields of the Italian Volcanic Province; Narcisi and Vezzoli, 1999), and the Nisyros tephra (Nisyros eruptions on the Island of Nisyros). They are mostly disseminated in clayey background; however, high numbers of glass shards (e.g., thousands in 13 cm³ sediment; Table 2.2) make the tephra layers discernible with sharp tops and bases in most of the cores. Their thicknesses display large variations ranging between 3 cm and 53 cm (Fig. 2.3a, b, c; Fig. 2.5a, b; Table 2.2).

2.3.1.4. Unit D

Unit D is composed of burrowed, foram-bearing dark calcareous mud showing occasional colour banding. It has a sharp top and base. The main trace fossil is *Chondrites*. The TOC content in cores MAR03-28, MAR03-2, MAR03-27 and MAR03-3 ranges from 1.05% to 3.16% averaging 1.74%. Due to the thickness (<10 cm) of the unit in core MAR03-25 the TOC content is determined from a single analysis and is 2.22%. The thickness of the unit shows large variations among the cores changing from 13 cm in core MAR03-25 to 59 cm in core MAR03-27. It is coloured in different tones of olive gray, changing in a patchy manner from darker (5Y3/2) to lighter (5Y4/2 and 5Y5/2; Fig. 2.3a, b, c; Fig. 2.5a, b).

2.3.1.5. Unit E

Unit E is a pale coloured mostly yellowish gray (5Y7/2) foram/small shell-bearing and burrowed calcareous mud with a significant thickness variation ranging from 40 cm to >140 cm. In cores MAR03-2 and MAR03-25 Unit E contains an ash layer disseminated in mud. The ash layer in core MAR03-25 was geochemically analysed by Aksu et al. (2008) and interpreted as the X1 tephra, most likely derived from the Aeolian Islands, Italy. Due to their similar stratigraphic positions in both cores (located below unit D), the tephra layer in core MAR03-2 also is interpreted to be X1 tephra. The TOC content ranges between 0.4% and 0.7% (Fig. 2.3a, b, c; Fig. 2.5a, b; Table 2.2).

2.3.1.6. Unit F

Unit F is composed of burrowed (*Chondrites*) and mottled calcareous foram-bearing mud with no primary sedimentary structures. Its thickness shows large variations ranging from 21 cm in core MAR03-25 to 51 cm in core MAR03-28. The colour of Unit F is generally olive gray (5Y 4/2, 5Y3/2 and 5Y2/2) and becomes darker or lighter according to the content of organic carbon. The TOC content of this sapropel/sapropelic mud unit varies noticeably from core to core with percentages in single samples ranging from 0.77% in core MAR03-3 to as high as 9.41% in core MAR03-28.

In core MAR03-25 the TOC contents progressively increase toward the upper half of the unit reaching its highest amount of 3.66%, and subsequently diminish to 1.41 % toward the top of the unit. In cores MAR03-2, MAR03-3, and MAR03-28, organic carbon percentage shows fluctuations across the unit creating a double-peaked plot. In core MAR03-3, unit F appears as a sapropel at its top and base with a TOC content of 1.24 % and 1.19 %, respectively. Between its upper and lower boundaries, organic

carbon content decreases and ranges from 0.47% to 0.59%. In core MAR03-2, the TOC content ranges between 1.17 % and 2.65 % and peaks at the top of the unit. Additionally, unit F displays two sapropelic mud horizons within its lower and upper halves where organic carbon contents decrease to 0.75% and 0.83%. The highest organic carbon content of 9.41% is observed within the lower portions of the unit in core MAR03-28. Unit F becomes a sapropelic mud in its middle section in this same core, with TOC content of 0.89%. The average TOC content of the unit across all six cores is 2.65% (Fig. 2.3a, b, c; Fig. 2.5a, b).

2.3.1.7. Unit G

Unit G is composed of colour-mottled foram-bearing mud burrowed by *Chondrites* traces. Colour ranges from yellowish gray (5Y7/2) to yellowish-orange (10YR 8/6). The TOC content of the unit ranges from 0.43% to 0.91%. It is thickest in core MAR03-25 (82 cm); however, 65% (~50 cm) of the unit is 'flow in', so only the upper 30 cm was sampled. Unit G is the deepest unit in three cores and has an indeterminate thickness in those cases (Fig. 2.3a, b, c; Fig. 2.5a, b).

2.3.1.8. Unit H

Unit H is only present in cores MAR03-28 (38 cm) and MAR03-3 (29 cm) and is composed of olive black (5Y2/1) to dark olive gray (5Y2/2) mud. It displays faint and occasional laminations with no obvious burrows. This sapropelic unit contains the highest organic carbon content reaching 12.65% at its middle in core MAR03-28 and averages in cores MAR03-28 and MAR03-3 of 9.49% and 6.15% (Fig. 2.3a, b).

2.3.1.9. Unit I

Unit I is likewise present only in cores MAR03-3 and MAR03-28. It is composed of calcareous mud with colours ranging from olive gray (5Y4/1) to medium gray (5GY5/1). Thickness is ~10 cm in core MAR03-3. In core MAR03-28 unit I is ~50 cm thick but the lower 40 cm is ignored as it appears to be 'flow-in' due to the suction force of the rising piston during coring (Fig. 2.3a, b, c; Fig. 2.5a, b). Neither thickness represents the entire unit.

2.3.2. Oxygen isotopes

Oxygen isotope curves were obtained from benthic foraminifera in all cores except core MAR03-27; in cores MAR03-2 and MAR03-28 oxygen isotope analyses were performed on both planktonic and benthic foraminifera (*Uvigerina*) tests. Below, reported $\delta^{18}\text{O}$ values are 3-point moving averages unless otherwise indicated.

The downcore variations in oxygen isotopic compositions of planktonic and benthic foraminifera reveal clear similarities among the cores in terms of large excursions and moderate amplitude oscillations (Fig. 2.3a, b, c). Low values of $\delta^{18}\text{O}$ characterize the upper segments of all cores, with changes from the underlying deposits of as much as 2.5‰ (Fig. 2.3a, b, c). This large core-top depletion in $\delta^{18}\text{O}$ values is ascribed to the most recent termination T1 associated with the glacial-interglacial transition of MIS2/1.

A prolonged yet consistent change towards more positive values is observed

within the lower portions of the cores with a maximum shift of 4‰ ($\delta^{18}\text{O}_p$ in core MAR03-28; Fig. 2.3a, b, c). In unit I, the $\delta^{18}\text{O}$ values seem to show enrichments (0.2‰ and 0.7‰ in cores MAR03-28 and MAR03-3, respectively) toward the top of the unit; however, absolute change from base to top cannot be determined as the total thickness of the unit was not penetrated. In the base of unit H, the $\delta^{18}\text{O}$ values display a depletion toward negative values decreasing by 1.1‰ and 1.5‰ in benthic and planktonic foraminifera, respectively.

The $\delta^{18}\text{O}$ values exhibit significant enrichments across unit G and in cores MAR03-28, MAR03-2 and MAR03-3, with a maximum increase of 3.1‰ in core MAR03-28. In cores MAR03-25 and MAR03-27 such enrichment cannot be demonstrated due to the fact that only the upper section of unit G was penetrated (Fig. 2.3c). In unit F, the $\delta^{18}\text{O}$ values show depletions toward the top of the unit and fluctuate by as much as 0.5‰. The $\delta^{18}\text{O}$ values are about the same at the base and top of unit E and display a positive inflection peaking just above the middle of the unit. Across the unit, the $\delta^{18}\text{O}$ values are generally heavier than those in units F and D and do not fluctuate more than 0.8‰, ranging from 1.5‰ to 2.3‰ and 3.2‰ to 4‰ for planktonic and benthic foraminifera, respectively (Fig. 3a, b, c). In unit D, the $\delta^{18}\text{O}$ values are lowest in the middle of the unit and exhibit values ranging from 1.5‰ to 1.9‰ for planktonic and 3.2‰ to 3.5‰ for benthic foraminifera tests. Across unit C, large fluctuations of ~2.7‰ are observed, with the base and top of the unit being marked by notable enrichment and depletion in oxygen isotope values, respectively. A high amplitude excursion is observed immediately above the enrichment observed at its base,

shifting the curves by 2.2‰ ($\delta^{18}\text{O}_p$) in core MAR03-27 and 0.8‰ ($\delta^{18}\text{O}_b$) in core MAR03-2.

The two top units, A and B, encompasses the interglacial isotopic stage 1. The base of unit B mainly coincides with the final stages of the transition from glacial to fully interglacial conditions during which the $\delta^{18}\text{O}$ values attain values close to that of the present day. Both planktonic and benthic $\delta^{18}\text{O}$ values fluctuate no more than 0.5‰ across units A and B ranging between 0.2‰ and 1‰ for $\delta^{18}\text{O}_p$ and from 2‰ to 3‰ for $\delta^{18}\text{O}_b$ (Fig. 2.3a, b, c).

2.4. Depth-to-Age Conversion

The cores were converted from a depth scale to a time scale by using a number of age control points and the AGER&TIMER (Imbrie and Kipp, 1971) depth-to-age conversion programs of the SPECMAP statistical package. Program AGER calculates constant sedimentation rates between adjacent age control points. Program TIMER interpolates the AGER output and produces a time series using a user-defined age increments and the interpolated values for each variable at each age increment (i.e., 120 yr).

The age control points in the Aegean Sea cores include (1) those determined by curve matching of the oxygen isotope signals from the cores with those in the global oxygen isotope curve: troughs (i.e., maximum enrichments) are considered most reliable because depleted oxygen isotope signals, particularly high amplitude values, could be generated by local/episodic changes (e.g., river input pulses) and, accordingly, may not

correspond to global climatic changes, (2) horizons, for which the age is well constrained, including the most recent sapropel layer S1 and tephra layers Z2, Y2, and Y5. The number of control points varies in each core according to the number of ash and sapropel layers they contain, where more sapropel layers in a core signify a longer period of time being spanned thus comprising more control points (e.g., MAR03-3 vs. MAR03-27; Fig. 2.6a, b, c; Table 2.3).

The most recent sapropel S1 has been extensively studied due to its omnipresence throughout the Aegean Sea. Its onset/termination ages are very well constrained by ^{14}C dating and extrapolation/interpolation (Aksu et al., 1995; Geraga et al., 2000; Gogou et al., 2007; Roussakis et al., 2004; Perissoratis and Piper, 1992; Kotthoff et al., 2008; Zachariasse et al., 1997; Mercone et al., 2000 and 2001; Casford et al., 2002; Rohling et al., 2002; Table 2.4). Radiocarbon (^{14}C) convention ages gathered from these previous studies were converted to calibrated years BP using the IntCal Marine 04 curve (Hughen et al., 2004) of the online version of Calib 5.02 (Stuiver et al., 2005), with its default reservoir correction of 408 yr. A reservoir age correction (ΔR) of 149 ± 30 yr was used for the Aegean Sea (Facorellis et al., 1998), giving a mean reservoir age of $408+149 = 557$ yr. Both uncalibrated and calibrated (cal.) radiocarbon ages and related details (e.g., sampling depth and location) are presented in Table 2.4. Median (cal. yr BP) ages were used for determination of the sapropel S1 top and base to minimize the intricacy of the calculations that would arise from using the minimum/maximum values for calibrated age ranges.

With the limited area of the Aegean Sea, it is expected that events would be

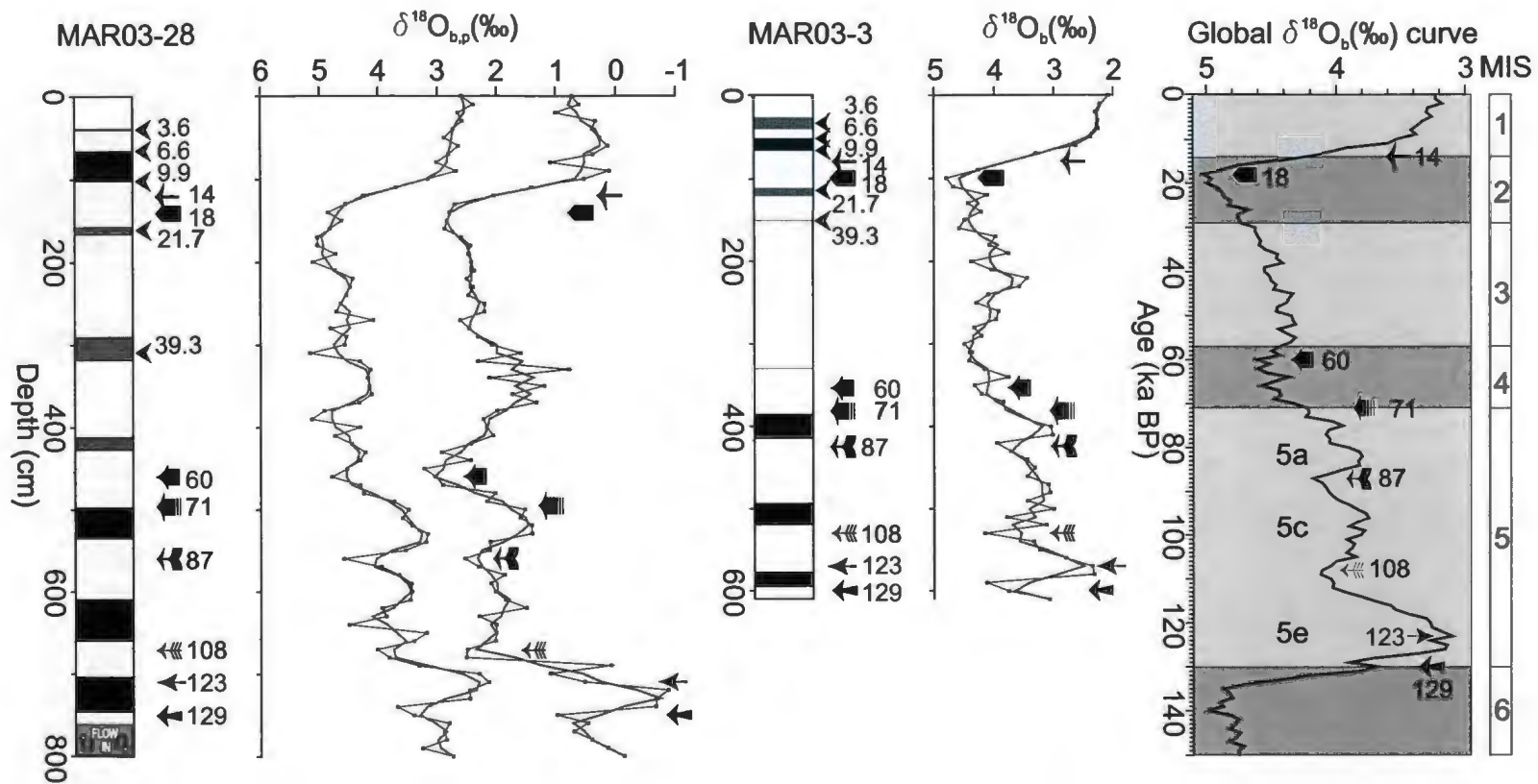


Figure 2.6a. Age control points throughout the cores. Triangular arrows are those obtained from the known ages of top/base S1 and the tephra layers Z2, Y2, and Y5. Other arrows symbolise age control points determined by matching of the oxygen isotope curves with the global curve. Red curve is the 3-point moving average. Global curve is from Lisiecki and Raymo (2005).

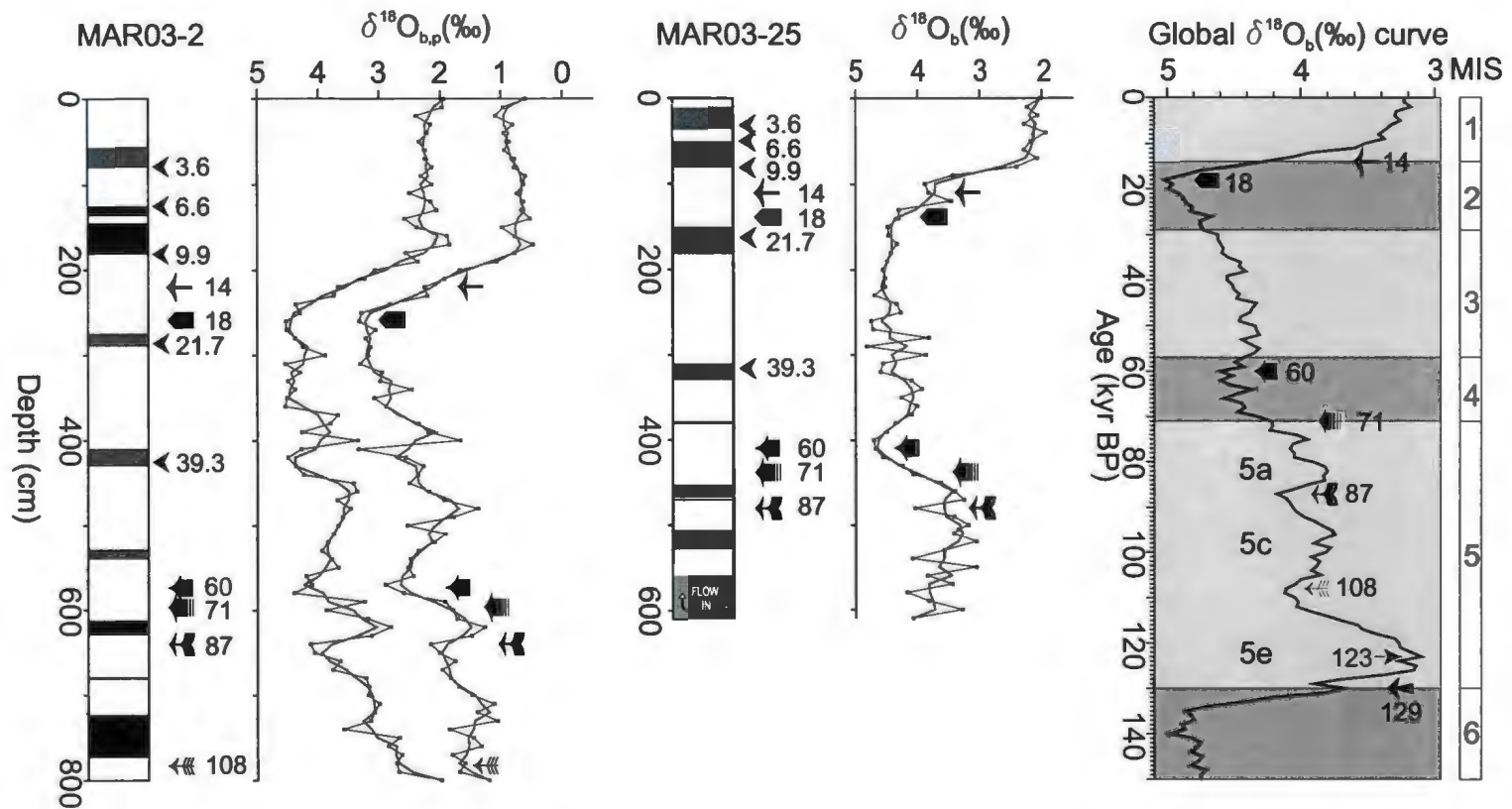


Figure 2.6b. Age control points throughout the cores. Triangular arrows are those obtained from the known ages of top/base S1 and the tephra layers Z2, Y2, and Y5. Other arrows symbolise age control points determined by matching of the oxygen isotope curves with the global curve. Red curve is the 3-point moving average. Global curve is from Lisiecki and Raymo (2005).

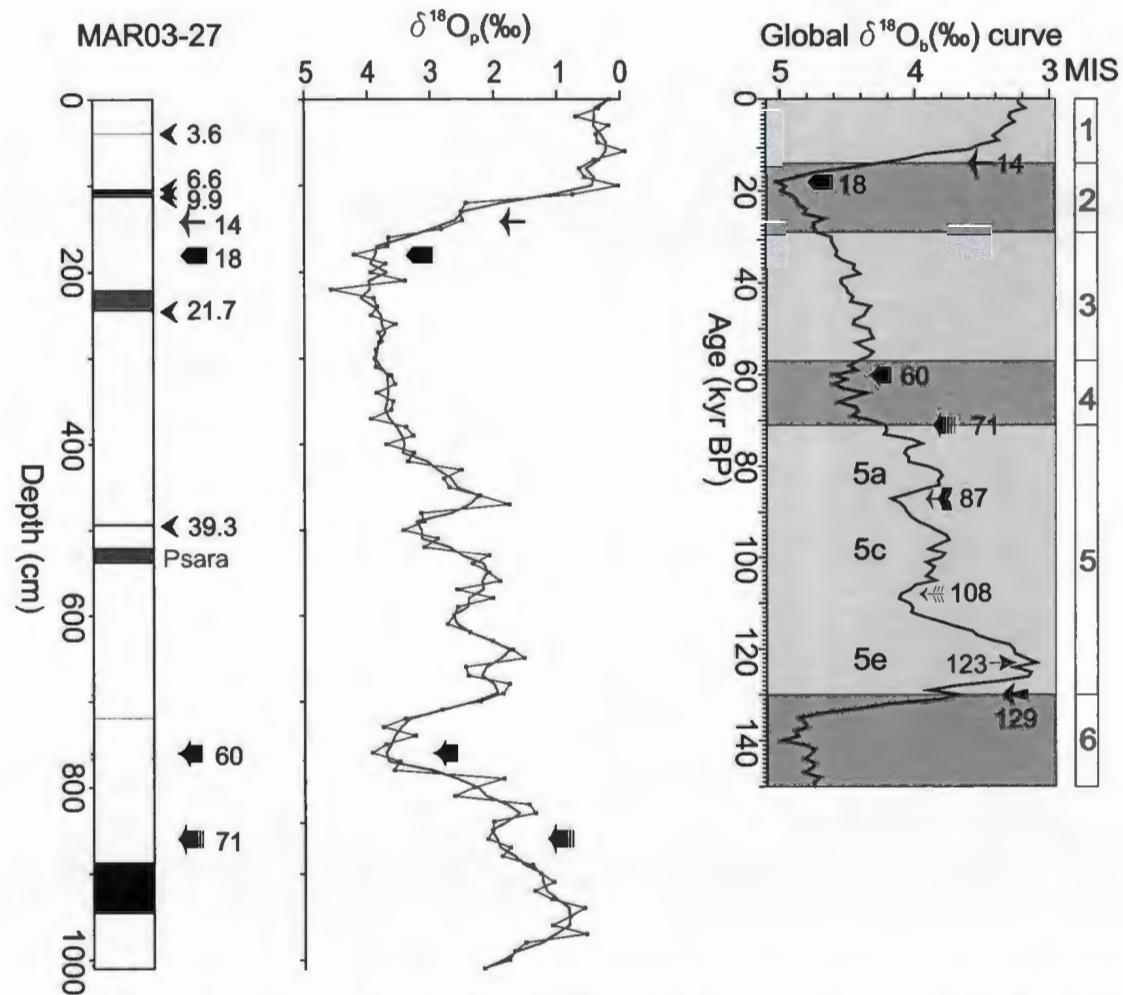


Figure 2.6c. Age control points throughout the cores. Triangular arrows are those obtained from the known ages of top/base S1 and the tephra layers Z2, Y2, and Y5. Other arrows symbolise age control points determined by matching of the oxygen isotope curves with the global curve. red curve is the 3-point moving average. Global curve is from Lisiecki and Raymo (2005).

MAR03-28		MAR03-2		MAR03-3		MAR03-25		MAR03-27	
Age (yr)	Depth (cm)	Age (yr)	Depth (cm)	Age (yr)	Depth (cm)	Age (yr)	Depth (cm)	Age (yr)	Depth (cm)
3613	40	3613	80	3613	33	3612	20	3613	40
6600	65	6600	125	6600	51	3613	33	6600	104
9900	102	9900	181	9900	66	6600	50	9900	113
14000	120	14000	220	14000	80	9900	81	14000	142
18000	141	18000	259	18000	100	14000	110.5	18000	180
21554	161	21554	286	21554	113	18000	138	21553	233
39279	283	39280	425	39280	151	21553	163	21554	245
39280	310	60000	574	60000	353	21554	190	39280	495
60000	460	71000	597	71000	381	39279	311	60000	760
71000	496	87000	640	87000	425	39280	324	71000	860
87000	560	108000	783	108000	531	60000	410		
108000	672			123000	571	71000	438		
123000	710			129000	600	87000	480		
129000	750								

Table 2.3. Age control points and their depths within the cores used in Age-to-Depth conversion.

Lab code	Age control point depths (cm) (Z2 tephra and ¹⁴ C dates)	¹⁴ C (yr BP)	error range	¹⁴ C(cal yr BP)	¹⁴ C(cal yr BP)	Median (cal yr BP)	Sapropel age (cal. yr BP)	Source	Location	
	15 cm above top S1 (285 cm bsf)	6580	70	6800	7010	6920	7134 top	Zachariasse et al., 1997*	Skopelos Basin(NAT)	
	15 cm below base S1 (525 cm bsf)	9640	80	10239	10435	10348	10134 base			
KIA28412	S1 top	6570	45	6828	6980	6904	6904 top	Kotthoff et al 2008 ***	Athos Basin NAT	
KIA28414	S1 base	9205	55	9653	9884	9769	9769 base			
Beta-166995	5 cm below top S1 (28 cm bsf)	5810	40	5990	6136	6066	4737 top	Geraga et al., 2005**	Myrtoon Basin	
Beta-142621	4 cm above S1 base (44 cm bsf)	8750	70	9167	9377	9258	10321 base			
Beta-157952	5 cm below S1 top (137-140 cm bsf)	7840	40	8068	8217	8155	7917 top	Roussakis et al., 2004 **	N. Skiros Basin	
Beta-157953	5 cm above S1 base (165-170 cm bsf)	9030	60	9466	9609	9542	9780 base			
	S1 top	6300	60	6494	6660	6584	6584 top	Jorissen et al., 1993 ***	Adriatic W. Mediterranean	
	S1 base	8300	70	8527	8760	8649	8649 base			
	S1 top	6400	60	6621	6787	6703	6703 top	Perissoratis and Piper (1992)	N. Aegean Sea	
	S1 base	9200	80	9605	9897	9771	9771 base			
TO-11151	230 cm below S1 base (400 cm bsf)	16930	140	19408	19600	19545	7545 top	Isler et al., 2008 **	Bababurnu Basin (NEAegean)	
TO-11152	502 cm below S1 base (672 cm bsf)	26100	250			31340	9962 base			
TO-3739	2.5 cm below S1 base (80 cm bsf) Z2 tephra (28 cm bsf)	9820	70	10450	10602	10531	6276 top 10171 base	Aksu et al., 1995*	NAT	
TO-3741	12 cm below S1 base (100 cm bsf) Z2 tephra (33 cm bsf)	10860	80	11936	12279	12103	6151 top 10185 base	Aksu et al., 1995*	N. Skiros Basin	
TO-3742	6 cm below S1 base (120 cm bsf) Z2 tephra (43 cm bsf)	9830	70	10462	10618	10541	6836 top 10002 base	Aksu et al., 1995*	S. Skiros Basin	
TO-3740	7 cm below S1 base (90 cm bsf) Z2 tephra (35 cm bsf)	10190	70	10919	11153	11019	4932 top 10077 base	Aksu et al., 1995*	S. Ikaria Basin	
TO-3743	2.5 cm below S1 base (50 cm bsf) Z2 tephra (12.5 cm bsf)	9670	70	10284	10472	10376	6809 top 9926 base	Aksu et al., 1995*	Cretan Trough	
KIA9468	13.75 cm below S1 top (65.75 cm bsf)	7950	60	8196	8336	8267	6860 top	Casford et al., 2007*	Central Aegean	
KIA9470	2.25 cm below S1 base (84.25 cm bsf)	9330	57	9890	10113	9983	9765 base			
KIA9473	1.5 cm below S1 top (71.5 cm bsf)	6445	55	6672	6831	6756	6647 top	Casford et al., 2007*	SW Aegean	
KIA9475	5.5 cm above S1 base (99.5 cm bsf)	8400	50	8689	8909	8790	9952 base			
CAMS-41315	11.5 cm below S1 top (151.5 cm bsf)	7480	60	7712	7867	7795	7043 top	Casford et al., 2007*	Karpathos Basin	
AA-30364	11.5 cm above S1 base (179.5 cm bsf)	9010	70	9442	9599	9525	10277 base			
S1 top/base calculation							Average		6576 ≈ 6600 top 9916 ≈ 9900 base	
		* = interpolation								
		** = extrapolation								
		*** = sample from top/base of sapropel								

Table 2.4. The radiocarbon ages are converted to calibrated calendar years (cal. yr BP) using the IntCal Marine04 curve (global reservoir correction of 408 yr) and the program Calib5.0.2 (Stuiver and Reimer, 1993; Hughen et al., 2004a). A local reservoir age correction (i.e., $\Delta R = 149 \pm 30$ yr) was used for the Aegean (Facorellis et al., 1998). ¹⁴C dates: first column is the actual measurements, the following two columns are the lower and upper ranges derived from the Calib5.0.2 program.

synchronous across the basin (Casford et al., 2007); however, calculated ages for sapropel S1 onset and termination reveal significant differences of as much as 556 yr and 1766 yr, respectively (see Table 2.4). Furthermore, even assuming an asynchronous sapropel initiation, deduced ages from single subbasins exhibit inconsistencies with variations of ~400 years (e.g., cores 22 and LC21). Radiocarbon dates showing such differences might arise because of a variable contribution of old carbon due to sedimentary processes such as remobilization and redeposition of previously deposited materials and/or bioturbational mixing, which might vary considerably between individual samples of biogenic carbonate. Bioturbation effects have been discussed by several authors and age falsifications of 1110–2525 years are reported for samples (i.e., *Globigerina bulloides*) collected from the same core two centimetres apart (Löwemark and Werner, 2001). Moreover, in a core from the Adriatic Sea, an 800 year difference between adjacent dates from below and above the base of sapropel S1 was shown (Fontugne et al., 1989). In a recent study, Casford et al. (2007) constructed an age model for the Aegean and eastern Mediterranean seas by using several ^{14}C dates from published papers and postulated that previously proposed age uncertainties (e.g., 800 yr) can be reduced to ± 350 yr.

Taking into account the abovementioned range of age “errors” and the low-resolution sampling interval (10 cm) of the cored sediments, the following calculations and further discussions will be based on the assumption that the range of age uncertainties is ± 350 yr and the timing of onset and termination of the most recent sapropel S1 are 9,900 cal yr BP and 6,600 cal yr BP, respectively. Ash accumulations are considered as instantaneous deposits providing age horizons that can reliably be used

in chronostratigraphic reconstructions. Accordingly, the top three tephra layers encountered in the majority of the cores are used as age control points (Fig. 2.6a, b, c). The ages of the tephra layers from top to bottom are 3613 cal. yr BP (median), 21,554 \pm 484 cal. yr BP, and 39,280 \pm 110 cal. yr BP (Aksu et al., 2008 and references therein). During depth-to-age conversion, ages are positioned in the middle of disseminated tephra layers; whereas, distinct tephra layers are 'collapsed' by assigning the same ages for the tops and bases since they are effectively instantaneous deposits (e.g., 39,279 and 39,280 cal. yr BP, respectively).

2.5. Discussion

2.5.1. Sedimentation rates

The downcore variations in sedimentation rates are regulated by several factors such as the basin physiography, core location (i.e., slope or deeper basinal setting), climatic conditions (e.g., pluviality or aridity) and sea level fluctuations. Sea level is a rather significant control on sedimentation rates; for example, falling sea level not only would result in the subaerial exposure of the shelf area leading to intense weathering and augmentation in terrigenous supply, but also would cause the seaward advance of the point source (e.g., river mouth) in accordance with the retrograding coastline, thus inducing higher sediment input. Besides sea level lowering, aridity and/or pluviality are rather decisive factors for the amount of sediment transported to a core site.

The downcore sedimentation rates for each core were calculated using the determined age control points where rates between two consecutive points are considered constant (Fig. 2.7a, b and Table 2.5). A generalized curve is constructed from mean

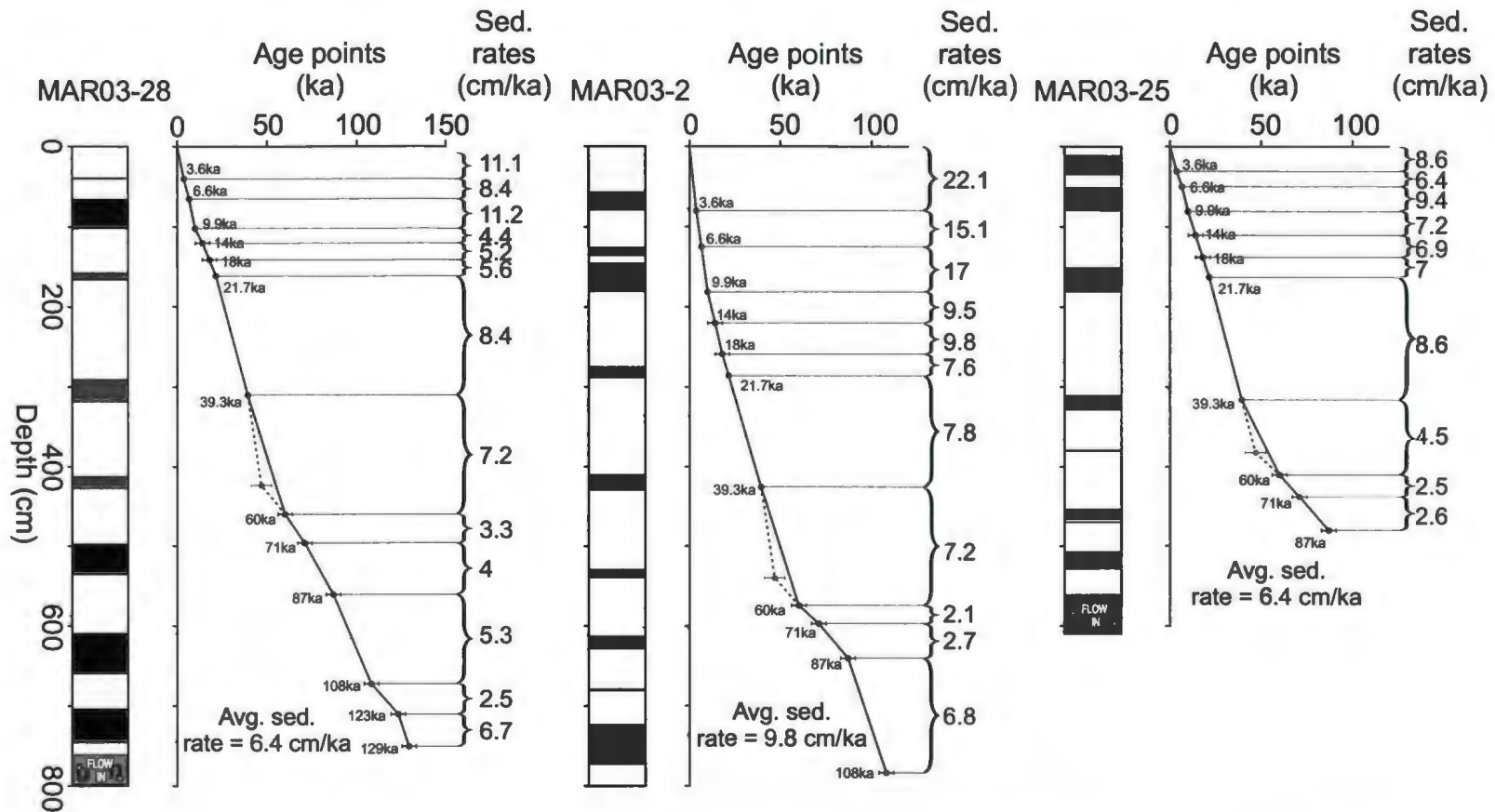


Figure 2.7a. Downcore variations of calculated sedimentation rates between successive age control points and average sedimentation rates of each core. Horizontal bars represent error bars determined for each core. The kink shown by dashed line and red dot is the Nisyros age from the literature. Gray areas at the bottom of cores MAR03-28 and MAR03-25 are flow-in.

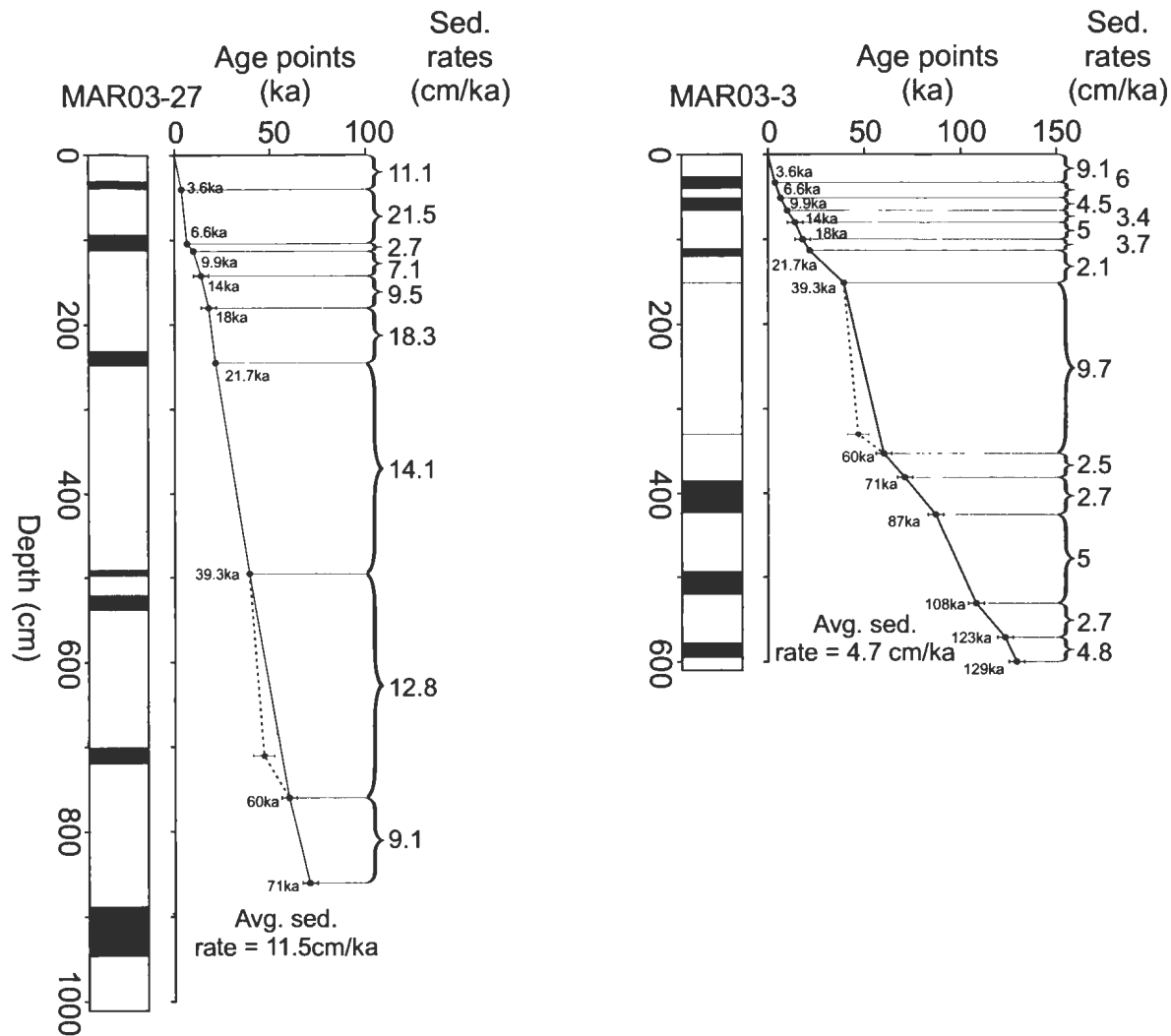


Figure 2.7b. Downcore variations of calculated sedimentation rates between successive age control points and average sedimentation rates of each core. Horizontal bars represent error bars determined for each core. The kink shown by dashed line and red dot is the Nisyros age from the literature.

Control point ages (yr BP)	MAR03-28	MAR03-2	MAR03-25	MAR03-3	MAR03-27
0	11.1	22.1	8.6	9.1	11.1
3618	8.4	15.1	6.4	6	21.5
6600	11.2	17	9.4	4.5	2.7
9900	4.4	9.5	7.2	3.4	7.1
14000	5.2	9.8	6.9	5	9.5
18000	5.6	7.6	7	3.7	18.3
21554	8.4	7.8	8.6	2.1	14.1
39280	7.2	7.2	4.5	9.7	12.8
60000	3.3	2.1	2.5	2.5	9.1
71000	4	2.7	2.6	2.7	
87000	5.3	6.8		5	
108000	2.5			2.7	
123000	6.7			4.8	
129000					
Average sed. rates (cm/ka)	6.4	9.8	6.4	4.7	11.8
Error ranges (yr)	±781	±526	±781	±1063	±434

Table 2.5. Sedimentation rates calculated for each successive age control point and mean sedimentation rates of the cores (i.e., average sedimentation rate of particular portion of the depocenter at which the core was recovered (e.g., slope or basinal setting). Error ranges are calculated assuming a maximum of 10 cm bioturbation.

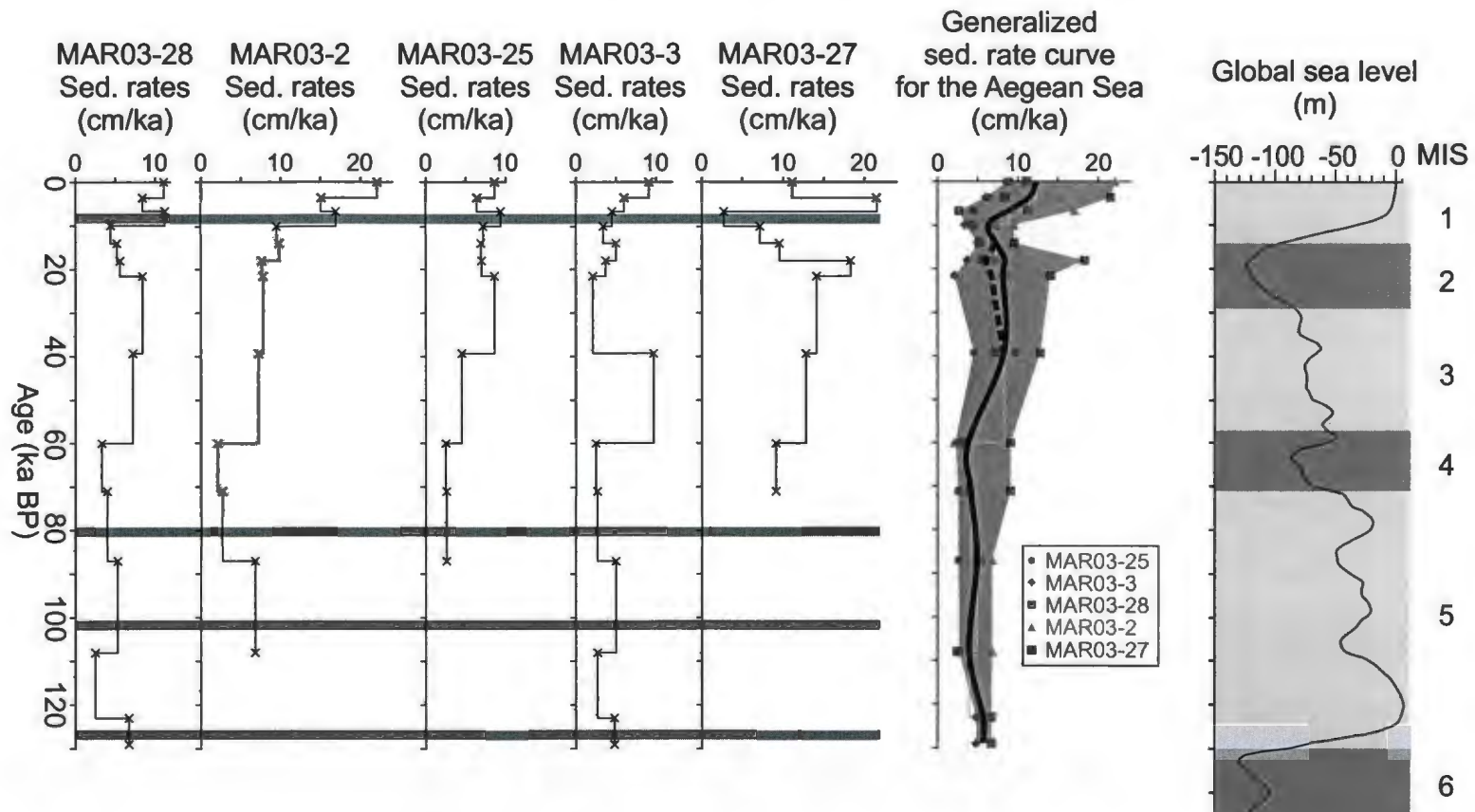


Figure 2.8. Age vs. sedimentation rate plots of the five cores. Gray bars represent the sapropel layers (units B, D, F, and H). 'x' symbols along the plots are age control points. Gray envelope shows the range of sedimentation rate including all of the calculated values. Heavy black dashed line shows the calculated sedimentation rate excluding the outlier in core MAR 03-27. Global sea level is from Waelbroeck et al. (2002).

values. The lowest mean sedimentation rates are observed during MISs 4 and 5, ranging from 3.9 cm/ka to 4.9 cm/ka between 123 and 57 ka BP, respectively (Fig. 2.8). Despite inadequate age control points, sedimentation rates appear to increase during MIS 3 changing from 4.5 cm/ka to 9.7 cm/ka between 60 ka BP and 39 ka BP. Until the last glacial maximum (18–20 ka BP) sedimentation rates appear to be relatively constant changing between 5.7 and 7.2 cm/ka. The dashed line is calculated by excluding the rates from MAR03-27 between 18 and 39.3 ka BP which are 1.6–2.4 fold higher than those in the other four cores and considered as outliers (Table 2.5). According to the dashed curve, sedimentation rates show a gradual drop toward the cold interval (18–20 ka BP) and change from 8.3 cm/ka to 6 cm/ka. Despite the fact that there is little difference between the two, a gradual decrease in sedimentation toward/during the glacial time is consistent with increased aridity which has been reported for the cold interval throughout the Aegean Sea. Towards the base of sapropel S1, sedimentation rates drop to 6.3 cm/ka and subsequently exhibit a continuous increase until present, reaching a maximum of 11.1 cm/ka. Although, sedimentation rates display moderate to large temporal and spatial variations throughout the Aegean Sea, the generalized curve can be used to guide interpretations.

The sedimentation rates calculated for different subbasins of the Aegean Sea show that highest mean rates of 11.8 and 9.8 cm/ka took place in core MAR03-27 (Euboea Basin) and in core MAR03-2 (North Ikaria Basin), respectively (Fig. 2.7a, b; Fig. 2.8; Table 2.5). The remaining three cores exhibit mean sedimentation rates changing between 4.7 cm/ka in core MAR03-3 (Mykonos Basin) and 6.4 cm/ka in cores MAR03-28 and MAR03-25 (North Skiros and South Ikaria basins; Table 2.5).

Due to the scarcity of age control points below 20 ka BP, variations in sedimentation rates cannot be discussed in full detail for individual units. Nonetheless, in general, a similar trend is discernible among the cores where the sedimentation rates appear to be relatively higher during MIS3 (6.8 cm/ka) than those below 60ka (<4 cm/ka) and, despite the high amplitude jump between 40 and 60 ka BP in core MAR03-3, sedimentation rates mainly display a progressive upward increase.

Notable fluctuation in core MAR03-3 is due to the position of the Y5 ash layer that results in >2-fold shift in sedimentation rate. Although no sedimentary disturbance had been noticed during macroscopic core description, the inconsistently shallow depth of the ash layer could possibly be the result of re-sedimentation processes.

During MIS5, sedimentation rates appear to be higher in core MAR03-3 and MAR03-28 during the initial stages of MIS5e between 129 and 123 ka BP ranging between 4.8 and 6.7 cm/ka, respectively. A similar increase in sedimentation rates is observed between 108 and 87 ka BP in cores MAR03-28, MAR03-3 and MAR03-2 ranging from 5 to 6.8 cm/ka that roughly coincide with the MISs 5d, c, b.

Except in core MAR03-27 (9.1 cm/ka), the remaining cores exhibit low sedimentation rates during MIS4 that range between 2.1 and 3.3 cm/ka. Despite the fact that global sea level was 55 and 85 m below present level, low sedimentation rates in all four cores may be suggestive of dry climatic conditions and accordingly diminished transportation of terrigenous input irrespective of the core locations. Three fold higher sedimentation rates in core MAR03-27 might be linked to its location and the surrounding seabed morphology that apparently enhanced sediment accumulation.

Between 60 and 20 ka BP, the progressive increase in sedimentation rates is in

agreement with the sea level fluctuations that show a consistent fall from -48 m to -118 m. Highest sedimentation rates ranging between 12.8 and 14.1 cm/ka are observed in core MAR03-27 whereas, in cores MAR03-28 and MAR03-2, sedimentation rates show a rather small variation and range from 7.2 to 8.4 cm/ka. Sedimentation rates in core MAR03-25 show a relatively notable rise from 60 to 20 ka BP, increasing from 4.5 to 8.6 cm/ka. This jump in sedimentation rates coincides with the final stages of MIS3 and the lower half of MIS2 during which global sea level fell continuously by 56 m.

Core MAR03-25 is situated seaward of the Büyük Menderes River and was collected from the western slope of the southeastern extension of South Ikaria Basin, ~20 km and ~60 km away from the shelf edge and the river mouth, respectively. Although during glacial maxima sedimentation rates are expected to be lower due to arid conditions, the doubled rates in core MAR03-25 between 40 and 20 ka BP could be attributed to its location as continuous sea level fall would have resulted in seaward advance toward the core site of the shoreline and river mouth. Core MAR03-2 (water depth 398 m) is also situated close to the shore and was collected from the northern slope of North Ikaria Basin, a relatively confined area ~70 km seaward of the Küçük Menderes River. Here, the sedimentation rates show little increase. A possible explanation is a lack of sufficient age control points to allow a more detailed assessment of temporal variation of sedimentation rates.

Core MAR03-27, being collected from the eastern end of the Euboea Basin where seafloor gradients are gentler than other core locations, exhibits rates two times higher than those in the other four cores. Smooth morphology might account for such consistently higher sedimentation rates (e.g., lutite flows).

Accumulation rates in Sapropel S1 (unit B) show mainly lower values than in unit A ranging between 2.7 and 17 cm/ka. In our study, sedimentation rates calculated for the most recent sapropel S1 are strictly controlled by its observed thicknesses among subbasins and fixed top/bottom ages in all five cores (i.e., 9.9 and 6.6 cal. ka BP). The sedimentation rates for sapropel S1 range from 2.7–4.5 cm/ka in cores MAR03-27 and MAR03-3 and from 9.4 cm/ka (MAR03-25) to as high as 17 cm/ka in core MAR03-2.

Furthermore, the top/bottom ages of the most recent sapropel are well constrained by ¹⁴C-dated samples collected from top/bottom and within sapropel S1, allowing reliable sedimentation rate calculations via extrapolation/interpolation. However, calculations from several papers exhibit a wide range of sedimentation rates from 4.08–9.58 cm/ka (Geraga et al., 2005, Gogou et al., 2007, Casford et al., 2007) and from 23.11 cm/ka to as high as 30.3 cm/ka (Roussakis et al., 2004, De Rijk et al., 1999, Kothoff et al., 2008). These results indicate very different sedimentation rates during the deposition of sapropel S1.

These noticeable variations both in this study and in other papers, displaying >6 fold difference in sedimentation rates for sapropel S1, could be attributed to a number of factors such as core localities (e.g., seabed morphology, depth and proximity to coastline/river mouth), possible compaction or stretching due to inconsistent suction during piston coring and existence of a burn-down front. Core location could be a factor that effects the sedimentation as some cores are proximal to the shore and situated off river mouths that receive comparatively more sediment thus thicker units.

A sapropel is referred to as 'burn-down' when the organic matter is oxidized following the termination of favorable conditions. Following the establishment of

normal marine sedimentation a diffusion front is developed within the upper few centimeters of the sediment-water interface where the oxygenated bottom waters are downward migrated to a depth of diffusion, whereby oxidizing some or all of the organic matter in the sediments. The intensity of the burn-down is largely controlled by (i) the original organic carbon content of the sapropel, which determines how rapidly the organic matter can be oxidized (ii) the sedimentation rate following the onset of normal marine sedimentation under oxygenated bottom waters conditions, which controls the amount of time surface sediments will be exposed to oxygenated bottom waters, and (iii) the degree of bottom water oxygenation, which also determines how effectively and rapidly the organic matter is oxidized. In addition, other factors such as local and regional setting and the intensity of the successive insolation maxima are also cited as possible influences for the preservation of organic matter in subsurface sediments. A burn-down front could reduce the original thickness of a sapropel by up to 90% as oxygen supply to the bottom increased after sapropel formation (Löwemark et al., 2006).

Lower accumulation rates during times of sapropel formation is a common observation throughout the Aegean Sea and the eastern Mediterranean Sea (Mercone et al., 2000; Roussakis et al., 2004; Gogou et al., 2007). The unusually high accumulation rate observed in core MAR03-2 violates this rule but can be explained by proximity to a terrigenous source (i.e., Küçük Menderes River; Fig. 2.2).

The sedimentation rates in the Aegean Sea range from 6 cm/ka to ~11 cm/ka (e.g., İşler et al., 2008). A quick review of the literature shows that sedimentation rates vary from 0.1 cm/ka in the isolated ridges and elevated terrains of the Arctic Ocean (e.g., Aksu 1985a,b) to 1-3 cm/ka over the crestal regions of seamounts (Levin and Nittrouer,

1987) to 10-30 cm/ky in deeper water settings fed by submarine canyons and fan systems (Hesse and Chough et al., 1980; Piper et al., 1985), to 100+ m in nearshore estuaries and deltaic settings (Hart et al., 2004). Within this framework, the rate of sedimentation calculated for the Aegean Sea basins rests on the high side relative to other deep basinal setting. However, this rate is normal, considering the close proximity of the land to the deep basin, the number of moderate size rivers draining considerable regions of the adjacent land mass, and the archipelago morphology of the Aegean Sea dotted by numerous islands.

Collectively, the variations in sedimentation rates calculated for different subbasins of the Aegean Sea show that the amount of terrigenous material delivered to each coring site is mainly controlled by relative sea level fluctuations that change the proximity of the core site to the source (i.e., river mouth). In addition, the locality (slope or basinal setting) of the coring site is rather critical, as it significantly affects the accumulation rate. Between slopes and basin floors there are inconsistent changes in sedimentation rates with the sea level fluctuations. In addition, seismic activity and bottom currents (Roussakis et al., 2004) cannot be ruled out as controls on changing accumulation rates.

2.5.2. Chronology

The correlation of the $\delta^{18}\text{O}$ plots with the global curve shows that sapropel and sapropelic mud units D, F, and H coincide with interstadials of the interglacial MIS 5 (Fig. 2.9a, b, c). Previous studies show that sapropels S3, S4 and S5 developed,

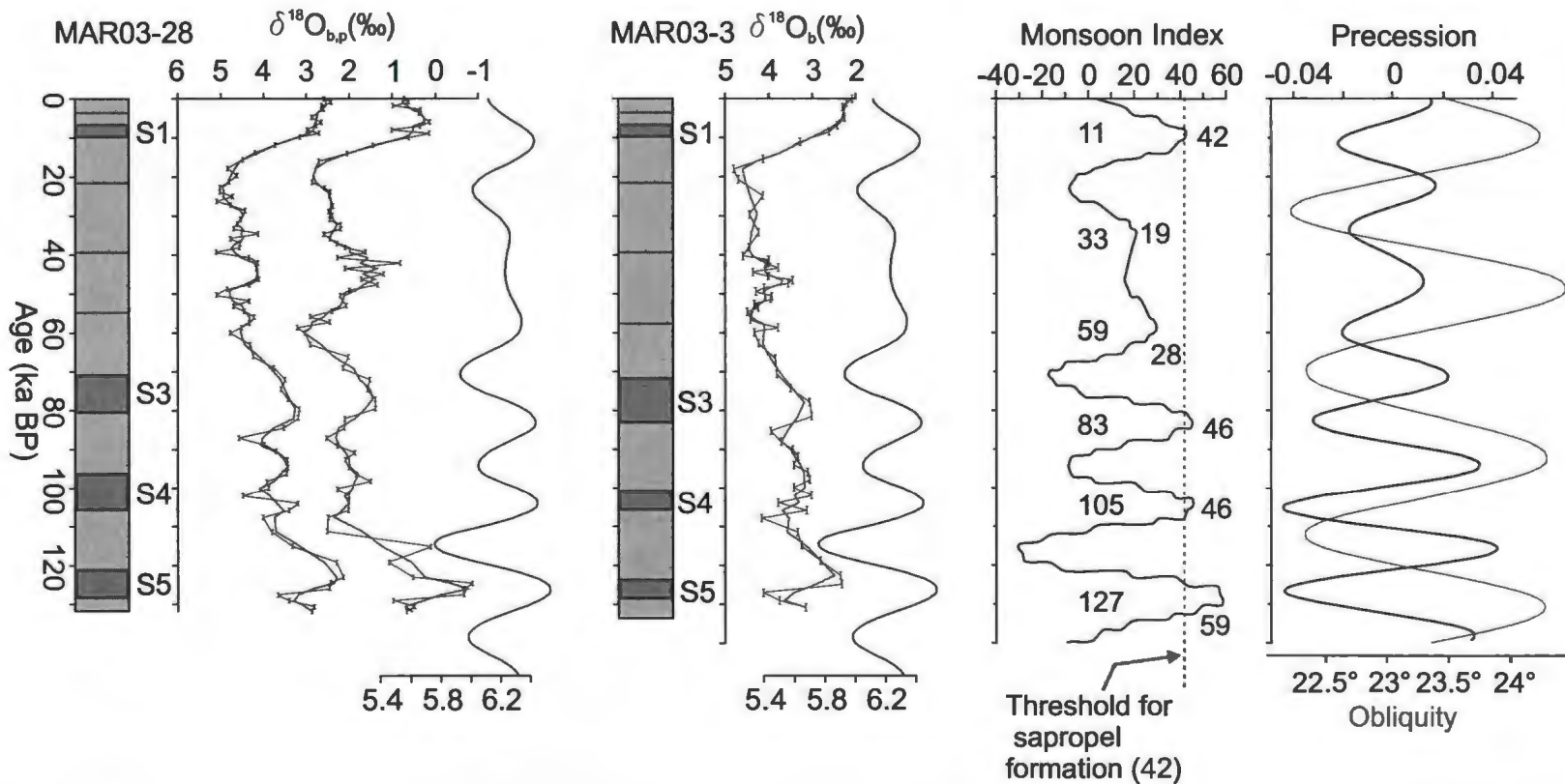


Figure 2.9a. Age-converted lithostratigraphic columns and their corresponding oxygen isotope measurements for the five cores. Embedded black curve is Northern Hemisphere summer insolation index at 35°N (redrawn from Peter Huybers-<http://www.people.fas.harvard.edu/~phuybers/Inso/index.html>; values in Giga Joules). Monsoon index is from Rossignol-Strick and Paterne (1999). Numbers to the left and right of the Monsoon Index curve are astronomical chronology and maximum values calculated at precession minima, respectively. Obliquity (red) is shown with the Precession curve to show its contribution. Red horizontal lines represent ash layers.

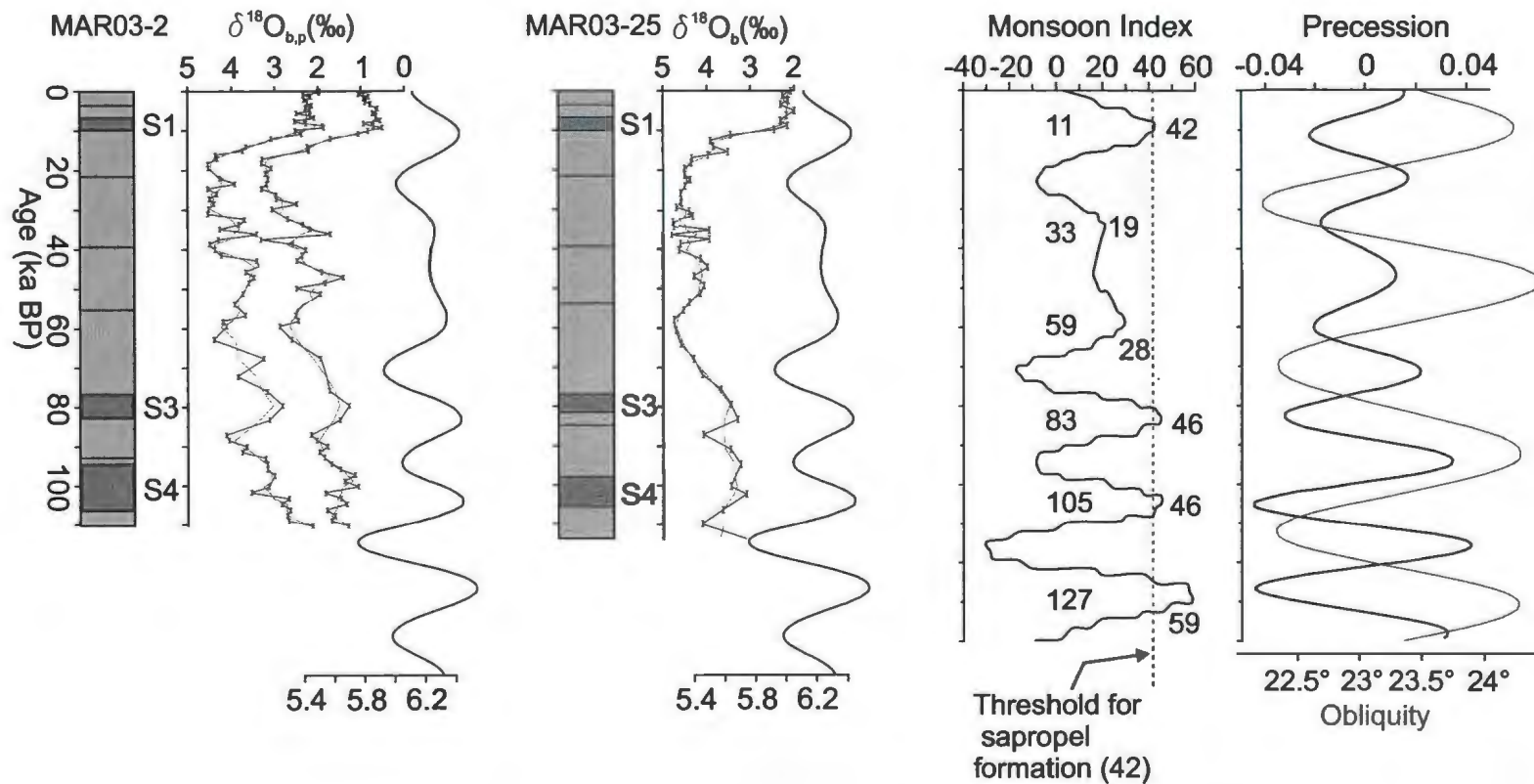


Figure 2.9b. Age-converted lithostratigraphic columns and their corresponding oxygen isotope measurements for the five cores. Embedded black curve is Northern Hemisphere summer insolation index at 35°N (redrawn from Peter Huybers-<http://www.people.fas.harvard.edu/~phuybers/Inso/index.html>; values in Giga Joules). Monsoon index is from Rossignol-Strick and Paterne (1999). Numbers to the left and right of the Monsoon Index curve are astronomical chronology and maximum values calculated at precession minima, respectively. Obliquity (red) is shown with the Precession curve to show its contribution. Red horizontal lines represent ash layers.

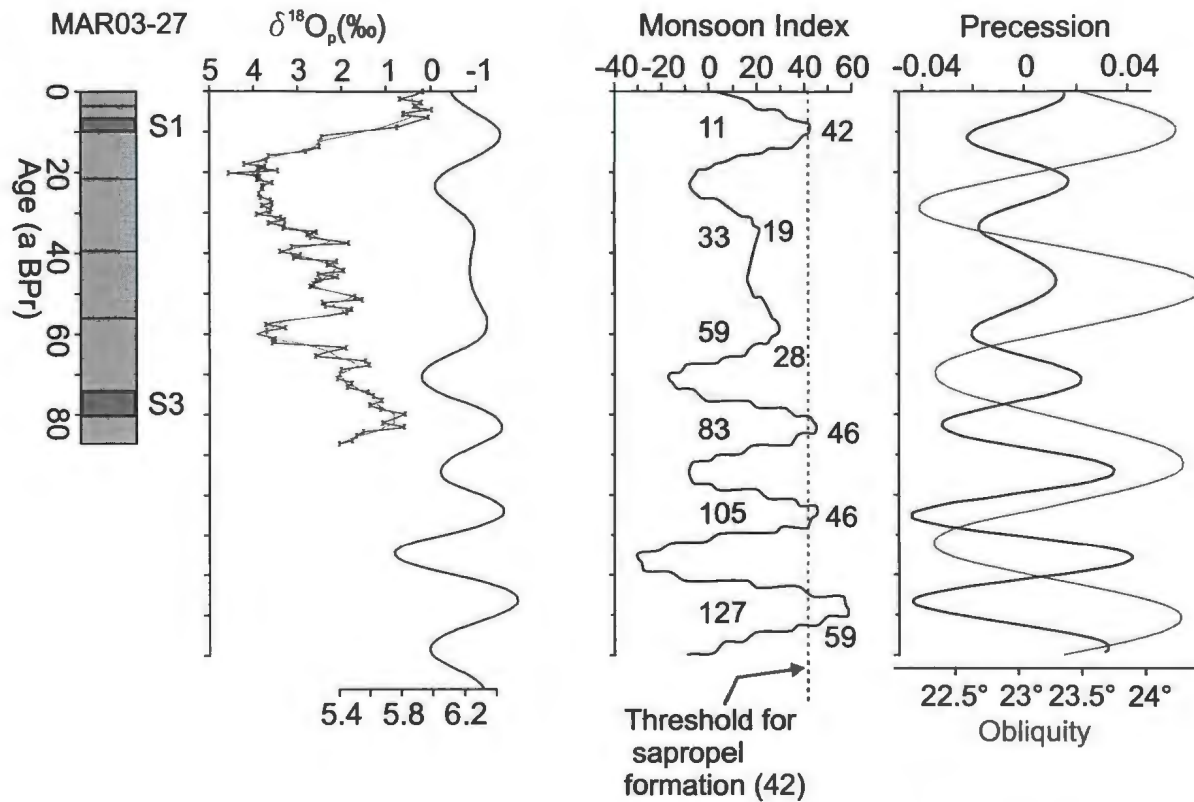


Figure 2.9c. Age-converted lithostratigraphic columns and their corresponding oxygen isotope measurements for the five cores. Embedded black curve is Northern Hemisphere summer insolation index at 35°N (redrawn from Peter Huybers-<http://www.people.fas.harvard.edu/~phuybers/Inso/index.html>; values in Giga Joules). Monsoon index is from Rossignol-Strick and Paterne (1999). Numbers to the left and right of the Monsoon Index curve are astronomical chronology and maximum values calculated at precession minima, respectively. Obliquity (red) is shown with the Precession curve to show its contribution. Red horizontal lines represent ash layers.

respectively, during marine isotopic stages 5a, 5c and 5e in the eastern Mediterranean during which climatic conditions were ameliorated and there was enhanced runoff (Rossignol-Strick, 1985; Emeis et al., 2003). The interpolated ages of units D, F and H are in good agreement with these published studies.

The overall bioturbated texture of the cored sediments (see Fig. 2.5a, b; a maximum of 10 cm is assumed for sediment stirring) and the calculated average sedimentation rates bring about varying error ranges to be attached to the S3–S5 sapropel ages inferred from the cores. For instance, the average sedimentation rate in core MAR03-2 is 9.8 cm ka^{-1} . This average sedimentation rate together with the maximum bioturbation of 10 cm result in a total error of 1052 years (± 526 years). Highest and lowest errors range between ± 434 years in core MAR03-27 (Euboea Basin) and ± 1063 years in core MAR03-3 (Mykonos Basin; Table 2.5).

Based on age-to-depth conversion, the oldest sediments recovered from the cores have an age of $131,800 \pm 781$ yrBP in core MAR03-28 and $130,800 \pm 1063$ yrBP in core MAR03-3, indicating that sediments in unit I were deposited during the latest stages of the transition from MIS 6 to MIS 5 (Fig. 2.9a, b, c; Tables 2.5 and 2.6).

Calculated ages of the onset of sapropel S3 range from 84,263–82,137 yrBP in core MAR03-3 (Mykonos Basin) and from 80,834–79,966 yrBP in core MAR03-27 (Euboea Basin; Table 6). The age ranges for S3 onset calculated from four cores appear to be clustered within a time interval of 84,263–79,966 yrBP and overlap between 80,400 and 83,200 yrBP (Fig. 2.10a, b; Table 2.6). Similarly, onset timings for sapropel S4 range from 106,580–105,020 yrBP in core MAR03-28 (North Skiros Basin), from 106,381–104,819 yrBP in core MAR03-25 (South Ikaria Basin), from 106,863–104,737

Sapropels	MAR03-28	MAR03-3	MAR03-2	MAR03-25	MAR03-27
	error range (± 781)	error range (± 1063)	error range (± 526)	error range (± 781)	error range (± 434)
	onset	onset	onset	onset	onset
S3	80,600	83,200	82,800	81,600	80,400
	81,381–79,819	84,263–82,137	83,326–82,274	82,381–80,819	80,834–79,966
S4	105,800	105,800	106,400	105,600	
	106,581–105,019	106,863–104,737	106,926–105,874	106,381–104,819	
S5	128,400	128,600			
	129,181–127,619	129,663–127,537			
	termination	termination	termination	termination	termination
S3	70,800	72,600	76,600	76,800	74,000
	71,581–70,019	73,663–71,537	77,126–76,074	77,581–76,019	74,434–73,566
S4	96,200	100,600	94,400	97,800	
	96,981–95,419	101,663–99,537	94,926–93,874	98,581–97,019	
S5	121,000	123,600			
	121,781–120,749	124,663–122,537			
Core bottoms	131,800 \pm 781	130,800 \pm 1063	110,200 \pm 526	113,800 \pm 781	87,200 \pm 434

Sapropel durations	MAR03-28	MAR03-3	MAR03-2	MAR03-25	MAR03-27	
S3	9,800±781	10,600±1063	6,200±526	4,800±781	6,400±434	
S4	9,600±781	5,200±1063	12,000±526	7,800±781		
S5	7,400±781	5,000±1063				

Onset timings	This study	This study (lagged, Euboea B.)	Lourens et al., 1996	Lourens et al., 1996 (lagged, eastern Med.)	Hilgen, 1991 (lagged, eastern Med.)	Hilgen (1991)	Muerdter et al., 1984	Capotondi and Vigliotti (1999)
S3	83.2–80.6	80.4	84	81	79	83	81-78	81
S4	106.4–105.6		105	102	102	106	100-98	102
S5	128.6–128.4		127	124	123	127	125-116	124

Nisyros	54,800	57,600	55,200	53,800	56,000	Nisyros ages 46.8±5.69 (Margari et al., 2007) 42-44 ka (Aksu et al., 2008)
X1			92,800	82,800		

Table 2.6. Calculated ages of sapropels S3, S4, S5 and Nisyros and X1 ash layers. Also shown are sapropel durations and comparison of the timing of sapropel initiations calculated in this study with those previously proposed from the eastern Mediterranean. Lagged sapropel ages proposed by Lourens et al. (1996) and by Hilgen (1991) are based on the observed consistent difference of 3-4 ka between orbital forcing and maximum climate response and sapropel formation.

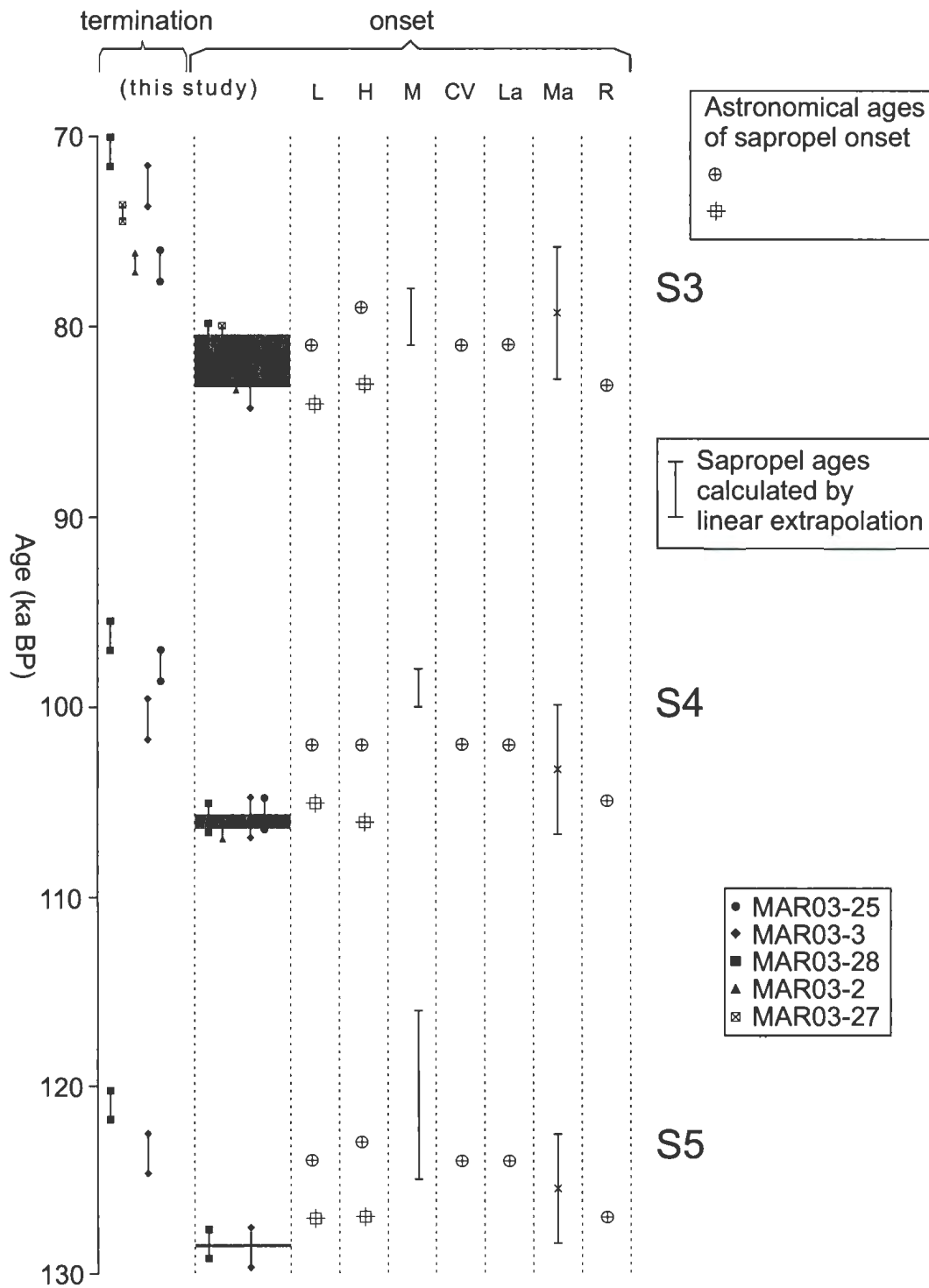


Figure 2.10a. Calculated onset/termination age ranges of sapropels S3, S4 and S5. Also shown are the previously published sapropel ages from Lourens, 1996 (L), Hilgen et al., 1991 (H), Muerdter et al., 1984 (M), Capotondi and Vigliotti (CV), Langereis et al., 1997 (La), Martinson et al., 1987 (Ma), and Rossignol-Strick and Paterne, 1999 (R).

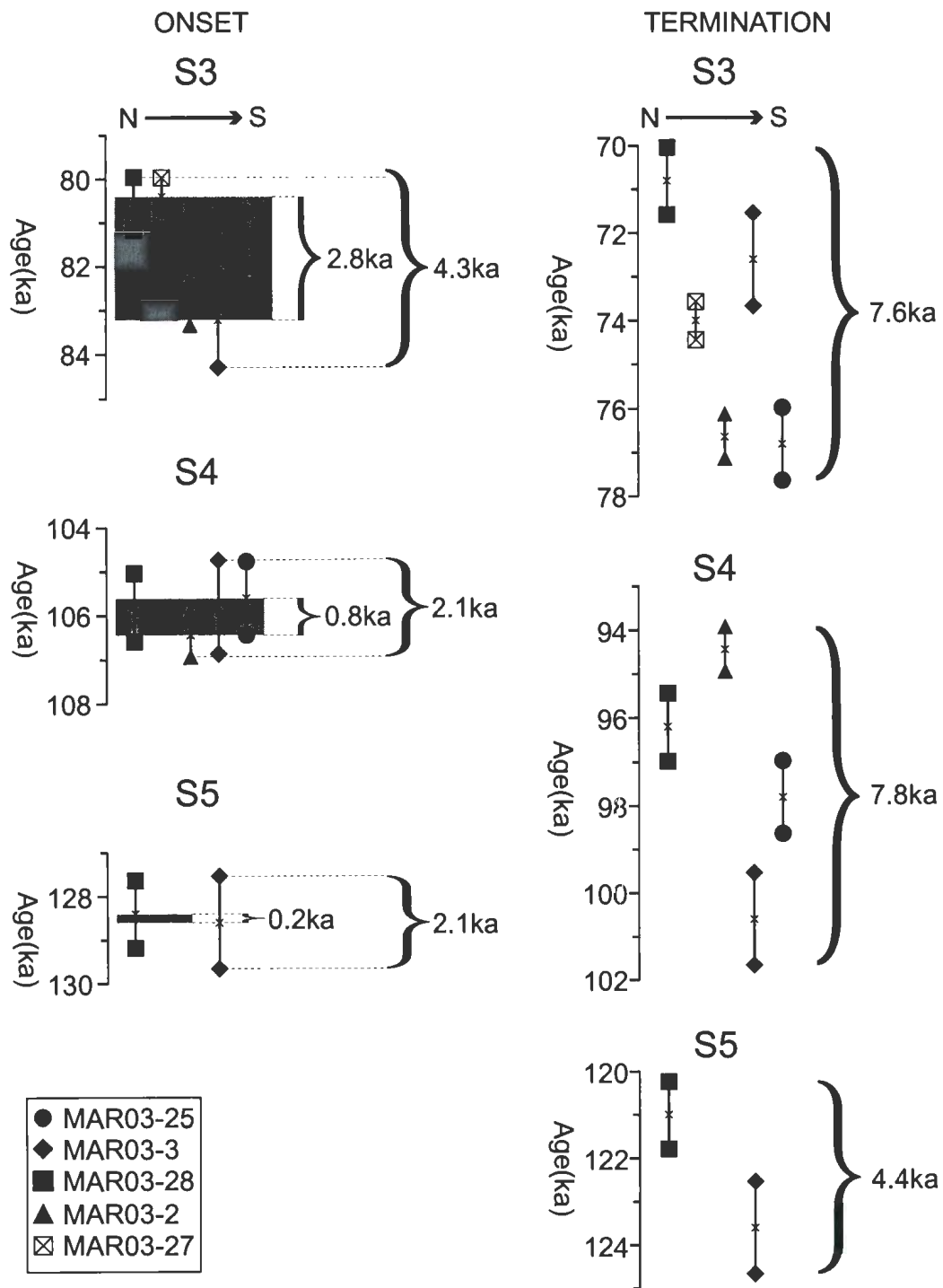


Figure 2.10b. Enlarged demonstration of calculated sapropel onset/termination age ranges. Gray horizontal bars represent the inferred age interval for the initiation of sapropel deposition. Note the notable differences between onset and termination age ranges.

in core MAR03-3 (Mikonos Basin) and from 106,926–105,874 in core MAR03-2 (North Ikaria Basin). The max/min age estimates range between 106,926 yrBP and 104,737 yrBP and overlap in the interval 106,400–105,600 yrBP (Fig. 2.10a, b; Table 2.6). For sapropel S5, the calculated onset timings are between 129,180 and 127,620 yrBP in core MAR03-28 (North Skiros Basin) and between 129,663 and 127,537 yrBP in core MAR03-3 with a time difference of 2120 years. According to these age ranges, an overlap time interval of 128,600–128,400 yrBP can be derived for the onset of sapropel S5; however, due to its limited presence at the bottom of only two cores, age variations cannot be assessed as reliably as for the younger sapropels (Fig. 2.10a, b; Table 2.6).

Given the error ranges, being as much as ± 1063 years, and despite the fact that sapropel S5 was detected only in two cores, the calculated timings for MIS5 sapropels seem to exhibit a narrow age range (Fig. 2.10b). Overall, the deduced age ranges seem to be suggestive of essentially synchronous onset. Consequently, the calculated timings for the onset of sapropels S3, S4 and S5 are 83.2–80.4 ka BP, 106.4–105.6 ka BP and 128.6–128.4 ka BP, respectively.

The calculated termination times for sapropel units demonstrate notable differences particularly for sapropels S3 and S4 ranging, respectively, from 70,020 yrBP (in core MAR03-28-North Skiros Basin) to 77,633 yrBP (in core MAR03-25-South Ikaria Basin) and from 93,874 yrBP (in core MAR03-2-North Ikaria Basin) to 101,663 yrBP (in core MAR03-3-Mykonos Basin) with a total variation of ~ 7.7 ka. The calculated termination ages for sapropel S5 range from 121,780–120,749 yrBP in core MAR03-28 and from 124,663–122,537 yrBP in core MAR03-3. These age ranges span comparatively a shorter time interval (4.4 ka) and suggest an overall termination time

interval 123.6–121 ka BP. However, given that sapropel S5 is present in just two cores, the termination age range could likely be more than suggested by this study.

Another outcome of these calculations is the discernable differences between the onset and termination time ranges. Taking into account error bars as much as ± 1063 yr, the onset timings for sapropels S3, S4 and S5 suggest a quasi-synchronous initiation throughout the Aegean Sea during MIS5. On the other hand, termination times covering a larger interval are indicative of diachroneity.

The age variations, particularly for sapropel S3 and S4, might result from a scarcity of age control points to accurately date sapropel tops. However, sapropel S3 in cores MAR03-28 and MAR03-3 and sapropel S4 in cores MAR03-28 and MAR03-2 are noticeably thicker than their counterparts in the other three cores and there must have been a three-order-of-magnitude increase in sedimentation rates to develop this greater thickness if the duration was the same at all sites. It is believed to be more likely that extended durations for the accumulation of sapropels S3 and S4 in North Skiros, Mykonos and North Ikaria basins are genuine. These prolonged durations in these three subbasins, and perhaps in other subbasins of the Aegean Sea, probably occurred because of hindered bottom-water exchange between subbasins (i.e., bottom-water stagnation). Such basin seclusion was previously proposed by Zervakis et al. (2004) who postulated that, during stagnation periods, North Skiros Basin was isolated from the subbasins of the central Aegean Sea below 400 meters.

According to the calculations presented here, basin seclusion likely took place during times of sapropel formation. Furthermore, the time spans of sapropel terminations show a significant difference, changing from 4.4 ka in sapropel S5 to 7.8 ka and 7.6 ka in

sapropels S4 and S3, respectively (Fig. 2.10b). Such differences can be attributed to the intensity of environmental changes that took place during sapropel formation and the response of the Aegean Sea subbasins. For instance, during the last 130 ka, the most intense environmental changes occurred at the time of sapropel S5 deposition which is manifested by high-amplitude abrupt shifts in the oxygen isotope values and the presence of S5 throughout the eastern Mediterranean. These intense climatic alterations must have affected the entire Aegean Sea synchronously, resulting in relatively more clustered sapropel termination times. On the other hand, during the deposition of sapropels S3 and S4 the environmental conditions leading to sapropel formation were comparatively less intense so that their effectiveness (e.g., sustainability, prolongation) throughout the Aegean Sea was most likely controlled by the physiography of the subbasins (e.g., basin morphology and proximity to source) and might have caused significant variations in sapropel durations from basin to basin.

Following the pioneering work of Martine Rossignol-Strick on the relationship between monsoonal maxima, sapropel formation, and the astronomically controlled insolation cycles, it has been confirmed that sapropels are generally associated with times when perihelion falls in boreal (Northern Hemisphere – NH) summer (i.e., precessional minima). This configuration causes enhanced summer insolation and, accordingly, higher seasonal contrast in the NH, resulting in strong atmospheric pressure differences over land (low pressure) and sea (high pressure). This difference leads to moisture-laden surface air flow from ocean to land and as the air rises and cools over the land it releases its vapour as rain (e.g., monsoonal rains).

Comparison of the sapropel record with variations in precession cycles during the

last 150 ka shows that the Aegean Sea sapropels S3, S4, and S5 coincide with times of precessional minima during which summer insolation maxima occurred in the NH (Fig. 2.9a, b, c; Rossignol-Strick, 1983, 1985; Hilgen, 1991; Hilgen et al., 1993). Furthermore, the timing of the onset of sapropels S4 and S5 demonstrates that increased organic carbon accumulations predated those in the eastern Mediterranean Sea by several thousand years. On the other hand, in sapropel S3, the calculated onset timings are consistent with the age of its eastern Mediterranean counterparts (Fig. 2.10a; Table 2.6).

2.5.2.1. Tephra chronology below Y5 (Nisyros and X1 tephras)

The upper three tephra layers (i.e., Z2, Y2 and Y5) are considered as dependable age control points and have been utilized for chronostratigraphic reconstructions of the Aegean Sea sediments. Nisyros and X1 tephras generally have limited dispersal throughout the Aegean Sea and are rarely detected in cores. Hence, their reliability as age control points is questionable. Although not used as age control points in this study, the consistent presence of the Nisyros ash in all five cores and appearances of X1 ash in cores MAR03-2 and MAR03-25 (North/South Ikaria basins) allowed us to calculate their ages from the constructed sedimentation curves and compare the derived ages with those from the literature.

The most recent paper by Margari et al. (2007) reported an age range of 41.11–52.49 ka BP for the Nisyros tephra (Fig. 2.11; 46.8 ± 5.69 ka). When used in our sedimentation curves, this proposed age and its stratigraphic position caused a kink in all 'age-depth' plots (see Fig. 2.7a, b). This deviation forced a dramatic and unreasonable drop in sedimentation rates; hence, the Nisyros tephra was omitted as an age control

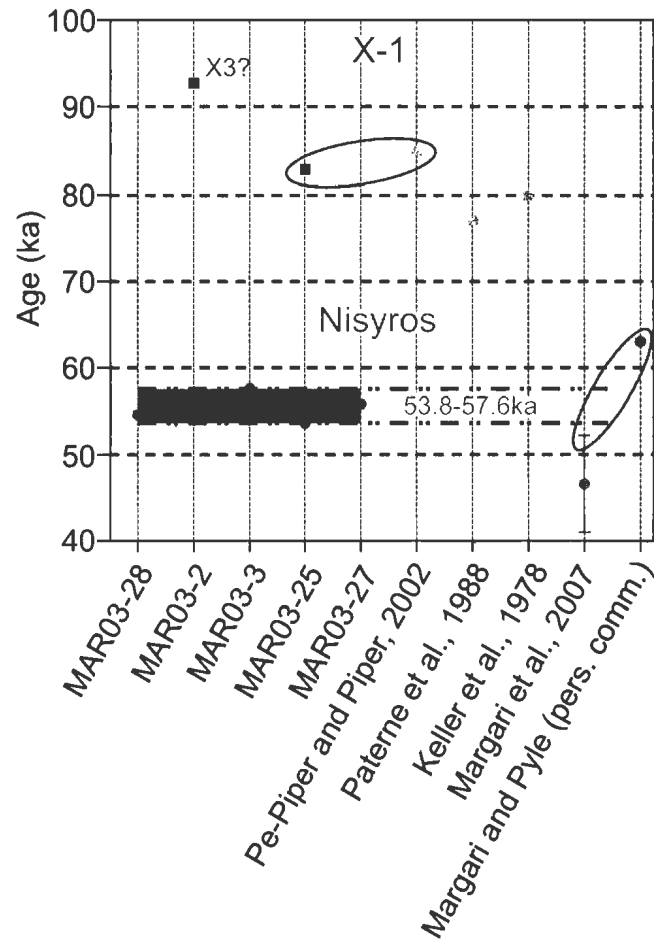


Figure 2.11. Calculated ages of the Nisyros and X1 tephras and their comparison with previously published ages.

point. This approach allows us to provide a fresh estimate for the true age of that tephra. The interpolated age of the Nisyros ash calculated from sedimentation curves is in the range 57.6–53.8 ka, within the acceptable upper limit of 63 ka BP based on uncertainties in dating and field relationships (Fig. 2.11; pers. comm. 2011, Vasiliki Margari and David Pyle).

The X1 tephra in cores MAR03-25 and MAR03-2 is immediately below S3 and 50 cm above S4 (Fig. 2.4). A sample from MAR03-25 was geochemically analysed and matched with X1 characteristics based on its major and trace element composition, with a high similarity coefficient of 0.93 (Aksu et al., 2008). The MAR03-2 occurrence, however, was identified as X1 solely because its stratigraphic position is similar to that in core MAR03-25 (situated between sapropels S3 and S4; see Fig. 2.4). If both occurrences are indeed X1, the ages calculated from sedimentation curves are 82,800 yr BP and 92,800 yr BP for cores MAR03-25 and MAR03-2, respectively (Table 2.6). The estimate of 82,800 yr BP is in good agreement with previous studies; however, the 92,800 yr BP result is closer to the proposed age of X3 (Fig. 2.11), so the correlation of these two horizons by Aksu et al. (2008) may be incorrect, and future geochemical study of shards from MAR03-2 is recommended.

2.6. Conclusions

Although limited by the penetration depth of the cores, organic carbon contents and chronostratigraphic reconstructions demonstrate the presence of MIS5 sapropels S3, S4 and S5 in the Aegean Sea subbasins. The omnipresence of sapropels S3 and S4 in all five cores and S5 occurrence in two cores with the longest records (North Skiros and

Mikonos basins) demonstrate the suitability of the Aegean Sea for sapropel deposition.

Calculated average sedimentation rates range between 4.7 and 11.8 cm/ka with highest rates being observed in Euboea and North Ikaria basins (11.8 and 9.8 cm/ka, respectively).

Throughout the Aegean Sea the initiation of sapropels S4 and S5 mostly predated those in the eastern Mediterranean with ages ranging from 106.4–105.6 and 128.6–128.4 ka BP, respectively. The overall age range of initiation of sapropel S3 (83.2–80.4 ka BP) agrees well with its eastern Mediterranean counterparts. However, calculated ages from the two northernmost cores seem to postdate (or agree with lagged ages) postulated ages from the eastern Mediterranean by several thousand years, connoting the heterogeneity of the Aegean Sea subbasins in terms of rapid vs. lagged response to changing climatic conditions.

The sapropel initiations were abrupt, whereas the timing of sapropel terminations was controlled both by the amplitude of paleoclimatic changes and the physiography/location of the subbasins. However, the impact of sapropel burndown-fronts cannot be ruled out and might partly account for apparent differences in the ages of terminations.

The calculated age of the Nisyros tephra does not agree with the previously published age and suggests that further studies might be necessary to provide a reliable age for this event. Until that time, its age cannot be used as a chronological control point.

The ash layer identified as X1 in core MAR03-2 by Aksu et al. (2008) must be geochemically analysed in order to make an accurate identification. Results based on sedimentation-rate curves suggest it might instead be X3.

References

- Aksu, A.E., 1985. Palaeomagnetic stratigraphy of the CESAR cores. *In: Initial Geological Report on CESAR The Canadian Expedition to Study the Alpha Ridge, Arctic Ocean*, R.H. Jackson, P.J. Mudie and S.M. Blasco (Eds.). Geological Survey of Canada Paper 84 22: 101–114.
- Aksu, A.E., 1985. Planktonic foraminiferal and oxygen isotopic stratigraphy of CESAR cores 102 and 103: preliminary results. *In: R.H. Jackson, P.J. Mudie and S.M. Blasco (Eds.). Geological Survey of Canada Paper 84 22: 115–124.*
- Aksu, A.E., Yaşar, D., Mudie, P.J., 1995a. Paleoclimatic and paleoceanographic conditions leading to development of sapropel layer S1 in the Aegean Sea. *Palaeogeography, Palaeoclimatology, Palaeoecology* 116, 71–101.
- Aksu, A.E., Jenner, G., Hiscott, R.N., İşler, E.B., 2008. Occurrence, stratigraphy and geochemistry of Late Quaternary tephra layers in the Aegean Sea and the Marmara Sea. *Marine Geology* 252, 174–192.
- Calvert, S. E., Karlin, R. E., 1998. Organic carbon accumulation in the Holocene sapropel of the Black Sea. *Geology*; February; v. 26; no. 2; p. 107–110.
- Casford, J.S.L., E.J. Rohling, R. H. Abu Zied, S. Cooke, C. Fontanier, M. Leng, and V. Lykousis 2002. Circulation changes and nutrient concentrations in the late Quaternary Aegean Sea: A nonsteady state concept for sapropel formation, *Paleoceanography*, 17, 1024, DOI:10.1029/2000PA000601.
- Casford, J. S. L., R. H. Abu Zied, E. J. Rohling, S. Cooke, C. Fontanier, M. J. Leng, A. Millard, and J. Thomson, 2007. A stratigraphically controlled multiproxy

- chronostratigraphy for the eastern Mediterranean, *Paleoceanography*, 22, PA4215, DOI:10.1029/2007PA001422.
- De Rijk, S., Hayes, A., Rohling, E.J., 1999. Eastern Mediterranean sapropel S1 interruption: an expression of the onset of paleoceanographic conditions leading to development of climatic deterioration around 7 ka BP. *Marine Geology*, 153, 337–343.
- Emeis KC, Schulz H, Struck U, Rossignol Strick M, Erlenkeuser H, Howell MW, Kroon D, Mackensen A, Ishizuka S, Oba T, Sakamoto T, Koizumi I, 2003. Eastern Mediterranean surface water temperatures and $\delta^{18}\text{O}$ composition during deposition of sapropels in the late Quaternary. *Paleoceanography* 18(1):1005. doi:10.1029/2000PA00061
- Facorellis Y, Maniatis Y, Kromer B., 1998. Apparent ^{14}C ages of marine mollusk shells from a Greek island: calculation of the marine reservoir effect in the Aegean Sea. *Radiocarbon* 40:963–973.
- Geraga, M., Tsaila Monopolis, S., Ioakim, C., Papatheodorou, G., Ferentinos, G., 2000. Evaluation of palaeoenvironmental changes during the last 18,000 years in the Myrtoon basin, SWAegean Sea. *Palaeogeogr. Palaeoclimatol. Palaeoecol.* 156, 1–17.
- Geraga, M., Tsaila Monopoli, St., Ioakim, Ch., Papatheodorou, G., Ferentinos, G., 2005. Short term climate changes in the southern Aegean Sea over the last 48,000 years. *Palaeogeography, Palaeoclimatology, Palaeoecology* 220, 311–332.
- Gogou, A., Bouloubassi, I., Lykousis, V., Arnaboldi, M., Gaitani, P., Meyers, P.A., 2007.

- Organic geochemical evidence of Late Glacial-Holocene climate instability in the North Aegean Sea. *Palaeogeography, Palaeoclimatology, Palaeoecology* 256, 1–20.
- Fontugne, M.R., Paterne, M., Calvert, S.E., Murat, A., Guichard F. and Arnold, M., 1989. Adriatic deep water formation during the Holocene: Implication for the reoxygenation of the deep eastern Mediterranean Sea. *Paleoceanography*, vol. 4, no. 2, 199–206.
- Fontugne, M.R., Calvert, S.E., 1992. Late Pleistocene variability of the carbon isotopic composition of organic matter in the eastern Mediterranean: monitor of changes in carbon sources and atmospheric CO₂ concentrations. *Paleoceanography*, 7, 1–20.
- Hart, B.S., Hamilton, T.S and Barrie, J.V., 2004. Sedimentation rates and patterns on a deep-water delta (Fraser Delta, Canada); integration of high-resolution seismic stratigraphy, core lithofacies, and ¹³⁷Cs fallout stratigraphy. *Journal of Sedimentary Research*, 68: 556-568.
- Hesse, R. and Chough, S.K., 1980. The Northwest Atlantic Mid-Ocean Channel of the Labrador Sea: II. deposition of parallel laminated levee-muds from the viscous sublayer of low density turbidity currents. *Sedimentology*, 27: 697-711.
- Hilgen, F.J., 1991a. Astronomical calibration of Gauss to Matuyama sapropels in the Mediterranean and implication for the Geomagnetic Polarity Time Scale. *Earth Planet. Sci. Lett.* 104, 226–244.
- Hilgen, F.J., 1991. Extension of the astronomically calibrated tional sequences and cycles in the eastern Mediterranean. *Earth Planet. Sci. Lett.* 107, 349–368.

- Hilgen, F.J., Rohling, E.J., van der Borg, K., Vergnaud Grazzini, C., Zachariasse, W., 1993. Late Quaternary central Mediterranean biochronology. *Marine Micropaleontology* 21, 169–189.
- Howell, M.W., Thunell, R.C., 1992. Organic carbon accumulation in Bannock Basin: evaluating the role of productivity in the formation of eastern Mediterranean sapropels. *Mar. Geol.* 103, 461–471.
- Kidd, R.B., Cita, M.B., Ryan, W.B.F., 1978. Stratigraphy of eastern Mediterranean sapropel sequences recovered during DSDP LEG 42A and their paleoenvironmental significance. In: Hsu, K.J., Mondrader, L., et al. (Eds.), *Initial Reports of the Deep Sea Drilling Project*. US Government Printing Office, Washington, DC, pp. 421–443.
- Kotthoff, U., Pross, J., Müller, U.C., Peyron, O., Schmiedl, G., Schulz, H., Bordon, A., 2008. Climate dynamics in the borderlands of the Aegean Sea during formation of sapropel S1 deduced from a marine pollen record. *Quaternary Science Reviews* 27, 832–845.
- Kullenberg, B., 1952. On the salinity of water contained in marine sediments. *Medd. Oceanogr. Inst. Goteberg* 21, 1–38.
- Laskar, J., Joutel, F., Boudin, F., 1993. Orbital, precessional, and insolation quantities for the Earth from -20Myr to +10Myr. *Astronomy and Astrophysics*, 270, 522–533.
- Levin, L.A. and Nittrouer, C.A., 1987. Textural characteristics of sediments on deep seamounts in the eastern Pacific Ocean between 10°N and 30°N. *Geophysical Monograph Series*, 43: 187-203.
- Löwemark, L. and Werner, F., 2001. Dating errors in high-resolution stratigraphy: a

- detailed X-ray radiograph and AMS-14C study of Zoophycos burrows. *Marine Geology*, 177, 191–198.
- Löwemark, L., Lin, Y., Chen, H.-F., Yang, T.-N., Beier, C., Werner, F., Lee, C., Song, S. R. and Kao, S. J., 2006. Sapropel burn-down and ichnological response to late Quaternary sapropel formation in two ~400 ky records from the eastern Mediterranean Sea. *Palaeogeography, Palaeoclimatology, Palaeoecology*, 239, 406–425.
- Lykousis, V., 2002. Circulation changes and nutrient concentrations in the late Quaternary Aegean Sea: a nonsteady state concept for sapropel formation. *Paleoceanography* 17, 1024–1034.
- Margari, V., Pyle, D., Bryant, C., Gibbard, P.L., 2007. Mediterranean tephra stratigraphy revisited: results from a long terrestrial sequence on Lesvos Island, Greece. *J. Volcanol. Geotherm. Res.* 163, 34–54.
- Mercone, D., Thomson, J., Croudace, I.W., Siani, G., Paterne, M., Troelstra, S., 2000. Duration of S1, the most recent sapropel in the eastern Mediterranean Sea, as indicated by accelerator mass spectrometry radiocarbon and geochemical evidence. *Paleoceanography* 15, 336–347.
- Mercone D, Thomson J, Abu Zied RH, Croudace IW, Rohling EJ., 2001. High resolution geochemical and micropaleontological profiling of the most recent eastern Mediterranean sapropel. *Marine Geology*, 177:25–44.
- Murat, A. and Got, H., 2000. Organic carbon variations of the eastern Mediterranean Holocene sapropel: a key for understanding formation processes. *Palaeogeography, Palaeoclimatology, Palaeoecology*, 158, 241–257.

- Narcisi, B., Vezzoli, L., 1999. Quaternary stratigraphy of distal tephra layers in the Mediterranean -an overview. *Global and Planetary Change* 21, 31–50.
- Ninkovich D. and Heezen, B. C., 1967. Physical and chemical properties of volcanic glass shards. *Nature (London)*, 213, pp. 582–584.
- Perissoratis, C., Piper, D.J.W., 1992. Age, regional variation and shallowest occurrence of S1 sapropel in the Aegean Sea. *Geo Mar. Lett.* 12, 49–53.
- Piper, D.J.W., Farre, J.A., and Shor, A.N., 1985. Late quaternary sumps and debris flows on the Scotian slope, *Geological Society of America Bulletin*, 96, 1508-1517.
- Rohling, E.J., Hilgen, F.J., 1991. The eastern Mediterranean climate at times of sapropel formation: a review. *Geol. Mij*n changes in the Mediterranean Sea: hydrographic and depositional effects. *Nature* 338, 493–496.
- Rohling, E.J., P. A. Mayewski, A. Hayes, R. H. Abu Zied, and J.S.L. Casford, 2002a. Holocene atmosphere ocean interactions: records from Greenland and the Aegean Sea, *Climate Dynamics*, 18, 587–593.
- Rosignol-Strick, M., Nesteroff, W., Olive, P., Vergnaud Grazzini, C., 1982. After the deluge: Mediterranean stagnation and sapropel formation. *Nature* 295, 105–110.
- Rosignol-Strick, M., 1983. African monsoons, an immediate climate response to orbital insolation. *Nature* 304, 46–49.
- Rosignol-Strick, M., 1985. Mediterranean Quaternary sapropels, an immediate response of the African monsoon to variation of insolation. *Palaeogeogr. Palaeoclimatol. Palaeoecol.* 49, 237–263.
- Roussakis, G., Karageorgis, A.P., Conispoliatis, N., Lykousis, V., 2004. Last glacial-Holocene sediment sequences in N. Aegean basins: structure,

- accumulation rates and clay mineral distribution. *Geo Marine Letters* 24, 97–111.
- Stuiver, M., Reimer, P. J., and Reimer, R. W. 2005. CALIB 5.0. [WWW program and documentation].
- Velaoras, D. and Lascaratos, A., 2005. Deep water mass characteristics and interannual variability in the North and Central Aegean Sea *Journal of Marine Systems* 53, 59–85.
- Waelbroeck, C., Labeyrie, L., Michael, E., Duplessy, J.C., McManus, J.F., Lambeck, K., Balbon, E. and Labracherie, M., 2002. Sea-level and deep water temperature changes derived from benthic foraminifera isotopic records. *Quaternary Science Reviews*, 21, 295–305.
- Yaltirak, C. Sakinc, M., Aksu, A.E., Hiscott, R.N., Galleb, B., Ulgen, U.B., 2002. Late Pleistocene uplift history along the southwestern Marmara Sea determined from raised coastal deposits and global sea level variations. *Marine Geology* 190 (2002) 283–305.
- Zachariasse, W.J., Gudjonsson, L., Hilgen, F.J., Langereis, C.G., Lourens, L.J., Verhallen, P. and Zijderveld, J., 1990. Late Gauss to early Matuyama invasions of *Neogloboquadrina atlantica* in the Mediterranean and associated record of climatic change. *Paleoceanography* 5(2): doi: 10.1029/89PA03635. issn: 0883–8305.
- Zervakis, V., Georgopoulos, D., Drakopoulos, P.G., 2000. The role of the North Aegean in triggering the recent Eastern Mediterranean climatic changes. *Journal Geophysical Research* 105 (C11), 26103–26116.
- Zervakis, V., D. Georgopoulos, A.P. Karageorgis, and A. Theocharis, 2004. On the

response of the Aegean sea to climatic variability: a review. *International Journal of Climatology*, 24, 1845–1858.

Chapter 3. LATE QUATERNARY PALEOCEANOGRAPHIC EVOLUTION OF THE AEGEAN SEA: A PLANKTONIC FORAMINIFERAL APPROACH

Abstract

Quantitative variations in the planktonic faunal assemblages identified in five cores collected from the northern and southern Aegean Sea demonstrate a sequence of bioevents during the last ~130, 000 years. This sequence allows definition of four major biozones. The distributional patterns of the most significant taxa exhibit the same trends among all core localities which suggests that the major changes in the planktonic foraminifera assemblages have taken place rather synchronously in the Aegean Sea. The sapropels S3, S4 and S5 were deposited under similar hydrographic conditions during which a distinct deep chlorophyll maximum (DCM) layer was established, indicating a stratified water column and increased primary productivity. On the other hand, the faunal contrast between the S1 and older sapropels indicates that the most recent sapropel was deposited in the absence of a DCM layer, devoid of a deep phytoplankton assemblage. Under such conditions, oxygen advection via intermediate water flow must have been significantly reduced which implies significant stagnation.

Cluster analysis shows consistent coupling of *G. bulloides* with *Gs. ruber* during times of non-sapropel deposition which is interpreted to be indicative of a stratified euphotic zone composed of a warm/nutrient-poor and a cooler/nutrient-rich upper and lower layers, respectively. This covariation of the two species further signifies the strong influence of increased river runoff that controls the fertility and stratification of the surface waters.

3.1. Introduction

Planktonic foraminifera are one of the most powerful tools used in Pleistocene – Recent paleoceanographic studies: they are particularly useful in constraining qualitative and quantitative reconstructions of the water mass characteristics as recorded in marine cores (Kucera et al., 2005; Melki et al., 2010). Numerous studies show that planktonic foraminifera have both geographic and water-depth preferences, occupying distinct ecological niches which are controlled by the surface water hydrography, water mass properties, and upwelling (e.g., Bé, 1960, 1977; Zhang, 1985; Deuser et al., 1981 Kroon and Ganssen, 1989; Sautter and Thunell, 1991). Variations in the oxygen and carbon isotopic compositions ($\delta^{18}\text{O}$, $\delta^{13}\text{C}$) and trace element ratios (e.g., Mg/Ca) in foraminiferal shells are reliable indicators of sea surface and bottom water temperatures and salinities, as well as the availability of food in the water column (e.g., Spero and Lea, 1993, 1996; Lea et al., 2003; Rohling et al., 2004; Geraga et al., 2005).

Almost all planktonic foraminifera species prosper in the euphotic layer within which significant food concentration (e.g., phytoplankton) and water temperature can vary vertically. Such gradients in the water column are often reflected in the assemblages of planktonic foraminifera as they prefer specific temperature ranges and directly graze upon phytoplankton and/or feed on other organisms (Hemleben et al., 1989). There has been particular interest in the planktonic foraminifera species *Globigerinoides ruber* (w) which indicates warm/oligotrophic summer mixed-layer conditions (Lourens et al., 1992; Rohling et al., 1993; Pujol and Vergnaud-Grazzini, 1995; Reiss et al., 2000); *Neogloboquadrina pachyderma* (dextral) and

Neogloboquadrina dutertrei which are intermediate water dwellers and may suggest shoaling of the pycnocline into the base of the euphotic layer and parallel formation of a distinct deep chlorophyll maximum (DCM); *Globigerina bulloides* which indicates eutrophic surface waters such as seen in upwelling zones, and *Globorotalia inflata* and/or *Globorotalia scitula* which reflect a cool, homogeneous and relatively eutrophic winter mixed layer.

This paper uses planktonic foraminiferal assemblages, $\delta^{18}\text{O}$ records in planktonic and benthic foraminifera and Mg/Ca ratios in planktonic foraminiferal shells collected in five long piston cores from the Aegean Sea. It aims (i) to delineate the Late Quaternary paleoceanographic evolution of the region, with special emphasis on the determination of sea surface temperature and salinity variations during the development of organic rich sediments (i.e., sapropels and sapropelic muds, Kidd et al., 1978) as well as the non-sapropelic background sedimentation and (ii) to examine temporal and spatial variations in the characteristics of the water column, in particular the degree of stratification and temporal variations in the depth and strength of the pycnocline.

3.2. Seabed morphology and hydrography of the Aegean Sea

The Aegean Sea is a shallow elongate embayment which forms the northeastern extension of the eastern Mediterranean Sea (Fig. 3.1). To the northeast, it is connected to the Black Sea through the Straits of Dardanelles and Bosphorus and the intervening small land-locked Marmara Sea. In the south, the Aegean Sea communicates with the eastern Mediterranean Sea through several broad and deep straits located between the

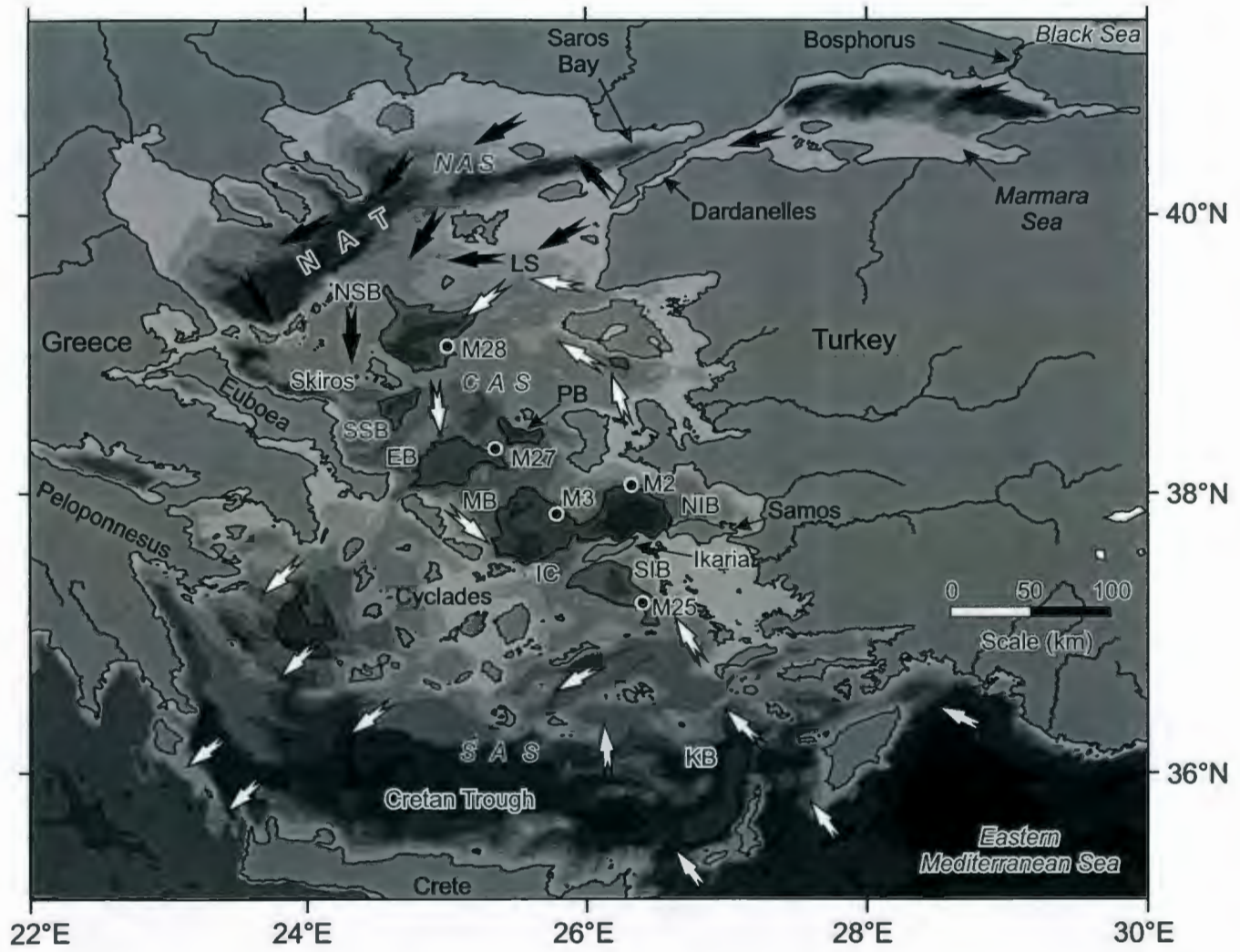


Figure 3.1. Simplified map of the Aegean Sea and surroundings showing core locations, major rivers, subbasins and circulation pattern. Light to progressively darker grey tones represent <100 m and 200-1000 m depths (at 200 m intervals). The black zone in the southeast of the map is >1200m deep. Outlined contours highlight the limits of subbasins. NAS-North Aegean Sea, NAT-North Aegean Trough, NSB-North Skiros Basin, SSB-South Skiros Basin, CAS-Central Aegean Sea, LS-Lesbos shelf, EB-Euboea Basin, MB-Mikonos Basin, PB-Psara Basin, NIB-North Ikaria Basin, IC-Ikaria Channel, SIB-South Ikaria Basin, SAS-South Aegean Sea, KB-Karpathos Basin. Black and white arrows illustrate the surface water circulation of the Black Sea and the Mediterranean Sea waters, respectively. Core names are abbreviated; e.g., 'M' stands for 'MAR03'.

Peloponnesus Peninsula, the Island of Crete and southwestern Turkey (Fig. 3.1). The Aegean Sea is divided into three physiographic regions: the northern Aegean Sea, including the North Aegean Trough, the central Aegean plateaux and basins, and the southern Aegean Sea including the Cretan Trough (Fig. 3.1).

The dominant bathymetric feature in the northern portion of the Aegean Sea is the 800–1200 m-deep depression referred to as the North Aegean Trough. It includes several interconnected depressions and extends from Saros Bay with a WSW–SW trend and widens toward the west (Fig. 3.1). The central Aegean Sea is characterized by a series of shallower (600–1000 m), mainly NE-oriented depressions and their intervening 100–300 m-deep shoals and associated islands (Fig. 3.1). The southern Aegean Sea is separated from the central Aegean Sea by the arcuate Cyclades archipelago, a convex-southward shallow volcanic arc dotted by numerous islands and shoals extending from the southern tip of Euboea Island to southwestern Turkey (Fig. 3.1). A large 1000–2000 m-deep, generally E–W trending depression, the Cretan Trough, occupies the southernmost portion of the Aegean Sea immediately north of Crete (Fig. 3.1).

The physical oceanography of the Aegean Sea is controlled primarily by the regional climate, the freshwater discharge from major rivers draining southeastern Europe, and the seasonal variations in the Black Sea surface-water outflow through the Strait of Dardanelles (Aksu et al., 1995a). Previous studies concerning the hydrographic conditions reveal that there is a general cyclonic water circulation in the Aegean Sea, although the most active dynamic features of the Aegean Sea are its mesoscale cyclonic and anticyclonic eddies (Lykousis et al., 2002). A branch of the westward flowing Asia Minor Current deviates toward the north from the eastern Mediterranean basin, carrying

the warm (16–25°C) and saline (39.2–39.5 psu) Levantine Surface Water and Levantine Intermediate Water along the western coast of Turkey. It occupies the uppermost 400 m of the water column. The Asia Minor Current reaches the northern Aegean Sea where it encounters the relatively cool (9–22°C) and less saline (22–23 psu) Black Sea Water and forms a strong thermohaline front. As a result, the water column structure in the northern and central Aegean Sea is comprised of a 20–70 m-thick surface veneer consisting of modified Black Sea water overlying higher salinity Levantine intermediate water which extends down to 400 m. The water column below 400 m is occupied by the locally formed North Aegean Deep Water with uniform temperature (13–14°C) and salinity (39.1–39.2 psu; Aksu et al., 1995; Zervakis et al., 2000; Zervakis et al., 2004; Velaoras and Lascaratos, 2005). The surface and intermediate waters follow the general counter-clockwise circulation of the Aegean Sea, and progressively mix as they flow southwards along the east coast of Greece.

3.3. Data and Methods

The data set consists of five long piston cores and five trigger-weight gravity cores collected during the 2003 cruise MAR-03 of the RV *Koca Piri Reis* of the Institute of Marine Sciences and Technology (Fig. 3.1; Table 3.1). Cores were collected using a 12 m-long Benthos piston corer (1000 kg head) with a 3 m-long gravity corer (180 kg head) used as trigger weight. The navigation was provided by the GPS instrument of the research vessel. The amount of core penetration was estimated by the mud-smear along the core barrels, and subsequently compared with the actual core recovery. A split-piston was used in all coring attempts, where the piston consists of two segments held together

Cores	Latitude	Longitude	PC length (cm)	TWC length (cm)	PC missing top (cm)	CompC length (cm)	Water depth (m)
MAR03-2	38°03.97'N	26°22.30'E	776	86	37	813	398
MAR03-3	37°51.72'N	25°49.17'E	580	50	24	604	720
MAR03-25	37°10.36'N	26°26.55'E	604	25	25	629	494
MAR03-27	38°18.68'N	25°18.97'E	952	106	80	1032	651
MAR03-28	39°01.02'N	25°01.48'E	726	165	100	826	453

Table 3.1. Core locations; piston (PC), gravity (TWC), composite (CompC) core lengths, and water depths.

by shear-pins. During the recovery of the corer, the upper segment of the piston shears the pins and moves upward to lock into the core head, while the lower segment remains at the top of the sediment in the core barrel, preventing flow-in. The gravity cores were used to determine and quantify potential core-top loss during the piston coring operation. All cores were kept upright onboard and during transport to Canada. Upon arrival to Memorial University of Newfoundland, cores were transferred to a cold storage facility and were kept at $\sim 4^{\circ}\text{C}$ until they were split. Cores were split and described by R.N. Hiscott in 2004. Sediment colour was determined using the "Rock-Color Chart" published by the Geological Society of America in 1984. Cores were sampled by the senior author in 2009 at 10 cm intervals. Approximately 7 cm^3 and 13 cm^3 sediment samples were collected for stable isotopic and faunal studies, respectively.

For oxygen and carbon isotopic analyses (i.e., $\delta^{18}\text{O}$, $\delta^{13}\text{C}$), samples were dried in a 40°C oven for 48 hours. The samples were transferred to glass beakers and were disaggregated in 100 cm^3 of distilled water containing 15 cm^3 of 1% Calgon (Na-hexametaphosphate) and 10 cm^3 of 30% hydrogen peroxide. The samples were then wet sieved through a $63\ \mu\text{m}$ sieve, were dried in a 40°C oven, and the $>63\ \mu\text{m}$ fractions were stored in glass vials.

Planktonic foraminifera were studied in five cores. Each sample was dry-sieved through 150 and $500\ \mu\text{m}$ screens. The $150\text{--}500\ \mu\text{m}$ fractions were divided into aliquots with a micro-splitter until a subsample contained at least 300 planktonic foraminifera specimens. Each aliquot was then transferred into a cardboard counting slide. All planktonic foraminifera were identified and counted in each sample. The taxa identified

in the samples were converted into percentages of the total number of planktonic foraminifera. Identifications follow the taxonomic descriptions of Parker (1962), Saito et al. (1981) and Hemleben et al. (1989). The total planktonic foraminiferal abundances in each sample were calculated as 'number of specimens per dry-weight sediment'.

Sea surface temperature (SST) and sea surface salinity (SSS) calculations were obtained from planktonic foraminifera assemblages using the transfer function technique developed by Imbrie and Kipp (1971). A transfer function is developed by studying modern assemblages and their environmental preferences and is used to suggest reasonable environmental conditions in the past based on fossil assemblages. To create a transfer function, a Q-mode, varimax-rotated factor analysis is applied to the assemblage percentages for modern samples which simplifies the data set into orthonormal factors. Next, a multiple linear regression of the obtained factors and recent oceanographic parameters is run to construct equations to determine temperature and salinity values of ancient sea water in which the same species lived. Modern planktonic foraminifera assemblage data and according transfer function equations are from Thunell (1979; see Appendix A for details). Proposed standard errors for summer and winter temperatures are 1°C and 1.2°C, respectively (Thunell, 1979).

For oxygen isotopic analyses, 16–20 planktonic and 4–6 benthic foraminiferal specimens of *Globigerinoides ruber* and *Uvigerina mediterranea* were collected from the >150 μm fractions, respectively. In a few intervals, *Gs. ruber* was absent and *Globigerina bulloides* and *Neogloboquadrina pachyderma* (dextral) were picked instead. Calibrations of the oxygen isotopic values between these three species were made in 30 samples containing both *Gs. ruber* and *G. bulloides* and 15 samples containing both *G.*

bulloides and *N. pachyderma* (dextral). The benthic foraminifer *U. mediterranea* was used in all but one core for better correlation with the global oxygen isotope curve (i.e., Lisiecki and Raymo, 2005), with the exception that only planktonic foraminiferal oxygen isotopic analyses were carried out for core MAR03-27. In cores MAR03-28 and MAR03-2, both benthic and planktonic oxygen isotopic curves were obtained, whereas only benthic foraminiferal isotopic curves were obtained in cores MAR03-3 and MAR03-25. All isotopic analyses were performed at the Stable Isotope Laboratory of the TERRA Facility at Memorial University of Newfoundland.

For trace element measurements on foraminiferal shells, five specimens of *Gs. ruber* from each sample were mounted on double-sided sticky taped glass slides (1"x3") with aperture side facing up. Trace element concentrations (i.e., Mg/Ca) in the carbonate tests of *Gs. ruber* were obtained using a Finnigan ELEMENT XR, a high-resolution double-focussing magnetic-sector inductively coupled plasma mass spectrometer (HR-ICPMS), and a GEOLAS excimer laser ($\lambda = 193\text{nm}$) at Memorial University of Newfoundland. The laser was focussed on the sample and fired at 5Hz repetition rate using an energy density of $5\text{J}/\text{cm}^2$ and 59μ laser spot diameter. Individual specimens were ablated with the laser five to six times to obtain adequate number of results from individual species and to increase the reliability of mean trace element contents in each foraminifera species. The results are expressed as Mg/Ca ratio. Standard deviation of the Mg content in *Gs. ruber* tests is calculated to be around $0.02\mu\text{g}$ based on replicate measurements on a number randomly selected samples at several depths from cores MAR03-28 and MAR03-2. Due to the logarithmic nature of the Mg/Ca temperature

equation, cooler temperatures (low Mg content) correspond to larger error bars. The resultant standard errors for cores MAR03-28 and MAR03-2 range between 1.7–6.8°C and 1.4–5°C with an average of 3°C and 2.5°C, respectively.

3.4. Lithostratigraphy

On the basis of visual core descriptions, organic carbon content and colour, four sapropel and five non-sapropel units are identified and labeled as 'A' through 'I' from top to bottom (Fig. 3.2a, b, c). The correlation of the units among the five cores was accomplished by matching peaks of oxygen isotopic curves (see Section 3.7 for discussion of this isotopic data) together with the stratigraphic positions of known ash layers (see units A and C; Fig. 3.3). Throughout the cores, sapropel units are distinguished by their comparatively darker colors and higher organic carbon contents. However, rather than a quantitative threshold (>0.5%, >1% or >2% TOC content), an organic carbon content twice that of the underlying and overlying units was used to classify a lithostratigraphic unit as a sapropel. Using this criterion, sediments with 1.0-12.65% TOC content are described in this paper as sapropels. Visual examination of the cores shows that most sediments consist of clay/silt-sized particles and are slightly to moderately burrowed. The coarse fraction is mainly composed of foraminifera, pteropods, bivalve and gastropod shells, and variable amounts of volcanic ash. Sediment accumulation is inferred to have occurred through hemipelagic rain due to paucity of terrigenous sand-sized material, lack of evidence for re-sedimentation (e.g., lack of normally graded event beds) and ubiquitous bioturbation.

Non-sapropel units A, C, E, G, I are composed of burrow-mottled foram-bearing

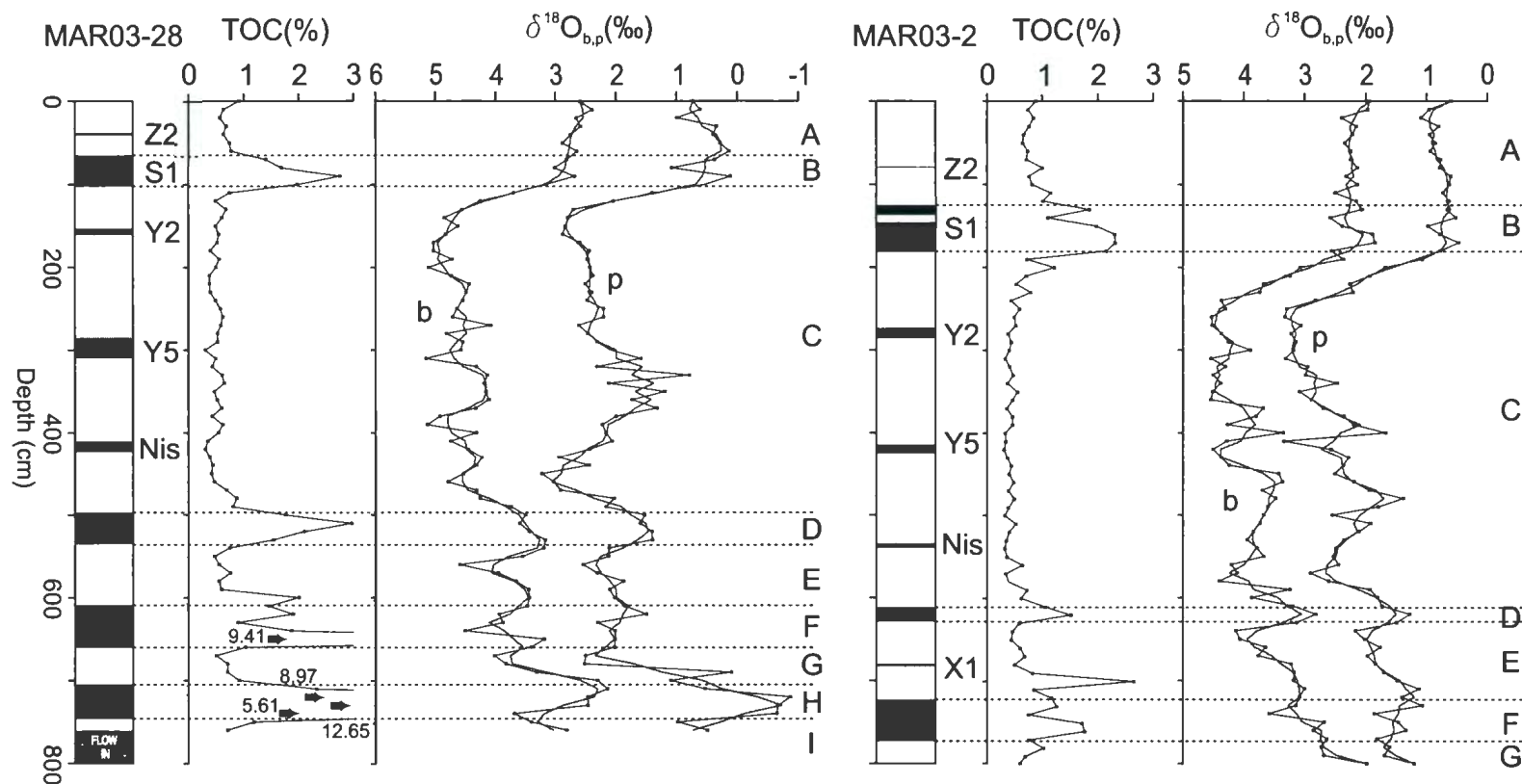


Figure 3.2a. Sapropel and non-sapropel units in the five cores and their assignment to one of nine lithologic units. Also shown are the downcore variations of TOC and oxygen isotope values. In all cores horizontal scales of TOC and $\delta^{18}\text{O}$ plots are the same. Red curves are 3-point moving averages. Grey area at the bottom of core MAR03-28 is flow-in. 'b' and 'p' stand for data from benthic and planktonic tests, respectively. Z2, Y2, Y5, Nis, X1 are ash horizons (Aksu et al., 2008)

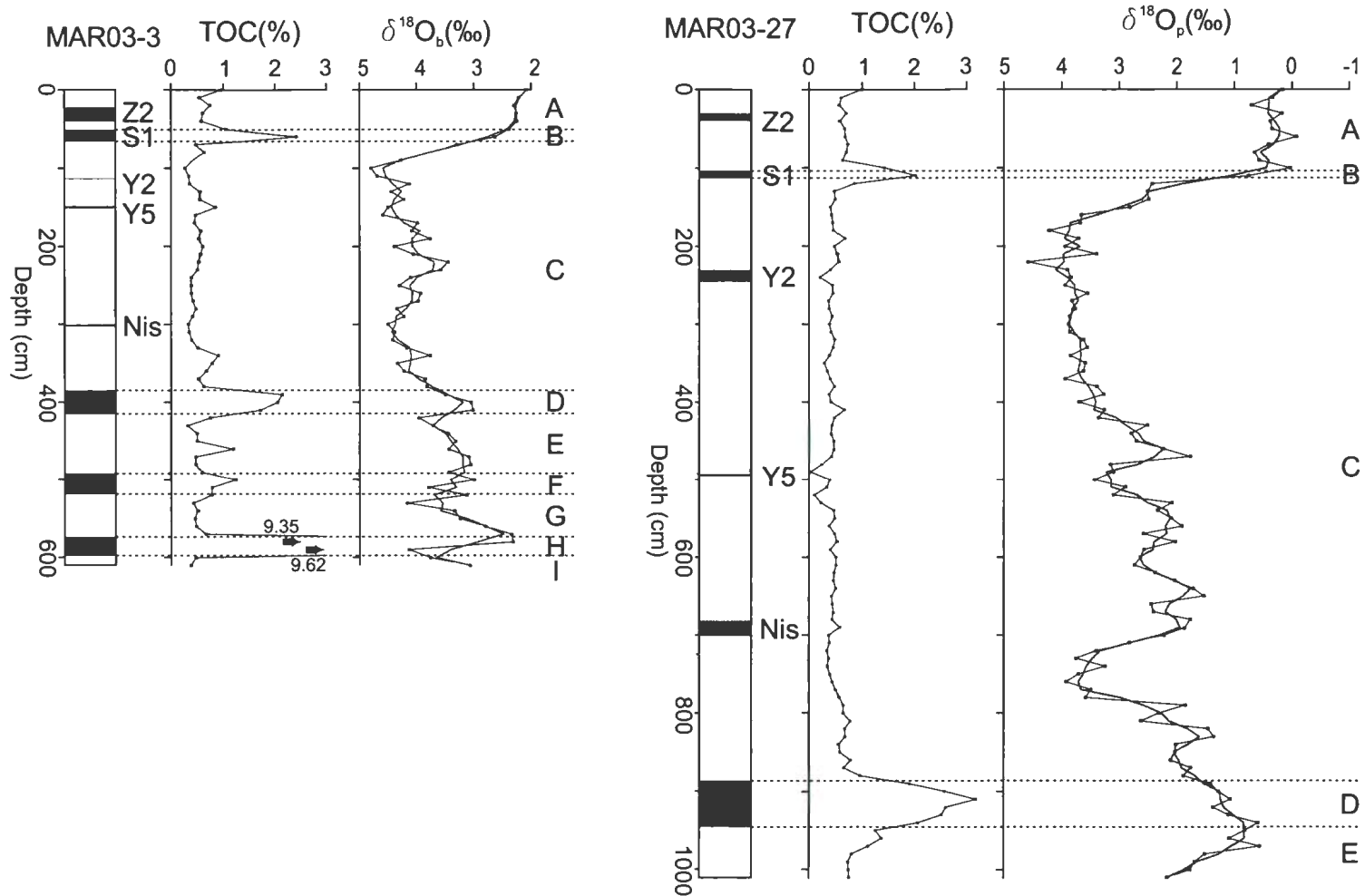


Figure 3.2b. Sapropel and non-sapropel units in the five cores and their assignment to one of nine lithologic units. Also shown are the downcore variations of TOC and oxygen isotope values. In all cores horizontal scales of TOC and $\delta^{18}\text{O}$ plots are the same. Red curves are 3-point moving averages.

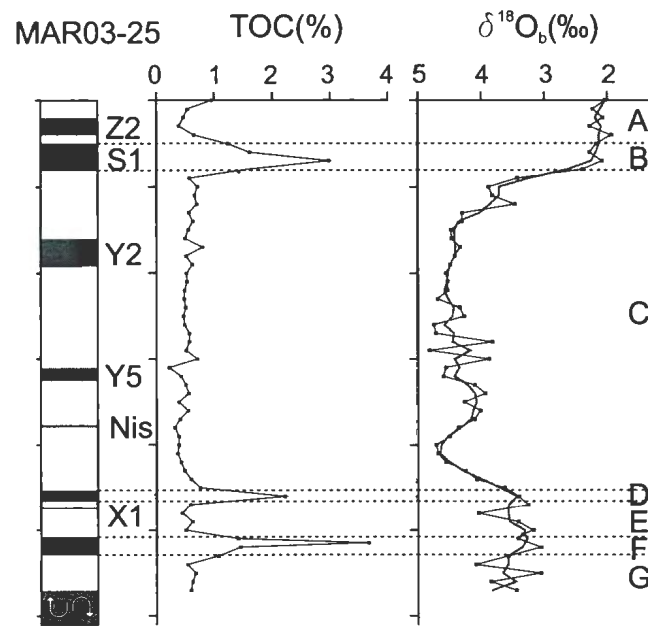


Figure 3.2c. Sapropel and non-sapropel units in the six cores and their assignment to one of nine lithologic units. Also shown are the downcore variations of TOC and oxygen isotope values. In all cores horizontal scales of TOC and $\delta^{18}O$ plots are the same. Red curves are 3-point moving averages. Grey area at the bottom of core is flow-in.

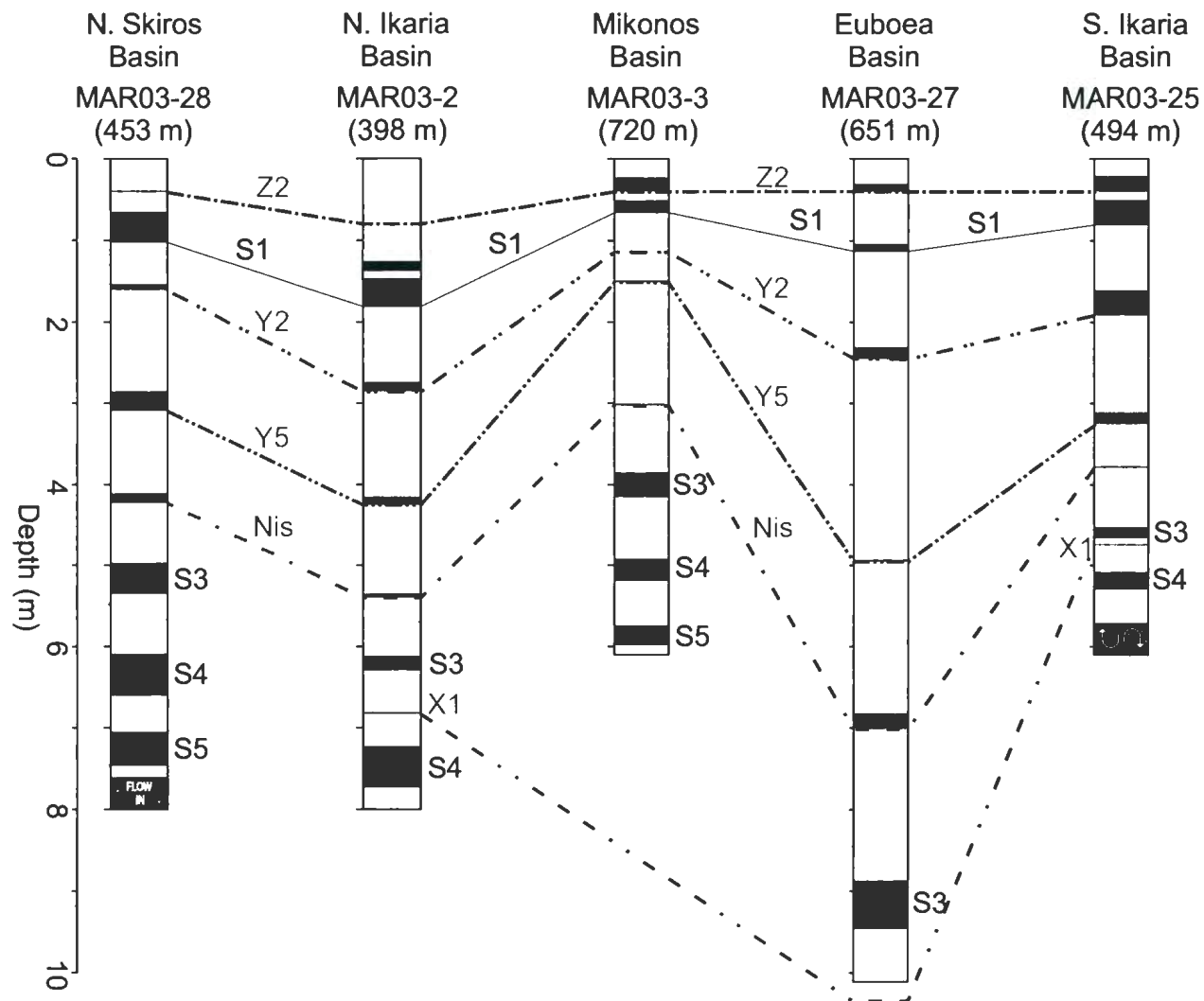


Figure 3.3. Correlation of ash layers (grey) and lithologic units among five cores. Ash correlations are from Aksu et al. (2008). Grey area at the bottom of cores MAR03-28 and MAR03-25 is flow-in.

calcareous clayey mud. The units are predominantly yellowish/dark yellowish brown (10YR5/4, 10YR4/2) and gray (i.e., yellowish, light and dark; 5Y5/2, 5Y6/1, 5GY6/1) in colour. The average TOC content is 0.5% and mainly ranges between 0.4% and 0.7% with relatively higher organic carbon contents in unit G reaching 0.9% (Fig. 3.2a, b, c). Unit A contains an ash layer which is largely disseminated in fine mud. The ash is widespread throughout the Aegean Sea and part of the eastern Mediterranean Sea and has been identified as the Z2 tephra from the Minoan eruption of Santorini Island (Aksu et al., 2008).

Unit C contains three tephra layers which are described in detail by Aksu et al. (2008), and identified by those authors using geochemical fingerprinting. Equivalent of these tephra layers are observed all around the eastern Mediterranean Sea including the Aegean, Adriatic and the Ionian seas. From top to bottom they are identified by Aksu et al. (2008) as the Y2 tephra (the Cape Riva eruption on the Island of Santorini also known as the Akrotiri eruption), the Y5 tephra (Campanian Ignimbrite eruption of the Phlegrean Fields of the Italian Volcanic Province; Narcisi and Vezzoli, 1999), and the Nisyros tephra (Nisyros eruptions on the Island of Nisyros). They are mostly disseminated in clayey background; however, high numbers of glass shards make the tephra layers discernible with sharp tops and bases in most of the cores. Unit E contains an ash layer disseminated in mud in cores MAR03-25 and MAR03-2. This tephra layer is correlated with the X1 tephra, most likely derived from the Aeolian Islands, Italy (Aksu et al., 2008).

Sapropel units B, D, F and H are distinguished from overlying/underlying units by their darker olive gray colour (5Y4/1, 5Y3/2, 5Y4/2, 5Y5/2, 5Y2/2, 5Y2/1). They are

composed of colour-banded clayey mud with a sharp base and include sharp-walled and oval-shaped burrows identified as *Chondrites*. The organic carbon contents display significant variations among sapropel units ranging between 1% and 12.65%. In unit B, the organic carbon content varies between 1.1% in core MAR03-2 and 2.98% in core MAR03-25 (Fig. 3.2a, b, c). In core MAR03-2, it changes upward from 2.3% to 1.1% to 1.8%, suggesting two peaks of organic matter accumulation in the North Ikaria Basin. The intervening decline in organic-matter accumulation is not recognized in the other cores, either because it is not present or because it was not captured by the 10 cm sample spacing (Fig. 2a,b,c). In unit D, the TOC content ranges from 1.05% to 2.97% averaging 1.74%. Due to the thinness (<10 cm) of the unit in core MAR03-25 the TOC content was determined from a single analysis (Fig. 3.2a, b, c). In unit F, maximum and minimum TOC contents of 9.41% and 0.47% are observed in cores MAR03-28 and MAR03-3. Moreover, in cores MAR03-2, MAR03-3, and MAR03-28, organic carbon percentages display fluctuations across unit F creating a double-peaked plot, with lower TOC contents within the mid portions ranging from 0.47-0.83% (Fig. 3.2a, b, c). Unit H contains the highest organic carbon content reaching 12.65% at its middle in core MAR03-28 and shows a noticeably higher average TOC content than the upper sapropels in cores MAR03-28 and MAR03-3 of 9.49% and 6.15%, respectively (Fig. 3.2a, b, c).

3.5. Age Models

The chronostratigraphy of the cores was established using a number of age control points which permit a depth-to-age conversion with the assumption that the sedimentation rate was constant between dated levels.

The age control points used in depth-to-age conversion consist of well constrained top/bottom ages of unit B (sapropel S1), tephra layers Z2, Y2 and Y5 and control points determined by curve matching of the oxygen isotope curves with the global oxygen isotope curve (see Aksu et al., 2008; Chapter 2 for details). The Nisyros ash (Fig. 3.3) was not used because the age proposed by Aksu et al. (2008) for this tephra is now in question (Margari et al., 2007; Chapter 2) and it is likely older than they reported, perhaps 54-58 ka BP rather than 42-44 ka BP (V. Margari and D. Pyle, pers. comm. 2011). Unit B is correlated with the most recent sapropel S1 due to its consistent stratigraphic position throughout the cores, situated between the ash layers Z2 and Y2, and its occurrence within MIS 1. Its top/bottom ages are well constrained by ^{14}C dates in the literature; calibrated dates based on these ^{14}C ages and a reservoir age of 557 yr (Facorellis et al., 1998) are used as age control points (see Chapter 2 for details). The ages derived from oxygen isotopic peak matching are presented as astronomically fixed dates in units of ka BP.

The depth-to-age conversion process reveals that the oldest sediment recovered in the cores (unit I) is ~130 ka BP at the transition from MIS 6 to MIS 5 (Table 3.2).

The interpolated basal ages of organic-rich Units D, F and H are 83.2-80.4 ka BP, 106.4-105.8 ka BP and 128.6-128.4 ka BP, respectively. These calculated ages coincide with the interstadials of MIS5 and are in good agreement with the previously published ages of sapropels S3, S4 and S5 developed, respectively, during marine isotopic stages 5a, 5c and 5e in the eastern Mediterranean Sea (Rossignol-Strick, 1985; Emeis et al., 2003). Consequently, Units D, F and H are identified in this paper as sapropels S3, S4 and S5, respectively (Table 3.2).

Sapropels	MAR03-28	MAR03-3	MAR03-2	MAR03-25	MAR03-27
	onset	onset	onset	onset	onset
S3	80,600	83,200	82,800	81,600	80,400
S4	105,800	105,800	106,400	105,600	
S5	128,400	128,600			
	termination	termination	termination	termination	termination
S3	70,800	72,600	76,600	76,800	74,000
S4	96,200	100,600	94,400	97,800	
S5	121,000	123,600			
Core bottoms	131,800±781	130,800±1063	110,200±526	113,800±833	87,200±434
Mean sed. rates (cm/kyr)	6.4	4.7	9.5	6.0	11.5

Table 3.2. Calculated ages of sapropels S3, S4, S5. Also shown are the average sedimentation rates.

The mean sedimentation rates calculated for cores MAR03-28, MAR03-3, MAR03-2, MAR03-25, MAR03-27 are 6.4 cm/ka, 4.7 cm/ka, 9.5 cm/ka, 6.0 cm/ka, 11.5 cm/ka, respectively (Table 3.2). Considering the sampling interval (10 cm), calculated accumulation rates reveal a temporal sample-to-sample resolution of 1562 yr, 2127 yr, 1052 yr, 1666 yr and 869 yr, respectively. Using core locations and the available temporal resolution, it is possible to perform a millennial-scale paleoceanographic reconstruction of the Aegean Sea.

3.6. Planktonic Foraminifera

3.6.1. Integrity of the faunal assemblages in the cores

Most studies assume that planktonic foraminiferal assemblages identified in sediments are accurate proxies for ancient surface water assemblages. However, this conjecture is not very straightforward. Following the death of a planktonic foraminifer, the protoplasmic envelope prevents the animal from rapid sinking through the water column. Oxidation of the protoplasm in the oxygenated surface waters may take considerable time (days to weeks), thus currents may carry the dead individuals away from their place of life. Scavenging by predators may also variably alter the surface water assemblage. Settling through the water column may expose the assemblage to dissolution. Finally, bioturbational mixing may contaminate the faunal record, smearing any shorter-term large amplitude spikes in the faunal assemblages. Except for dissolution and bioturbation, none of these factors can be readily evaluated and quantified.

An understanding of the preservation state of calcium carbonate skeletons in the Aegean Sea is critical for the use of planktonic foraminiferal assemblages as paleoproxies of water mass characteristics. The preservation state of calcium carbonate skeletons is mainly controlled by the chemistry of the water column. Dissolution of the calcium carbonate particles on the seafloor occurs due to the greater corrosiveness of sea water with increasing depth. In addition, the size, wall thickness, microstructure and porosity of calcareous foraminifera influence dissolution. For example, dissolution-susceptible species are relatively small in size, and have large pores and thinner walls, whereas the dissolution-resistant species have relatively large tests with small pores and thick walls. Similarly, spinose species are generally more susceptible to dissolution than non-spinose species. In lower latitudes, such as the Aegean Sea, most dissolution-resistant species tend to be warm-water species; thus, dissolution modifies the assemblage toward the warm end of the spectrum, and the resultant assemblage gives temperature estimates warmer than the contemporary water mass. Thus, in order to make accurate paleoecological and paleoceanographic interpretations, it is necessary to differentiate between faunal changes that resulted from environmental changes and those superimposed by dissolution. Fortunately, the samples examined in this study show little evidence of dissolution. Microscopic examination shows that all samples contain diverse assemblages which include numerous thin-shelled, fragile and near-transparent juveniles. Moreover, none of the foraminiferal tests show enlarged pores and deeply incised sutures. Crude estimates of the benthic to planktonic ratios range from 10 to 40. All these observations suggest that the samples examined in the Aegean Sea cores sustained little to no dissolution. Furthermore, all samples examined for foraminifera included

variable amounts of pteropods. The shells of pteropods are aragonitic in composition. Aragonite has higher solubility, therefore is more susceptible to dissolution in sediments than either calcite or magnesian calcite. The presence of pteropods in most, if not all of the samples, further confirms that the planktonic foraminiferal fauna in the Aegean Sea cores likely represent the surface water assemblages near each core site at the time of deposition.

3.6.2. Down-core distribution of planktonic faunal assemblages - Ecozones

Seventeen planktonic foraminiferal species were identified in the Aegean Sea cores. The dominant species that constitute >85% of the total assemblage are *Neogloboquadrina pachyderma* (dextral), *Globigerina bulloides*, *Globigerinoides ruber* (white), *Turborotalita quinqueloba*, *Globorotalia inflata*, *Globigerinita glutinata*, *Globorotalia scitula*, *Orbulina universa*, and *Neogloboquadrina dutertrei*. The remaining eight species (*Globigerinella aequilateralis*, *Globigerinoides sacculifer*, *Globigerinoides ruber* (pink), *Globigerinella calida*, *Globorotalia crassaformis*, *Globigerinoides rubescens*, *Globigerinoides tenellus* and *Neogloboquadrina pachyderma* (sinistral)) display sporadic appearances and rarely exceed abundances of 5%. Tropical taxa (i.e., *Ge. aequilateralis*, *Gs. sacculifer*, *Gs. ruber* (pink), *Ge. calida*, *Gr. crassaformis*, *Gs. rubescens*, *Gs. tenellus*) occur together and are only present in low abundances; they are plotted together as the parameter 'warm'.

Downcore assemblage distributions of the identified planktonic foraminifera show striking similarities among the studied five cores which, in turn, indicate the wide influence of large scale climatic and hydrographic changes throughout the Aegean Sea.

Moreover, correlatable abundance variations of certain planktonic foraminifera species, *N. pachyderma* (d), *Gs. ruber*, *G. bulloides*, *N. dutertrei* and *Ga. inflata* in particular, allow individual zones (a.k.a. 'ecozones') to be distinguished that characterize particular ecological water masses. Although the ecozone boundaries initially were picked by visual interpretation and qualitative trends, we applied Cluster Analysis (i.e., hierarchical cluster analysis, CONISS) to our data set in order to provide a quantitative basis for the foraminiferal zones. Among four categories in CONISS we preferred the 'Mean-within cluster sum of squares' which presents the most useful information in terms of zone definition (Grimm, 1987). Furthermore, clusters (i.e., biozones) were identified by drawing a straight line from a certain height on each dendrogram (0.40) which delineated five biozones in core MAR03-27, seven biozones in cores MAR03-2 and MAR03-25 and nine biozones in cores MAR03-28 and MAR03-3 (Fig. 3.4a, b, c).

While the percentages of taxa differ between the cores, increases, decreases and peaks predominantly occur within approximately the same time interval. The calculated ecozone boundary ages from one core to another show differences mainly ranging between 1000 yr and 1400 yr with a maximum variation of 4100 yr observed at biozone boundary BII-BIII. Besides these variations, the ages of the boundaries BIV to BIII and BIII to BII calculated for core MAR03-25, the southernmost core collected from South Ikaria Basin, differ from the same age boundaries in the other four cores by more than the uncertainty associated with those ages. In contrast, the overall age differences among the four cores MAR03-28, MAR03-2, MAR03-27 and MAR03-3 remain within the ranges of uncertainty set by sampling resolution and deduced sedimentation rates (Table 3.3). The 'outlier' (2400 yr) age for the BIVd-BIVe boundary (core MAR03-3) might be explained

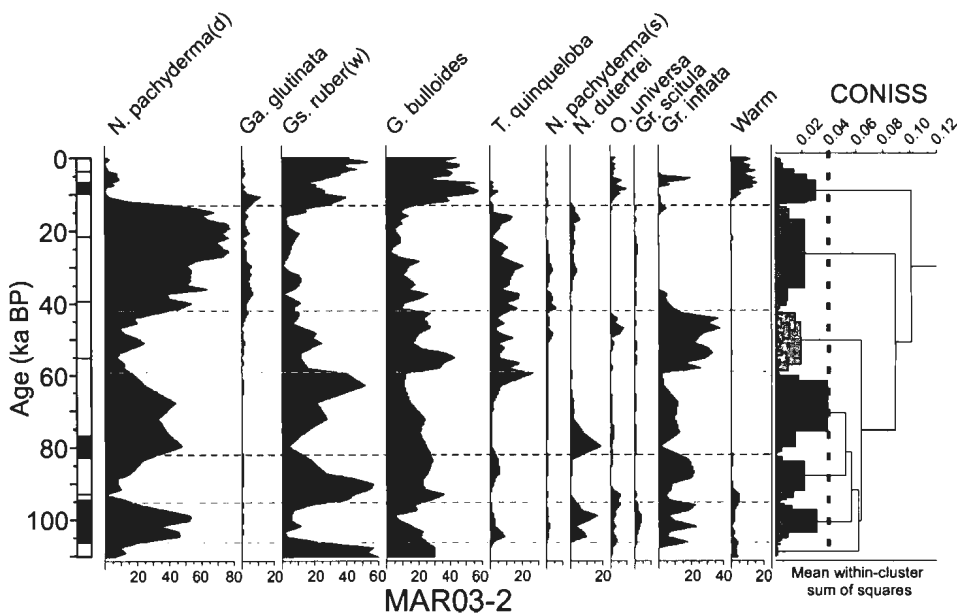
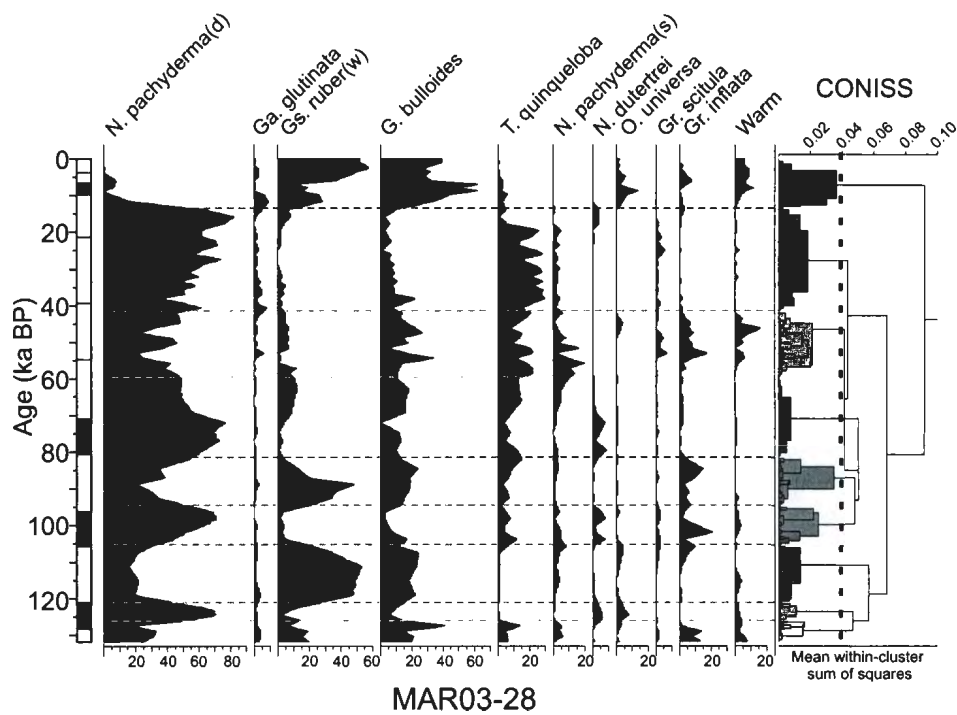


Figure 3.4a. Downcore assemblage distributions of planktonic foraminifera and identified biozones.

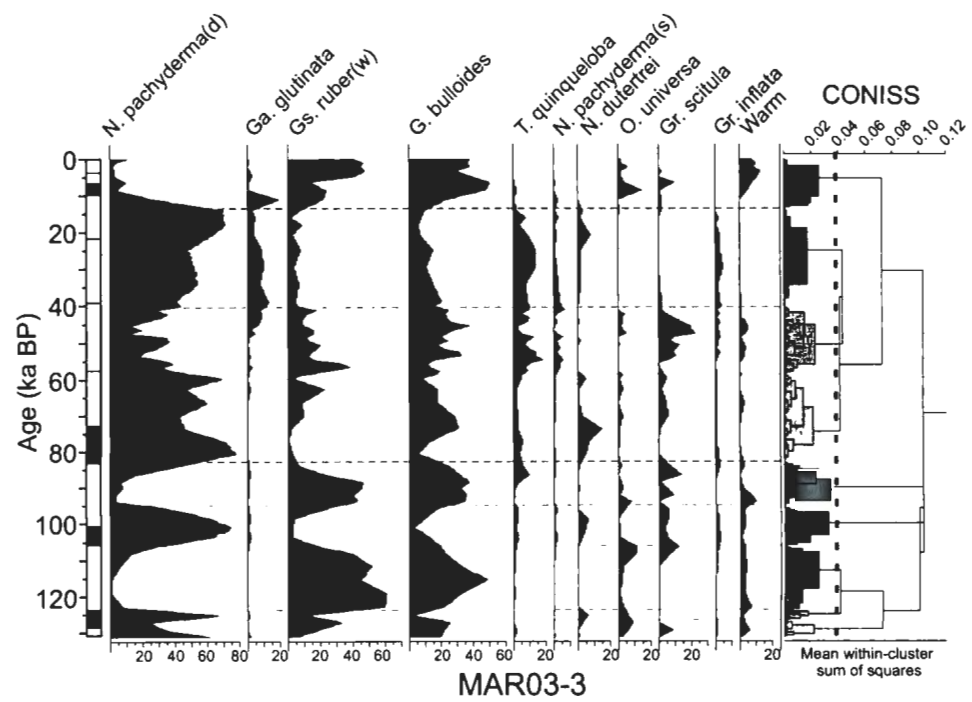
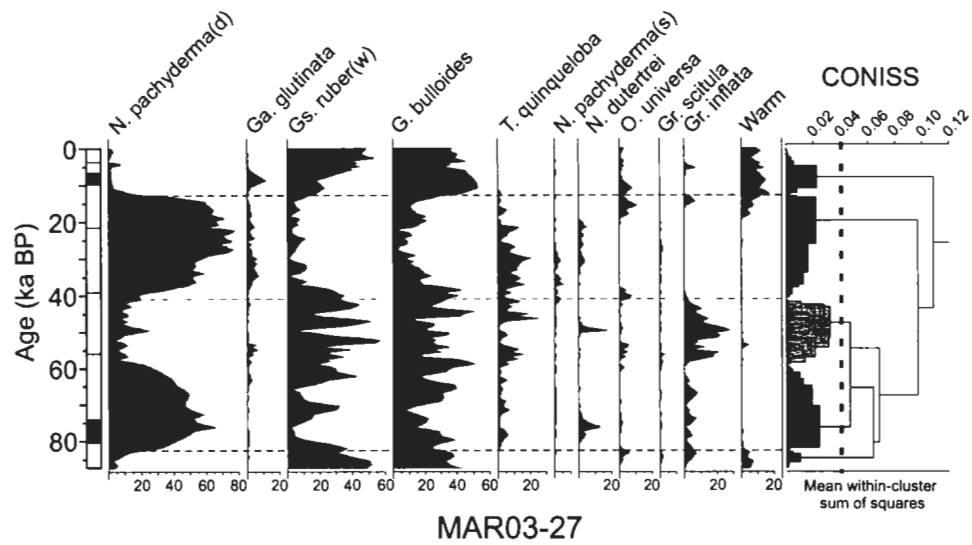


Figure 3.4b. Downcore assemblage distributions of planktonic foraminifera and identified biozones

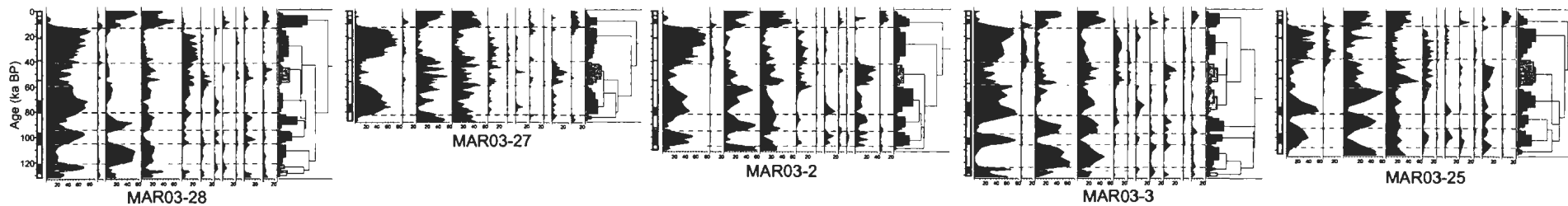
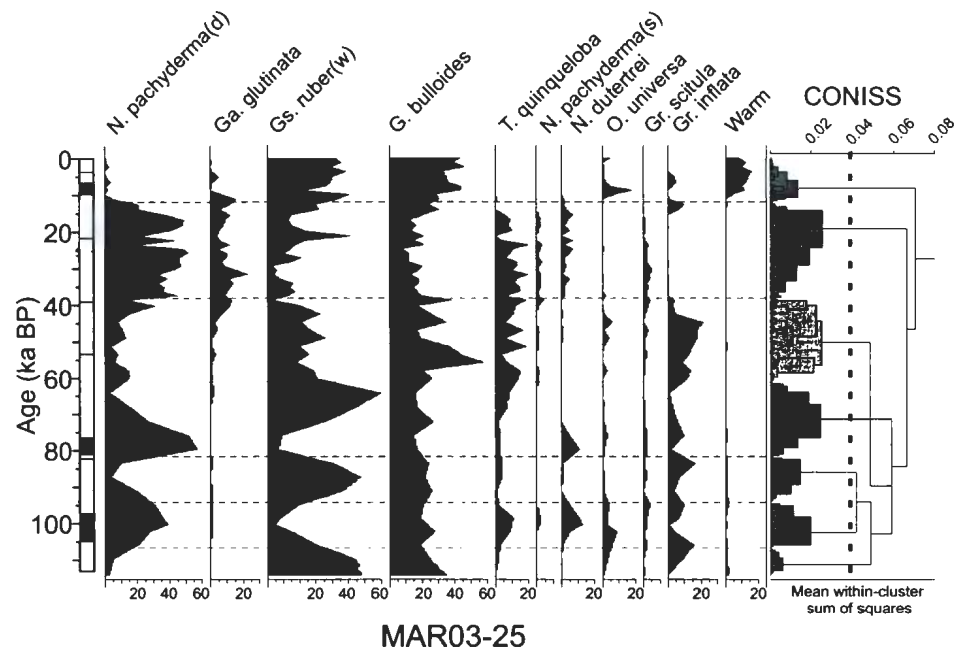


Figure 3.4c. Downcore assemblage distributions of planktonic foraminifera and identified biozones. Assemblage distribution and identified biozones from all five cores are also shown for comparison.

Biozone boundary ages (ka BP)	MAR03-2	MAR03-3	MAR03-28	MAR03-27	MAR03-25	min	max	Δ (max-min)	Δ -MAR03-25
BI-BII	13100	13400	13400	12900	12000	12000	13400	1400	500
BII-BIII	42100	40500	41300	41000	38000	38000	42100	4100	1600
BIII-BIVa	59200	58600	59600	59300	61000	58600	61000	2400	1000
BIVa-BIVb	82100	82800	81500	82700	81600	81500	82800	1300	1300
BIVb-BIVc	95200	95000	94500		94200	93000	94200	1000	700
BIVc-BIVd	106400	106000	105200		106500	105200	106500	1300	1200
BIVd-BIVe		123500	121100			121100	123500	2400	2400
BIVe-BIVf		126600	126100			126100	126600	500?	500

Biozone Durations	MAR03-2	MAR03-3	MAR03-28	MAR03-27	MAR03-25
BI	13100	13400	13400	12900	12000
BII	29000	27100	27900	28100	26000
BIII	17100	18100	18300	18300	23000
BIVa	22900	24200	21300	23400	20600
BIVb	13100	12200	13600		11400
BIVc	11200	11000	10700		14600
BIVd		17500	15900		
BIVe		3100	5000		

Table 3.3. Calculated biozone boundary ages and biozone durations.

by relatively lower sedimentation rates so that bioturbation could mix foraminifera above or below the original level. The notable age difference of biozone boundaries between MAR03-25 and the other four cores suggests temporal variation (i.e., diachroneity) in the establishment of similar ecological water masses in the northern (i.e., north of Ikaria Channel) and southern (i.e., south of Ikaria Channel) portions of the Aegean Sea. To its north, environmental modifications seem synchronous (within the limits of the available temporal resolution) across the northern part of the Aegean Sea.

Biozone I (0–13 ka BP) is characterized by high abundances of *Gs. ruber* and *G. bulloides*, consistent presence of the tropical species ('warm' parameter) and episodic appearances of *N. pachyderma*(s), *Gr. inflata* and *O. universa*. The dominant species constitute >85% of the total foram assemblage and mainly show double-peaked positive excursions (Fig. 3.4a, b, c). *Gs. ruber* exhibits a relatively higher amplitude variation particularly within the upper half of the biozone. This variation is more pronounced in cores MAR03-2, MAR03-3, MAR03-28 and MAR03-27, changing from 13% to a maximum of 57% (MAR03-28) at the core tops. *G. bulloides*, on the other hand, generally shows higher abundances within the lower half of the biozone, peaking at around 10–6 ka BP with abundances ranging between 20% and 61% (MAR03-28; Fig. 3.4a, b, c). *O. universa* is mostly present within the lower half of Biozone I and peaks (maximum 18% in core MAR03-25) at around 8 ka BP which is followed by spiky and concomitant appearances of *N. pachyderma* (d) and *Gr. inflata* with abundance variations ranging from 3% (MAR03-25) to 11% (MAR03-2) for *N. pachyderma* (d) and 18% (MAR03-2) to 5% (MAR03-25) for *Gr. inflata* (Fig. 3.4a, b, c). Tropical species display a persistent increase toward the middle portion of the biozone reaching abundances of

12–15%; they generally maintain their abundances toward core tops with small-amplitude, low-frequency variations. *Ga. glutinata* is consistently present at the bottom of Biozone I with abundances ranging between 10% and 19% before that species steeply decreases and mostly disappears below the middle of the biozone. A minor later reappearance of *Ga. glutinata* (2–5%) post-dates a peak in *Gr. inflata* seen in all cores. Biozone I is marked at its bottom by a prominent and sharp decrease of *N. pachyderma*, steep increases of *Gs. ruber* and *G. bulloides*, and the appearances of *O. universa* and tropical species (Fig. 3.4a, b, c).

Biozone II spans ~40–13 ka BP and is characterized by the dominance of *N. pachyderma* (d), low percentages of *Gs. ruber* and *G. bulloides* and the absence of *Gr. inflata*. *N. pachyderma* (d) generally demonstrates an upward increasing trend changing from 43% to a maximum of 81% in core MAR03-28, whereas in core MAR03-25 relatively smaller abundance variations are observed ranging between 27% and 51% (Fig. 3.4a, b, c). *Gs. ruber* shows low percentages (<10%) and, particularly in the most northerly core MAR03-28, abundances do not exceed 5% and even drop to 0% in the middle portion of the biozone. The percentages of *Gs. ruber* are comparatively higher in the most southerly core MAR03-25 changing from 6% to 15% and exhibit an ephemeral spike within the upper part of the biozone reaching a maximum of 40%. *G. bulloides* mainly displays an upward decreasing trend among the cores changing from 30% to 5%. In core MAR03-25, despite the sharp drop from 37% to 15% at the bottom of Biozone II, abundance variations range between 12% and 20% and do not show an upward decline. *T. quinqueloba* exhibits highest average abundances in core MAR03-28 (15–30%) and is consistently present in all cores with variations ranging from 1% to >30% (MAR03-28).

This species disappears and/or drops sharply to <2% immediately below the upper boundary of the biozone (Fig. 3.4a, b, c). Biozone II is the only interval where *Ga. glutinata* shows an uninterrupted presence ranging between 1–6% in cores MAR03-27, MAR03-2 and MAR03-28; and 6–22% in cores MAR03-3 and MAR03-25. *Gr. scitula*, *N. pachyderma* (s) and *N. dutertrei* are also present in Biozone II exhibiting percentages <10%.

Biozone III is characterized by the continuous presence of *Gr. inflata* and comparatively lower abundance variation of *N. pachyderma* (d) compared to Biozone II. *Gr. inflata* exhibits a weak upward increase attaining a maximum abundance of 37% (core MAR03-2) followed by a decline to 1–3% below the upper boundary of the biozone (Fig. 3.4a, b, c). Lowest abundances of generally <10% are observed in the most northerly core MAR03-28. Additionally, in core MAR03-27, *Gr. inflata* shows a progressive decrease toward the upper boundary of the biozone. *N. pachyderma* (d) generally displays a negative excursion reaching maximum and minimum abundances of 16–47% at the base and top of the biozone, and 5–9% in the middle of the biozone. In the most southerly core MAR03-25, comparatively low percentages are maintained throughout the biozone and mostly range between 10% and 20% (Fig. 3.4a, b, c). *Gs. ruber* and *G. bulloides* exhibit moderate frequency and high amplitude variations throughout the cores. *Gs. ruber* shows lowest abundances in the most northerly core MAR03-28 and remains predominantly below 10%. Among the remaining cores, percentages change between 10% and 37% with the highest abundances observed in the most southerly core MAR03-25 (19–37%). *G. bulloides* mainly ranges between 10% and 40% but increases to a maximum of 58% in the southernmost core MAR03-25 within the

lower half of Biozone III (Fig. 3.4a, b, c). *T. quinqueloba* exhibits a negative excursion similar to *N. pachyderma* (d) attaining high percentages of 20–25% at the base and top of the biozone and decreasing to 4–11% in the middle portions. Biozone III is marked at its base by a mostly sharp to locally gradual downward disappearance of *Gr. inflata*.

Biozone IV is characterized by large amplitude variations in the abundances of *N. pachyderma* (d), *Gs. ruber* and *G. bulloides* and episodic appearances of *N. dutertrei*. According to those downcore variations and ages of the cores, subbiozones IVa–IVf are identified (Fig. 3.4a, b, c).

Biozone IVa is characterized by the dominance of *N. pachyderma* (d), downward reappearance of *N. dutertrei* in the lower half and consistent upward increase of *Gs. ruber* (Fig. 3.4a, b, c). *Gs. ruber* reaches maximum abundances immediately below the upper boundary. In cores MAR03-3 and MAR03-28, the percentage of *Gs. ruber* is comparatively low with maximum abundances of 23% and 13%, respectively, whereas in cores MAR03-2 and MAR03-25 that species reaches noticeably higher abundances changing from 49% to as high as 70% in the latter. *N. pachyderma* (d) generally decreases toward the top of Biozone IVa except in core MAR03-3 where it drops from 76% to 42% at the base then increases toward the top reaching 67%. In cores MAR03-2 and MAR03-28 (farthest north), upward decreases in *N. pachyderma* (d) are comparatively more gradual and smaller than those in MAR03-25 (farthest south); percentages in these three cores change from 48% to 18%, from 76% to 49%, and from 57% to 4%, respectively. *N. dutertrei* exhibits a sharp upcore increase immediately above or at the lower boundary of the subbiozone and reaches maximum abundances of 7–15% in cores MAR03-25, MAR03-28 and core MAR03-3, and 20% in core MAR03-2.

G. bulloides varies from 35% to 12% and decreases toward the top of the subbiozone in cores MAR03-2 and MAR03-3. *T. quinqueloba* shows a consistent upward increase in the upper half of the sub-biozone (except in core MAR03-27) and reaches its maximum abundance at the top ranging between 14% (MAR03-28) and 24% (MAR03-2). Biozone IVa is marked by a downward reappearance (most cores) or significant increase (MAR03-3) in the abundance of *N. dutertrei* and abrupt downward disappearance of *Gr. inflata* at its bottom (Fig. 3.4a, b, c).

Biozone IVb is characterized by the dominance of *Gs. ruber* and *G. bulloides* (>80%), disappearance or near-disappearance of *N. dutertrei* and general upward increasing trend of *Gr. inflata*. *Gs. ruber* exhibits large amplitude positive excursions in all cores ranging from 38–58% with spikes mainly within the lower half of the sub-biozone (in the middle in core MAR03-25; Fig. 3.4a, b, c). *G. bulloides* shows little variation throughout the biozone changing between 13–21% (most northerly core MAR03-28), 20–28% (MAR03-2) and 20–25% (most southerly core MAR03-25) except in core MAR03-3 where it exhibits a similar positive inflection to *Gs. ruber* and changes from 37% in the lower half to 10% at the top. *N. pachyderma* (d) consistently displays large amplitude negative inflections with highest percentages at the top/bottom ranging from 33% to 65% and low percentages within the lower to middle portions generally ranging from 2–5% with the exception of 23% in the most northerly core MAR03-28. *Gr. inflata* mostly exhibits a steep upward increase within the upper half of the biozone close to the upper boundary with abundances changing from 6–10% near the bottom and middle portions of the sub-biozone to 15–21% toward its top (Fig. 3.4a, b, c).

Biozone IVc is characterized by a notable increase of *N. pachyderma* (d) relative

to overlying IVb and underlying IVd, low abundances and/or near absence of *Gs. ruber* and *G. bulloides* and reappearance of *N. dutertrei* which was largely absent in sub-biozone IVb (Fig. 3.4a, b, c). *N. pachyderma* (d) exhibits a positive excursion and peaks mainly within the middle portions at around 102 ka BP. Relatively higher abundances of *N. pachyderma* (d) are observed in cores MAR03-3 and MAR03-28 ranging from 28–75% and from 35–71%, respectively. In core MAR03-2, *N. pachyderma* (d) shows a double-crested upward increase changing from 15% to 53% (Fig. 3.4a, b, c). *Gs. ruber* mostly displays very low abundances (<6%) in cores MAR03-2, MAR03-3 and MAR03-28; however, in the most southerly core MAR03-25 it exhibits a prominent negative inflection changing between 33% and 42% at the top and bottom becoming 5% in the middle. Similar to *Gs. ruber*, *G. bulloides* shows consistently higher percentages in core MAR03-25 than in other cores ranging between 20% and 25%. In MAR03-28, MAR03-3 and MAR03-2, *G. bulloides* displays a negative excursion dropping below abundances seen at the top and bottom by 12%, 18% and 20%, respectively. Depending on which core is considered, minimum abundances are attained either in the upper part of the sub-biozone (at 3–5%) or in the middle of the sub-biozone (at ~10%) (Fig. 3.4a, b, c). *N. dutertrei* reappears in this sub-biozone and is continuously present except in core MAR03-25 where it is observed only within the upper part. The abundance variations of *N. dutertrei* show a double-crested trend in cores MAR03-2 (5–18%) and MAR03-28 (3–8%) and a positive inflection in cores MAR03-3 (to 9%) and MAR03-25 (to 14%). Maximum abundances of *N. dutertrei* coincide with the minimum abundances of *Gr. inflata* (Fig. 3.4a, b, c).

Biozone IVd is characterized by low *N. pachyderma* percentages, increased

abundances of *Gs. ruber* and *G. bulloides* relative to IVc, and disappearance of *T. quinqueloba* and *N. dutertrei*. Although the lower boundary of the sub-biozone is defined only in cores MAR03-3 and MAR03-28, similar changes in abundance variations are observed in all cores (Fig. 3.4a, b, c). *Gs. ruber* exhibits higher abundances within the lower/middle portions, ranging between 61% and 54%, and decreases upward becoming 20% at the top. *G. bulloides* shows comparatively smaller variations in core MAR03-28 than in core MAR03-3 and ranges from 15–25% whereas percentages in the latter core range between 19–21% at the top and bottom and reach a maximum of 50% immediately below the middle of the sub-biozone. Additionally, in cores MAR03-3 and MAR03-28, *Gr. inflata* reappears in the uppermost portions reaching 11% at the BIVc-BIVd boundary (Fig. 3.4a, b, c).

N. pachyderma (d) is the abundant species in Biozone IVe with abundances ranging from 65–70%. *Gs. ruber* and *G. bulloides* exhibit negative excursions in both cores with higher abundances (20–40%) at the top and bottom becoming 5–15% in the middle. *N. dutertrei* and *O. universa* are consistently present across the biozone and respectively show maximum abundances of 6% and 9% in cores MAR03-3 and MAR03-28 (Fig. 3.4a, b).

Biozone IVf encompasses the lowermost portions of cores MAR03-3 and MAR03-28 and accordingly bottom-to-top variation of the planktonic foraminifera species are not fully known. *G. bulloides* show abundances of ~20% with a sharp upward increase in core MAR03-28 becoming 40% below the top boundary. *N. pachyderma* (d) shows a notable decrease toward the top in core MAR03-3 changing from 59% to 25%.

3.7. Oxygen isotopes

Oxygen isotope curves were obtained from benthic foraminifera *U. mediterranea* in all cores except core MAR03-27; in cores MAR03-2 and MAR03-28 oxygen isotope analyses were performed on both *Gs. ruber* and *U. mediterranea*. Unless otherwise indicated the descriptions and $\delta^{18}\text{O}$ values reported in this section are 3-point moving averages.

The stacked $\delta^{18}\text{O}$ curves for planktonic and benthic foraminifera demonstrate the general variation in oxygen isotopic composition of the Aegean Sea for the last 130 ka. There are moderate to large amplitude excursions that correspond to glacial and interglacial stages (Fig. 3.5). In particular, abrupt depletions in the $\delta^{18}\text{O}$ values characterize the upper segments of all cores with changes of as much as 4‰ at the most recent termination T1 associated with the glacial-interglacial transition of marine isotopic stages (MISs) 2/1 (Fig. 3.5). A prolonged yet consistent change towards more positive values is observed within the middle portions of the cores (80–60 ka BP) reflecting the transition from MIS5 to MIS4 with a maximum shift of 3‰ ($\delta^{18}\text{O}_p$; Fig. 3.5). A more abrupt enrichment with similar amplitude is observed in MIS5 associated with the upward transition from interstadial 5e to stadial isotopic stage 5d. Moreover, interglacial MISs 1, 3 and interstadial stages 5a, 5c, 5e are manifested by moderately depleted (1.2‰; during MIS3) to highly depleted $\delta^{18}\text{O}_p$ values (-0.2‰ and -0.6‰ during MIS1 and MIS5), whereas $\delta^{18}\text{O}_p$ values are comparatively heavier during glacial times (2.8–3.2‰; MIS2 and MIS4) suggesting cooler and possibly more saline conditions (Fig. 3.5). In addition, according to the downcore variations in oxygen isotope compositions, the

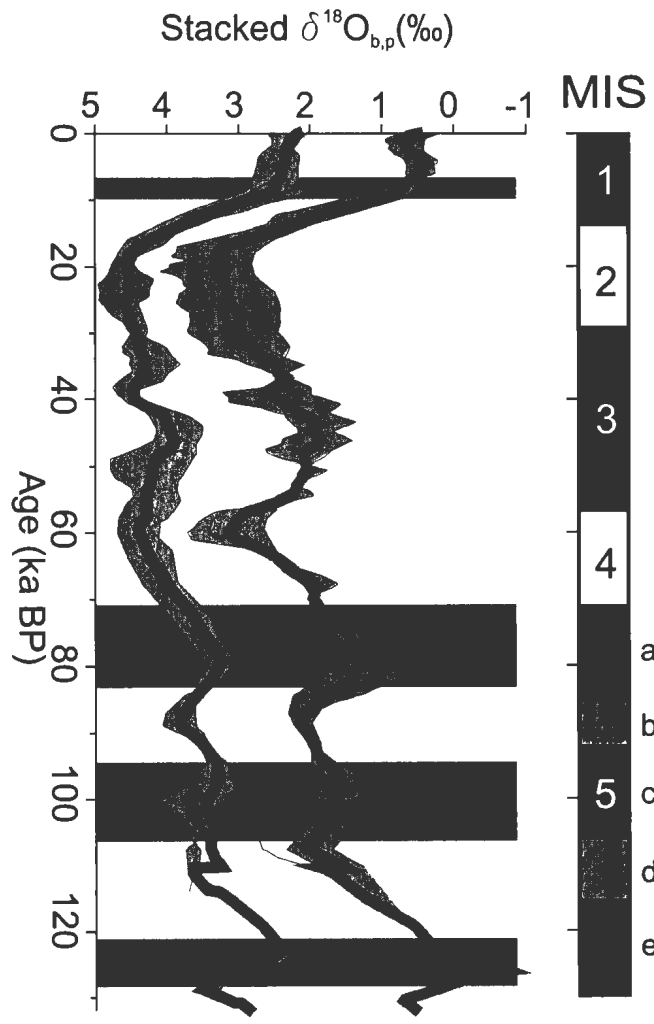


Figure 3.5. Generalized downcore variations of planktonic and benthic oxygen isotopic compositions in the Aegean Sea since MIS 5. Horizontal bars represent the maximum duration of sapropels observed in all five cores. Heavy blue (benthic) and purple (planktonic) lines are the averaged values.

transitions to glacial/stadial maxima seem to be attained more slowly than the depletions associated with retreat of ice sheets (Fig. 3.5). The depleted $\delta^{18}\text{O}$ values during MISs 1 and 5 show clear association with times of sapropel formation. Depletions are strongest after and during the accumulation of sapropels S1 and S5 ranging from 0.6–0.9‰ ($\delta^{18}\text{O}_b$) and from 0.3– -0.6‰ ($\delta^{18}\text{O}_p$), respectively (Fig. 3.5). On the other hand, in sapropels S3 and S4, oxygen isotope values show similar yet modest variations changing on average between 1.4‰ and 1.8‰ relative to adjacent units. In cores MAR03-28 and MAR03-2, the $\delta^{18}\text{O}_p$ and the $\delta^{18}\text{O}_b$ values demonstrate similar-magnitude depletions and enrichments (Fig. 3.6). Such close covariation allows credible interpretations of the surface water conditions for cores with only $\delta^{18}\text{O}_b$ data available.

During MIS5, the $\delta^{18}\text{O}$ values show moderate amplitude fluctuations (of $\sim 0.4\%$, MAR03-27) to high amplitude fluctuations (of $\sim 3.2\%$, MAR03-28). In sapropel S5, $\delta^{18}\text{O}$ values show a consistent depletion toward the top, changing from 3.2‰ to 2.3‰ ($\delta^{18}\text{O}_b$) and 0.4‰ to -0.6‰ ($\delta^{18}\text{O}_p$) in core MAR03-28, and from 3.7‰ to 2.6‰ ($\delta^{18}\text{O}_b$) in core MAR03-3. The largest depletion is observed within the uppermost portion of sapropel S5 at around 127–125 ka BP (Fig. 3.6). Subsequently, the $\delta^{18}\text{O}$ values exhibit significant enrichments across the overlying non-sapropel unit G with amounts of enrichment ranging from 1.8‰ ($\delta^{18}\text{O}_b$, cores MAR03-3, MAR03-28) to 3.2‰ ($\delta^{18}\text{O}_p$, core MAR03-28). The highest positive values of 4.1–4.0‰ ($\delta^{18}\text{O}_b$) and 2.5‰ ($\delta^{18}\text{O}_p$) are reached below sapropel S4 at 107 ka BP. In cores MAR03-3, MAR03-2, MAR03-25 and MAR03-27, depletion at 108 ka BP is recognizable (except in core MAR03-27). In sapropel S4, the $\delta^{18}\text{O}$ values generally show an upward depletion in planktonic values

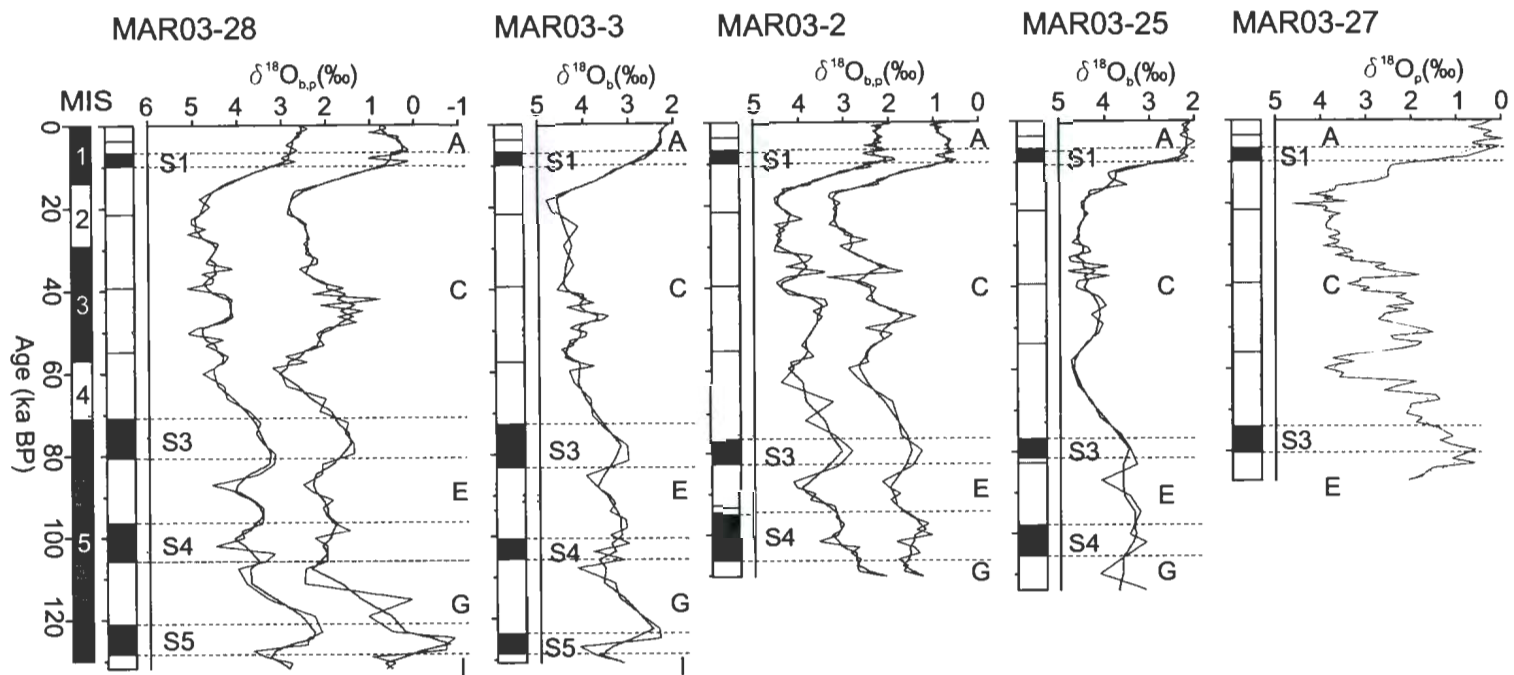


Figure 3.6. Age-converted lithostratigraphic columns and their corresponding oxygen isotope measurements for five cores. All ages derived from radiocarbon dates are calibrated to calendar years. Letters 'b' and 'p' near the curves stand for 'benthic' and 'planktonic', respectively.

except in core MAR03-2 ($\delta^{18}\text{O}_b$) where they progressively become heavier changing from 2.7‰ to 3.2‰ (Fig. 3.6). Values for $\delta^{18}\text{O}_b$ display comparatively smaller variations than those for $\delta^{18}\text{O}_p$ changing from 3.6‰ to 3.3‰ and from 2.2‰ to 1.4‰, respectively. Moreover, benthic and planktonic oxygen isotope plots for MAR03-28, MAR03-2 and MAR03-3 exhibit negative excursions (not three-point averaged data) in the middle of S4 that mirror the double-spiked TOC content of the sapropel; however, 3 point moving-average plots for $\delta^{18}\text{O}_p$ do not preserve this detail.

Within the overlying non-sapropel unit E, oxygen isotope values display a consistent enrichment changing from 3.2‰ to 4‰ (benthic) and 1.5‰ to 2.2‰ (planktonic). Maximum enrichments are attained at around 86 ka BP followed by an abrupt depletion that persists into the lower half of sapropel S3 (Figs. 3.5 and 3.6). In core MAR03-27, on the other hand, $\delta^{18}\text{O}_p$ values consistently become heavier and change from 0.8‰ to 1.7‰. Enrichments of 0.4‰ are present within the upper sections of sapropel S3 which spans the interglacial to glacial transition (MIS5/4). Throughout the overlying non-sapropel unit C, glacial MIS4, MIS2 and interstadial MIS3 can be identified in the oxygen isotope curves. During the transition from stage 5a to MIS4, the $\delta^{18}\text{O}$ values show a progressive enrichment from 80 ka BP until 60 ka BP, changing from 3.7‰ to a maximum of 4.7‰ ($\delta^{18}\text{O}_b$, MAR03-25; Fig. 3.6). The $\delta^{18}\text{O}_p$ values exhibit comparatively larger shifts of 1.4–2.7‰ (MAR03-27; Fig. 3.6).

Interstadial MIS3 is characterized by relatively depleted oxygen isotope values with variations ranging from 1–2‰ ($\delta^{18}\text{O}_p$) and from 0.6–0.8‰ ($\delta^{18}\text{O}_b$; Fig. 3.6). The transition from MIS4 to MIS3 is marked by a consistent depletion that continued until

~48 ka BP. Between 48 and 38 ka BP, oxygen isotope values remained significantly depleted with a distinct enrichment of about 0.6–1‰ at around 40 ka BP. Until 18 ka BP, oxygen isotope values subsequently display a progressive upward enrichment across the interstadial to glacial transition from MIS3 to MIS2. Maximum enrichments of 4.5–4.9‰ ($\delta^{18}\text{O}_b$) and 3.8–2.8‰ ($\delta^{18}\text{O}_p$) are followed by a conspicuous depletion until 9 ka BP that characterizes the progressive shift toward present-day climatic conditions associated with the transition from MIS2 to MIS1. In cores MAR03-25, MAR03-27 and MAR03-2, the $\delta^{18}\text{O}_p$ values show enrichments of ~0.5‰ at around 14 ka BP which may be related to the Younger Dryas event (Fig. 3.6). During the time of deposition of the most recent sapropel S1, the $\delta^{18}\text{O}$ values exhibit a consistent depletion of 0.5‰ relative to pre-sapropel values. Toward the core tops, $\delta^{18}\text{O}_b$ remains depleted reaching minimum values of 2.0‰ (2.6‰ in MAR03-28), whereas $\delta^{18}\text{O}_p$ values define a negative peak at around 5 ka BP and subsequently show upward enrichments of about 0.4‰.

3.8. Carbon isotopes

Carbon isotope values obtained from planktonic and benthic foraminifera generally range between 0.0‰ and 1.5‰ with conspicuous depletions (-0.5‰ and -1.0‰) in the uppermost part of cores MAR03-25 and MAR03-2, coinciding with sapropel S1 (Fig. 3.7). Consecutive and large amplitude excursions of as much as 1.0‰ are recognized in the lower half of the cores (encompassing MIS5), where sapropel layers S3, S4, S5 generally correlate with the $\delta^{13}\text{C}$ depletions.

Across sapropel S5, in cores MAR03-28 and MAR03-3, the $\delta^{13}\text{C}_b$ values display a

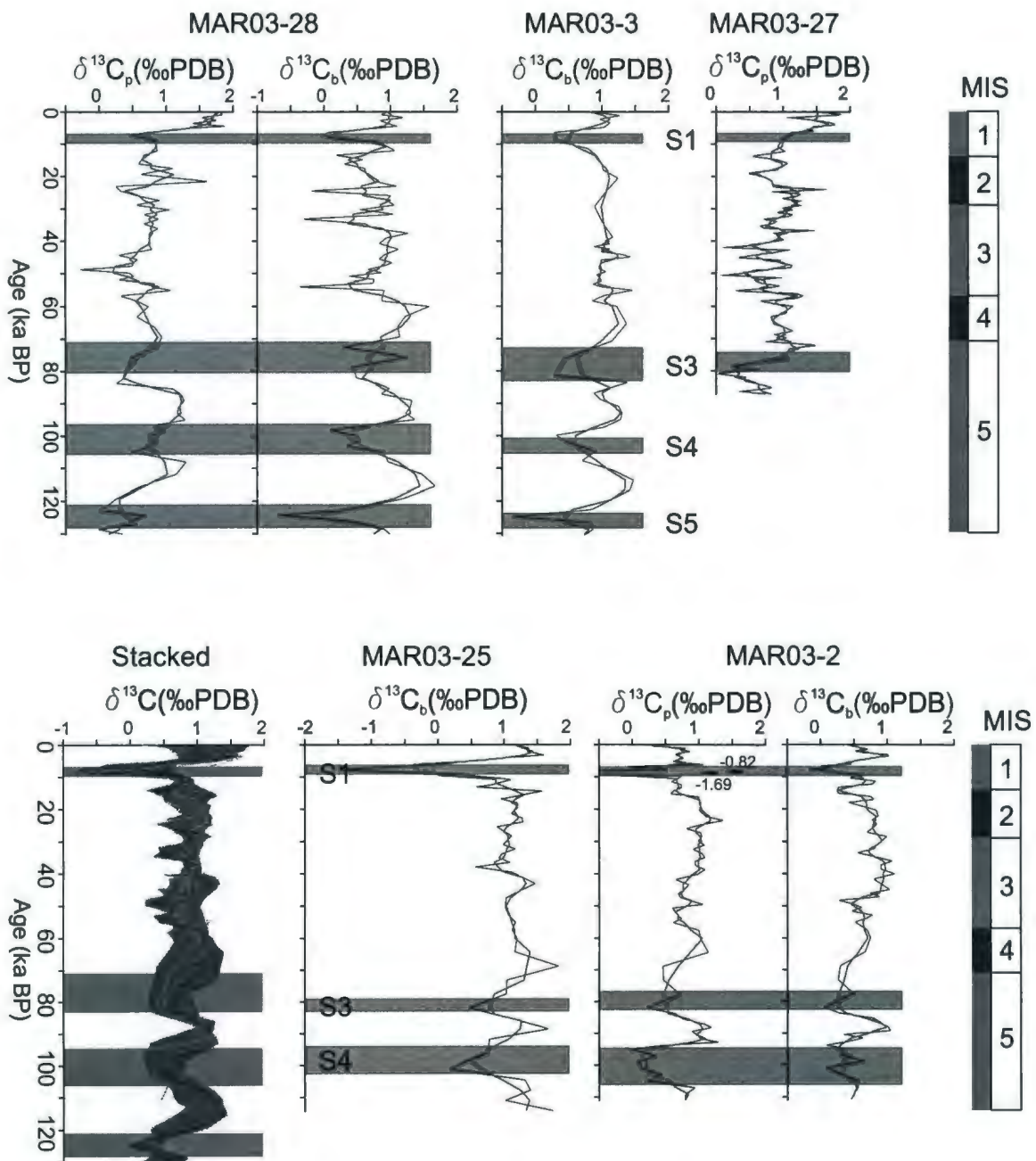


Figure 3.7. Downcore variations in carbon isotopes of five cores. Subscripts 'p' and 'b' stand for planktonic and benthic. Horizontal gray bars represent sapropels.

single negative spike whereas $\delta^{13}\text{C}_p$ values are more variable showing enrichments toward the middle of the sapropel (Fig. 3.7). The variation in the $\delta^{13}\text{C}_b$ record ranges between 0‰ and 0.4‰. The values at the top and bottom of the sapropel are rather similar at 0.55–0.6‰ in both cores whereas at around 125 ka BP in the middle of S5 there are, respectively for MAR03-28 and MAR03-3, minima of -0.6‰ and -0.7‰ (not averaged). Based only on core MAR03-28, the $\delta^{13}\text{C}_p$ values change from 0.3‰ at the top and bottom of S5, becoming 0.5‰ at around 126 ka BP (Fig. 3.7).

In cores MAR03-3 and MAR03-28, the $\delta^{13}\text{C}_b$ values exhibit variations of 0.8‰ in the overlying non-sapropel unit G, changing from 0.6‰ at the top and bottom to 1.4‰ in the middle portions at 114 ka BP. In core MAR03-28, the $\delta^{13}\text{C}_p$ values display a similar positive excursion with a progressive upward enrichment changing from values of 0.3‰ (bottom) to 0.7‰ (top) with a maximum positive value of 1.0‰ at 112 ka BP. Furthermore, the upward depletion within the upper half of the non-sapropel unit G continues into the base and middle of sapropel S4. In core MAR03-2, $\delta^{13}\text{C}$ values remain mostly depleted throughout S4 ranging between 0.3‰ and 0.5‰. Within the remaining four cores, $\delta^{13}\text{C}$ values show continuous upward enrichments across the upper part of sapropel S4 changing from 0.4–0.65‰ to 0.9–1.3‰ with highest variations (0.7‰) observed in cores MAR03-28 ($\delta^{13}\text{C}_b$) and MAR03-3 (Fig. 3.7). Following maximum enrichments at around 90 ka BP, depletions of 0.5‰ to as high as 0.8‰ (core MAR03-28; $\delta^{13}\text{C}_b$) are continued until 82 ka BP (immediately below sapropel S3) except in core MAR03-3 where depletions are observed well into the upper half of sapropel S3 until around 76 ka BP. Across sapropel S3, $\delta^{13}\text{C}$ values display persistent enrichments ranging

from mostly 0.5–1‰ until around 65 ka BP (60 ka BP in core MAR03-2; Fig. 3.7).

Throughout MIS3, the $\delta^{13}\text{C}$ values show incoherent fluctuations in all cores ranging between 0.2‰ and 1.3‰. In cores MAR03-25 and MAR03-3, the $\delta^{13}\text{C}$ values mainly range between 1‰ and 1.1‰ despite a positive excursion in the middle portions of MIS3 attaining maximum values of 1.2‰ at 43 ka BP. In cores MAR03-28 and MAR03-2, $\delta^{13}\text{C}_b$ shows deflection toward more negative values within the upper/lower portions and enrichments in the middle. Deflections in the 3-point moving average are as large as 1.0‰. $\delta^{13}\text{C}_p$ values are depleted in the lower half of MIS3 changing from 0.8‰ at the base to 0.3‰ just above the base of MIS3. Values become more positive within the upper half of MIS3 ranging between 0.8‰ and 1.0‰. In MAR03-27, similar but higher frequency upward variations are observed where $\delta^{13}\text{C}$ values change from 1.2‰ to 0.5‰ within the lower half becoming enriched toward the top attaining a maximum positive value of 1.2‰ by 25 ka BP (Fig. 3.7).

In cores MAR03-25 and MAR03-3, $\delta^{13}\text{C}$ values across MIS2 and into MIS1 show upward enrichments of 0.1–0.3‰ until 16 ka BP and 20 ka BP, followed by steep to relatively gentle depletions of as much as 1.0‰ that continue until the top and bottom of sapropel S1, respectively. In core MAR03-28, $\delta^{13}\text{C}$ values exhibit relatively high amplitude changes ranging between 0.4‰ and 1.1‰. During MIS2, in core MAR03-2, both planktonic and benthic $\delta^{13}\text{C}$ values show upward depletions changing from 0.9‰ to 0.3‰ and 1.2‰ to 0.6‰, respectively (Fig. 3.7).

In both cores MAR03-28 and MAR03-2, a positive excursion immediately below sapropel S1 culminates at around 11 ka BP reaching minimum values of 0.7–0.9‰

($\delta^{13}\text{C}_b$) and 0.6–0.8‰ ($\delta^{13}\text{C}_p$). Maximum depletions are followed by steep and mainly large enrichments ranging from 0.7‰ in $\delta^{13}\text{C}_b$ to 0.2‰ and 1.6‰ in $\delta^{13}\text{C}_p$ in cores MAR03-28 and MAR03-2, respectively. Depletions culminate mostly within the upper portions of sapropel S1 where measured values change from 0‰ to 0.1‰ ($\delta^{13}\text{C}_b$) and from -0.9‰ to 0.7‰ ($\delta^{13}\text{C}_p$). Toward the core tops, $\delta^{13}\text{C}$ become more positive reaching maximum enrichments at around 4 ka BP. Different than the other cores, $\delta^{13}\text{C}_p$ values in core MAR03-27 show a continuous increase across sapropel S1 changing from 0.9‰ to 1.6‰ and continue to rise until 4 ka BP (Fig. 3.7).

3.9. Sea surface temperature (SST) and sea surface salinity (SSS)

In this section, the parameter SST (red lines in figures) is used to indicate averaged winter (SSTw) and summer (SSTs) estimates of sea surface temperature, unless otherwise indicated. The SST and sea surface salinity (SSS) values were calculated from the transfer functions of Thunell (1979) using foraminiferal data summarized in Fig. 3.8 (see Appendix A for details).

High amplitude temperature and salinity variations of ~8–12°C and 1.5 psu are estimated to have occurred during MIS5 and during the transition from MIS2 to MIS1. Fluctuations during MIS5 are notably larger in cores MAR03-28 and MAR03-3 than those in cores MAR03-25 and MAR03-2 (Fig. 8a, b). The location of the various sites (Fig. 3.1) with MAR03-28 farthest north and MAR03-25 farthest south is a major factor controlling these variations.

During accumulation of sapropel S5 in cores MAR03-28 and MAR03-3, SST and

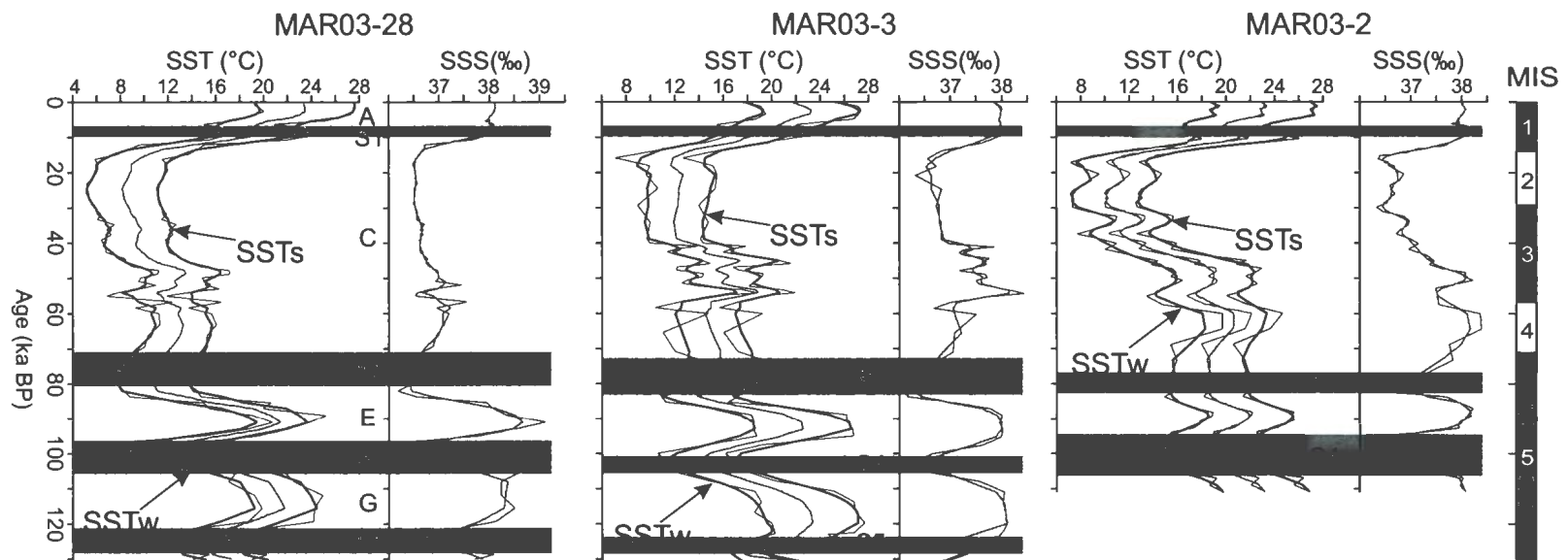


Figure 3.8a. Sea surface temperature (SST) and sea surface salinity (SSS) variations of five cores. Red SST curve is the average of SSTs and SSTw. Red SSS curve is a 3-point moving average. Horizontal grey bars highlight the sapropel intervals.

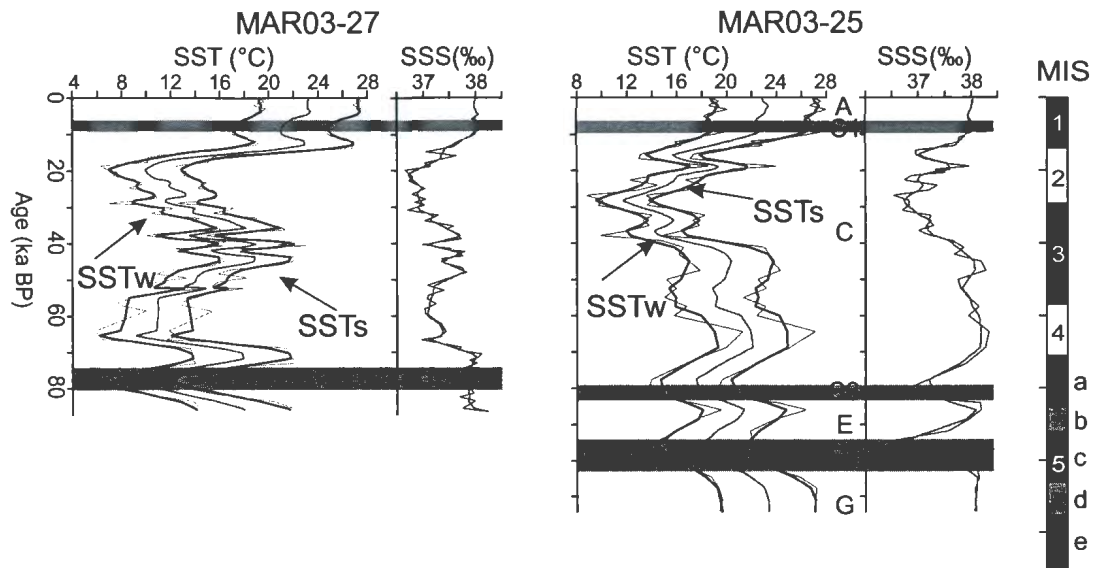


Figure 3.8b. Sea surface temperature (SST) and sea surface salinity (SSS) variations of five cores. Red SST curve is the average of SSTs and SSTw. Red SSS curve is a 3-point moving average. Horizontal grey bars highlight the sapropel intervals.

SSS values show a progressive upward increase into the overlying non-sapropel unit G changing from 14°C to 23°C and from 36.7 psu to 38.3 psu. In core MAR03-28, SST and SSS estimates are around 16°C and 37.3 psu at the top and bottom of sapropel S5 and are lower (13.6°C and 35.2 psu) immediately above the middle of the sapropel at around 125 ka BP (Fig. 3.8a, b). Toward and well into the time of accumulation of sapropel S4, temperature and salinity decreased at all core sites where minima were attained mainly close to the sapropel top (except in core MAR03-2). At core sites MAR03-28 (most northerly) and MAR03-3, the magnitude of these drops was as much as 10°C and 1.8 psu. During the deposition of sapropel S4, surface waters were comparatively warmer and more saline at southernmost core site MAR03-25 than at other sites, changing between 21°C and 37.9 psu at the base to 19°C and 36.7 psu at the top. Minimum temperature and salinity values of 11.8°C and 36.5 psu were calculated within the upper half of sapropel S4 in the most northerly core site MAR03-28, becoming 16–17°C and 37.6 psu at the bottom and top of S4 (Fig. 8a, b). In core MAR03-2, SST shows a continuous upward increase across S4 with relatively consistent surface salinity (~37 psu) and change from 17°C to 21.8°C. Successive SST and SSS increases continued above S4 until 86 ka BP at core site MAR03-25 and until around 91 ka BP at the remaining four core sites reaching temperatures and salinities ranging mainly between 21.5–22.5°C and 38–38.6 psu.

Toward the onset of sapropel S3, SST and SSS show a persistent drop until around 82 ka BP reaching minimum values of 18–18.5°C and 37.3–37.1 psu at core sites MAR03-25 and MAR03-2 and 12–14°C and 36.4–36.1 psu in cores MAR03-3 and MAR03-28. SST and SSS exhibited small variations during the deposition of sapropel

S3 and ranged from 10°C to 13°C and 36.4 psu to 37.1 psu at northerly core sites MAR03-28 and MAR03-27 and from 16°C to 18°C and 36.7 psu to 37.3 psu at core sites MAR03-25, MAR03-3 and MAR03-2. Until 46 ka BP, SST and SSS gradually increased and generally show 2–3°C and 1 psu variations ranging from 11.5–13.5°C and 36.5–37.2 psu in the most northerly core MAR03-28 and from 18–20.2°C and 37–38.1 psu and 19.2–22°C and 37.2–38.2 psu in more southerly cores MAR03-2 and MAR03-25, respectively. In core MAR03-27, on the other hand, relatively extended periods of temperature and salinity increases are observed until 36 ka BP (Fig. 3.8b). This relatively warm interval is followed by a continuous drop in surface water temperatures and salinities, indicating the gradual change from interglacial to glacial conditions associated with the transition from MIS3 to MIS2. At core sites MAR03-2, MAR03-3 and MAR03-28, glacial conditions were attained rather more rapidly (at ~39 ka BP) than at core sites MAR03-27 and MAR03-25. The former core sites showed 4–8°C and 0.4–1psu drops attaining minimum temperatures of 11–12°C at core sites MAR03-3 and MAR03-2 and 8–10°C at the most northern core site MAR03-28. These glacial temperature and salinity values were maintained until 18 ka BP. Between 18 ka BP and core tops (Recent), continuous and very high amplitude temperature and salinity increases are observed at all core sites, associated with the transition from MIS2 to MIS1. SSTs show 1–2°C temperature decreases immediately below the most recent sapropel S1 (Fig. 3.8a, b). Relatively cooler and less saline surface waters lingered during the deposition of sapropel S1 and then the sea surface warmed up to its previous state following the cessation of sapropel formation. SSTs continued to rise toward the core tops, becoming ~2–3°C warmer since 5 ka BP.

3.10. Interpretation

3.10.1. Reliability of SST derived from transfer functions

Sea surface temperature calculations from transfer functions have been extensively used since first introduced by Imbrie and Kipp (1971) (Kipp, 1976; Thunell, 1979; Pujol, 1980; Molino et al., 1982; Aksu et al., 1995). However, particularly for geographically confined seas (e.g., Aegean Sea, Adriatic Sea), it has been speculated that paleoceanographic parameters cannot be reliably estimated due to likely high amplitude temperature, salinity and productivity fluctuations (Sperling et al., 2003). In addition to several other paleotemperature methods (e.g., Modern Analogue Technique - MAT and alkenone unsaturation ratios - U37k'), Mg/Ca in foraminiferal calcite is one of the most promising techniques. The advantage of foraminiferal Mg/Ca thermometry over other marine paleotemperature proxy methods lies in its high sensitivity to temperature changes (exponential increase of Mg incorporation given by $Mg/Ca = B^{AxT}$) and the fact that it provides an independent temperature calculation for the ambient seawater during calcification of the foraminifera test (Nuernberg et al., 1996; Mashiotta et al., 1999; Lea et al., 1999; Elderfield and Ganssen, 2000; Lea et al., 2000; Dekens et al., 2002; Rosenthal and Lohmann, 2002; Anand et al., 2003).

In cores MAR03-28 and MAR03-2, Mg/Ca temperature calculations were performed using the equation ($Mg/Ca=0.34^{0.102xT}$) from Anand et al. (2003). This equation is preferred because it was constructed for *Gs. ruber* (w) (250–350 μ m) which is the same species and size range used in this study.

The SST values obtained from Mg/Ca ratios show close correlation with SST_{summer}

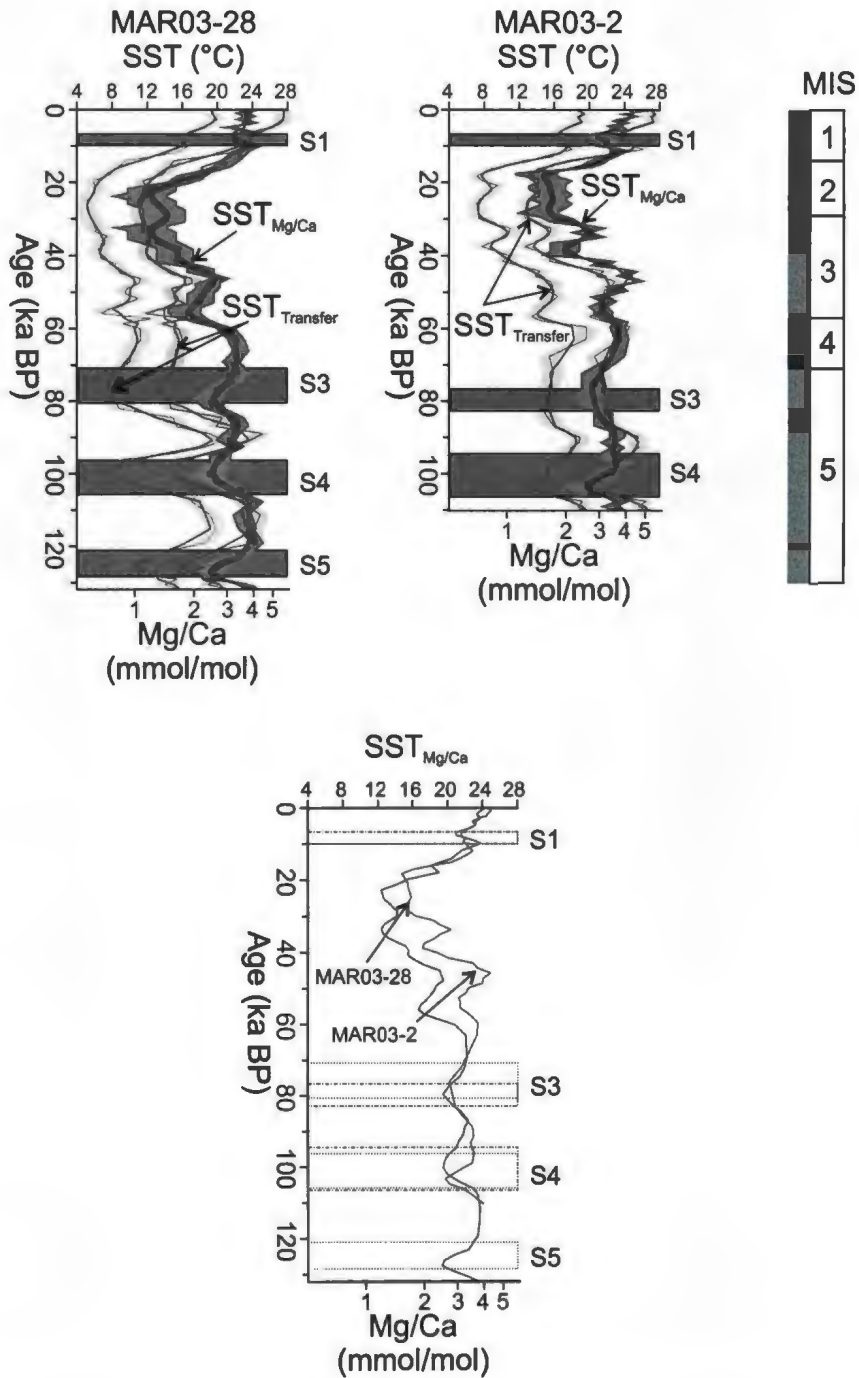


Figure 3.9. Comparison of the calculated sea surface temperatures obtained both from transfer functions and Mg/Ca in cores MAR03-28 and MAR03-2. Grey and yellow envelopes show the calculated values with error bars.

values calculated from the transfer functions rather than SST_{winter} temperatures (Fig. 3.9). This apparent similarity is not unexpected as Mg/Ca was obtained from *Gs. ruber* species which is a reliable warm-water indicator and has been used to estimate summer paleo seawater temperatures. In particular, temperature shifts estimated by these independent methods are synchronous, which confirms the timing of temperature changes. Of particular interest, such synchronicity supports the presence of cooler surface waters during times of sapropels S5, S4, S3 and S1.

In core MAR03-2 temperature estimates from transfer functions and Mg/Ca show better coherency than those in core MAR03-28 with maximum temperature differences between the two methods of 1–3°C observed particularly during MISs 3, 2 and 1. In core MAR03-28, however, higher temperature differences of as much as 6°C are observed during interstadials 5a, 5c, 5e and MISs 4 and 1. Furthermore, transfer function temperature variations during transitions from interstadials to stadials of MIS5 show large amplitude fluctuations in cores MAR03-28 and MAR03-3 ranging between 9°C and 10°C, whereas in cores MAR03-2 and MAR03-25 those variations are rather small and change between 3°C and 5°C. These variations show similarities to those reported by van der Meer et al. (2007). Taking into account the overall oxygen isotopic change of ~1.2‰ during transitions (e.g., MIS5d/5c), temperature fluctuations of 9–10°C are rather unrealistic if a change of 0.2‰/°C is assumed (Emeis et al., 2000). The percentage of tests identified as the subpolar species *N. pachyderma* (d) in cores MAR03-28 and MAR03-3 is at least 20% higher than in other cores, and it is these abundance peaks that account for the calculated much cooler temperatures and higher amplitude temperature variations (~10°C) in these cores. These large shifts are believed to be overestimates and

the smaller fluctuations based on Mg/Ca ratios (~4°C; Fig. 3.9) are considered more accurate.

In spite of abovementioned discrepancies, both transfer functions based on foraminiferal data and Mg/Ca ratios provide good evidence for trends in past sea water temperature during times of sapropel formation and glacial/interglacial transitions.

3.10.2. Significance of downcore distribution of *G. bulloides*

G. bulloides is one of the more dominant planktonic foraminifera species that inhabit the Mediterranean region including the Aegean and Adriatic seas. It has been shown to have no distinct temperature and depth preference; however, it is an indicator of eutrophic waters and upwelling (Rohling et al., 1993, 1997; Lourens et al., 1992; Zaric et al., 2005).

During sapropel S1 deposition, higher abundances of both *G. bulloides* and *Gs. ruber* (w) are observed throughout the Aegean and Adriatic seas. This has been ascribed to either elevated nutrient concentrations in surface waters due to enhanced river runoff or lower oxygen content within the photic zone as a result of phyto- and zooplankton blooms (Rohling et al., 1993; Zachariasse et al., 1997; Principato et al., 2003; Geraga et al., 2005). This covariation of *G. bulloides* and *Gs. ruber* (w) during sapropel S1 deposition has also been consistently observed in our five cores (Figs. 3.4a, b, c and 3.10). Surprisingly, however, increased abundances of both species are highly correlated with non-sapropel intervals at greater depths, particularly between sapropels S3, S4 and S5 during MIS5 (Fig. 3.4a, b, c). This quite different foraminiferal abundance pattern indicates significant differences between the most recent and the older sapropels in terms

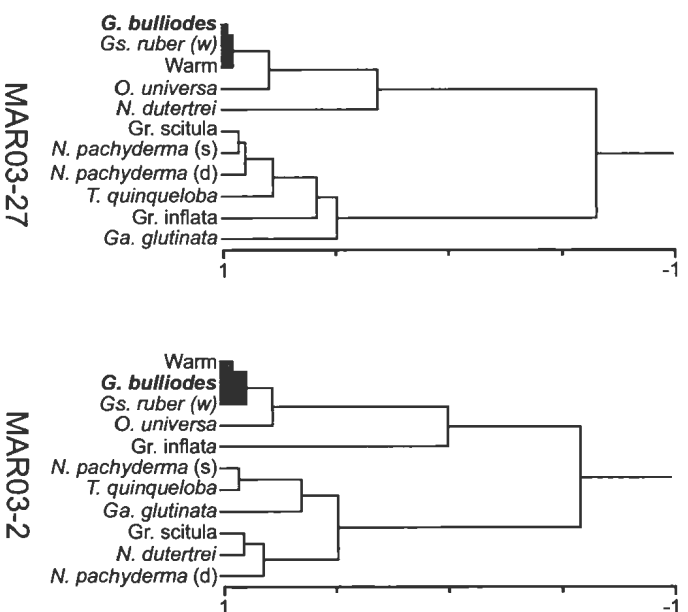
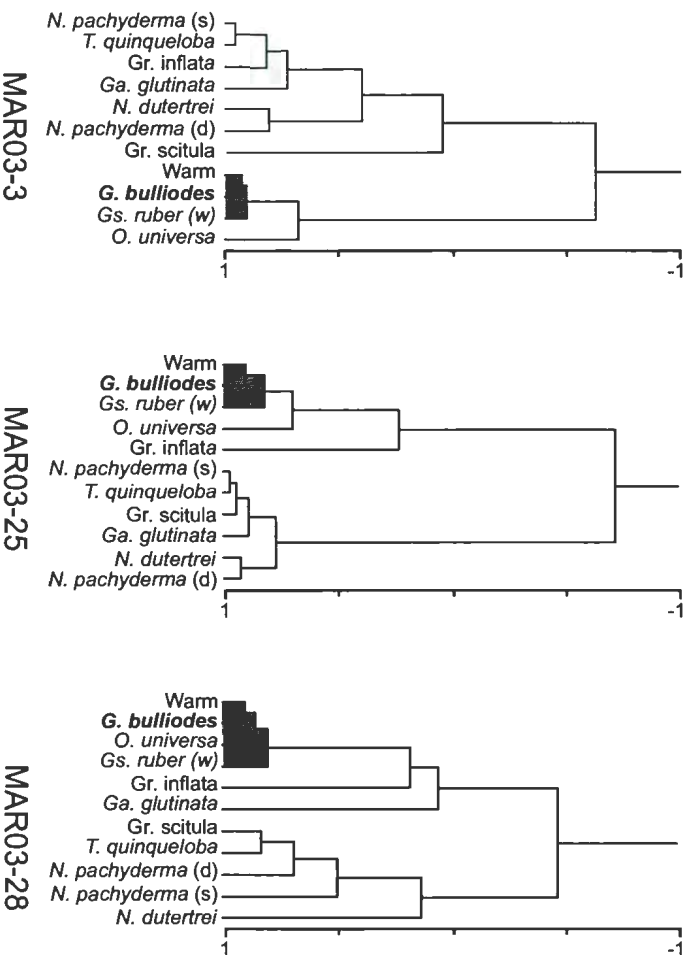


Figure 3.10. Dendrograms resulting from R-mode hierarchical cluster analysis (centroid linkage method, distance metric is 1-Pearson correlation coefficient). warm = sum of tropical species

of nutrient levels and hydrographic conditions of the water column. Also, since *G. bulloides* and *Gs. ruber* are known to inhabit eutrophic and oligotrophic waters, respectively, their co-occurrence is potentially problematic. The resolution of this issue depends on interpretations given below, so is delayed to the Discussion (under Biozone IV).

3.10.3. Significance of downcore distribution of *N. pachyderma* (d)

The stratigraphic distribution of *N. pachyderma* (d) shows notable and consistent differences between S1 and the older sapropels S3, S4 and S5 (Fig. 3.4a, b, c). *N. pachyderma* (d) exhibits very low percentages and is occasionally absent in S1, whereas the older sapropels contain peak abundances constituting 50% to >70% of the total planktonic foraminifera assemblage. Similar abundance discrepancies between the most recent and older sapropels were also observed in other eastern Mediterranean cores (Thunell et al., 1977; Rohling and Gieskes, 1989; Rohling et al., 1993). *N. pachyderma* (d) is rare to absent in oligotrophic waters (Rohling et al., 1993). On the other hand, its presence in eutrophic waters is well documented and closely associated with development of a Deep Chlorophyll Maximum (DCM; Tolderlund and Bé, 1971; Thunell, 1978; Kipp, 1976; Rohling and Gieskes, 1989; Rohling et al., 1993). A DCM layer develops when the pycnocline lies close to the base or within the euphotic zone where there is enough light for primary production (Rohling et al., 1993). Rising of the pycnocline occurs when the density contrast between the intermediate and surface water decreases. Additionally, in such conditions, the nutricline usually is found closely associated with the pycnocline.

In the modern Aegean Sea, surface waters consist mainly of brackish Black Sea waters, whereas intermediate waters are mainly more saline Mediterranean waters (i.e., Mediterranean Intermediate Water_MIW). Hence, pycnocline depth (essentially a halocline) is regulated by density contrast that depends primarily on environmental parameters such as rate of freshwater/brackish water input, evaporation, and winter cooling. It is our view that the downcore frequency distribution of *N. pachyderma* (d) can be interpreted as a record of the interactions between surface and intermediate waters of the Aegean Sea, and perhaps changes in the end-member properties of these water masses.

3.10.4. Stable carbon isotopes ($\delta^{13}\text{C}$)

Inorganic carbon isotope signals reflect changes occurred within the surface waters and, to a lesser extent, the upper portions of the intermediate waters. Those intervals are depths where planktonic foraminifera dwell during their life span. Theoretically, surface and deep waters should display heavier (most ^{13}C enriched) and relatively lighter $\delta^{13}\text{C}_{\text{DIC}}$ values in the water column, respectively, as ^{12}C is preferentially sequestered by marine algae during photosynthesis within the euphotic layer and removed from the surface layers by export production and delivered to the deep water ('biological pump'; Rohling et al., 2004). Foraminifera living in such surface waters would form calcitic tests enriched in ^{13}C . In areas where enhanced river input occurs, however, surface waters can exhibit depleted $\delta^{13}\text{C}$ values due to light carbon content of the freshwater that can range from -5‰ to -10‰ (inorganic carbon) to as light as -27‰

(suspended organic carbon; Fontugne and Calvert, 1992). The $\delta^{13}\text{C}$ composition of the surface water in Black Sea is approximately -13‰ (Abrajano et al., 2002).

In our cores, stable carbon isotopes obtained from planktonic foraminifera show maximum depletions (most ^{12}C enriched) during and/or immediately below the sapropels. Depleted $\delta^{13}\text{C}_p$ values may not necessarily indicate low primary productivity in the surface waters. In fact, because the Aegean Sea is surrounded by numerous freshwater/brackish water sources, a typical heavy $\delta^{13}\text{C}$ signal of productive surface waters could be camouflaged as a result of excess ^{12}C input that is capable of restoring the amount of light carbon (^{12}C) delivered to deep waters via export production. Moreover, $\delta^{13}\text{C}_b$ signals (from benthic foraminifera) displaying similar trends and values ($\sim 0.2\%$ difference) to those of contemporary planktonic foraminifera could be interpreted to carry an 'adjusted' deep water $\delta^{13}\text{C}_{\text{DIC}}$ signal due to persistent downward advection of surface waters. Uninterrupted presence of benthic foraminifera and burrowers during times of sapropel formation also is suggestive of bottom water replenishment to counteract any tendency to dysoxia or anoxia.

3.11. Discussion

The distributional pattern of the most common taxa (*N. pachyderma* (d), *G. bulloides*, *Gs. ruber*, *Gr. inflata*) show very similar trends among the studied cores which suggests that the major changes in planktonic foraminifera assemblages took place rather synchronously throughout the Aegean Sea since ~ 130 ka BP. Dissimilarities in the precise times of reappearance/disappearance and the percentages of other species

together with percentage variations of the common taxa from one core to another may be ascribed to local variations in hydrographic settings, such as temperature/salinity gradients, water depth, or proximity to different freshwater/brackish water sources. However, the main features of the biozones/subbiozones are the same, in spite of minor differences.

Biozone IV (>60 ka BP)

Biozone IV spans a time interval during which successive moderate amplitude fluctuations are observed in SST, SSS, $\delta^{13}\text{C}$ values, and in the frequency distributions of the most common taxa (i.e., *N. pachyderma* (d), *Gs. ruber* and *G. bulloides*) that collectively resulted in the formation of sapropels S3, S4 and S5.

The dominance of *N. pachyderma* (d) during times of sapropel formation indicates the establishment of a sustained and distinct DCM layer within the euphotic zone. Such conditions indicate stratification of the water column and result from shoaling of the pycnocline into the euphotic zone. The formation of a DCM layer is promoted by increased river runoff which is consistent with decreased sea surface temperatures and depletions in $\delta^{13}\text{C}$ values (Fig. 3.11). Another important observation is the close association of *N. dutertrei* with sapropels S3, S4 and S5 and peak abundances of *N. pachyderma* (d). The subsurface-dwelling foraminifera *N. dutertrei* is exclusively herbivorous so its population increases after phytoplankton blooms (Be and Tolderlund, 1971, Thunell and Reynolds, 1984; Hemleben et al., 1989). The appearance of *N. dutertrei* during times of maximum abundances of *N. pachyderma* (d) might coincide

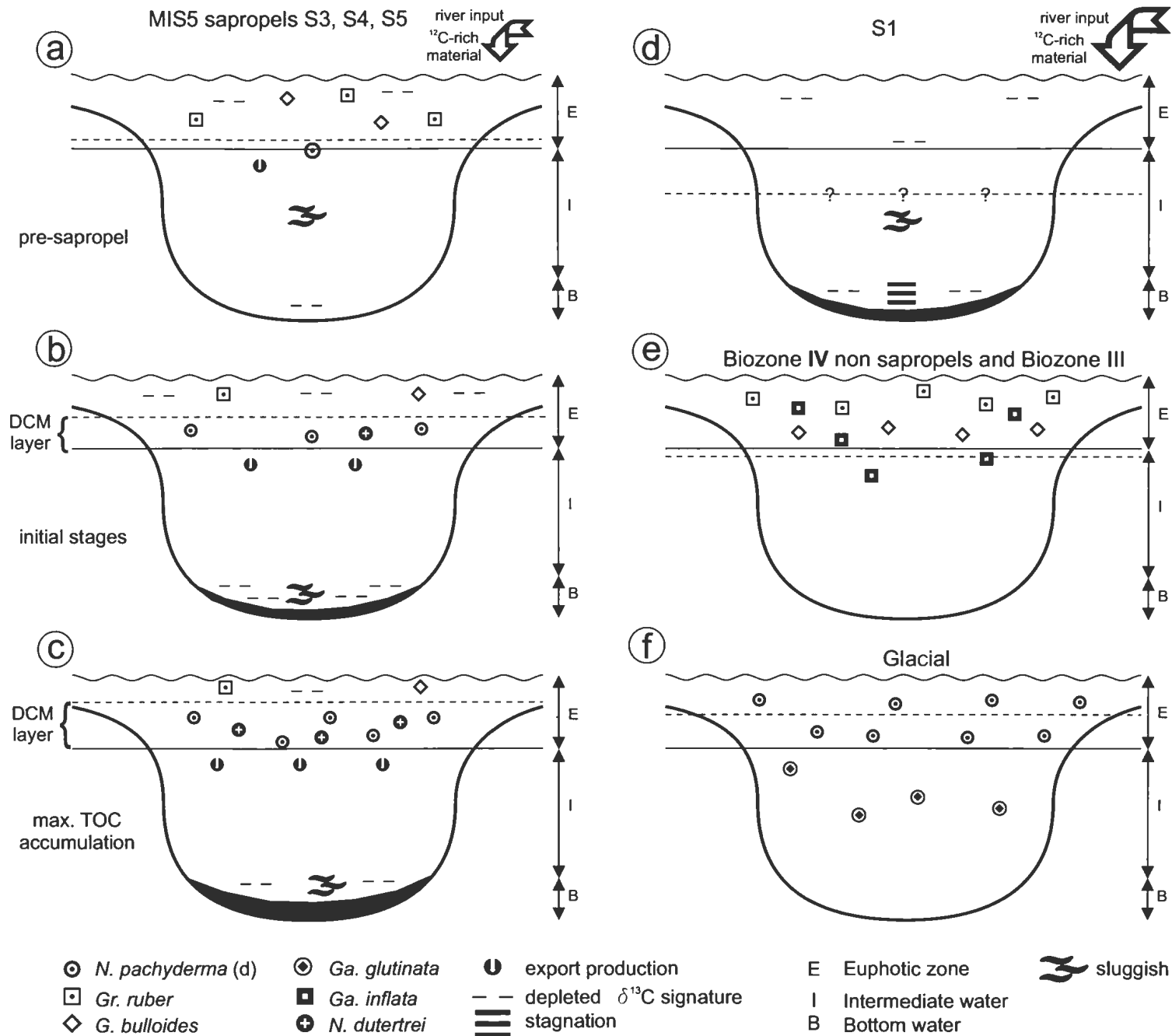


Figure 3.11. Schematic demonstration of water column hydrographic conditions during the formation of sapropels S3, S4 (and) S5 (parts a, b and c); sapropel S1 (part d), non-sapropel layers (part e) and glacial times (part f).

with the shallowest depth of the DCM layer when large phytoplankton populations would be expected (Fig. 3.11). In addition, the highest organic carbon concentrations also coincide with the appearances of *N. dutertrei*, suggesting a positive correlation between shoaling of the DCM layer and enhanced organic carbon deposition. A close covariation of *Gs. ruber* and *G. bulloides* is consistently observed during deposition of non-sapropel sediments within Biozone IV. *Gs. ruber* is a warm oligotrophic mixed-layer dweller, whereas *G. bulloides* is highly dependant on enhanced food levels with no depth preference. This relation could be explained by stratification of the euphotic zone, with a warmer and nutrient-poor upper layer and a relatively cooler lower layer with high nutrient content (Fig. 3.11). Such conditions could provide favorable habitats for both species to thrive at slightly different depths in the water column.

During the formation of MIS5 sapropels (S3, S4, S5), $\delta^{18}\text{O}$ and sea surface temperature/salinity values show contradictory relationships where depletions in oxygen isotope values coincide with decreased SST and SSS values. Although not commonly observed, drops in sea surface temperatures of 2°C (S5) and 6°C (S4) have also been observed from the eastern Mediterranean Sea in core MD84-641 collected off the Nile River where increasing surface temperatures are associated with $\delta^{18}\text{O}_{\text{ruber}}$ enrichments (Kallel et al., 2000). The association of lower SST/SSS values with more negative $\delta^{18}\text{O}$ values in our cores can be attributed to the presence of less saline (brackish?) cool waters (fluvial?) and/or increased precipitation (with a low $^{18}\text{O}/^{16}\text{O}$ ratio).

The more negative planktonic and benthic $\delta^{13}\text{C}$ values are a consequence of river runoff bringing ^{12}C -enriched nutrients, and a distinct DCM layer situated well within the

euphotic layer providing additional nutrients that resulted in augmented ^{12}C -enriched 'export' to the sea floor. Furthermore, close covariation between benthic and planktonic $\delta^{13}\text{C}$ signals suggests advected deep waters with a carbon isotope signal that has been 'set' to surface water conditions while retaining an oxygen isotope signal that reflects the deep water signature. Coincident depletions/enrichments both in carbon and oxygen isotope values support our belief that fluvial ^{12}C - and ^{16}O -enriched waters inundated the Aegean Sea resulting in depletions.

According to terrestrial (i.e., Ionnina_ western Greece, Tenaghi Philippon_ northeastern Greece; Tzedakis et al., 1997, 2006) and marine (MD84-627 and MD84-642_ northeast off the Nile River) pollen records; climatic conditions during interstadials were humid and warm, characterized by high abundances of arboreal pollen percentages up to 97% (e.g., *Quercus*, *Pinus*, *Pistacia*; Fig. 3.12), whereas stadials were relatively cooler and more arid (e.g., increase in *Artemisia*; Tzedakis et al., 1997; Cheddadi and Rossignol-Strick, 1995). Maximum depletions in $\delta^{13}\text{C}$ and $\delta^{18}\text{O}$ signals are in good agreement with increased arboreal pollen percentages (AP%) particularly during interstadial stage 5a. On the other hand, depletions during the deposition of sapropels S5 and S4 do not reflect the extended periods of high AP% encompassing the entire interstadial stages 5e and 5c and seem to be rather 'short lived'. In fact, they coincide well with times of maximum insolation (with an ~ 3 ka lag) suggesting that the intensity of the monsoon system played an important role in the climatic conditions over the Aegean Sea.

In the eastern Mediterranean, MIS5 sapropels deposited during interstadials 5a

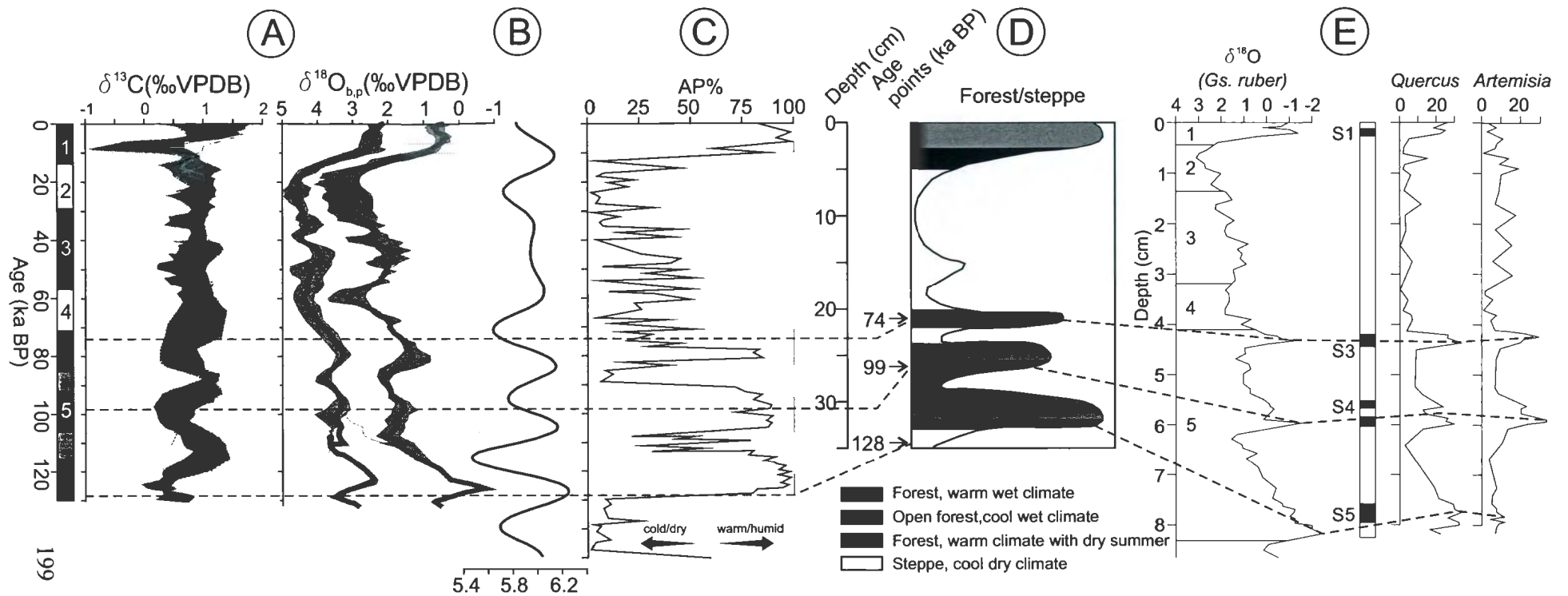


Figure 3.12. Comparison of stacked $\delta^{13}\text{C}$ and $\delta^{18}\text{O}$ curves from this study with pollen records from NE Greece and the eastern Mediterranean. A) Stacked $\delta^{13}\text{C}$ and $\delta^{18}\text{O}$ curves from the studied five cores. Dashed horizontal bars represent sapropels identified in the cores; B) Summer insolation curve (35N); C) Arboreal Pollen (AP) percentage curve from Tenaghi Philippon sequence (NE Greece; modified from Tzedakis et al., 2003); D) Changing climatic conditions since MIS5 inferred from pollen assemblages in the Tenaghi Philippon core (modified from Mommersteeg et al. (1995) and Wijmstra and Young (1992)); E) Downcore variations of *Quercus* and *Artemisia* species (wet/warm_forest and arid/cool climate indicators, respectively) in MD84-627 (off the Nile River; modified from Cheddadi and Rossignol-Strick, 1995)

(S3), 5c (S4) and 5e (S5) are associated with $\delta^{18}\text{O}$ depletions and increased surface temperatures. Depleted oxygen isotope values are also observed in MIS5 sapropels from the Aegean Sea, however the $\delta^{18}\text{O}_p$ values are mainly more enriched ($\sim 1\text{‰}$ more positive) than in counterparts from the eastern Mediterranean Sea which corresponds to about 5°C lower surface temperatures (Fig. 3.13). This enrichment is caused more likely by temperature differences than by higher salinity because of the confined geographic position and high fresh/brackish water input through surrounding rivers and the Black Sea. Hence, comparatively enriched $\delta^{18}\text{O}$ signals further support the presence of cooler surface waters during the formation of MIS5 sapropels in the Aegean Sea with respect to those in the eastern Mediterranean Sea.

Biozone III (60–40 ka BP)

The reappearance of *Gr. inflata* and decreased percentages of *N. pachyderma* (d) indicate a weaker stratification of the surface waters. Moreover, in more southern cores MAR03-25 and MAR03-2, comparatively higher abundances of *Gr. inflata* reaching 36% and low abundances of *N. pachyderma* (d) suggest a stronger vertical mixing of the surface waters than at other core localities. These hydrographic conditions show similarities to those that existed during non-sapropel times in Biozone IV; however, SST values are significantly lower by as much as 4°C , consistent with relatively enriched $\delta^{18}\text{O}$ signatures and lower *Gs. ruber* abundances.

Higher percentages of *N. pachyderma* (d) and *T. quinqueloba* at the upper and lower boundaries of the biozone suggest cooler and less saline surface waters, confirmed

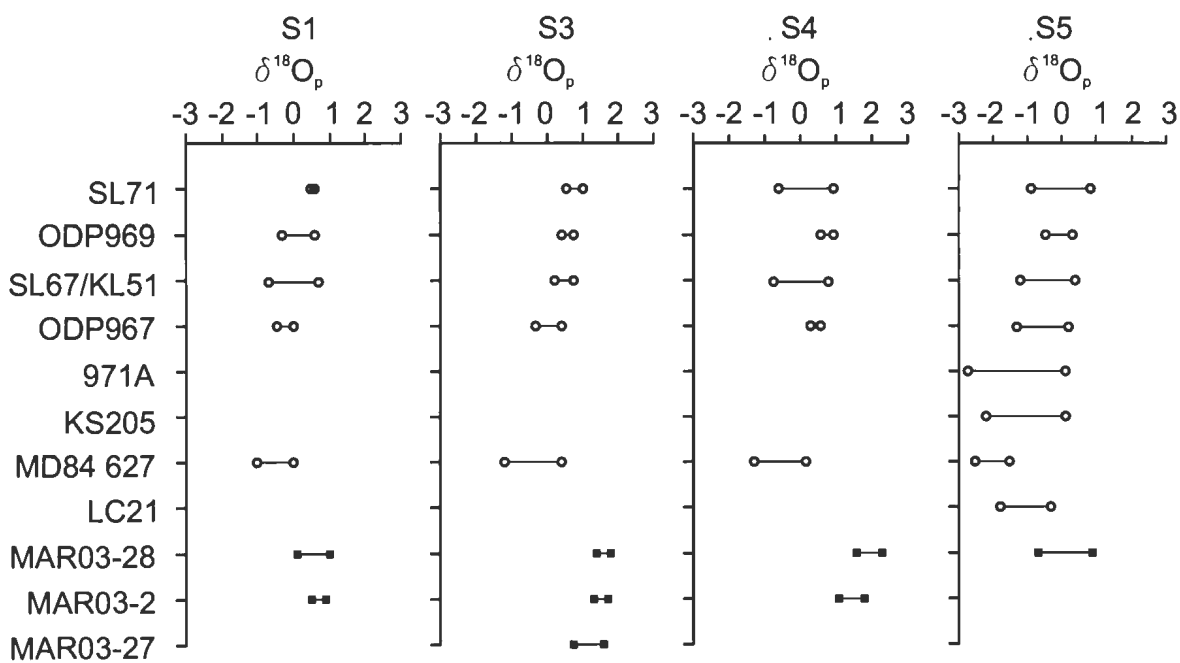


Figure 3.13. Comparison of the across-sapropel $\delta^{18}\text{O}_p$ variations from the eastern Mediterranean and the Aegean seas. Note the relatively more enriched values from the Aegean Sea particularly during sapropels S3 and S4. Open circles and filled squares are from the eastern Mediterranean and the Aegean seas, respectively.

by SST and SSS plots. *Ga. glutinata* appears for the first time within the upper portions of Biozone III, signaling the initial stages of glacial conditions associated with the transition into MIS2. Furthermore, SST plots show that the temperature drop of 2°C to 4°C toward the top of the biozone is more pronounced than the earlier drop at the lower boundary.

Biozone II (40–12.5 ka BP)

During the development of Biozone II, the upward increase in the abundance of *N. pachyderma* (d) together with the presence of *N. pachyderma* (s) and *T. quinqueloba* indicate progressive cooling into a cold interval corresponding to the glacial MIS2. This climatic change is also demonstrated by an enrichment in $\delta^{18}\text{O}$ values and decreased surface water temperatures. $\text{SST}_{\text{transfer}}$ and $\text{SST}_{\text{Mg/Ca}}$ temperature calculations show that glacial temperatures range between 11°C and 15°C, suggesting that surface waters were about 6°C cooler than today's waters. Biozone II demonstrates similar frequency distributions (e.g., dominance of *N. pachyderma* (d), decreased *Gs. ruber* and *G. bulloides* percentages) to those observed in subbiozones IV a, c and e, suggesting that similar water masses existed during glacial periods and during times of formation of sapropels S3, S4 and S5.

An important difference is that glacial-age sedimentation appears to have taken place under oxygenated bottom water conditions unfavorable for increased organic carbon accumulation. Taking into account the dominance of *N. pachyderma* (d) during MIS2, some constraints can be placed on the conditions prevailing when MIS5 sapropels

developed. It is believed that MIS2 and sapropel intervals of MIS5 coincided with a permanent pycnocline within the euphotic zone suggesting density contrast between intermediate and surface waters was of the same order of magnitude. Moreover, a shallow position of the permanent pycnocline during MIS2 can be explained by glacio-eustatic sea-level lowering (Rohling and Gieskes, 1989; Rohling, 1991). A shallow permanent pycnocline and related frequency increases in *Neogloboquadrinids* during glacial times has been observed in the eastern Mediterranean and attributed to glacio-eustatic sea-level lowering that results in reduction of inflow from the Strait of Sicily (Rohling, 1991). Similar conditions could easily be envisaged for the semi-enclosed Aegean Sea where reduced inflow of eastern Mediterranean and Black sea waters could cause comparable conditions where reduced inflow would result in less buoyancy contrast between the surface and the intermediate waters resulting in shallower pycnocline. Episodic appearances of *Gr. inflata*, an indicator of a cool and homogeneous winter mixed layer, during the formation of MIS5 sapropels and its complete absence throughout Biozone II are suggestive of a sustained/stronger stratification of the water column particularly during glacial times (e.g., MIS2). However, the fact that bottom water oxygen deficiency did not develop throughout the entire glacial time span implies that surface water temperatures were sufficiently low to hinder downwelling, causing bottom water replenishment and accordingly precluding sapropel formation.

Biozone I (12.5 ka BP – Present)

The dominance of *Gs. ruber* in Biozone I together with relatively high

abundances of warm water species indicate the establishment of fully interglacial conditions. SST calculations support the presence of warm waters that mainly ranged between 17°C and 24°C. Significant depletions in $\delta^{13}\text{C}$ values, particularly during sapropel S1 accumulation, suggest excessive amounts of freshwater and/or brackish water input to the Aegean Sea, most likely from the Black Sea and rivers draining into the Black Sea and possibly in lesser amounts from the Nile River. The noticeable drop in $\delta^{13}\text{C}$ values during S1 deposition coincides with only minor cooling of surface water temperatures (Fig. 3.10). The lack of greater cooling at this time can be ascribed to warming of the Black Sea waters as they flowed across the surface of the Marmara Sea before entering the Aegean Sea (Poulos et al., 1997; Zervakis and Georgopoulos, 2002). The abrupt disappearance of *N. pachyderma* (d) during deposition of S1 suggests unfavorable conditions for the development of a DCM layer (Fig. 3.12). This might have been caused by deepening of the pycnocline far below the euphotic zone or even by complete disruption of the pycnocline. This situation would require a (nearly) complete shutdown of intermediate water formation, causing a diminished oxygen supply at intermediate depths, thus resulting in strongly stagnant bottom water conditions. Increased abundances of *G. bulloides* during deposition of S1 have also been recognized in the Adriatic Sea (Rohling et al., 1993; Jorissen et al., 1993) and by other workers in the Aegean Sea (Zachariasse et al., 1997; Geraga et al., 2008) and have been attributed by those authors to increased river discharges creating high nutrient levels.

Stratification occurs in the water column when there is a high density contrast between the surface mixed layer and the intermediate and/or bottom waters. Stagnation

can take place locally in bottom waters where there is strong vertical stratification. Stratified water column would diminish or even halt the vertical advection of oxygen-laden surface waters resulting in sluggish/stagnant bottom waters. In shallow basins with a shallow surface layer, stratification can often be broken during intense storms, which would cause the thermocline/nutricline to rise well within the surface mixed layer. As a result, nutrient-rich waters would increase the rate of photosynthesis, accordingly, enhancing the rate of increased primary production. Stagnation can also occur in regions where there is a marked reduction in the rate of production (or cessation) of bottom water formation. These regions of quasi-permanent zones of downwelling can be situated many 100s or 1000s of km away from the basins. Please note that during the last 150 ka the Aegean Sea never developed conditions that were comparable to those observed in the present-day Black Sea, which is an anoxic and euxinic basin, where waters below ~150-200 m depth contain no dissolved oxygen and are saturated with H₂S.

3.12. Conclusions

Quantitative variations in the planktonic faunal assemblages identified in five cores collected from the northern to southern Aegean Sea demonstrate a sequence of bioevents during the last ~130,000 years. This sequence allows the definition of four major biozones. The distributional patterns of the most significant taxa exhibit the same trends at all core sites, which suggests that major oceanographic changes occurred rather synchronously across the Aegean Sea.

The sapropels S3, S4 and S5 were deposited under similar hydrographic conditions during which a distinct DCM layer was established, indicating a stratified

water column and increased primary productivity. On the other hand, the faunal contrast between sapropel S1 and older sapropels indicates that the most recent sapropel was deposited in the absence of a DCM layer, so the water column lacked a deep phytoplankton assemblage. Under such conditions, oxygen advection via intermediate water flow must have been significantly reduced which implies significant stagnation. During the deposition of sapropels S3, S4 and S5 the modifications in the hydrographic conditions leading to sapropel formation were initiated several thousand years (~5 ka to 7 ka) before sapropel onset; the onset of sapropel formation coincided with maximum depletions ($\delta^{13}\text{C}$) and lowest SST values. The dominant factor for the formation of MIS5 sapropels seems to have been increased productivity, however presence of sluggish intermediate waters and weakened bottom water replenishment cannot be disregarded. On the other hand, the formation of the most recent sapropel is attributed to intense freshwater/brackish-water input that resulted in near stagnation of the bottom water.

Cluster analysis shows consistent coupling of *G. bulloides* with *Gs. ruber* during times of non-sapropel deposition which is interpreted to suggest a stratified euphotic zone composed of a warm/nutrient-poor and a cooler/nutrient-rich upper and lower layer, respectively. This covariation further points to increased river runoff to explain the fertility and stratification of the surface waters.

In sapropel layers S3, S4 and S5, appearances of *N. dutertrei* are interpreted to represent maximum shoaling of the pycnocline and highest levels of primary productivity.

References

- Aksu, A.E., Yaşar, D., Mudie, P.J., 1995a. Paleoclimatic and paleoceanographic conditions leading to development of sapropel layer S1 in the Aegean Sea. *Palaeogeography, Palaeoclimatology, Palaeoecology* 116, 71- 101.
- Aksu, A.E., Jenner, G., Hiscott, R.N., İşler, E.B., 2008. Occurrence, stratigraphy and geochemistry of Late Quaternary tephra layers in the Aegean Sea and the Marmara Sea. *Marine Geology* 252, 174-192.
- Anand, P., H. Elderfield, and M. H. Conte, 2003. Calibration of Mg/Ca thermometry in planktonic foraminifera from a sediment trap time series, *Paleoceanography*, 18(2), 1050, doi:10.1029/2002PA000846.
- Bé, A. W. H., 1960. Ecology of Recent planktonic foraminifera; Part 2 - Bathymetric and seasonal distributions in the Sargasso Sea off Bermuda. *Micropaleontology*, vol. 6, no. 4, pp. 373–392, text-figures 1–19.
- Bé, A. and Tolderlund, D. S., 1971. Distribution and ecology of living planktonic foraminifera in surface waters of the Atlantic and Indian oceans. In: B.M. Funnel, W.R. Riedel (Eds.), *Micropaleontology of the Oceans*, Cambridge Univ. Press, London, pp. 105–149.
- Bé, A. W. H., 1977. An ecological, zoogeographic and taxonomic review of recent planktonic foraminifera, in Ramsay, A.T.S. (ed.), *Oceanic Micropaleontology*, vol. 1, 1-100. Academic Press, London.
- Cheddadi, R., Rossignol Strick, M., 1995. Improved preservation of organic matter and pollen in Eastern Mediterranean sapropels. *Paleoceanography* 10 (2), 301–309.

- Dekens, P. S., D. W. Lea, D. K. Pak, and H. J. Spero, 2002. Core top calibration of Mg/Ca in tropical foraminifera: Refining paleotemperature estimation, *Geochem. Geophys. Geosyst.*, 3(4),1022, doi:10.1029/2001GC000200.
- Deuser, W.G., Ross, E.H., Anderson, R.F., 1981. Seasonality level during the past 130,000 years. *Nature*,346, 456–458.
- Elderfield, H., and G. Ganssen. 2000. Past temperature and $\delta^{18}\text{O}$ of surface ocean waters inferred from foraminiferal Mg/Ca ratios, *Nature*, 405, 442–445.
- Emeis KC, Schulz H, Struck U, Rossignol Strick M, Erlenkeuser H, Howell MW, Kroon D, Mackensen A, Ishizuka S, Oba T, Sakamoto T, Koizumi I, 2003. Eastern Mediterranean surface water temperatures and $\delta^{18}\text{O}$ composition during deposition of sapropels in the late Quaternary. *Paleoceanography* 18(1):1005. doi:10.1029/2000PA00061
- Geraga, M., Tsaila Monopoli, St., Ioakim, Ch., Papatheodorou, G., Ferentinos, G., 2005. Short term climate changes in the southern Aegean Sea over the last 48,000 years. *Palaeogeography, Palaeoclimatology, Palaeoecology* 220, 311-332.
- Geraga, M., Mylona, G., Tsaila Monopolis, St, Papatheodorou, G., Ferentinos, G., 2008. Northeastern Ionian Sea: palaeoceanographic variability over the last 22 ka. *Journal of Marine Systems*, 74, 623–638.
- Grimm, E.C. 1987. CONISS: a FORTRAN 77 program for stratigraphically constrained cluster analysis by the method of incremental sum of squares. *Computers & Geosciences*,13, 13–35.
- Facorellis Y, Maniatis Y, Kromer B., 1998. Apparent ^{14}C ages of marine mollusk shells

- from a Greek island: calculation of the marine reservoir effect in the Aegean Sea. *Radiocarbon* 40:963–973.
- Fontugne, M.R., Calvert, S.E., 1992. Late Pleistocene variability of the carbon isotopic composition of organic matter in the eastern Mediterranean: monitor of changes in carbon sources and atmospheric CO₂ concentrations. *Paleoceanography*, 7, 1-20.
- Hemleben, C., Spindler, M., Anderson, O.R., 1989. *Modern Planktonic Foraminifera*. Springer Verlag, pp. 363.
- Imbrie, J. and Kipp, N.G., 1971. A new micropaleontological method for quantitative paleoclimatology.- application to a late Pleistocene Caribbean core. In Turekian, K.K. (ed.): *The late Cenozoic glacial ages*. Yale University Press, New Haven, 71-182.
- Jorissen, F.J., Asioli, A., Borsetti, A.M., Capotondi, L., De Visscher, J.P., Hilgen, F.J., Rohling, E.J., Van der Borg, K., Vergnaud Grazzini, C., Zachariasse, W.J., 1993. Late Quaternary central Mediterranean biochronology. *Marine Micropaleontology*, 21, 169-189.
- Kallel, N., Duplessy, J.C., Labeyrie, L., Fontugne, M., Paterne, M. and Montacer, M., 2000. Mediterranean pluvial periods and sapropel formation over the last 200 000 years. *Paleogeography, Paleoclimatology, Paleoecology*, 157, 45–58.
- Kipp, N.G., 1976. New transfer function for estimating past sea-surface conditions from sea-bed distribution of planktonic foraminiferal assemblages in the North Atlantic, in Cline, R.M. and Hays, J.D. (eds.), *Investigation of late Quaternary paleoceanography*.- Geological Society of America Memoir, 145, 3–41.

- Kidd, R.B., Cita, M.B., Ryan, W.B.F., 1978. Stratigraphy of eastern Mediterranean sapropel sequences recovered during DSDP LEG 42A and their paleoenvironmental significance. In: Hsu, K.J., Mondrader, L., et al. (Eds.), Initial Reports of the Deep Sea Drilling Project. US Government Printing Office, Washington, DC, pp. 421- 443.
- Kroon, D. and Ganssen, G., 1989. Northern Indian Ocean upwelling cells and stable isotope composition of living planktonic foraminifers. *Deep-Sea Research* 36: 1219-1236.
- Kucera, M., Weinelt, M., Kiefer, T., Pflaumann, U., Hayes, A., Weinelt, M., Chen, M., Alan C., Barrows, T., Cortijo, E., Duprat, J., Juggins, S., Waelbroeck, C.. 2005. Reconstruction of sea-surface temperatures from assemblages of planktonic Foraminifera; multi-technique approach based on geographically constrained calibration data sets and its application to glacial Atlantic and Pacific Oceans. *Quaternary Science Reviews*, May, 24, 7-9, 951–998.
- Lea, D. W., T. A. Mashiotta, and H. J. Spero, 1999. Controls on magnesium and strontium uptake in planktonic foraminifera determined by live culturing, *Geochimica et Cosmochimica Acta*, 63, 2369–2379.
- Lea, D. W., D. K. Pak, and H. J. Spero, 2000. Climate impact of Late Quaternary equatorial Pacific sea temperature variations, *Science*, 289, 1719-1724.
- Lea, D. W., Pak, D. K., Peterson, L. C. and Hughen, K. A., 2003. Synchronicity of tropical and high-latitude Atlantic temperatures over the Last Glacial Termination. *Science* v. 301, no5638, pp.1361-1364.
- Lisiecki, L. E. and Raymo, M. E., 2005. A Pliocene-Pleistocene stack of 57 globally

- distributed benthic $\delta^{18}\text{O}$ records. *Paleoceanography*, 20, 1–17.
- Lourens L. J., Hilgen F. J., Gudjonsson L. and Zachariasse W. J., 1992. Late Pliocene to Early Pleistocene astronomically forced sea surface productivity and temperature variations in the Mediterranean. *Marine Micropaleontology*, 19, 49–78.
- Lykousis, V., 2002. Circulation changes and nutrient concentrations in the late Quaternary Aegean Sea: a nonsteady state concept for sapropel formation. *Paleoceanography* 17, 1024-1034.
- Margari, V., Pyle, D., Bryant, C., Gibbard, P.L., 2007. Mediterranean tephra stratigraphy revisited: results from a long terrestrial sequence on Lesbos Island, Greece. *J. Volcanol. Geotherm. Res.* 163, 34-54.
- Mashiotta, T. A., D. W. Lea, and H. J. Spero, 1999. Glacialinterglacial changes in subantarctic sea surface temperature and $\delta^{18}\text{O}$ -water using foraminiferal Mg/Ca, *Earth Planet. Sci. Lett.*, 170, 417-432.
- Melki, T., Kallel, N., and Fontugne, M., 2010. The nature of transitions from dry to wet condition during sapropel events in the Eastern Mediterranean Sea. *Palaeogeography, Palaeoclimatology, Palaeoecology*, 291, 3-4, 267–285.
- Molfino, B., Kipp, N. G. and Morley, J., 1982. Comparison of foraminiferal, Coccolithophorid, and Radiolarial paleotemperature equations: Assemblage coherency and estimate concordancy, *Quaternary Research*, 17, 279–313.
- Mommersteeg, H.J.P.M., Loutre, M.F., Young, R., Wijmstra, T.A., Hooghiemstra, H., 1995. Orbital forced frequencies in the 975,000 year pollen record from Tenagi Philippon (Greece). *Climate Dynamics* 11, 4–24.
- Narcisi, B., Vezzoli, L., 1999. Quaternary stratigraphy of distal tephra layers in the

- Mediterranean -an overview. *Global and Planetary Change* 21, 31-50.
- Nuernberg, D., J. Bijma, and C. Hemleben, 1996. Assessing the reliability of magnesium in foraminiferal calcite as a proxy for water mass temperatures, *Geochimica Cosmochimica Acta*, 60, 803- 814.
- Poulos SE, Drakopoulos PG, Collins MB., 1997. Seasonal variability in sea surface oceanographic conditions in the Aegean Sea (Eastern Mediterranean): an overview. *Journal of Marine Systems*, 13:225-244.
- Principato, M.S., Giunta, S., Corselli, C., Negri, A., 2003. Late Pleistocene/Holocene planktic assemblages in three box cores from the Mediterranean Ridge area (W-SW of Crete): paleoecological and paleoceanographic reconstruction of sapropel S1 interval. *Palaeogeography, Palaeoclimatology, Palaeoecology*, 190, 61-77.
- Pujol, C., 1980. Les foraminifères de l' Atlantique Nord au Quaternary Ecologie -Stratigraphie-Environnement. *Memoire d' Institut Geologique Bassin Aquitaine*, 10, 25pp.
- Pujol C, Vergnaud Grazzini C., 1995. Distribution patterns of live planktic foraminifers as related to regional hydrography and productive systems of the Mediterranean Sea. *Marine Micropaleontology*, 25, 187-217.
- Reiss, Z., Halicz, E. and Luz, B., 2000. Late Holocene foraminifera from the SE Levantine Basin. *Isr J Earth Sci* 48: 1-27.
- Rohling, E.J., Gieskes, W.W.C., 1989. Late Quaternary changes in Mediterranean intermediate water density and formation. *Micropaleontology*, 3, 147-173.
- Rohling, E., 1991. A simple two layered model for shoaling of the eastern Mediterranean

- pycnocline due to glacio eustatic sea level lowering. *Paleoceanography*, 6, 537-541.
- Rohling EJ, Jorissen FJ, Vergnaud Grazzini C, Zachariasse WJ, 1993. Northern Levantine and Adriatic quaternary planktic foraminifera: reconstruction of paleoenvironmental gradients. *Marine Micropaleontology*, 21,191-218.
- Rohling, E.J., F.J. Jorissen, and H.C. De Stigter, 1997. A 200 Year interruption of Holocene sapropel formation in the Adriatic Sea, *Journal of Micropaleontology*, 16, 97-108.
- Rohling, E.J., Sprovieri, M., Cane, T., Casford, J.S.L., Cooke, S., Bouloubassi I., Emeis, K.C., Schiebel, R., Rogerson, M., Hayes, A., Jorissen, F.J. and Kroon, D., 2004. Reconstructing past planktic foraminiferal habitats using stable isotope data: a case history for Mediterranean sapropel S5. *Marine Micropaleontology*, 50, 89-123.
- Rosenthal, Y., and G. P. Lohman, 2002. Accurate estimation of sea surface temperatures using dissolution- corrected calibrations for Mg/Ca paleothermometry, *Paleoceanography*, 17(3), 1044, doi:10.1029/2001PA000749.
- Rosignol Strick, M., 1985. Mediterranean Quaternary sapropels, an immediate response of the African monsoon to variation of insolation. *Palaeogeogr. Palaeoclimatol. Palaeoecol.* 49, 237-263.
- Sautter, L.R. and Thunell, R.C., 1991. Seasonal variability in the $\delta^{18}\text{O}$ and $\delta^{13}\text{C}$ of planktonic foraminifera from an upwelling environment: Sediment trap results from the San Pedro basin, southern California big. *Paleoceanography* 6(3): doi:

10.1029/91PA00385. issn: 0883-8305.

- Sperling, M., G. Schmiedl, C. Hemleben, K. C. Emeis, H. Erlenkeuser, and P. M. Grootes, 2003. Black Sea impact on formation of eastern Mediterranean sapropel S1? Evidence from the Marmara Sea, *Palaeogeography, Palaeoclimatology, Palaeoecology*, 190, 9-21.
- Spero, H.J. and Lea, D.W., 1993. Intraspecific stable isotope variability in the planktic foraminifera *Globigerinoides sacculifer*: Results from laboratory experiments. *Marine Micropaleontology*, 19, 221-234.
- Spero, H. J. and Lea, D. W., 1996. Experimental determination of stable isotope variability in *Globigerina bulloides*: implications for paleoceanographic reconstructions. *Marine Micropaleontology*, 28, 231-246.
- Stuiver, M., Reimer, P. J., and Reimer, R. W. 2005. CALIB 5.0. [WWW program and documentation].
- Thunell, R. C., Williams, D. F., and Kennett, J. P., 1977. Late Quaternary paleoclimatology, stratigraphy, and sapropel history in eastern Mediterranean deep-sea sediments. *Marine Micropaleontology*, 2, 377-388.
- Thunell R. C., 1978. Distribution of recent of planktonic foraminifera in surface sediments of the Mediterranean Sea. *Mar Micropaleontology*, 3, 147-173.
- Thunell R. C., 1979. Eastern Mediterranean Sea during the last glacial maximum; an 18000 year BP reconstruction. *Quaternary Research*, 11, 353-372.
- Thunell, R.C. and Reynolds, L.A., 1984. Sedimentation of planktonic foraminifera: Seasonal changes in species flux in the Panama Basin. *Micropaleontology*, 30, 243-262.

- Tolderlund, D.S., and Be', A.W.H., 1971. Seasonal distribution of planktonic foraminifera in the western North Atlantic. *Marine Micropaleontology*, 8, 315-336.
- Tzedakis, P.C., Andrieu, V., de Beaulieu, J.L., Crowhurst, S., Follieri, M., Hooghiemstra, H., Magri, D., Reille, M., Sadori, L., Shackleton, N.J. and Wijmstra, T.A., 1997. Comparison of terrestrial and marine records of changing climate of the last 500,000 years. *Earth and Planetary Science Letters*, 150, 171 - 176.
- Tzedakis, P.C., Hooghiemstra, H. and Palike, H., 2006. The last 1.35 million years at Tenaghi Philippon: revised chronostratigraphy and long-term vegetation trends. *Quaternary Science Reviews*, 25, 3416–3430.
- van der Meer M. T. J., Baas M., Rijpstra W. I. C., Marino G., Rohling E. J., Damsté J. S. S., Schouten S., 2007. Hydrogen isotopic compositions of long-chain alkenones record freshwater flooding of the Eastern Mediterranean at the onset of sapropel deposition. *Earth and Planetary Science Letters*, 262, 594–600.
- Velaoras, D. and Lascaratos, A., 2005. Deep water mass characteristics and interannual variability in the North and Central Aegean Sea *Journal of Marine Systems* 53, 59–85.
- Zaric, S., Donner, B., Fischer, G., Mulitza, S., and Wefer, G., 2005. Sensitivity of planktic foraminifera to sea surface temperature and export production as derived from sediment trap data, *Marine Micropaleontology*, 55, 75-105, 2005.
- Zachariasse, W.J., Jorissen, F.J., Perissoratis, C., Rohling, E.J., Tsapralis, V., 1997. Late Quaternary foraminiferal changes and the nature of sapropel S1 in Skopelos Basin. *Proc. 5th Hellenic Symposium on Oceanography and Fisheries, Kavala*,

Greece, 1, pp. 391-394.

Zervakis, V., Georgopoulos, D., Drakopoulos, P.G., 2000. The role of the North Aegean in triggering the recent Eastern Mediterranean climatic changes. *Journal Geophysical Research* 105 (C11), 26103-26116.

Zervakis V, Georgopoulos D. 2002. Hydrology and circulation in the north Aegean (eastern Mediterranean) throughout 1997-1998. *Mediterranean Marine Sciences* 3(1): 7-21.

Zervakis, V., D. Georgopoulos, A.P. Karageorgis, and A. Theocharis, 2004. On the response of the Aegean sea to climatic variability: a review, *International Journal of Climatology*, 24, 1845-1858.

Zhang, J., 1985. Living planktonic foraminifera from the Eastern Arabian Sea.- *Deep-Sea Research*, 32, 789-798.

Chapter 4. GEOCHEMISTRY OF THE AEGEAN SEA SEDIMENTS: IMPLICATIONS FOR SURFACE/BOTTOM WATER CONDITIONS DURING TIMES OF SAPROPEL FORMATION SINCE THE MIS 5 INTERGLACIAL

Abstract

Five long piston collected throughout the Aegean Sea provide a continuous record of the sapropel sequence S1–S5 which accumulated since the beginning of the Marine Isotopic Stage 5 interglacial. These sapropels have been analysed for their elemental and isotope geochemistry in order to elucidate the surface and bottom water conditions leading to increased organic carbon accumulations.

Primary productivity (PP) calculations were performed using the equations of Muller and Suess (1979) and Howell and Thunell (1992) which suggest two different productivity settings during deposition of the sapropels. According to the equations of Muller and Suess (1979), surface productivities ranged from 120–210 g C m⁻² yr⁻¹ and from 370–800 g C m⁻² yr⁻¹ for sapropels with 1–3% and 9–12% TOC, respectively. The equations of Howell and Thunell (1992) point to increased surface productivities during the deposition of the most recent sapropel S1 (90–410 g C m⁻² yr⁻¹) and surface productivities close to today's values (~50 g C m⁻² yr⁻¹) during deposition of sapropels S3 and S4 (1–3% TOC) which implies an increased export production due to the presence of a Deep Chlorophyll Maximum (DCM) layer within the euphotic zone. This scenario is supported by the presence then upward disappearance of *N. pachyderma* (d) immediately below the most recent sapropel S1. Both sets of equations indicate the significance of

increased productivity for the deposition of sapropels containing 1–3% organic carbon. However, bottom water stagnation leading to enhanced preservation during deposition of sapropels S4 and S5 with their very high TOC contents is rather essential.

Both marine and terrestrial organic matter contributed equally to MIS5 sapropels S3, S4 and S5. An upward enrichment in $\delta^{13}\text{C}_{\text{org}}$ values across the most recent sapropel S1 is suggestive of a progressively diminishing terrigenous input toward the end of sapropel deposition. Additionally, carbon isotope values for the Aegean Sea sapropels are more depleted than their counterparts in the eastern Mediterranean Sea, denoting a stronger terrestrial contribution of organic matter, thus enhanced riverine input during the deposition of MIS5 sapropels.

In general, the sapropels seem to have been deposited under normal marine conditions with temporary establishment of semi-euxinic? bottom water conditions. Highly depleted and somewhat uniform $\delta^{34}\text{S}$ values together with the absence of fully euxinic conditions during sapropel intervals suggest that bacterially mediated sulphate reduction took place consistently below the sediment-water interface. Development of semi-euxinic bottom waters, particularly during accumulation of sapropels with particularly high TOC contents, should not be ruled out.

4.1. Introduction

The composition of the terrigenous fraction in marine sediments reflects the geology of the surrounding landmass, as well as the processes associated with the deposition of the sediments in a given oceanic setting. The terrigenous fraction in the

Aegean Sea is very much in line with the geology of the Aegean islands, as well as the drainage area of the moderate size rivers feeding sediments into the Aegean Sea. In addition, multiple layers of dark-coloured sediments rich in organic carbon (i.e., sapropels) have been recognized as common features of the sedimentary record of the Mediterranean Sea (among others: Vergnaud-Grazzini et al., 1977, 1986; Cita and Grignani, 1982; Thunell et al., 1984; Rohling, 1994; Murat and Got, 2000; van der Meer et al., 2007). These sapropel intervals are extraordinary because the expected fate of most organic matter in the oceans is destruction through oxidation and bacterial grazing rather than accumulation on the seafloor. These unusual accumulations required substantial modifications within the surface and bottom waters and are thought to have occurred as a response to distinct changes of the Mediterranean's hydrographic regime and biogeochemical cycling linked to global and regional climatic variations. Since the first discovery of Mediterranean Upper Pleistocene–Holocene sapropels (Kullenberg, 1952), several hypotheses have been postulated to explain their formation. However, the precise mechanisms leading to these unusual accumulations of organic matter are still a matter of debate. The question of organic carbon accumulation has been addressed either in terms of enhanced preservation due to favourable anoxic conditions (e.g. Olausson, 1961; Demaison and Moore, 1980) or in terms of increased productivity and associated high organic matter fluxes to the seafloor (e.g. Calvert, 1983; Pedersen and Calvert, 1990). Evidence from previous studies has indicated that sapropel formation is the result of a combination of high organic matter fluxes (ascribed to enhanced export production), intense oxygen consumption in the water column and reduced oxygen advection.

Studying the organic geochemistry (elemental and isotope data) of sapropels

provides a variety of indicators that can be used to understand the bottom and surface water conditions that led to their formation. Discernment of bottom water conditions can clarify the original environment of high organic carbon accumulation and the roles of preservation and productivity.

The aim of this study is to determine the surface and bottom water conditions during times of sapropel formation in the Aegean Sea and to elucidate the primary mechanism(s) leading to increased organic carbon accumulations.

4.1.1. Seabed morphology and hydrography of the Aegean Sea

The Aegean Sea is a shallow elongate embayment which forms the northeastern extension of the eastern Mediterranean Sea (Fig. 4.1). To the northeast, it is connected to the Black Sea through the Straits of Dardanelles and Bosphorus and the intervening small land-locked Marmara Sea. In the south, the Aegean Sea communicates with the eastern Mediterranean Sea through several broad and deep straits located between the Peloponnesus Peninsula, the Island of Crete and southwestern Turkey (Fig. 4.1). The Aegean Sea is divided into three physiographic regions: the northern Aegean Sea, including the North Aegean Trough, the central Aegean plateaux and basins, and the southern Aegean Sea including the Cretan Trough (Fig. 4.1).

The dominant bathymetric feature in the northern portion of the Aegean Sea is the 800–1200 m-deep depression referred to as the North Aegean Trough. It includes several interconnected depressions and extends from Saros Bay with a WSW–SW trend and widens toward the west (Fig. 4.1). The central Aegean Sea is characterized by a series of relatively shallower (600–1000 m), mainly NE-oriented depressions and their intervening

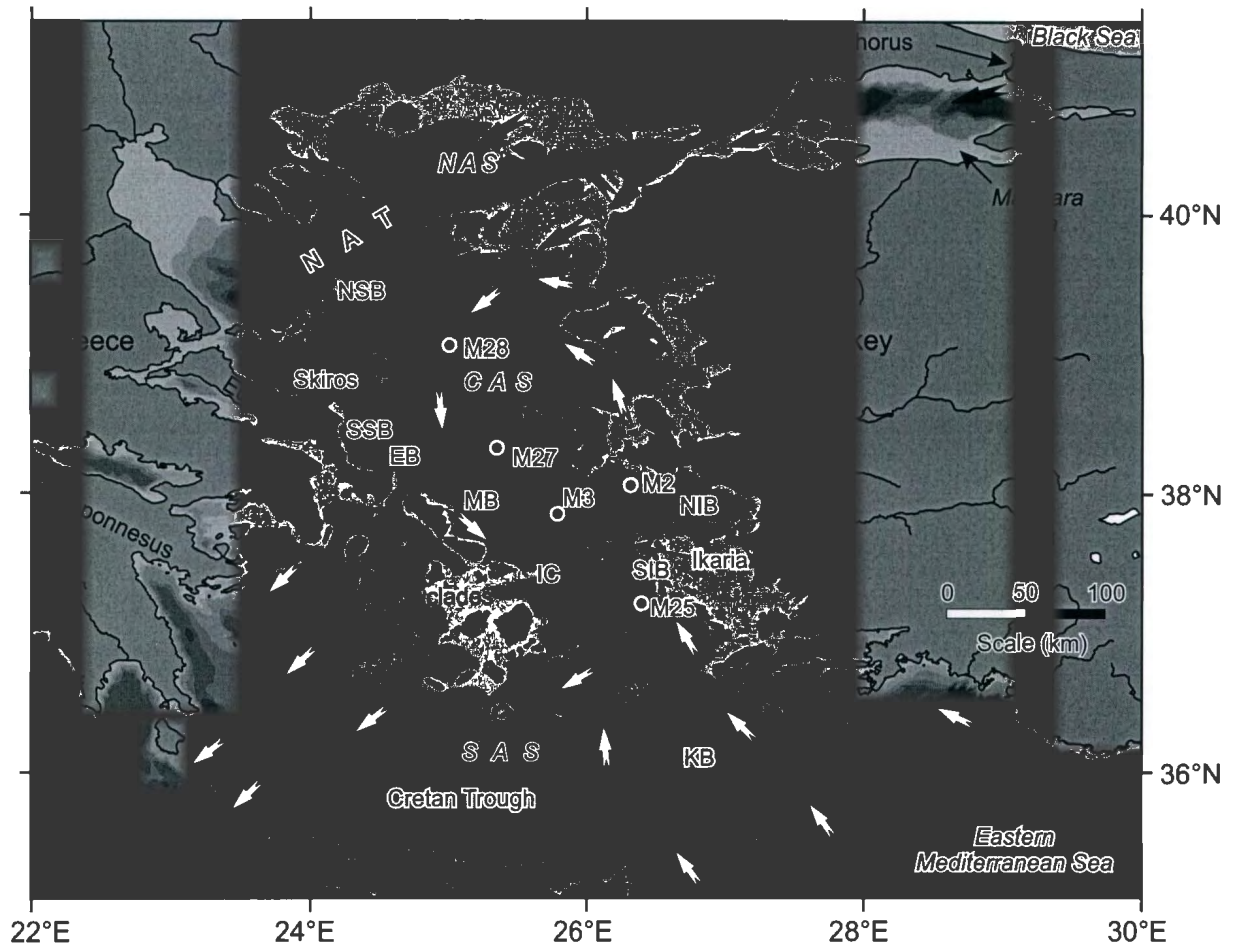


Figure 4.1. Simplified map of the Aegean Sea and surroundings showing the core locations, major rivers, subbasins and circulation pattern. Light gradually darker grey tones represent 100 m and 200-1000 m (200 m intervals) depths. Black zone, southeast of the map is >1200m. Outlined contours highlight the subbasins' limits. NAS-North Aegean Sea, NAT-North Aegean Trough, NSB-North Skiros Basin, SSB-South Skiros Basin, CAS-Central Aegean Sea, EB-Euboea Basin, MB-Mikonos Basin, PB-Psara Basin, NIB-North Ikaria Basin, IC-Ikaria Channel, SIB-South Ikaria Basin, SAS-South Aegean Sea. Black and white arrows illustrate the surface water circulation of the Black Sea and the Mediterranean Sea waters, respectively. Please note that core names are also shortened; 'M' stands for 'MAR03'.

100–300 m-deep shoals and associated islands (Fig. 4.1). The southern Aegean Sea is separated from the central Aegean Sea by the arcuate Cyclades archipelago, a convex-southward shallow volcanic arc dotted by numerous islands and shoals extending from the southern tip of Euboea Island to southwestern Turkey (Fig. 4.1). A large 1000–2000 m-deep, generally E–W-trending depression, the Cretan Trough, occupies the southernmost portion of the Aegean Sea, immediately north of Crete.

The physical oceanography of the Aegean Sea is controlled primarily by the regional climate, the freshwater discharge from major rivers draining southeastern Europe, and seasonal variations in the Black Sea surface-water outflow through the Strait of Dardanelles (Aksu et al., 1995a; Zervakis et al., 2004). Previous studies concerning the hydrographic conditions reveal that there is a general cyclonic water circulation in the Aegean Sea, although the most active dynamic features of the Aegean Sea are its mesoscale cyclonic and anticyclonic eddies (Lykousis et al., 2002). A branch of the westward flowing Asia Minor Current deviates toward the north into the Aegean Sea, carrying the warm (16–25°C) and saline (39.2–39.5 psu) Levantine Surface Water and Levantine Intermediate Water along the western coast of Turkey. It occupies the uppermost 400 m of the water column. The Asia Minor Current reaches the northern Aegean Sea where it encounters the relatively cool (9–22°C) and less saline (22–23 psu) Black Sea Water and forms a strong thermohaline front. As a result, the water column structure in the northern and central Aegean Sea is comprised of a 20–70 m-thick surface veneer consisting of modified Black Sea water overlying a higher salinity Levantine intermediate water mass which extends down to 400 m. The water column below 400 m is occupied by the locally formed North Aegean Deep Water with uniform temperature

(13–14°C) and salinity (39.1–39.2 psu; Aksu et al., 1995a; Zervakis et al., 2000; Zervakis et al., 2004; Velaoras and Lascaratos, 2005). The surface and intermediate waters follow the general counter-clockwise circulation of the Aegean Sea, and progressively mix as they flow southwards along the eastern coast of Greece.

4.2. Data and Methods

4.2.1. Core collection and sample preparation

The data set is derived from five long piston cores and five trigger-weight gravity cores collected during the 2003 cruise MAR-03 of the RV *Koca Piri Reis* of the Institute of Marine Sciences and Technology (Dokuz Eylül University, Izmir, Turkey). Piston cores were acquired with a 9–12 m-long Benthos piston corer (1000 kg head weight) along with a 2 m-long trigger-weight gravity corer (300 kg head weight) to allow quantification of the amount of missing section at the tops of the piston cores. Core locations are provided in Figure 4.1 and Table 4.1. Core locations were taken using an onboard GPS (Global Positioning System) receiver; water depths at the coring sites were calculated from 12 kHz echo-sounder data using an acoustic velocity of 1480 ms⁻¹.

Cores were recovered from different subbasins of the Aegean Sea to establish a comprehensive understanding of the past oceanographic and climatic changes that occurred during the late Pleistocene to Holocene. Three cores (MAR03-28, MAR03-25, MAR03-2) were collected from the slopes of the basins at a depth range of 400–500 metres. Cores MAR03-27 and MAR03-3 were collected from deeper basin centres at depths of 651 m and 720 m, respectively (Table 4.1).

Cores	Latitude	Longitude	PC length (cm)	TWC length (cm)	PC missing top (cm)	CompC length (cm)	Water depth (m)
MAR03-2	38°03.97'N	26°22.30'E	776	86	37	813	398
MAR03-3	37°51.72'N	25°49.17'E	580	50	24	604	720
MAR03-25	37°10.36'N	26°26.55'E	604	25	25	629	494
MAR03-27	38°18.68'N	25°18.97'E	952	106	80	1032	651
MAR03-28	39°01.02'N	25°01.48'E	726	165	100	826	453

Table 4.1. Core locations; piston (PC), gravity (TWC), composite (CompC) core lengths, and water depths.

Cores were shipped to Memorial University of Newfoundland, where they were split and described by R.N. Hiscott. Sediment colour was determined using the 'Rock-Color Chart' published by the Geological Society of America in 1984. Sample preparation involved collection of 2 cm-wide "half-round" samples (~20 cm³) at 10 cm intervals from each core, then subsampling of approximately 7 cm³ of sediment for organic geochemical/stable isotopic analyses, and 13 cm³ of sediment for inorganic stable isotope analyses and faunal studies.

4.2.2. Laboratory Methods

For oxygen isotopic analyses, only clean and intact planktonic and benthic specimens of >150 µm *Globigerinoides ruber* and *Uvigerina mediterranea* were used. At a few intervals, where *Gs. ruber* was absent, *Globigerina bulloides* and *Neogloboquadrina pachyderma* (d) were used instead. Calibration of the oxygen isotope values between these three species was determined in 30 samples containing both *Gs. ruber* (w) and *G. bulloides* and 15 samples containing both *G. bulloides* and *N.pachyderma* (d). The downcore oxygen isotope variations of the five cores were obtained predominantly from carbonate tests of benthic foraminifera (except core MAR03-27) for a better correlation with the global oxygen isotope curve. Cores MAR03-27 and MAR03-28 were sampled in 2004 and oxygen isotope analyses were conducted on planktonic foraminifera. In cores MAR03-28 and MAR03-2, both benthic and planktonic oxygen isotope curves were obtained.

For each sampling interval, 16–20 (average 18) planktonic and 4–6 (average 5) benthic foraminifera specimens were hand-picked (~0.25 mg of CaCO₃), cleaned in

distilled water, dried in an oven at 50°C and placed in 12 ml autoinjector reaction vessels. The vials were covered with Exetainer screw caps with pierceable septa, and were placed in a heated sample holder held at 70°C. Using a GC Pal™ autoinjector, the vials were flushed with He (Ultra High Purity grade) for 5 min using a double-holed needle connected by tubing to the He gas source. Sample vials were then manually injected with 0.1 ml of 100% H₃PO₄ using a syringe and needle. A minimum of 1 hour was allowed for carbonate samples to dissolve in the phosphoric acid. The samples were analysed using a triple-collector Thermo Electron Delta V Plus™ isotope ratio mass spectrometer. The GC Pal™ autoinjector collects the headspace in each vial using a double-holed needle. The needle is flushed with a He carrier gas. The sample gas from the vial and the He are carried through the tubing and into a Thermo Electron Gas Bench II™. The Gas Bench II™ acts as an interface between the samples in the vials and the mass spectrometer. Using a sampling loop, portions of the sample gas are injected onto a 25 m x 0.32 mm Poraplot Q™ fused silica capillary gas chromatograph (GC) column in the Gas Bench II™ to isolate the CO₂ fraction. Nafion™ water traps remove water vapour from the gas stream. The CO₂ sample gas is then carried by the He carrier gas via an open split tube into the source of the mass spectrometer. Eight injections of sample gas were taken for each sample analysis. Another open split tube allows the injection of a reference gas (CO₂) into the source. Reference gases were prepared from three different standards of known isotopic composition using the same methods employed for the unknown samples, and were used to calibrate each run. The δ¹⁸O values are reported with respect to the Pee Dee Belemnite standard.

The amount of total carbon (TC), sulfur (TS), carbon and sulfur isotopic compositions were determined using a Carlo-Erba NA 1500 Elemental Analyzer coupled to a Finnegan MAT 252 isotope-ratio mass spectrometer (IRMS). Samples were acidified using 30% HCl, and carbonate-free residues were dried overnight in an oven at 40°C. 15 mg of sample was transferred into 4x6mm tin capsules which were then sealed for analysis. Total organic carbon and sulfur in the samples was converted to CO₂, SO₂, H₂O and other oxidized gases in the oxidation chamber and then passed through a reduction reagent, a Mg(ClO₄)₂ water trap and a 1.2 m Poropak QS 50/80 chromatographic column at 70°C for final isolation. TOC and TS quantification from measurement of generated CO₂ and SO₂ was accomplished using an external standard (sulphanilamide, C₆H₈N₂O₂S) and a thermal conductivity detector (TCD). From the TCD, the CO₂ and SO₂ was carried by He to a ConFloII interface, which allows a portion of the He and combustion gases to enter directly into the ion source of the IRMS for carbon and sulfur isotopic measurements. The TOC and TS concentrations in the samples are back-calculated as a percentage of the dry weight of the sediment. Isotopic analyses for δ¹³C_{org} and δ³⁴S are reported in standard notation referenced to the standards VPDB and VCDT, respectively.

4.3. Lithostratigraphy

On the basis of microscopic and macroscopic core descriptions, organic carbon content and colour, four sapropel and five non-sapropel units are identified and labeled as 'A' through 'I' from top to bottom (Fig. 4.2). The correlation of the units among the five cores is accomplished by matching peaks of oxygen isotopic curves together with

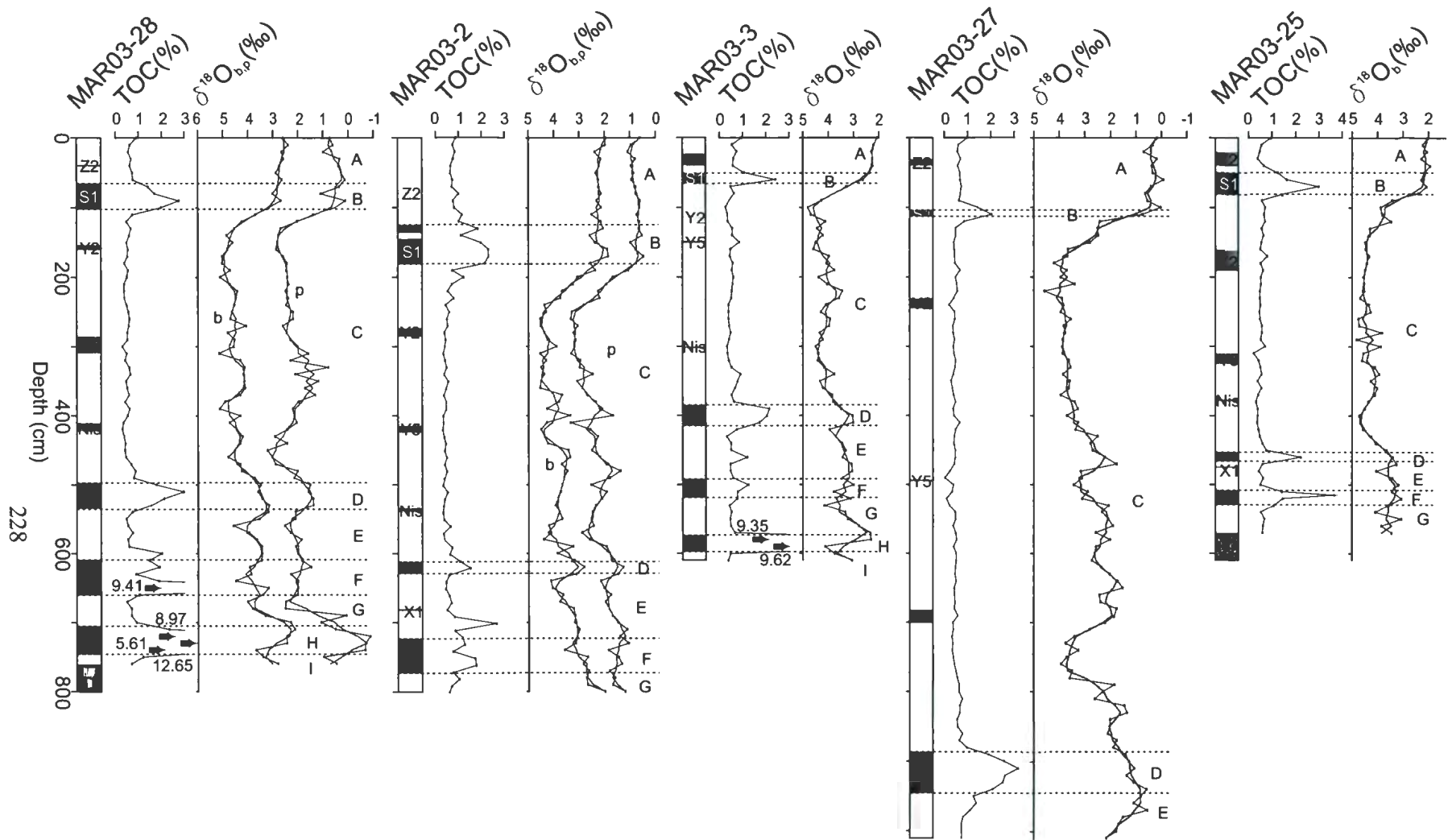


Figure 4.2. Sapropel and non-sapropel units in the five cores. Also shown are the downcore variations of TOC and oxygen isotope values. In all cores horizontal scales of TOC and $\delta^{18}\text{O}$ plots are the same. Red curves are 3-point moving averages. Grey area at the bottom of cores MAR03-28 and MAR03-25 is flow-in. 'b' and 'p' stand for data from benthic and planktonic tests, respectively. Z2, Y2, Y5, Nis, X1 are ash horizons (Aksu et al., 2008)

stratigraphic positions of the known ash layers (see units A and C; Fig. 4.3). Throughout the cores, sapropel units are distinguished by their comparatively darker colors and ~2x background organic carbon contents (see Chapter 2 for details). Using these criteria, sediments with 1.0-12.65% organic carbon content are described in this paper as sapropels (Fig. 4.2). Visual examination of the cores shows that most sediments consist of clay/silt-sized particles and are slightly to moderately burrowed (Fig. 4.4). The coarse fraction is mainly composed of foraminifera, pteropods, bivalve and gastropod shells, and variable amounts of volcanic ash. Sediment accumulation is inferred to have occurred through hemipelagic rain due to paucity of terrigenous sand-sized material, lack of evidence for re sedimentation (e.g., lack of normally graded event beds) and continual presence of bioturbation.

Non-sapropel units A, C, E, G, I are composed of burrow-mottled foram-bearing calcareous clayey mud (Fig. 4.4). The units are predominantly yellowish/dark yellowish brown (10YR5/4, 10YR4/2) and gray (i.e., yellowish, light and dark; 5Y5/2, 5Y6/1, 5GY6/1) in colour (Fig. 4.4 description). The average TOC content is 0.5% and mainly ranges between 0.4% and 0.7% with relatively higher organic carbon contents in unit G reaching 0.9% (Fig. 4.2). Unit A contains an ash layer which is largely disseminated in fine mud. The ash is widespread throughout the Aegean Sea and part of the eastern Mediterranean Sea and has been identified as the Z2 tephra from the Minoan eruption of Santorini Island (Aksu et al., 2008).

Unit C contains three tephra layers which are described in detail by Aksu et al. (2008), and identified by those authors using geochemical fingerprinting. Equivalents of these tephra layers are observed all around the eastern Mediterranean Sea including the

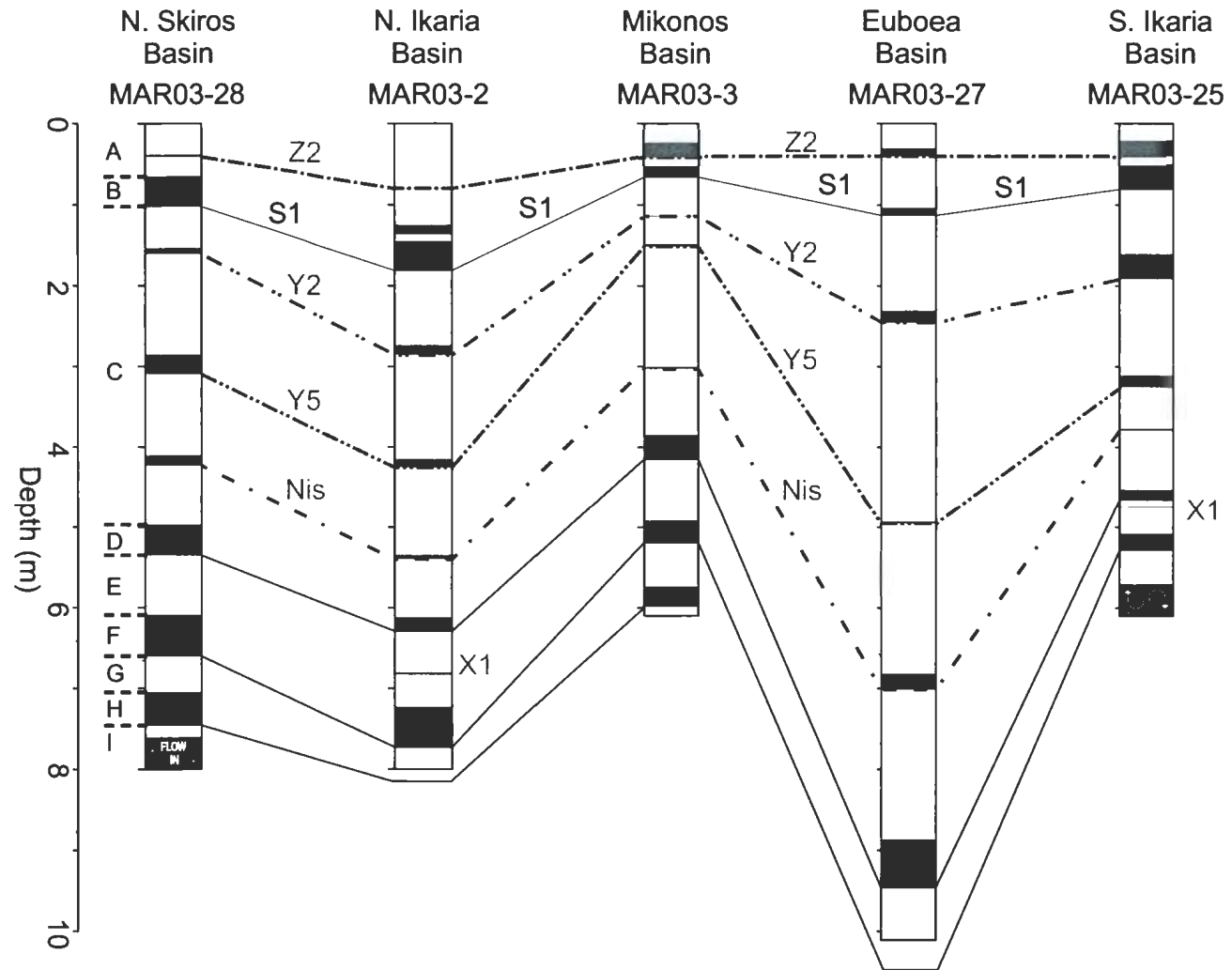


Figure 4.3. Correlation of ash layers (grey) and lithologic units among five cores. Ash correlations are from Aksu et al. (2008). X1 only is recognized in two cores so no correlation lines are drawn. Grey area at the bottom of cores MAR03-28 and MAR03-25 is flow-in.

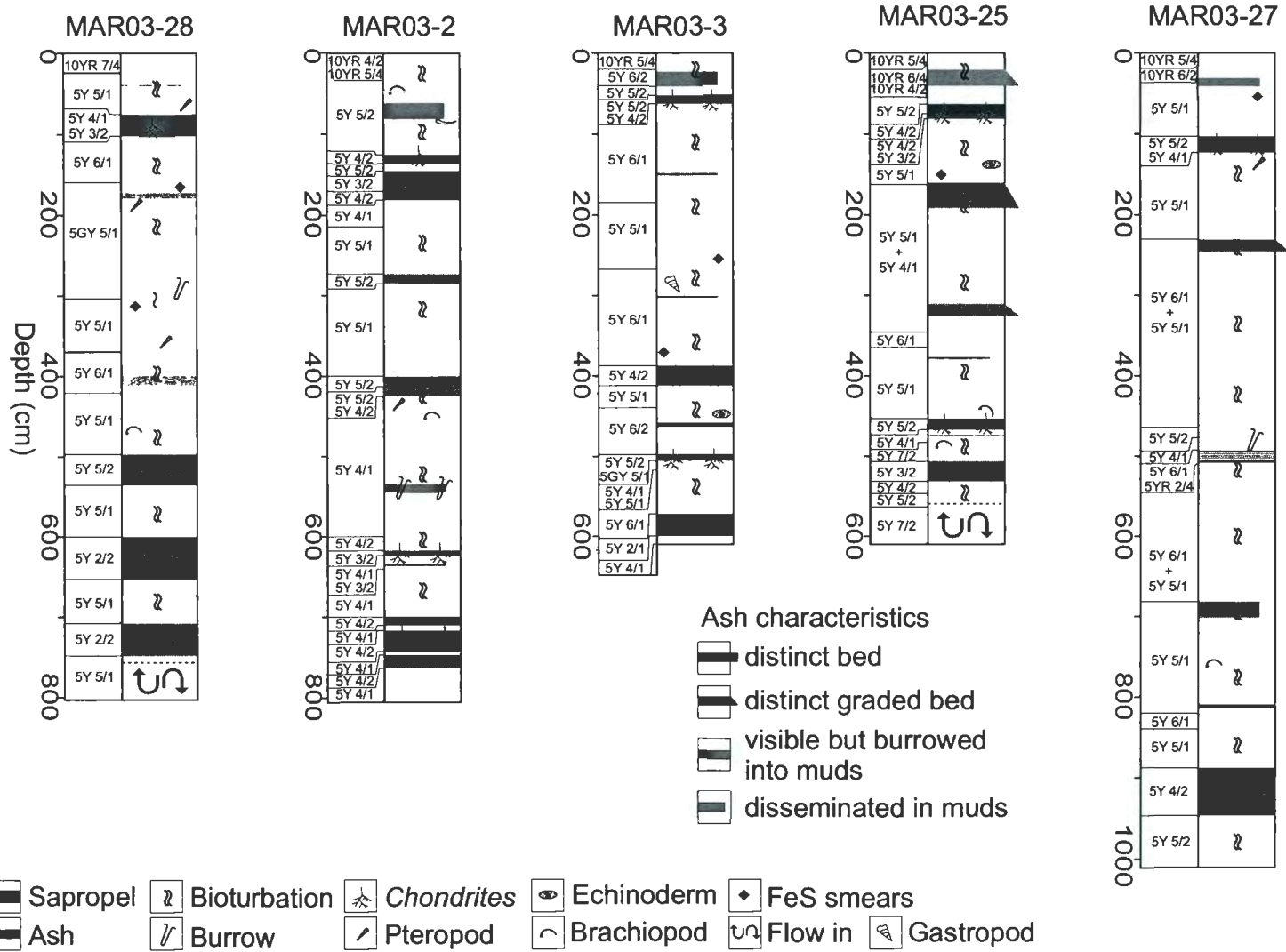


Figure 4.4. Lithologic attributes of the five studied cores. Dashed line in cores MAR03-28 and MAR03-25 indicates the beginning of flow-in.

Aegean, Adriatic and the Ionian seas. From top to bottom they are identified by Aksu et al. (2008) as the Y2 tephra (the Cape Riva eruption on the Island of Santorini also known as the Akrotiri eruption), the Y5 tephra (Campanian Ignimbrite eruption of the Phlegran Fields of the Italian Volcanic Province; Narcisi and Vezzoli, 1999), and the Nisyros tephra (Nisyros eruptions on the Island of Nisyros). They are mostly disseminated in clayey background; however, high numbers of glass shards make the tephra layers discernible with sharp tops and bases in most of the cores (Fig. 4.4). Unit E contains an ash layer disseminated in mud in cores MAR03-25 and MAR03-2. This tephra layer is correlated with the X1 tephra, most likely derived from the Aeolian Islands, Italy (Aksu et al., 2008).

Sapropel units B, D, F and H are distinguished from overlying/underlying units by their darker olive gray color (5Y4/1, 5Y3/2, 5Y4/2, 5Y5/2, 5Y2/2, 5Y2/1). They are composed of colour-banded clayey mud with a sharp base and include ~1 mm-diameter sharp-walled and oval-shaped burrows identified as *Chondrites* (Fig. 4.4). The organic carbon contents display significant variations among sapropel units ranging between 1% and 12.65%. In unit B, the organic carbon content varies from 1.1% in core MAR03-2 to 2.98% in core MAR03-25 (Fig. 4.2). In core MAR03-2, it changes upward from 2.3% to 1.1% to 1.8%, suggesting two peaks of organic matter accumulation in the North Ikaria Basin. The intervening decline in organic-matter accumulation is not recognized in the other cores, either because it is not present or because it was not captured by the 10 cm sample spacing (Fig. 4.2). In unit D, the TOC content ranges from 1.05% to 2.97% averaging 1.74%. In unit F, maximum and minimum TOC contents of 9.41% and 0.47% are observed in cores MAR03-28 and MAR03-3; it is certainly a non-sapropel mud in the

latter core (Fig. 4.2). Moreover, in cores MAR03-2, MAR03-3, and MAR03-28, organic carbon percentages display fluctuations across unit F creating a double-peaked plot, becoming lower in TOC contents within the mid portions ranging from 0.47-0.83% (Fig. 4.2). Unit H contains the highest organic carbon content reaching 12.65% at its middle in core MAR03-28 and shows a noticeably higher average TOC content than the upper sapropels of 9.49% and 6.15% in cores MAR03-28 and MAR03-3, respectively (Fig. 4.2).

4.4. Age Models

The chronostratigraphy of the cores was established using a number of age control points which permitted a depth-to-age conversion with the assumption that the sedimentation rate was constant between dated intervals (Fig. 4.5). Programs AGER and TIMER (Imbrie and Kipp, 1971) were used to convert sample values into results at a time step of 200 years.

The age control points used in depth-to-age conversion consist of well constrained top/bottom ages of the uppermost sapropel layer, tephra layers Z2, Y2 and Y5 and control points determined by curve matching of the core-specific oxygen isotope curves with the global oxygen isotope curve (see Aksu et al., 2008; Chapter 2 for details). The uppermost sapropel layer is correlated with the most recent sapropel S1 due to its consistent stratigraphic position throughout the cores, situated between the ash layers Z2 and Y2, and its occurrence within MIS 1. Its top/bottom ages are well constrained by ^{14}C dates in the literature. Calibrated ages based on these radiocarbon dates and are used as age control points (see Chapter 2 for details). Other picks are based on astronomically

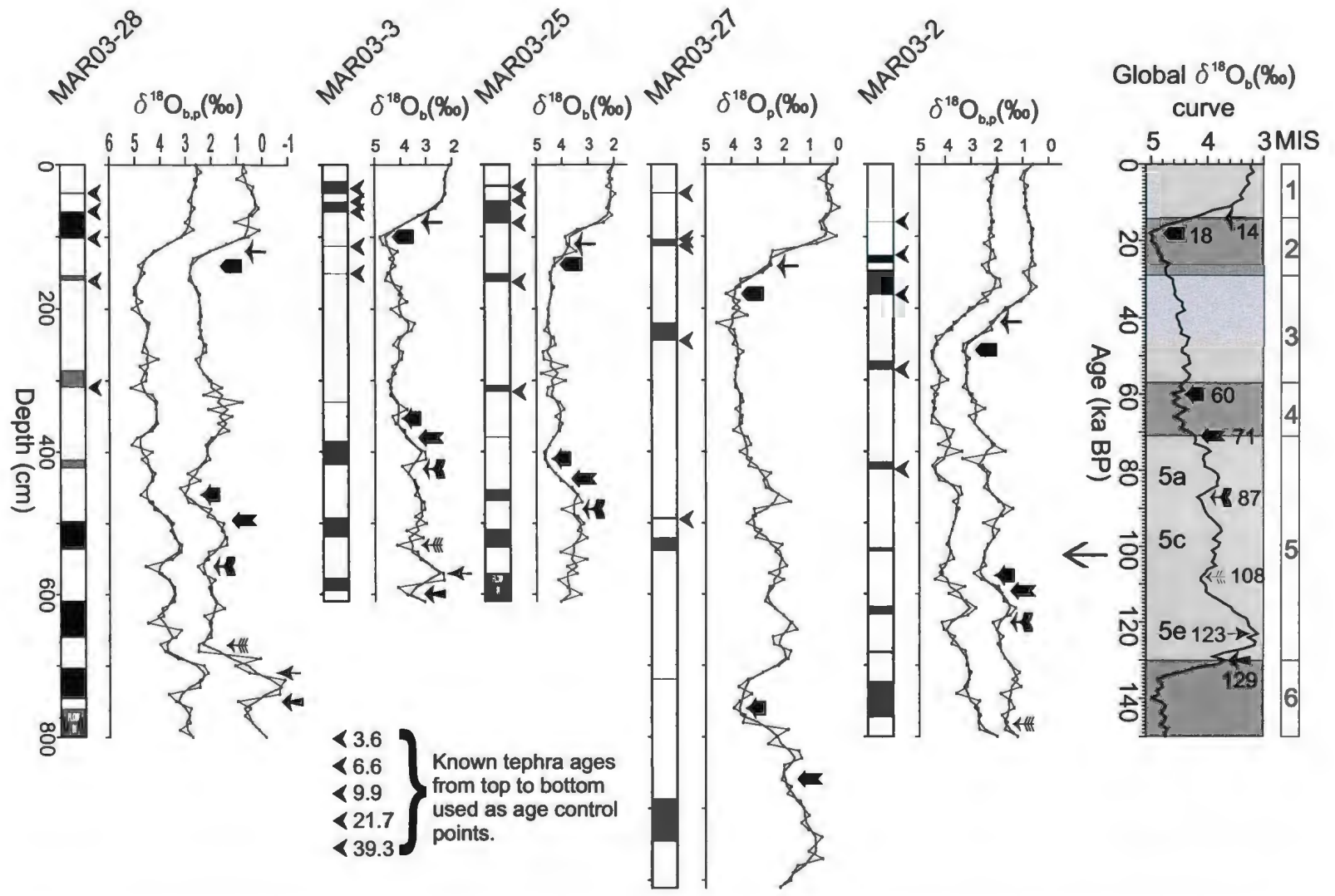


Figure 4.5. Age control points throughout the cores. Triangular arrows are those obtained from the known ages of top/base S1 and the tephra layers Z2, Y2, and Y5. Other arrows symbolise age control points determined by matching of the oxygen isotope curves with the global curve. Red curve is the 3-point moving average. Global curve is from Lisiecki and Raymo (2005).

fixed dates for inflections in oxygen isotopic curves.

The depth-to-age conversion process reveals that the oldest sediment recovered in the cores (unit I) dates from ~130 ka BP at the transition from MIS 6 to MIS 5 (Fig. 4.6).

The interpolated basal ages of MIS 5 organic-rich layers from top to bottom are 83.2–80.4 ka BP, 106.4–105.8 ka BP and 128.6–128.4 ka BP (Table 4.2). These calculated ages coincide with the interstadials of MIS 5 and are in good agreement with the previously published ages of sapropels S3, S4 and S5 developed, respectively, during marine isotopic stages 5a, 5c and 5e in the eastern Mediterranean Sea (Fig. 4.6; Rossignol-Strick, 1985; Emeis et al., 2003).

The mean sedimentation rates calculated for cores MAR03-28, MAR03-3, MAR03-2, MAR03-25, MAR03-27 are 6.4 cm/kyr, 4.7 cm/kyr, 9.5 cm/kyr, 6.0 cm/kyr, 11.5 cm/kyr, respectively (Table 4.2).

4.5. Data presentation

4.5.1. Oxygen isotopes

Oxygen isotope curves were obtained from benthic foraminifera *U. mediterranea* in all cores except core MAR03-27; in cores MAR03-2 and MAR03-28 oxygen isotope analyses were performed on both *Gs. ruber* and *U. mediterranea*. Unless otherwise indicated the descriptions and $\delta^{18}\text{O}$ values in this section are 3-point moving averages.

The stacked $\delta^{18}\text{O}$ curves for planktonic and benthic foraminifera demonstrate the general variation in oxygen isotopic composition of the Aegean Sea since 130 kyr BP and

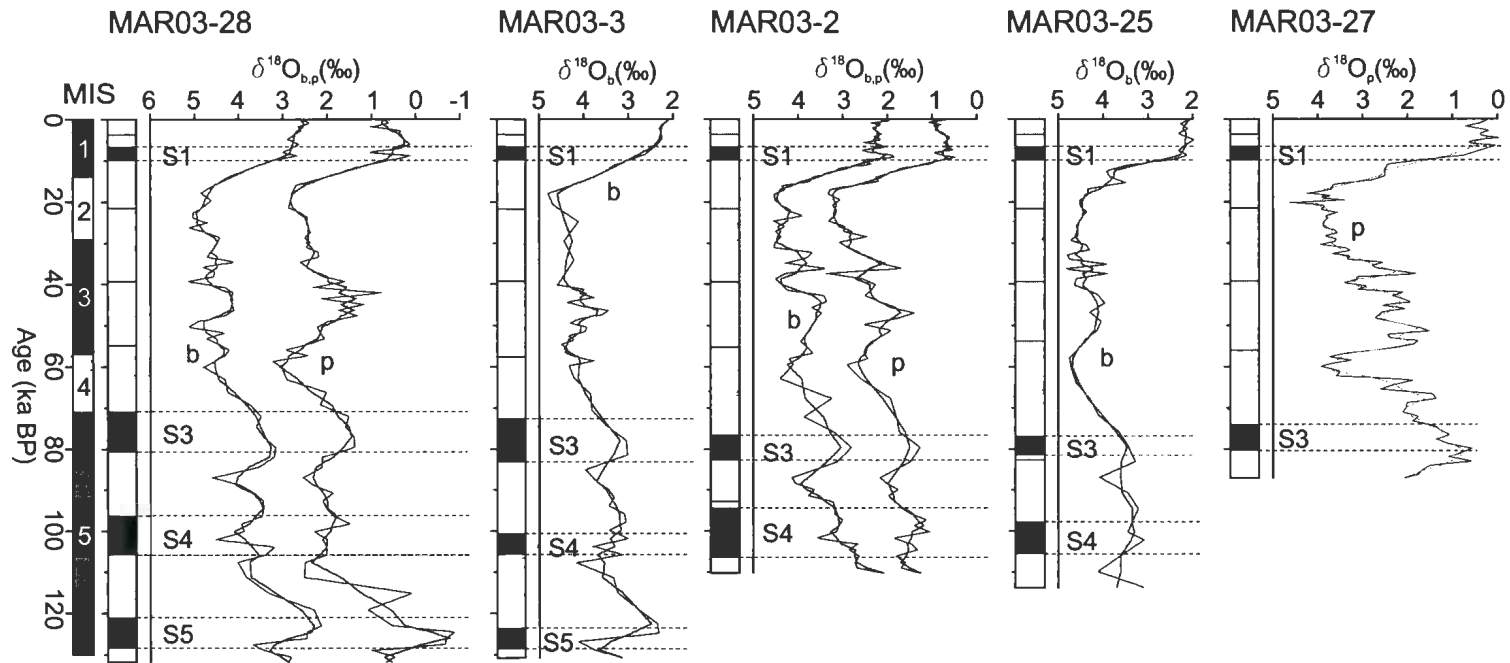


Figure 4.6. Age-converted lithostratigraphic columns and their corresponding oxygen isotope measurements for five cores. All ages derived from radiocarbon dates are calibrated to calendar years with a reservoir age of 557 yr (reservoir corrections of 408 yr and 149 yr are from Marine04 curve and Facorellis et al., 1998). Letters 'b' and 'p' near the curves stand for 'benthic' and 'planktonic', respectively. Criteria for picking the top of S4 are weaker than for other sapropels, resulting in apparent durations that do not correspond to significant contrasts in TOC values (Fig. 4.7).

	MAR03-28 (453 m)	MAR03-3 (720 m)	MAR03-2 (398 m)	MAR03-25 (494 m)	MAR03-27 (651 m)
Sapropels	onset	onset	onset	onset	onset
S3	80,600	83,200	82,800	81,600	80,400
S4	105,800	105,800	106,400	105,600	
S5	128,400	128,600			
	termination	termination	termination	termination	termination
S3	70,800	72,600	76,600	76,800	74,000
S4	96,200	100,600	94,400	97,800	
S5	121,000	123,600			
Core bottoms	131,800±781	130,800±1063	110,200±526	113,800±833	87,200±434
Mean sed. rates (cm/kyr)	6.4	4.7	9.5	6.0	11.5

Table 4.2. Calculated ages of sapropels S3, S4, S5. Also shown are the average sedimentation rates.

have moderate to large amplitude excursions that correspond to glacial and interglacial stages (Fig. 4.6). In particular, abrupt depletions in the $\delta^{18}\text{O}$ values characterize the upper segments of all cores with changes of as much as 4‰ at the most recent termination T1 associated with the glacial-interglacial transition of MISs 2/1 (Fig. 4.6). A prolonged yet consistent change towards more positive values is observed within the middle portions of the cores (80–60 kyr BP) reflecting the transition from MIS5 to MIS4 with a maximum shift of 3‰ ($\delta^{18}\text{O}_p$; Fig. 4.6). A more abrupt enrichment with similar amplitude is observed in MIS5 associated with the transition from interstadial 5e to stadial isotopic stage 5d. Moreover, interglacial MISs 1, 3 and interstadial stages 5a, 5c, 5e are manifested by moderately depleted (1.2‰; during MIS3) to highly depleted $\delta^{18}\text{O}_p$ values (-0.2‰ and -0.6‰ during MIS1 and MIS5), whereas $\delta^{18}\text{O}$ values are comparatively heavier during glacial times (2.8–3.2‰; MIS2 and MIS4) suggesting cooler and/or more saline conditions (Fig. 4.6). In addition, according to the downcore variations in oxygen isotope compositions, the transitions to glacial/stadial maxima seem to be attained more slowly than the transitions to interglacial/interstadials (Fig. 4.6). The depleted $\delta^{18}\text{O}$ values during MISs 1 and 5 show clear association with times of sapropel formation. Depletions are strongest during the accumulation of sapropels S1 and S5 ranging from 0.6–0.9‰ ($\delta^{18}\text{O}_b$) and from 0.3 to -0.6‰ ($\delta^{18}\text{O}_p$), respectively (Fig. 4.6). On the other hand, in sapropels S3 and S4, oxygen isotope values show similar yet modest variations decreasing on average by between 1.4‰ and 1.8‰ relative to adjacent units.

4.5.2. Elemental carbon and sulfur (TC, TS)

TC and S percentages show close covariation among the five studied cores. Across non-sapropel intervals, TOC and S values mainly change between 0.3–0.6% and 0.1–0.4%, respectively (Fig. 4.7). In cores MAR03-27, MAR03-25 and MAR03-28, sulfur concentrations are higher between 40 and 18 kyr BP, showing values ranging generally from 0.4% to 1% (cores MAR03-28 and MAR03-3). Within the most recent sapropel S1, TOC values show small variations and range between 2.1% and 2.8%. Sulfur values on the other hand display a larger variation and range from 0.5% to 1.6%. In sapropel S3 TOC values range between 2% and 3.1% with higher concentrations being observed in cores MAR03-28 and MAR03-27. In general, TOC concentrations peak within the middle portion of sapropel S3, but in core MAR03-3 organic carbon concentrations of 2% seem to be maintained across the sapropel interval. In parallel to TOC amounts, higher sulfur abundances are observed for S3 in cores MAR03-28 and MAR03-27, reaching 1.2% and 2.4%, respectively. Among the remaining three cores, sulfur concentrations range between 0.5% and 0.7%. In sapropel S4, TOC and S values generally range from 1.1% to 3.8% and from 0.8% to 1.35%, respectively. In core MAR03-28, TOC and S concentrations show a prominent spike within the lower portions of S4 where they increase to 9.65% and 3.5%. Highest concentrations are observed in sapropel S5 with maximum TOC and sulfur values of 12.65% and 2.8%, respectively.

4.5.3. Carbon and Sulfur isotopes ($\delta^{13}\text{C}_{\text{org}}$ and $\delta^{34}\text{S}$)

Sulfur isotopes show large fractionations of 40–50‰ within the uppermost

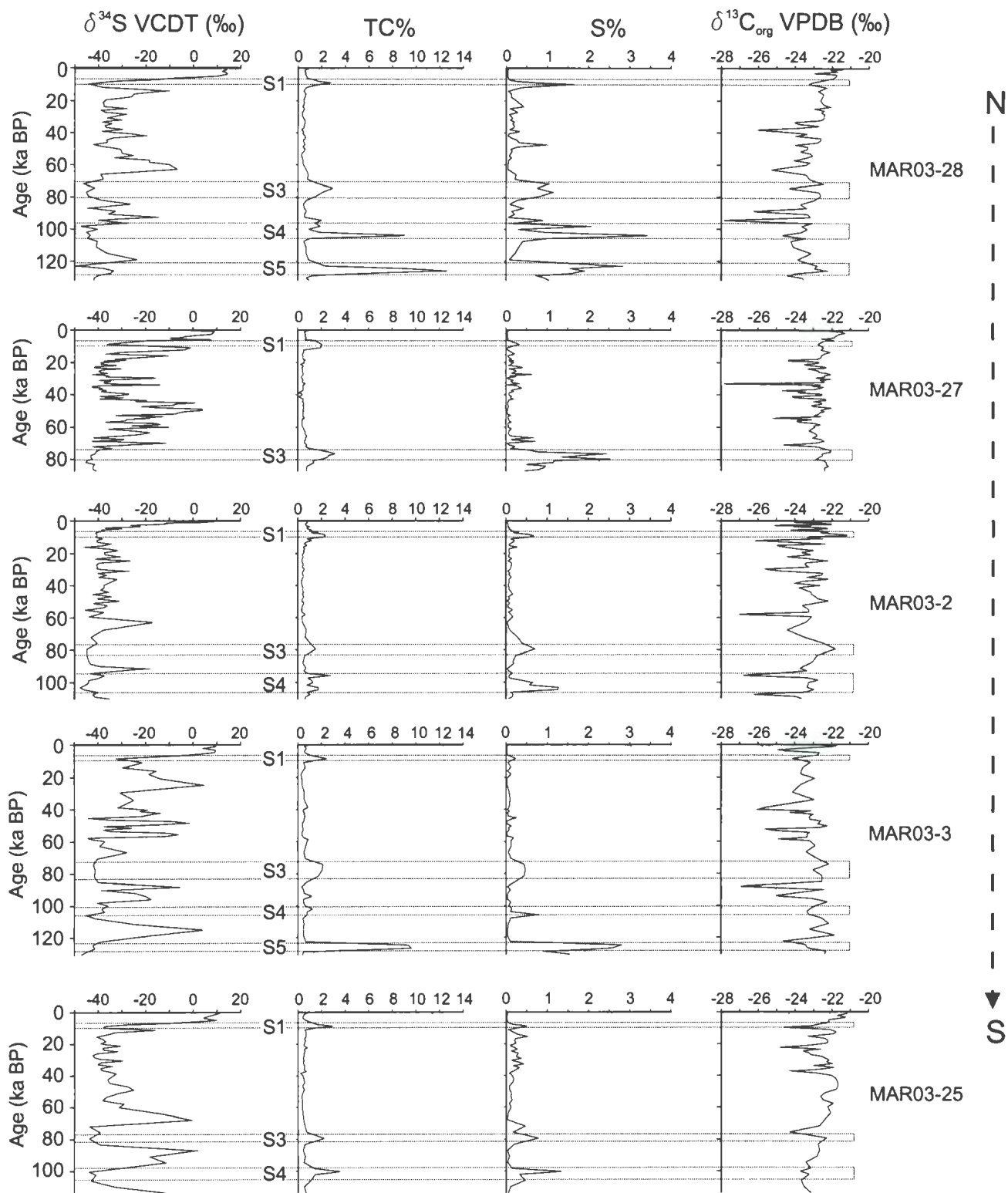


Figure 4.7. Downcore changes in elemental and isotopic carbon and sulfur compositions among the five studied cores. Northern and southernmost cores (i.e., MAR03-28 and MAR03-25) are arranged at the top and bottom.

portions of the cores and across MIS5 associated with interstadial/stadial transitions (Fig. 4.7). Maximum depletions are observed within sapropels S3, S4 and S5 where $\delta^{34}\text{S}$ values range between -38‰ and -45‰. Cores MAR03-28, MAR03-25, MAR03-27 and MAR03-2 exhibit similar upward trends between sapropel S3 and S1. A high amplitude positive excursion changing by as much as 42‰ in core MAR03-25, above sapropel S3, is followed by consistently more depleted small amplitude changes until below the most recent sapropel S1 (around 17–20 ka BP) where an abrupt enrichment occurs prior to sapropel S1 onset (except in core MAR03-2). A persistent enrichment in $\delta^{34}\text{S}$ starts at the onset or middle portions of sapropel S1 and continues until the core tops with shifts of as much as 52‰ (core MAR03-28).

Among the five studied cores, carbon isotope values mainly range between -22.5‰ and -24‰ with episodic occurrences of maximum depletions (<-27‰) in most of the cores (except in core MAR03-25). During MIS5, sapropel intervals S3–S5 are characterized by less negative $\delta^{13}\text{C}_{\text{org}}$ values with respect to the intervening non-sapropel sediments than is the case for S1.

4.6. Discussion

4.6.1. Bottom water conditions

The deposition of high organic carbon accumulations has been a topic of great debate and several factors have been reported to play a role. These are sedimentation rates, bottom water conditions [i.e., oxygen content (oxic–suboxic–anoxic/euxinic)], the

amount of export production and bioturbation.

The role of O_2 in the preservation of organic matter in marine sediments has been a subject of considerable debate. Classically, high concentrations of organic carbon in marine sediments have been attributed to deposition in an O_2 -free (euxinic) water column (DeMaison and Moore, 1980). The rationale has been that in such an environment anaerobic processes of organic carbon decomposition would dominate, which are less efficient than decomposition in the presence of O_2 . However, sedimentation rate plays a significant role as shown by the fact that at high rates (i.e., $>40 \text{ cm ka}^{-1}$), preservation of organic carbon does not vary with the O_2 content of the bottom waters and decomposition occurs mostly under anaerobic conditions below the sediment-water interface. At sedimentation rates $<40 \text{ cm ka}^{-1}$, enhanced preservation requires low- O_2 or euxinic environments. Since sedimentation rates are calculated to be always $<40 \text{ cm kyr}^{-1}$ throughout the eastern Mediterranean Sea including the Aegean Sea, the enhanced accumulation of organic carbon leading to sapropel formation must be explained by some combination of bottom water oxygen contents and rate of export production.

4.6.1.1. C/S ratios

Sulfur and organic carbon relationships in modern and ancient sediments have been used to estimate bottom water conditions at the time of deposition (e.g., Berner, 1982, 1984, 1989; Terashima et al., 1983; Glenn and Arthur, 1985; Koma and Suzuki, 1985; Boesen and Postma, 1988; Davis et al., 1988; Lin and Morse, 1991; Schimmelmann and Kastner, 1993). The relationship between these elements can be a useful indicator for depositional environments (i.e., freshwater, normal marine and

anoxic/euxinic), since the biogeochemical cycle of sulfur is inseparable from that of carbon, and the relationship depends on the depositional environment (Berner, 1989). The sulfur in marine sediments is primarily contained in iron sulfide minerals (e.g., hydrotroilite, pyrite). Their amount in a sediment is governed by the amount/reactivity of organic matter, the availability of dissolved sulfate and the content/reactivity of iron minerals (Berner, 1984). In normal marine sediments there is a good correlation between organic carbon and pyrite sulphur with a constant C/S ratio of about 2.8 (Berner, 1970, 1984; Goldhaber and Kaplan, 1974). According to Berner (1984), the constant C/S ratio in normal marine sediments is due to constant fractions of organic carbon and reduced sulphur being preserved in the sediments, with organic matter limiting the amount of iron sulphide formed. For freshwater sediments, the availability of sulphate limits the amount of iron sulphide formed, resulting in a much higher C/S ratio than in normal marine sediments (Berner and Raiswell, 1983, 1984). In euxinic sediments, given the excessive presence of H₂S both in the water column and at the sediment-water interface, reactive iron determines the amount of iron sulphide formed irrespective of the amount of organic carbon present.

C/S plots constructed for the five cores show positive correlations ($0.63 < r < 0.86$) indicating that with increasing amounts of C_{org} a larger amount of organic matter is metabolizable and more sulfide is produced. Such a relationship suggests that the main factor controlling the sulfur content in Aegean Sea sediments is the amount of organic matter rather than availability of dissolved sulfate or iron (Fig. 4.8).

The majority of the C/S ratios from sapropels plot around the normal marine line suggesting that sapropels were formed under normal marine conditions. In all five cores,

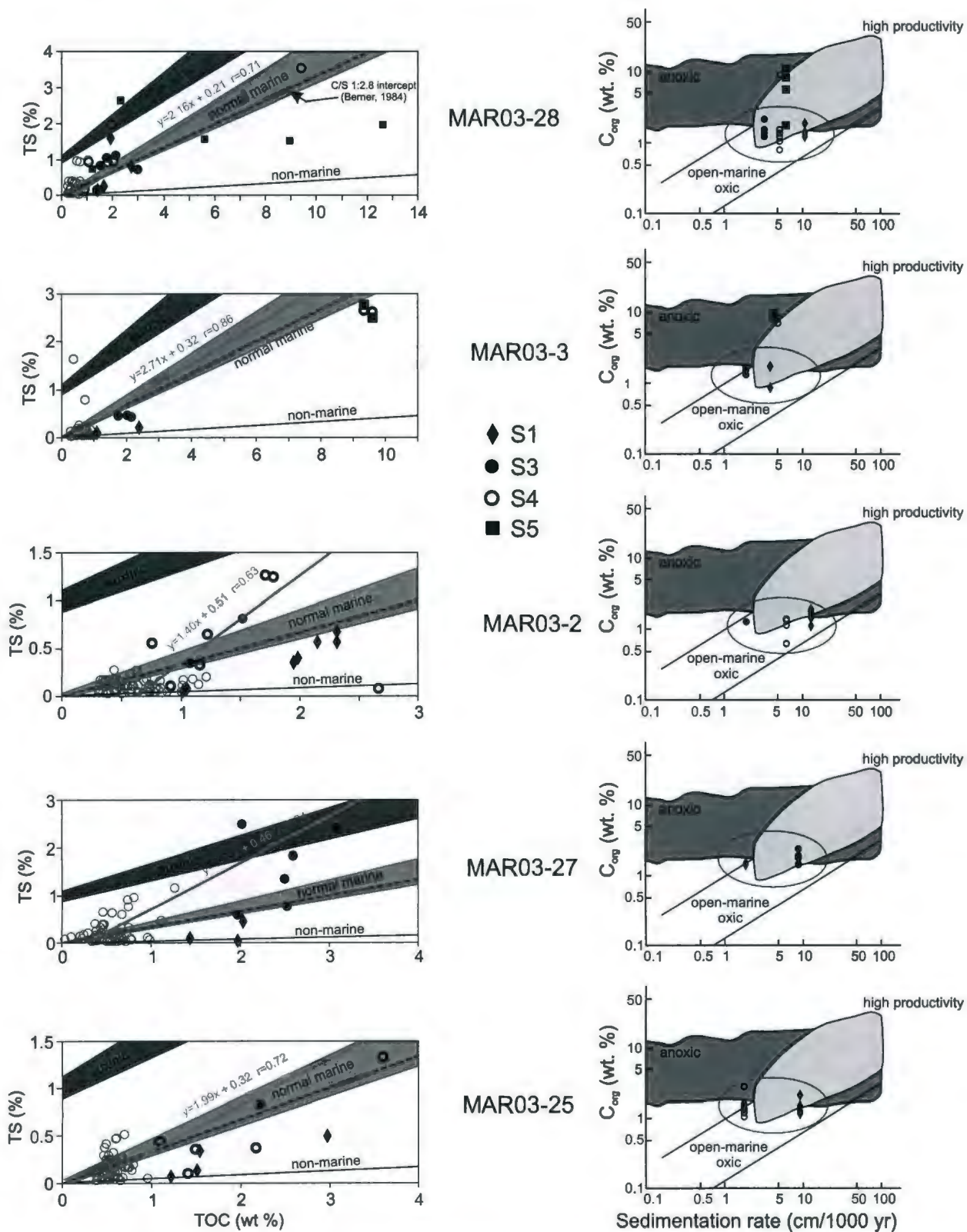


Figure 4.8. C/S plots (left; modified from, Leventhal, 1995) and C_{org} vs. sed. rate plots across sapropels S1, S3, S4 and S5 (right) showing the bottom water conditions. Red circles are results from non-sapropel levels. Regression lines are based on all data points. C_{org} vs. sed. rate graph is modified from Stein, 1986b. Anoxic, high-productivity and normal-marine fields are determined based on C_{org} and sedimentation rates data base derived from Recent to Miocene sediments deposited under oxic and anoxic sea water conditions.

C/S ratios from upper/top portions of S1 plot on the non-marine line (Fig. 4.8). Such low ratios can be attributed to an increase in freshwater/brackish water budget towards the end of sapropel formation during which low $[\text{SO}_4^{2-}]$ limited the amount of S deposition. C/S ratios plotting well above the normal marine line and within the euxinic (i.e., low oxygen and high sulphide) zone are observed in cores MAR03-28 and MAR03-27.

Interestingly, the samples with extremely high C_{org} values (e.g., 9% and 12.5%) in sapropel S5 (core MAR03-28) plot below the normal marine line (Fig. 4.8). With such high organic carbon contents, higher sulfur concentration would be expected. Reduced sulfide formation and/or sulfur uptake in the sediment might be ascribed to relatively higher fresh/brackish water input during S5 time, perhaps elevated at the MAR03-28 site which is at the northern end of the Aegean Sea nearest the Dardanelles outlet (Fig. 4.1).

Plots of sedimentation rate versus C_{org} show a clear clustering around the upper limit of 'open marine oxic' and lower limit of 'high productivity zones', except that samples with very high TOC values (S4 and S5 in cores MAR03-28 and MAR03-3) plot within or near the anoxic zone (Fig. 4.8). Those same samples plot either along the normal marine line or below it. This inconsistency stems from the sensitivity of the amount of deposited organic carbon to the sedimentation rate. The sedimentation rates calculated for sapropels S4 and S5 in cores MAR03-28 and MAR03-3 are below the average sedimentation rates obtained throughout the eastern Mediterranean. Thus, the inconsistency between two plots might result from an underestimation of the sedimentation rates for S4 and S5 alone, since the available age control only allows their rates to be determined as part of an average for both the sapropels and the surrounding section. Ages for the base and top of S4, in particular, are not well constrained by nearby

age control points (Fig. 4.5).

4.6.1.2. $\delta^{34}\text{S}$

Core top $\delta^{34}\text{S}$ values among the five studied cores range mainly between +9 and +11‰ with maximum and minimum values of +14‰ and -0.8‰ in cores MAR03-28 and MAR03-27, respectively (Fig. 4.7). These values are comparatively lighter than the Mediterranean seawater value of +20.6‰ observed by de Lange et al. (1990). The $\delta^{34}\text{S}$ signal difference of 10–20‰ between the Aegean core tops and Mediterranean seawater can be attributed to a number of factors: 1) the $\delta^{34}\text{S}$ values of sulphate diffusing into Aegean Sea sediments is probably lighter than that of seawater as a consequence of preferential diffusion of ^{32}S (Jorgensen, 1978; Chanton et al., 1987b); 2) part of the sulfur pool in the partly isolated Aegean Sea may originate from freshwater sulphate; 3) isotope exchange reactions may have weakened the isotope signal (Fossing and Jorgensen, 1990); 4) coretop samples might have a mixture of sulfur with a primary seawater-sulfate signature and sulfur (as FeS) fixed by the first stages of early diagenetic sulfate reduction.

During the deposition of MIS5 sapropels, the $\delta^{34}\text{S}$ values range between -40‰ and -45‰ whereas during the deposition of the most recent sapropel S1, values range between -30‰ and -35‰ in cores MAR03-27, MAR03-25 and MAR03-3 and -40‰ to -42‰ in cores MAR03-28 and MAR03-2 (Fig. 4.7). Collectively, these light values imply that fractionations of at least 59‰ to 65‰ occurred relative to Mediterranean seawater. To achieve fractionations of sulphur isotopes of this magnitude between sulphate and pyrite, sulphate reduction must proceed with a continuous supply of abundant dissolved

sulphate (open system) where exchange with seawater readily occurred, and must be followed by further ^{34}S depletion in the sulphide pool by reoxidation and disproportionation processes in the sulphur cycle (Passier et al., 1999). Provided that benthic fauna were continuously present during sapropel accumulation and hence bottom waters were never devoid of oxygen, the appropriate geochemical conditions likely occurred immediately below the sediment-water interface as a result of large SO_4 supply via diffusion or advection relative to the SO_4 reduction rates, and SO_4 was never depleted.

Across sapropel layers, $\delta^{34}\text{S}$ values show similar values irrespective of the amount of TOC deposited. Even in sapropel S5 (12% TOC) $\delta^{34}\text{S}$ fractionations are similar to those with TOC contents of ~2% implying that all sulphate reduction occurred below the sediment-water interface. It must be highlighted that significantly lighter values at sapropel intervals (~40‰) as opposed to intervening non-sapropel layers (~2‰) are suggestive of less oxygenated bottom waters (semi-euxinic?) which are also supported by the presence *Chondrites* observed across the sapropels. Moreover, maximum depletions across sapropels are even more negative than those observed in euxinic Black Sea (e.g., ~-32‰; Hiscott et al., 2007) bottom waters which further advocates the idea that the fractionations took place under continuous supply of abundant sulphate

4.6.2. Source of organic matter

During sapropel formation, $\delta^{13}\text{C}_{\text{org}}$ values vary within a narrow range showing about 1‰ variation ranging from -23.7‰ to -23‰ in S4, -23‰ to -22‰ in S3 and -

23.2‰ to -22.2‰ in S5 (Fig. 4.9). These small variations indicate a spatial uniformity of the organic carbon isotopic value during sapropel formation with a slightly higher terrigenous component in S4. Unlike older sapropels, S1 demonstrates larger variations in $\delta^{13}\text{C}_{\text{org}}$ values (-21.1‰ to -24.7‰) suggesting stronger alternation between marine and terrestrial organic-matter input. Significant increases in riverine and Black Sea water input may account for these large variations.

Organic carbon isotopic values have been used to identify the source of organic matter using a linear mixing model (Sutherland et al., 1984; Ten Haven et al., 1987; Fontugne and Calvert, 1992; Aksu et al., 1995). Although the end members for the marine and terrestrial components have been reported to be -22‰ and -27‰ (Deuser, 1970; Deines, 1980), it is difficult to accurately determine the end members. Considering the range of measured $\delta^{13}\text{C}_{\text{org}}$ values (between -21.5‰ and -27.4‰) and those from the eastern Mediterranean Sea (maximum of -19.5‰) it is reasonable to assume a range of -18‰ to -20‰ for the marine end member and -28‰ for the terrestrial end member. Our terrestrial fraction graphs are constructed by using -19‰ and -28‰ marine and terrestrial end members, respectively. The graphs show that terrestrial- and marine-sourced organic carbon have contributed somewhat equally during the deposition of sapropels S5, S4 and S3 (Fig. 4.9).

During the deposition of S1, however, there seems to be an upward trend in $\delta^{13}\text{C}_{\text{org}}$ with lighter values at the bottom becoming heavier towards the top. Such a trend implies that fluvial delivery of isotopically light organic carbon had a greater contribution during the onset of sapropel formation.

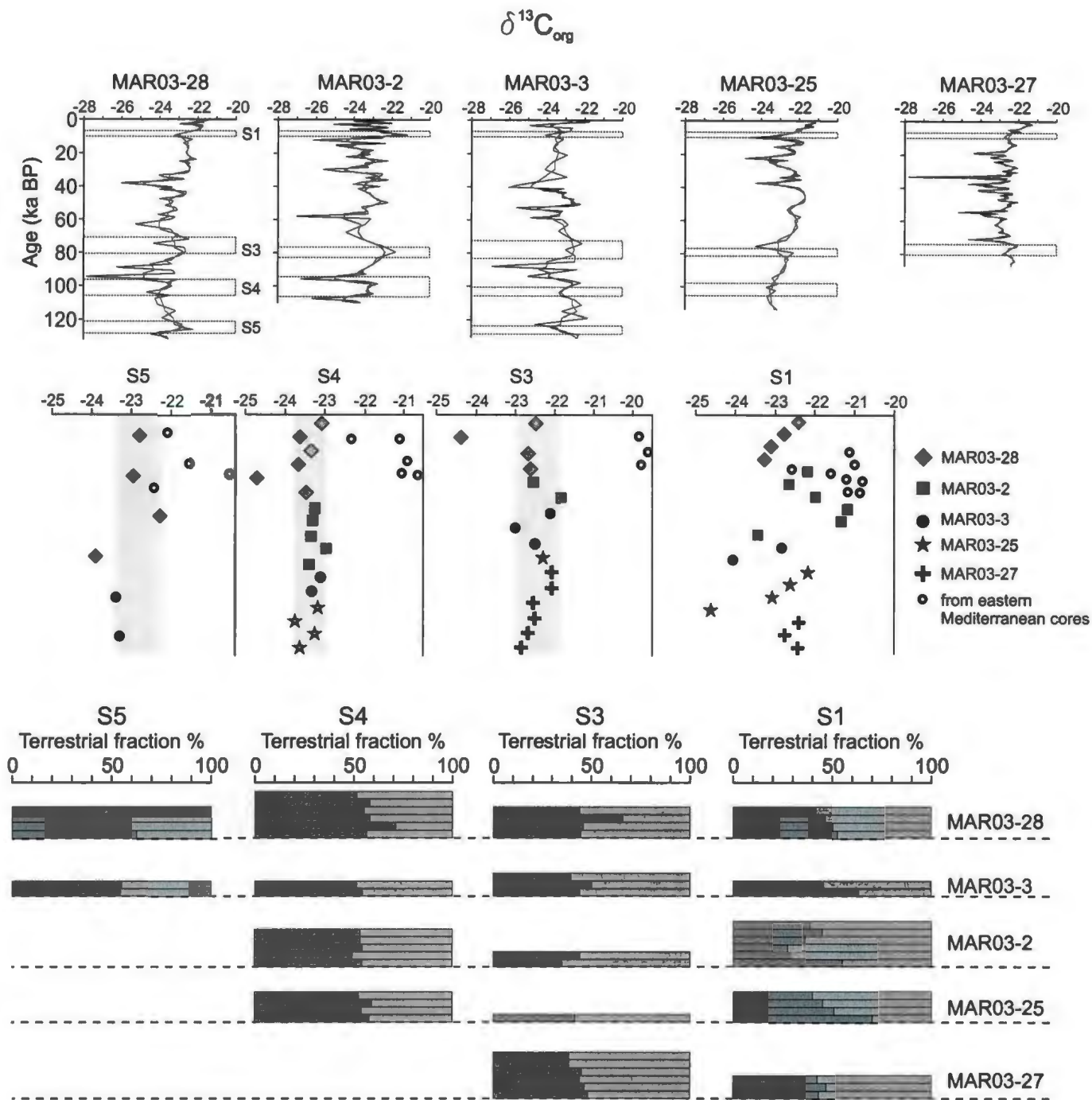


Figure 4.9. $\delta^{13}\text{C}_{\text{org}}$ values and terrestrial fraction across sapropels S1, S3, S4 and S5. For comparison, carbon isotopic values from the eastern Mediterranean (black circles) are also shown with end members specified in the text and $F_{\text{terr}} = \text{terrestrial fraction} = F_{\text{terr}} (-28\text{‰}) + (1-F_{\text{terr}})(-18\text{‰})$ (data from M. Paterné, unpublished eastern Mediterranean data; Ten haven et al., 1987; Sutherland et al., 1984).

On average, $\delta^{13}\text{C}_{\text{org}}$ values from MIS5 sapropels in the eastern Mediterranean are 1‰ to 2‰ heavier than those in the Aegean Sea which indicates a noticeably higher contribution of terrestrial organic carbon during sapropel deposition in the Aegean Sea relative to the eastern Mediterranean (Fig. 4.9). Similarly, in sapropel S1, $\delta^{13}\text{C}_{\text{org}}$ values from the eastern Mediterranean are generally more enriched than those from the Aegean Sea.

4.6.3. Paleoproductivity

Sapropels are reported to form at times of elevated productivity in the surface waters (e.g. Rossignol-Strick et al., 1982; Calvert et al., 1992; Murat and Got, 2000; Kouli et al., 2012). Estimates of the export palaeoproductivity (the organic carbon that is exported from the photic zone into the deep sea) have been obtained through empirical formulas: Equation 1 from Howell and Thunell (1992) and Equation 2 from Muller and Suess (1979).

$$\text{AR}_{\text{sed}} = 10 * \text{LSR} * (d_w - (1.025 * \Phi))$$

$$\text{ARC}_{\text{org}} = (\text{AR}_{\text{sed}} * C_{\text{org}}) / 100$$

$$\text{PP} = \text{ARC}_{\text{org}} / \text{pf} \tag{1}$$

and

$$\text{PP} = (C_{\text{org}} * d_g * (1 - \Phi)) / (0.003 * \text{LSR}^{0.3}) \tag{2}$$

where pf is the preservation factor, PP is the primary productivity ($\text{g C m}^{-2} \text{ yr}^{-1}$), ARC_{org} ($\text{g C m}^{-2} \text{ yr}^{-1}$) and AR_{sed} ($\text{g m}^{-2} \text{ yr}^{-1}$) are the organic carbon and sediment accumulation rates, C_{org} is the organic carbon content by weight percent, LSR is the linear

sedimentation rate (cm ka^{-1}), d_w is the sediment wet density, d_g is the dry bulk density (1.5 g cm^{-3} and 2.7 g cm^{-3} , respectively) and Φ is the fractional porosity (set at 0.72 in Equation 1 and 2). The multiplication factor of 10 in the equation for AR_{sed} stems from the fact we use different units for this variable than Howell and Thunell (1992).

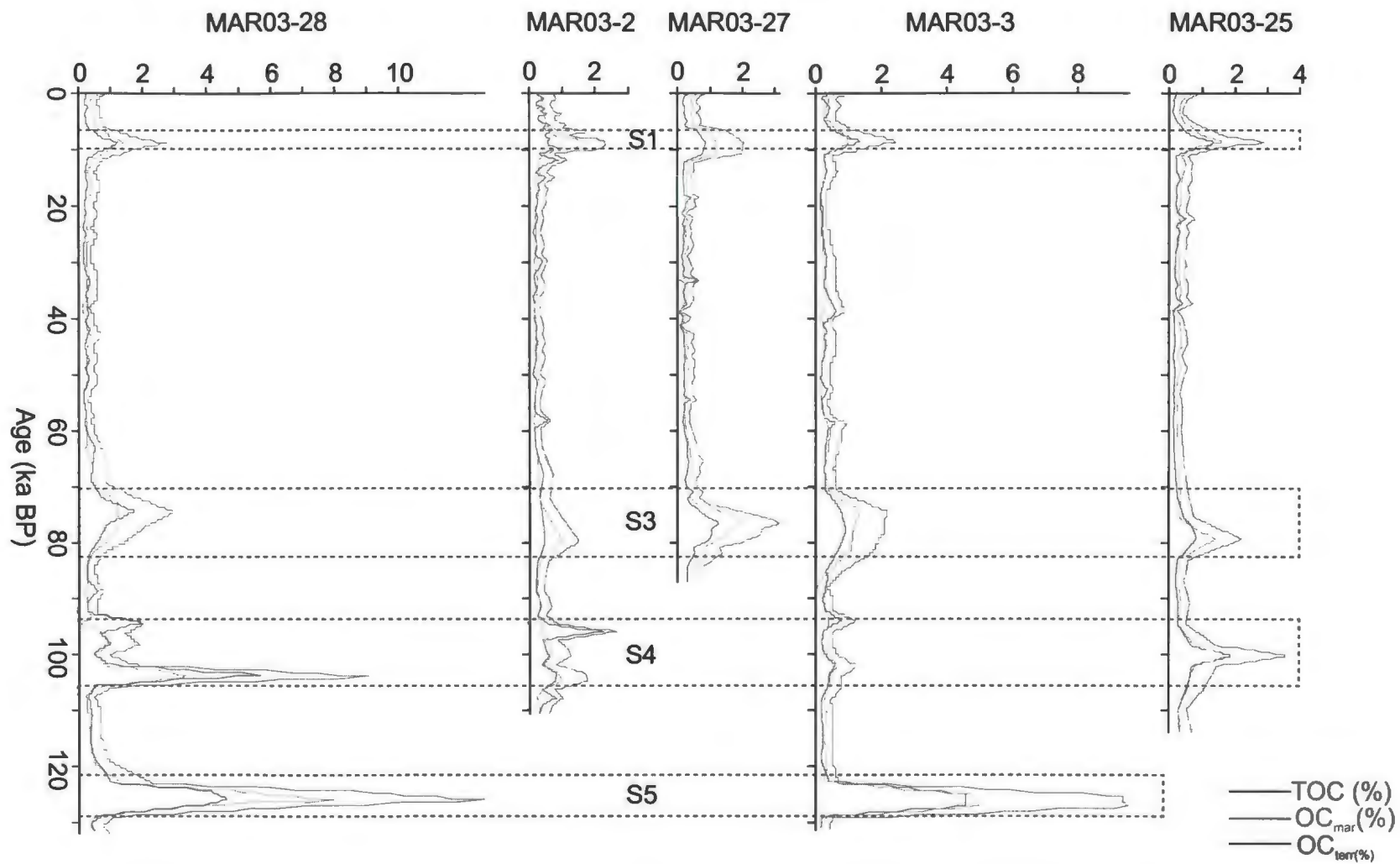
The amount of organic carbon preserved in sediments is primarily controlled by the sedimentation rate and the amount of primary productivity within the photic zone. According to the equations, primary productivity calculations are highly dependent on the accuracy of the sedimentation rates. For example, for Equation 2 the organic content of sediment doubles with a 10-fold increase in the sedimentation rate (assuming other factors remain constant).

Paleoproductivity reflects the amount of productivity in the surface waters which is high dependant on the rate of sedimentation rate. PP is the rate of photosynthetic activity of the present surface waters. PP is often considered to be higher in coastal regions where there is a high concentrations of floral activity, often represented by diatoms, dinoflagellates and coccoliths in sediments. Future work on phytoplanktonic flora will undoubtedly help clarify the Corg versus sedimentation relationships.

The sedimentation rate at a core location is controlled by several factors such as distance to source (e.g., river mouth), depth and sea bed morphology. Higher sedimentation rates will increase the burial rate of the organic matter thus decreasing the time of exposure to oxic (aerobic) degradation. Accordingly, higher primary production not only will increase the amount of organic matter available (export production) but also it causes an increase in the number of particles delivered to the sea floor and therefore the

burial rate. On the other hand, it should be noted that high sedimentation rates will also dilute organic carbon concentrations so that C_{org} content of a sampled interval (e.g., sapropel) may not represent the actual organic carbon flux to the sea floor. This is the reason why variability in organic carbon is considered in terms of accumulation rates. The calculation of paleproductivity values thus depends on how accurately we know the sedimentation rate (sediment accumulation rate), accordingly the organic carbon flux, at the corresponding time interval.

For their primary productivity calculations, Muller and Suess (1979; Equation 2) did not include sediments accumulating under permanently anoxic bottom water in their regression analysis. Since the bottom water conditions during accumulation of sapropels S1–S5 in the Aegean Sea were never anoxic (Aksu et al., 1995) it is valid to use Equation 2 to infer past sea water productivity variations. Both equations assume negligible delivery of terrigenous organic matter to the sediments which is not the case for the Aegean Sea because of its semi-enclosed geography and significant riverine input through several rivers and the Dardanelles Strait. $\delta^{13}\text{C}_{\text{org}}$ values show equally important organic matter contribution from both marine and terrestrial sources (Fig. 4.9). Hence, it is necessary to segregate the marine fraction of the TOC to compare with paleproductivity estimations from Equations 1 and 2, since it is only the marine fraction that is tied to sea-surface productivity levels. Marine (OC_{mar}) and terrestrial (OC_{ter}) organic carbon fractions were calculated for each sample using $\delta^{13}\text{C}_{\text{org}}$ values (Fig. 4.10). Contributions from these two sources are mostly approximately equal, except in sapropel S5 in core MAR03-28 where the OC_{mar} fraction (8%) is approximately twice the OC_{ter}



253

Figure 4.10. Marine and terrestrial organic carbon fractions derived from $\delta^{13}\text{C}_{\text{org}}$ values.

(~4.5%). In addition, relatively higher OC_{mar} input is recognized in sapropel S3 in all four cores (except core MAR03-28; Fig. 4.10).

Although quantitative paleoproductivity calculations might be viewed with scepticism due to their high sensitivity to sedimentation rates, they do have the potential to provide valuable insight into our understanding of the past primary productivity fluctuations at the sea surface.

Sedimentation rates throughout the Aegean Sea exhibit a significantly wide range changing from 2.9 cm ka⁻¹ to as high as 58.5 cm ka⁻¹ (Aksu et al., 1995; Roussakis et al., 2004; Casford, et al., 2007) with an average range of 10–13 cm ka⁻¹.

In Equation (1) the organic carbon content in sediments is ultimately controlled by the preservation factor which can be calculated by dividing organic carbon accumulation rate by primary production (Howell and Thunell, 1992). If we were to take today's primary production rate of 30 g C m⁻² yr⁻¹ (Lykousis et al., 2002) and use the calculated sedimentation rates (Fig. 4.11), downcore preservation factors required to reproduce the inferred OC_{mar} values show increased values at the most recent sapropel S1 and sapropels S4 and S5 with high organic carbon percentages (Fig. 4.12). The preservation factor at the core tops show unexpectedly high values ranging mainly between 1.2% and 1.5% with a maximum value of 3% in core MAR03-2. Such high values can be ascribed to sedimentation rates and organic carbon contents higher than the older non-sapropel intervals. Additionally, the maximum preservation factor observed in core MAR03-2 is due to sedimentation rates much higher than those of the other four cores (Fig. 4.11). The average downcore preservation factor across non-sapropel intervals is mainly ~0.5%. In cores MAR03-3 and MAR03-27, however, preservation

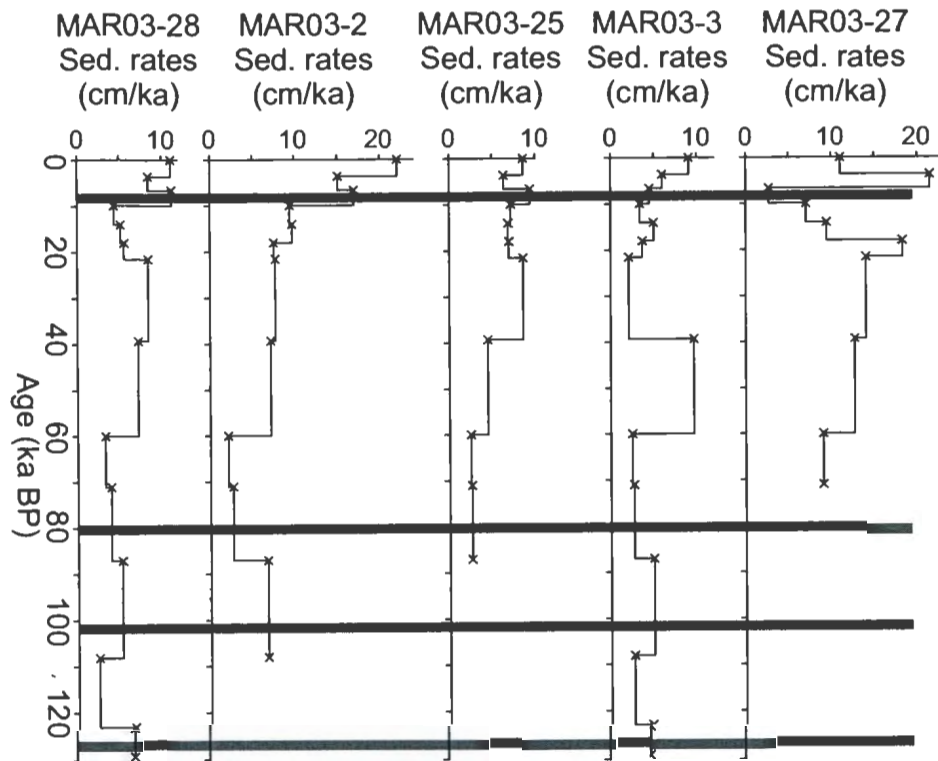


Figure 4.11. Age vs. sedimentation rate plots of the five cores. Gray bars represent the sapropel layers (units B,D, F, and H). 'x' symbols along the plots are age control points. Global sea level is from Waelbroeck et al. (2002).

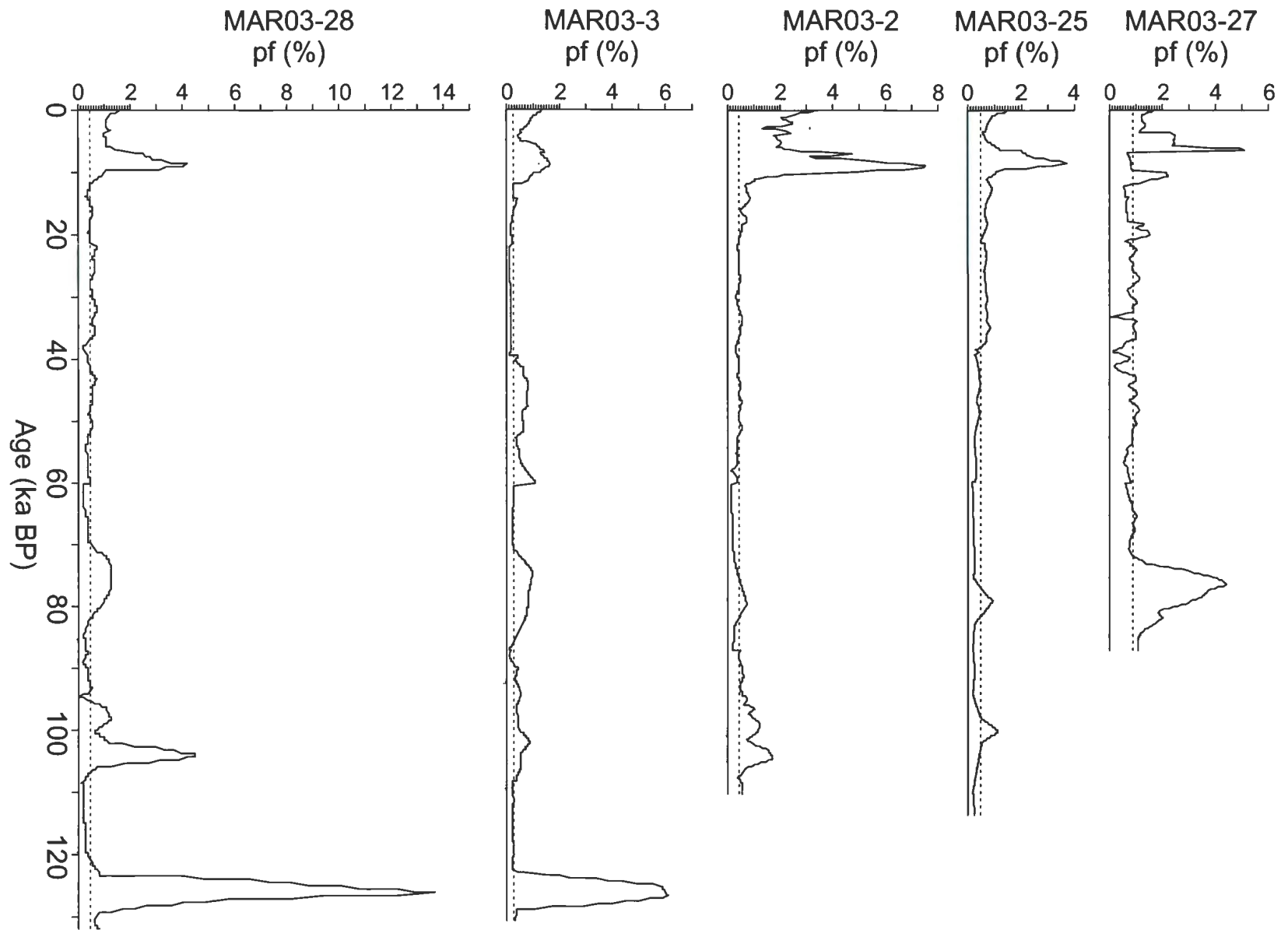


Figure 4.12. Downcore preservation factors derived from Equation 1 using the modern primary production rate, calculated sedimentation rates and OC_{mar} values displayed graphically in Fig. 4.10. Vertical dashed lines show the overall preservation factor for non-sapropel intervals.

factors appear to be 0.3% and 0.9%, respectively, coincident with the lowest and highest average sedimentation rates in the studied cores (Figs. 4.11 and 4.12). Nonetheless, except for core MAR03-27, the calculated modern preservation factors (0.3–0.5%) are within the range of 0.2–0.5% postulated for the oxic marine environments (Bannock Basin; Howell and Thunell, 1992; Fig. 4.12).

Higher than 20 cm ka⁻¹ sedimentation rates have been reported for sapropel S1; however, they mainly range between 9 cm ka⁻¹ and 14 cm ka⁻¹ with an average sedimentation rate of 12 cm ka⁻¹ (Casford et al., 2002; Roussakis et al., 2004; Gogou et al., 2007; Aksu et al., 1995). Furthermore, the sedimentation rates for MIS5 sapropels range between 2.9 cm ka⁻¹ and 9.1 cm ka⁻¹ with an average range of 4 to 6 cm ka⁻¹ (a rate of 25.2 cm ka⁻¹ has been reported for S5 in core LC21-NE Crete).

It is instructive to rearrange the same PP equations to calculate the marine-sourced organic carbon content in recent and non-sapropel sediments as a check on the non-sapropel sedimentation rates calculated for the cores (Fig. 4.11). Rearranging equations (1) and (2) for C_{org} :

$$C_{org} = (PP * pf * 100) / (10 * LSR * (d_w - (1.025 * \Phi))) \quad (3)$$

and

$$C_{org} = (0.003 * PP * LSR^{0.3}) / (d_g * (1 - \Phi)) \quad (4)$$

and with today's primary productivity levels (i.e., 30 g C m⁻² yr⁻¹) in the Aegean Sea, calculated marine-sourced organic carbon content in sediments deposited since 130 ka BP under oxygenated bottom waters like those today range between 0.25% and 0.8%

with a mean value of 0.4% (Fig. 4.13). In general, these values agree well with the average measured OC_{mar} content (i.e., ~0.3–0.5%) in non-sapropel ‘background’ sediments among the five studied cores. However, particularly those estimates obtained from Equation (3) show inconsistencies at certain intervals revealing ~0.5% higher marine-sourced organic carbon contents than measured background values (Fig. 4.13). Those intervals coincide with the lowest sedimentation rates (2–3 $cm\ ka^{-1}$) which, in turn, suggest that these very low sedimentation rates are underestimates. This problem arises from the scarcity of the age control points across MIS5 (Fig. 4.5). Given that the inconsistencies are generally at sapropel intervals (Fig. 4.13), the two age control points (123 and 129 ka BP) situated immediately above and below sapropel S5 in cores MAR03-28 and MAR03-3 could provide a better constraint for sedimentation rate across MIS5 sapropels. According to those two age control points, the sedimentation rates are 5 $cm\ ka^{-1}$ and 6.6 $cm\ ka^{-1}$ in cores MAR03-3 and MAR03-28, respectively. Using an average constant sedimentation rate of 5.8 $cm\ ka^{-1}$ for sediments >60 ka BP might therefore be a better approach for primary productivity calculations. A much better agreement between measured and calculated OC_{mar} values is obtained after recalculating OC_{mar} from Equations (3) and (4) using this inferred constant sedimentation rate (Fig. 4.13).

It is worthwhile to investigate the sensitivity of Equations (1) and (2) to sedimentation rates. If we were to take 3 $cm\ ka^{-1}$ and 25 $cm\ ka^{-1}$ as the two end members, the resultant PP values show significant differences particularly at low sedimentation rates for which Equation (2) gives values in excess of Equation (1) by 250 $g\ C\ m^{-2}\ yr^{-1}$ (for 3% TOC) to 1004 $g\ C\ m^{-2}\ yr^{-1}$ (for 12% TOC; Fig. 4.14). For high sedimentation

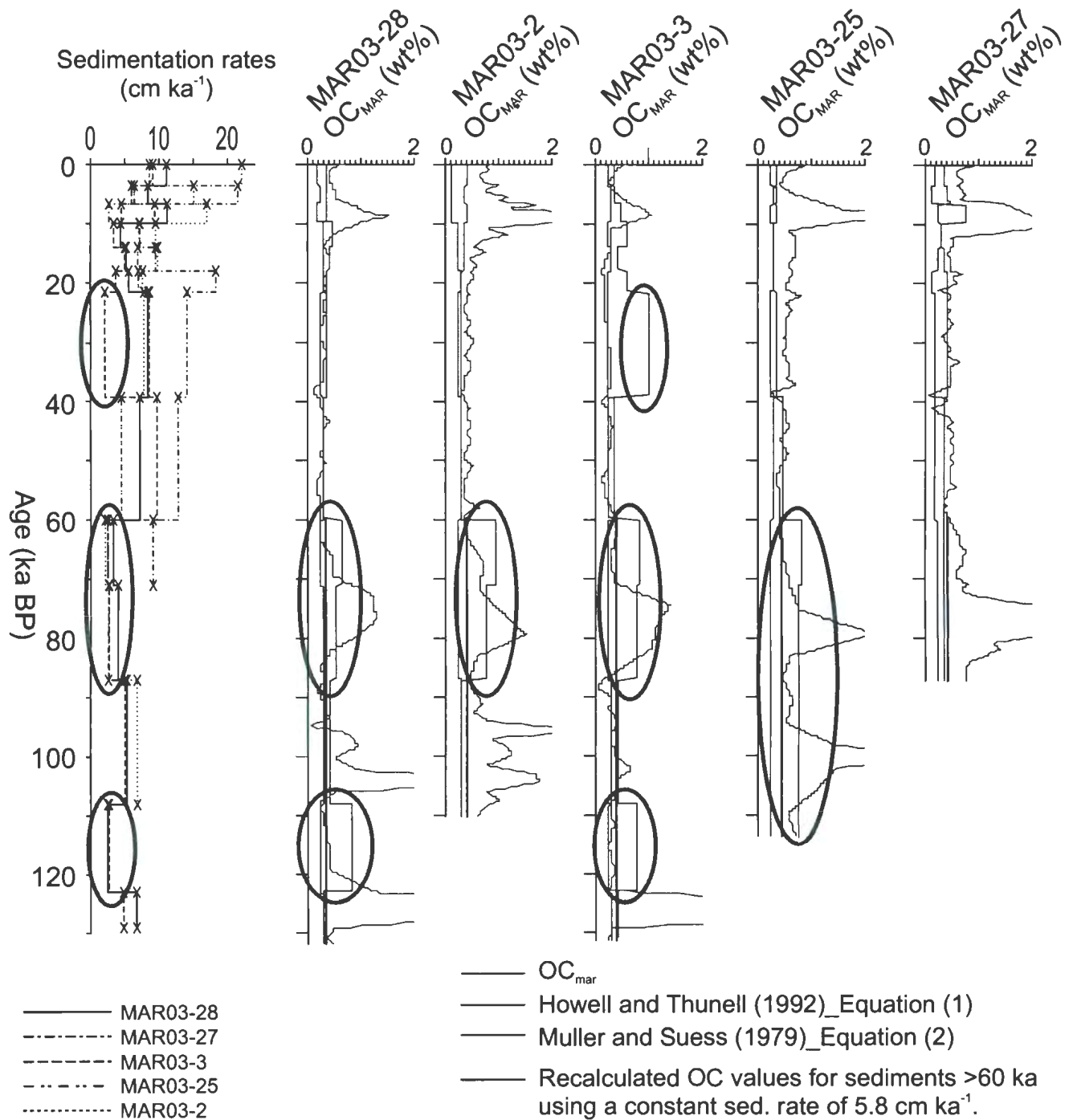


Figure 4.13. Downcore plots showing measured (red line) and calculated (blue, green, black lines) OC_{mar} contents in the five cores, with measured values in sapropels shown with a thinner line weight. The calculated values are based on an assumption of non-sapropel conditions throughout. Preservation factor (pf) is 0.005 for cores MAR03-28, MAR03-2, MAR03-25; 0.003 for core MAR03-3; 0.009 for core MAR03-27. Please note that OC_{mar} values in all cores are trimmed at 2% in order to accentuate the background organic carbon comparisons. Purple ellipses show the inconsistencies in relation to low sedimentation rates (~3 cm ka⁻¹).

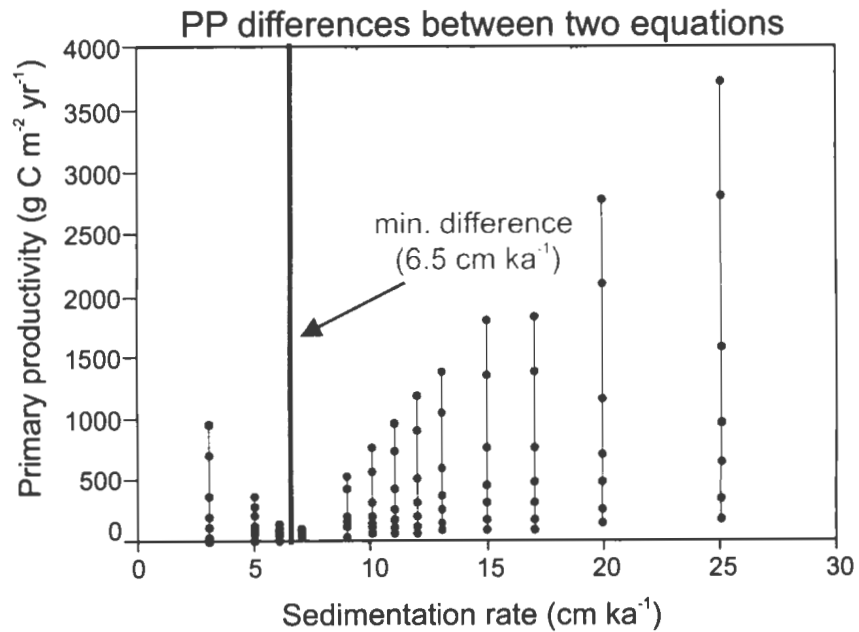
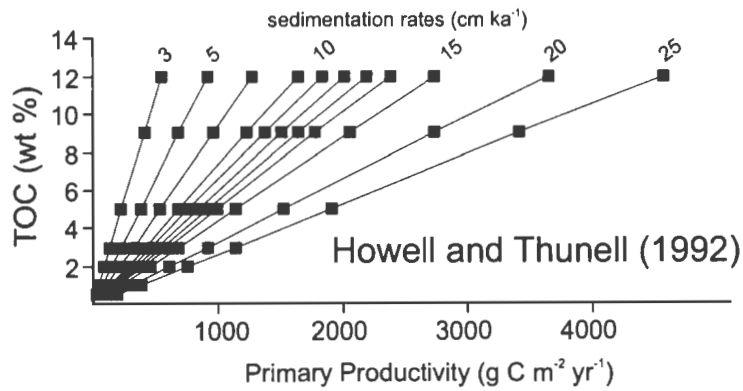
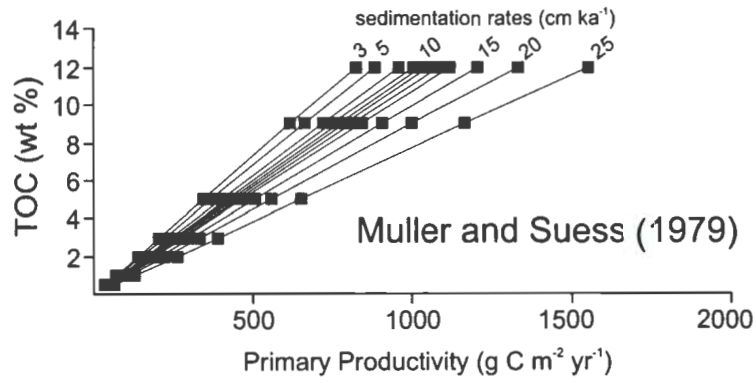


Figure 4.14. Primary productivity variations between the two equations according to changing sedimentation rates.

rates, even larger differences are observed with Equation (1) giving values in excess of Equation (2) ranging from $937 \text{ g C m}^{-2} \text{ yr}^{-1}$ to $3749 \text{ g C m}^{-2} \text{ yr}^{-1}$ for TOC contents of 3% and 12%, respectively (Fig. 4.14). Figure 4.14 also shows the optimum sedimentation rate (6.5 cm ka^{-1}) that results in a minimum difference between the two PP equations.

Given the high sensitivity to sedimentation rates and scarcity of age control points in MIS 5, there might have been increases or decreases in sedimentation rates across sapropel intervals that are not captured by our analysis. Nonetheless, PP calculations, using the sedimentation rates discussed above, still provide significant insight into changes in past sea surface productivity during times of sapropel formation. The PP values calculated with Equations 1 and 2 show striking differences from one another in sapropel intervals which suggest two different scenarios for changes in productivity (Fig. 4.15).

The PP values calculated by Equation 2 (Muller and Suess, 1979) show noticeable elevations at sapropel intervals ranging between 120 and $220 \text{ g C m}^{-2} \text{ yr}^{-1}$ which, in turn, suggest the surface productivity was at least 4 to 6 times higher than present day surface productivity in the Aegean Sea ($30 \text{ g C m}^{-2} \text{ yr}^{-1}$). These values imply a substantial increase in the surface productivities during times of sapropel formation which are comparable to those in modern upwelling regions with primary productivity values up to $500 \text{ g C m}^{-2} \text{ yr}^{-1}$. Similar high PP values have also been deduced from the eastern Mediterranean (Weldeab et al., 2003). For sapropels S4 and S5 in cores MAR03-28 and MAR03-3, with high OC_{mar} contents (e.g., 5 and 8 wt%; Fig. 4.10), Equation 2 returns unrealistically high values ranging from 360 – $550 \text{ g C m}^{-2} \text{ yr}^{-1}$ to a maximum of $810 \text{ g C m}^{-2} \text{ yr}^{-1}$. These values are equal to, or higher than, values in the most productive modern

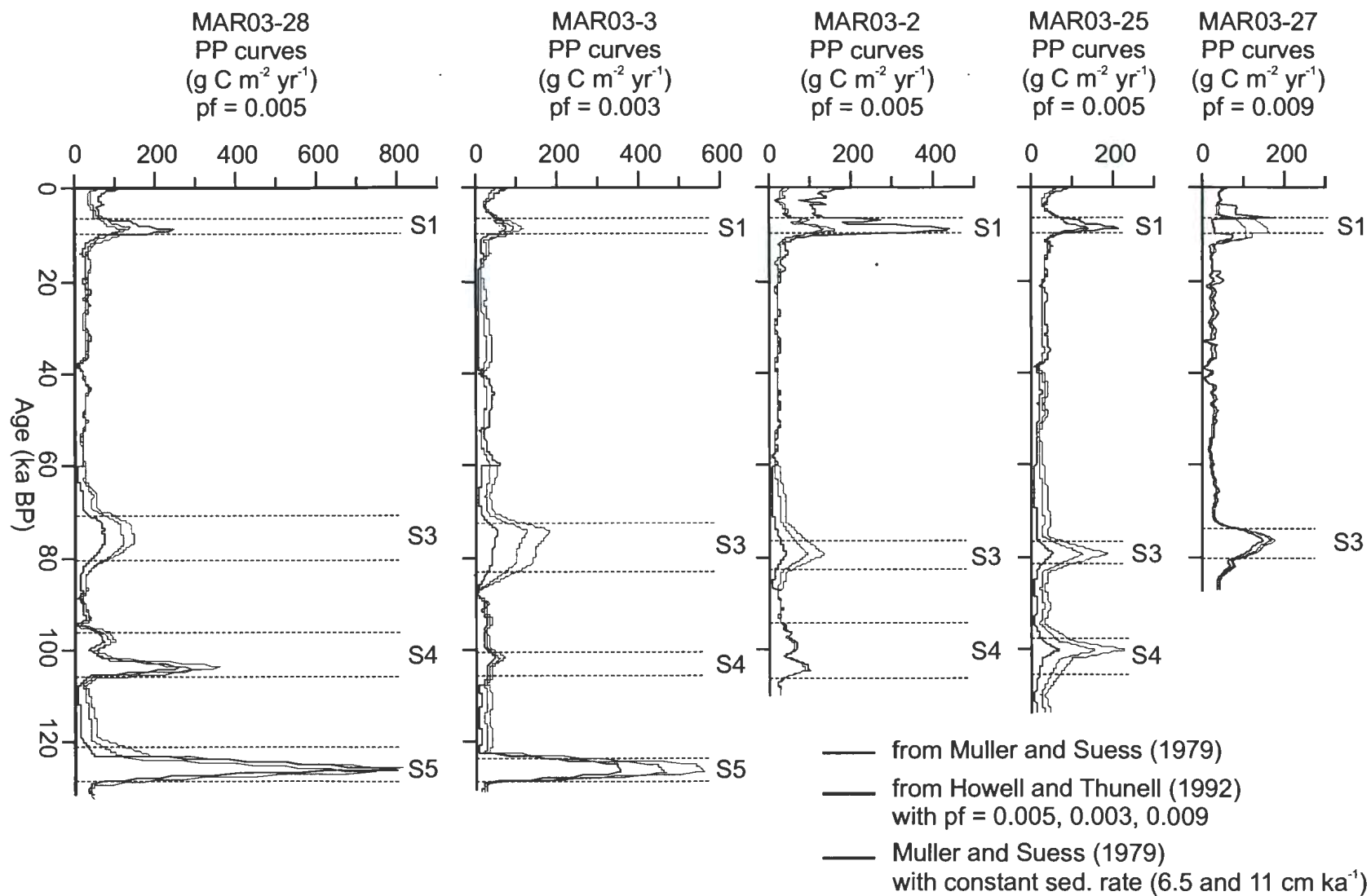


Figure 4.15. Primary productivity values calculated for the five studied cores using PP equations of Muller and Suess (1979) and of Howell and Thunell (1992), and measured values of OC_{mar} for C_{org} in the calculations. For comparison, PP values using a constant sedimentation rate are also shown (11 cm ka⁻¹ in core MAR03-27, 6.5 cm ka⁻¹ for the remaining four cores). Horizontal dashed lines represent sapropel horizons.

coastal regions.

The very high OC_{mar} contents in sapropels S4 and S5 cannot be achieved by increased productivity alone or just by improved preservation; instead, both factors are required. Recall that preservation factors necessary to account for observed OC_{mar} values were calculated under the assumption that past productivity levels were identical to today's levels ($30 \text{ g C m}^{-2} \text{ yr}^{-1}$). In many cases (S1 in all cores but MAR03-3; S3 in MAR03-27; S4 in MAR03-28; S5 in MAR03-28 and MAR03-3) the required preservation factor (4-13.5%; Fig. 4.12) is close to or exceeds the limiting value of 5% that characterizes the modern Black Sea, so the assumption of a productivity level of $\sim 30 \text{ g C m}^{-2} \text{ yr}^{-1}$ at those times must be incorrect, and larger PP values must have existed. Furthermore, the Black Sea preservation factor of 5% applies to an anoxic basin, whereas burrowing in the Aegean Sea sapropels indicates moderately dysoxic conditions at most. Howell and Thunell (1992) determined $pf = 2.5\%$ for the most poorly oxygenated sites in the Bannock Basin, so it is probably reasonable to decrease the limiting value for the Aegean Sea sapropels to perhaps 2%, not 5%. In that case, all sapropels but S3 in core MAR03-28 have unrealistic calculated preservation factors, unless paleoproductivity levels at those times were higher than today. Certainly, increased preservation factors across sapropels indicate modification of the bottom waters towards oxygen starvation (i.e., stagnation, dysoxia?) as a result of diminished advection (surface water stratification). However, since Aegean Sea bottom waters were never anoxic (or euxinic), other factor(s) such as increased export productivity must have existed in addition to some degree of bottom water stagnation.

If the sedimentary C_{org} content were to be explained by increased PP only,

unlikely high productivity levels would be required. Assuming that the preservation factor did not change during both non-sapropel and sapropel intervals (i.e., ~0.5%), then the PP would be $360 \text{ g C m}^{-2} \text{ yr}^{-1}$ and $800 \text{ g C m}^{-2} \text{ yr}^{-1}$ for the very high OC_{mar} contents of 5% and 8%, respectively. These calculated productivity levels, the latter in particular, are very high compared to those reported in present-day marine settings. We can conclude that both productivity and preservation must have been higher during the formation of sapropels S1–S5. It is likely that sluggish bottom water conditions due to water column stratification together with increased PP as a result of increased surface productivity are the causative factors that resulted in higher organic carbon content in the sediments resulting in sapropel formation.

Calculated PP values from Equation 1 (except MAR03-27) are higher than those from Equation 2 for the most recent sapropel S1 and generally much lower than those from Equation 2 for sapropels S3 and S4 (Fig. 4.15). At intervals with very high OC_{mar} contents (S5 and lower S4 in core MAR03-28), PP calculations attain values ranging from $250 \text{ g C m}^{-2} \text{ yr}^{-1}$ to a maximum of $800 \text{ g C m}^{-2} \text{ yr}^{-1}$. Although the OC_{mar} contents do not fluctuate significantly in sapropels S1, S3 and S4 (averaging between 1% and 1.5%) the calculated PP values generally show very high values for S1 ($210\text{--}410 \text{ g C m}^{-2} \text{ yr}^{-1}$) while those calculated for sapropels S3 and S4 using Equation 1 are close to current productivity values (except for the lower part of S4 in core MAR03-28) and range between $55 \text{ g C m}^{-2} \text{ yr}^{-1}$ and $90 \text{ g C m}^{-2} \text{ yr}^{-1}$. If we were to assume these low values to be correct then the high organic carbon concentrations would require complete anoxia during the deposition of these two sapropels in order to create favourable bottom water conditions under surface waters with low surface productivity. However, these low

values do not necessarily require low export production, particularly if there were a DCM layer during their deposition. DCM occurs as nutricline/chemocline rises toward shallower waters as a result of decreased density contrast between the surface and then intermediate waters. Shoaling of the pycnocline above the thermocline, situated within the lower portions of the photic zone, could contribute greatly to the export production. Such a scenario would involve high export production sourced from the lower portions of the photic zone even though the productivity of the surface waters was not exceptional. In contrast, relatively high PP values calculated for the most recent sapropel S1 are needed in that case to provide sufficient carbon flux because a DCM layer was absent at that time, as demonstrated by the disappearance of *N. pachyderma* (d) immediately below the sapropel (Rohling and Gieskes, 1989; Rohling et al., 1993; Chapter 3).

According to PP values obtained from constant sedimentation rate (i.e., 6.5 cm ka⁻¹), primary production during times of sapropel formation mainly ranged between 100 g C m⁻² yr⁻¹ and 130 g C m⁻² yr⁻¹ with significantly higher amounts during portions of the S4 and S5 development at core sites MAR03-28 and MAR03-3, for which the range is mostly 300–470 g C m⁻² yr⁻¹ (800 g C m⁻² yr⁻¹ for 8% OC_{mar} in S5 in core MAR03-28). The overall similar range for sapropels S1–S4 suggests that primary production of the surface waters during times of sapropel formation was approximately the same except for a high amplitude spike at the bottom of S4 in core MAR03-28 (Fig. 4.15). This spike suggests a jump in surface productivity, although a more negative $\delta^{13}\text{C}_{\text{org}}$ value coinciding with this spike also implicates an increase in terrestrial organic carbon input. Very high PP values during S5 suggest much higher productivity of the surface waters

during its deposition. Such a difference is also suggested by several other studies in the eastern Mediterranean Sea. As a caveat, $\delta^{13}\text{C}_{\text{org}}$ values in S5 are relatively more depleted with respect to those in younger sapropels suggesting a higher terrigenous contribution which could be ascribed to higher pluviality during its deposition and, to a lesser extent, to higher sea levels, hence more extensive shallow shelves.

4.6.4 Role of terrestrial carbon

The paleoproductivity discussion ignored the OC_{ter} component of Aegean Sea sapropels. Preservation of OC_{ter} is considerably higher in sapropels S1–S5 than in background sediments. This might indicate higher fluxes from coastal rivers at those times, but it is also possible that higher OC_{mar} production, moderate bottom-water stagnation and elevated preservation factors facilitated an enhanced level of preservation for OC_{ter} , even if its delivery into the Aegean Sea was approximately constant through time. The extra carbon load from terrigenous input would intensify water column stratification and impede advection of oxygenated surface waters, further promoting bottom water stagnation, thus improved preservation (e.g., dysoxia). In this scenario, the marine flux and structure of the water column provided the trigger for sapropel onset, and the terrestrial flux amplified these conditions so as to guarantee strong organic-matter preservation.

4.7. Conclusions

Primary productivity calculations using equations from Muller and Suess (1979)

and from Howell and Thunell (1992) reveal two different settings: 1) according to Muller and Suess surface productivities range from 120–220 g C m⁻² yr⁻¹ for sapropels with 1–1.8% OC_{mar} contents and from 360–810 g C m⁻² yr⁻¹ for marine-sourced organic carbon accumulations of 5–8% (i.e., S4 and S5); 2) according to the equations of Howell and Thunell (1992), however, increased surface productivities during the most recent sapropel S1 (90–410 g C m⁻² yr⁻¹) and surface productivities are close to today's values (~50 g C m⁻² yr⁻¹) during deposition of sapropels S3 and S4 (1–1.8% OC_{mar}), implying that the export production during MIS5 was sourced from the establishment of a distinct DCM layer. The lack of such a layer during S1 deposition is indicated by the disappearance of *N. pachyderma* (d), a DCM indicator, just below S1. In either scenario, elevated export productivities appear to be the primary factor causing the deposition of sapropels containing 1–1.8% marine-sourced organic carbon. However, it must be highlighted that bottom water stagnation (i.e., increased preservation) is rather essential for the accumulation of sediments with very high organic-matter contents, as for sapropels S4 and S5 with OC_{mar} contents of 5–8%.

$\delta^{13}\text{C}_{\text{org}}$ values show that both marine and terrestrial organic matter constitute equally important fractions of MIS5 sapropels S3, S4 and S5. Across the most recent sapropel S1, upward carbon-isotopic enrichment suggests a progressively diminishing terrigenous input toward the end of sapropel deposition. In addition, carbon isotope values obtained from the Aegean Sea sapropels clearly distinguish them from their counterparts in the eastern Mediterranean. The Aegean values are 1–2‰ more depleted signifying a stronger terrestrial contribution to the pool of organic matter, thus likely an

enhanced riverine input during the deposition of the MIS5 sapropels S3, S4 and S5.

According to C/S plots, all of the sapropels seem to have been deposited under normal marine conditions with temporary establishment of semi-euxinic? bottom water conditions. Highly depleted and somewhat uniform $\delta^{34}\text{S}$ values together with the absence of euxinic conditions during sapropel intervals collectively suggest that sulphate reduction took place consistently below the sediment-water interface. On the other hand, development of semi-euxinic bottom waters, particularly during development of high-TOC-content sapropels, should not be ruled out.

References

- Aksu, A.E., Yaşar, D., Mudie, P.J., 1995a. Paleoclimatic and paleoceanographic conditions leading to development of sapropel layer S1 in the Aegean Sea. *Palaeogeography, Palaeoclimatology, Palaeoecology* 116, 71–101.
- Aksu, A.E., Yasar, D., Mudie, P.J., Gillespie, H., 1995b. Late glacial-Holocene paleoclimatic and paleoceanographic evolution of the Aegean Sea: micropaleontological and stable isotopic evidence. *Marine Micropaleontology*, 25, 1–28.
- Aksu, A.E., Jenner, G., Hiscott, R.N., İşler, E.B., 2008. Occurrence, stratigraphy and geochemistry of Late Quaternary tephra layers in the Aegean Sea and the Marmara Sea. *Marine Geology* 252, 174–192.
- Berner, R.A., 1970. Sedimentary pyrite formation. *American Journal of Science*, 268, 1–23.
- Berner, R.A., 1982. Burial of organic carbon and pyrite sulphur in the modern ocean - its geochemical and environmental significance. *American Journal of Science*, 282, 451–473.
- Berner RA, Raiswell R. 1983. Burial of organic carbon and pyrite sulfur in sediments over Phanerozoic time: a new theory. *Geochimica et Cosmochimica Acta*, 47, 55–62.
- Berner RA, Raiswell R. 1984. C/S method for distinguishing freshwater from marine sedimentary rocks. *Geology*, 12, 65–68.
- Berner, R.A., 1984. Sedimentary pyrite formation: An update. *Geochimica et*

- Cosmochimica Acta,48, 605–615.
- Berner, R.A., 1989. Biogeochemical cycles of carbon and sulfur and their effect on atmospheric oxygen over phanerozoic time. *Global and Planetary Change*,75, 97–122.
- Boesen, C. and Postma, D., 1988. Pyrite formation in anoxic environments of the baltic. *American Journal of Science*,288, 575–603.
- Calvert, S.E., 1983. Geochemistry of Pleistocene sapropels and associated sediments from the eastern Mediterranean. *Oceanologica Acta*, 6, 255–267.
- Calvert, S.E., Nielsen, B., Fontugne, M.R., 1992. Evidence from nitrogen isotope ratios for enhanced productivity during formation of eastern Mediterranean sapropels. *Nature*,359, 223–225.
- Casford, J.S.L., E.J. Rohling, R. H. Abu Zied, S. Cooke, C. Fontanier, M. Leng, and V. Lykousis 2002. Circulation changes and nutrient concentrations in the late Quaternary Aegean Sea: A nonsteady state concept for sapropel formation, *Paleoceanography*, 17, 1024, DOI:10.1029/2000PA000601.
- Casford, J. S. L., R. H. Abu Zied, E. J. Rohling, S. Cooke, C. Fontanier, M. J. Leng, A. Millard, and J. Thomson, 2007. A stratigraphically controlled multiproxy chronostratigraphy for the eastern Mediterranean, *Paleoceanography*, 22, PA4215, DOI:10.1029/2007PA001422.
- Chanton, J.P., 1987. Sulfur mass balance and isotopic fractionation in an anoxic marine sediment. Ph.D. Thesis, University of North Carolina, Chapel Hill, USA.
- Cita, M.B., and D. Grignani, 1982. Nature and origin of Late Neogene Mediterranean sapropels. In: Schlanger, S.O., and M.B. Cita (Eds.), *Nature and Origin of*

- Cretaceous Carbon rich Facies, London (Academic Press), 165–196.
- Davis, H. R., Byers, C. W. and Dean, W. E. (1988) Pyrite formation in the lower Cretaceous Mowry shale: effect of organic matter type and reactive iron content. *American Journal of Science*, 288, 873–890.
- Deines, P., 1980. The isotopic composition of reduced organic carbon. In: P. Fritz and J.Ch. Fontes (Editors), *Handbook of Environmental Isotope Geochemistry, Vol 1: The Terrestrial Environment (A)*. Elsevier, Amsterdam, pp. 329–406.
- De Lange, G.J., Middelburg, J.J., Van der Weijden, C.H., Catalano, G., Luther III, G.W., Hydes, D.J., Woittiez, J.R.W., Klinkhammer, G.P., 1990. Composition of anoxic hypersaline brines in the Tyro and Bannock Basin, eastern Mediterranean. *Marine Chemistry*, 31, 63–88.
- Demaison, G. J. and Moore, G. T., 1980. Anoxic environments and oil source bed genesis. *American Association of Petroleum Geologists Bulletin*, 64:1179.209.
- De Rijk, S., Hayes, A., Rohling, E.J., 1999. Eastern Mediterranean sapropel S1 interruption: an expression of the onset of paleoceanographic conditions leading to development of climatic deterioration around 7 ka BP. *Marine Geology*, 153, 337–343.
- Deuser, W. G., 1970. Extreme $^{13}\text{C}/^{12}\text{C}$ variations in Quaternary dolomites from the continental shelf. *Earth Planetary Science Letters*, 8, 118–124.
- Emeis KC, Schulz H, Struck U, Rossignol Strick M, Erlenkeuser H, Howell MW, Kroon D, Mackensen A, Ishizuka S, Oba T, Sakamoto T, Koizumi I, 2003. Eastern Mediterranean surface water temperatures and $\delta^{18}\text{O}$ composition during deposition of sapropels in the late Quaternary. *Paleoceanography* 18(1):1005.

doi:10.1029/2000PA00061.

- Gogou, A., Bouloubassi, I., Lykousis, V., Arnaboldi, M., Gaitani, P., Meyers, P.A., 2007. Organic geochemical evidence of Late Glacial–Holocene climate instability in the North Aegean Sea. *Palaeogeography, Palaeoclimatology, Palaeoecology* 256, 1–20.
- Goldhaber, MR, Kaplan, I.R., 1974. The sulfur cycle. In: Goldberg, E.D. (Ed.), *The Sea*, vol. 5. Wiley, New York, pp. 569–655.
- Fontugne, M.R., Calvert, S.E., 1992. Late Pleistocene variability of the carbon isotopic composition of organic matter in the eastern Mediterranean: monitor of changes in carbon sources and atmospheric CO₂ concentrations. *Paleoceanography*, 7, 1–20.
- Fossing, H., and Jørgensen, B.B., 1990. Oxidation and reduction of radiolabeled inorganic sulfur compounds in an estuarine sediment, Kysing Fjord, Denmark. *Geochimica et Cosmochimica Acta*, 54: 2731–2742.
- Glenn, C. R. and Arthur, M. A., 1985. Sedimentary and geochemical indicators of productivity and oxygen contents in modern and ancient basins: The Holocene Black Sea as the "type" anoxic basin. *Chem. Geol.* 48, 325–354.
- Hiscott, R. N., Aksu, A. E., Mudie, P. J., Marret, F., brajano, T., Kaminski, M. A., Evans, J., Cakiroglu, A. I., Yasar, D., 2007. Gradual drowning of the southwestern Black Sea shelf: Evidence for a progressive rather than abrupt Holocene reconnection with the eastern Mediterranean Sea through the Marmara Sea Gateway *Quaternary International* 167–168 (2007) 19–34
- Howell M. W. and Thunell R. C., 1992. Organic carbon accumulation in Bannock Basin:

- Evaluating the role of productivity in the formation of eastern Mediterranean sapropels. *Marine Geology*, 103, 461-471.
- Imbrie, J. and Kipp, N.G. 1971. A new micropaleontological method for paleoclimatology: Application to a Late Pleistocene Caribbean core, p. 71-181. *The Late Cenozoic Glacial Ages*. New Haven, Yale University Press.
- Jørgensen, B.B., 1978. A comparison of methods for the quantification of bacterial sulfate reduction in coastal marine sediments. I. Measurements with radiotracer techniques. *Geomicrobiology Journal*, 1:11-27.
- Koma, T. and Suzuki, Y. (1985) Forms of sulfur, carbon and iron in marine sediments with special reference to their depositional environments. *Marine and Estuarine Geochemistry* (Sigleo, A. C. and Hattori, eds.), 197-208, Lewis Publishers, 331 pp.
- Kouli, K., Gogou, A., Bouloubassi, I., Triantaphyllou, M. V., Ioakim, Chr., Katsouras, G., Roussakis, G. and Lykousis, V., 2012. Late postglacial paleoenvironmental change in the northeastern Mediterranean region: Combined palynological and molecular biomarker evidence *Quaternary International* Volume 261, 30 May 2012, Pages 118-127
- Kullenberg, B., 1952. On the salinity of water contained in marine sediments. *Medd. Oceanogr. Inst. Goteberg* 21, 1-38.
- Lin, S. and Morse, J. W., 1991. Sulfate reduction and iron sulfide mineral formation in Gulf of Mexico anoxic sediments. *American Journal of Science*, 291, 55-89.
- Lisiecki, L. E., and M. E. Raymo, 2005. A Pliocene-Pleistocene stack of 57 globally distributed benthic $\delta^{18}\text{O}$ records, *Paleoceanography*, 20, PA1003,

doi:10.1029/2004PA001071.

- Lykousis, V., 2002. Circulation changes and nutrient concentrations in the late Quaternary Aegean Sea: a nonsteady state concept for sapropel formation. *Paleoceanography* 17, 1024-1034.
- Muller, P.J., Suess, E., 1979. Productivity, sedimentation rate, and sedimentary organic matter in the oceans - I. Organic carbon preservation. *Deep Sea Res.* 26 A, 1347-1362.
- Murat, A. and Got H., 2000. Organic carbon variations of the eastern Mediterranean Holocene sapropel: a key for understanding formation processes. *Palaeogeography, Palaeoclimatology, Palaeoecology*, 158, 241-257
- Narcisi, B., Vezzoli, L., 1999. Quaternary stratigraphy of distal tephra layers in the Mediterranean -an overview. *Global and Planetary Change* 21, 31-50.
- Olausson, E., 1961. Studies of deep-sea cores. *Reports Swedish Deep-Sea Expedition*, 8(4): 337-391.
- Passier, H. F., Bottcher, M. E. and De Lange, G. J., 1999. Sulphur Enrichment in Organic Matter of Eastern Mediterranean Sapropels: A Study of Sulphur Isotope Partitioning *Aquatic Geochemistry* 5: 99-118, 1999.
- Pedersen, T.F., Calvert, S.E., 1990. Anoxia vs. productivity: What controls the formation of organic-carbon-rich sediments and sedimentary rocks?. *AAPG Bull.* 74, 454-466.
- Rohling, E.J., Gieskes, W.W.C., 1989. Late Quaternary changes in Mediterranean intermediate water density and formation. *Micropaleontology*, 3, 147-173.
- Rohling EJ, Jorissen FJ, Vergnaud Grazzini C, Zachariasse WJ, 1993. Northern

- Levantine and Adriatic quaternary planktic foraminifera: reconstruction of paleoenvironmental gradients. *Marine Micropaleontology*, 21, 191-218.
- Rohling, E.J., 1994. Review and new aspects concerning the formation of eastern Mediterranean sapropels. *Marine Geology*, 122, 1-28.
- Rossignol Strick, M., Nesteroff, W., Olive, P., Vergnaud Grazzini, C., 1982. After the deluge: Mediterranean stagnation and sapropel formation. *Nature* 295, 105-110.
- Rossignol Strick, M., 1985. Mediterranean Quaternary sapropels, an immediate response of the African monsoon to variation of insolation. *Palaeogeogr. Palaeoclimatol. Palaeoecol.* 49, 237-263.
- Roussakis, G., Karageorgis, A.P., Conispoliatis, N., Lykousis, V., 2004. Last glacial-Holocene sediment sequences in N. Aegean basins: structure, accumulation rates and clay mineral distribution. *Geo Marine Letters* 24, 97-111.
- Schimmelmann, A. and Kastner, M. (1993) Evolutionary changes over the last 1000 years of reduced sulfur phases and organic carbon in varved sediments of the Santa Barbara Basin, California. *Geochim. Cosmochim. Acta* 57, 67-78.
- Sutherland, H., Calvert, S.E., Morris, R.J., 1984. Geochemical studies of the recent sapropel and associated sediment from the Hellenic outer ridge, eastern Mediterranean Sea: I. Mineralogy and chemical composition. *Mar. Geol.* 56, 79-92.
- Ten Haven, H.L., Baas, M., Kroot, M., De Leeuw, J.W., Schenk, P.A., Ebbing, J., 1987. Late Quaternary Mediterranean sapropels: III. Assessment of source of input and palaeotemperature as derived from biological markers. *Geochimica et Cosmochimica Acta* 51, 803-810.

- Terashima, S., Yonetani, H., Matsumoto, E. and Inouchi, Y., 1983. Sulfur and carbon contents in recent sediments and their relation to sedimentary environments. *Bull. Geol. Surv. Jpn.* 34, 361-382.
- Thunell, R.C., Williams, D.F., Belayea, P., 1984. Anoxic events in the Mediterranean Sea in relation to the evolution of late Neogene climates. *Marine Geology*, 59, 105-134.
- van der Meer M. T. J., Baas M., Rijpstra W. I. C., Marino G., Rohling E. J., Damsté J. S. S., Schouten S., 2007. Hydrogen isotopic compositions of long-chain alkenones record freshwater flooding of the Eastern Mediterranean at the onset of sapropel deposition. *Earth and Planetary Science Letters*, 262, 594–600.
- Velaoras, D. and Lascaratos, A., 2005. Deep water mass characteristics and interannual variability in the North and Central Aegean Sea. *Journal of Marine Systems* 53, 59–85.
- Vergnaud Grazzini, C., Ryan, W.B.F., Cita, M.B., 1977. Stable isotopic fractionation, climate change and episodic stagnation in the eastern Mediterranean during the Late Quaternary. *Marine Micropaleontology* 2, 353-370.
- Vergnaud Grazzini, C., Devaux, M., Znaidi, J., 1986. Stable isotope anomalies in Mediterranean Pleistocene records. *Marine Micropaleontology* 10, 35-69.
- Weldeab, S., Emeis, K.C., Hemleben, C., Schmiedl, G. and Schultz, H., 2003. Spatial productivity variations during formation of sapropels S5 and S6 in the Mediterranean Sea: evidence from Ba contents. *Palaeogeography, Palaeoclimatology, Palaeoecology*, 191, 169–190.
- Zervakis, V., D. Georgopoulos, A.P. Karageorgis, and A. Theocharis, 2004. On the

response of the Aegean sea to climatic variability: a review, *International Journal of Climatology*, 24, 1845-1858.

Chapter 5. Summary

Geochemical, micropaleontological and isotopic analyses on five long piston cores dated by eight radiocarbon ages, tephra layers Z2, Y2 and Y5, sapropel and marine isotope stage (MIS) boundaries from the Aegean Sea have revealed the following salient conclusions:

- Organic carbon analyses show the consistent presence of three sapropel layers (S3, S4 and S5) among the studied five cores. The cores collected from North Skiros (northern) and Mikonos (central) basins also have a fourth sapropel layer with very high organic carbon contents of 9–12.65%.
- Average sedimentation rates range between 4.7 and 11.8 cm/ka with highest rates being observed in Euboea and North Ikaria basins.
- Chronostratigraphic reconstructions based on oxygen isotopic curve matching and stratigraphic positions of the well-dated tephra layers show that the cores MAR03-28 AND MAR03-3 contain apparently a continuous record of sediments deposited during MIS5 core bottoms are determined to be 130.8 ka and 131.8 ka years old. Furthermore, the onset ages accord well with those from the eastern Mediterranean Sea which allowed identification of the sapropels as S3, S4 and S5 developed during interstadials of the MIS5.
- The calculated onset ages of sapropels S4 (106.4–105.6 ka BP) and S5 (128.6–128.4 ka BP) predated those in the eastern Mediterranean whereas the ages of sapropel S3 from northern portions of the Aegean Sea postdated the previously published ages from the eastern Mediterranean by several thousand

years, which collectively imply the heterogeneity of the Aegean Sea subbasins in terms of rapid vs. lagged response to changing climatic conditions and physiography.

- Narrow age ranges determined for sapropel onsets suggest synchronous initiation across the Aegean Sea and imply an abrupt modification of the surface and bottom waters towards more conducive conditions leading to increased organic carbon accumulations. On the other hand, much broader age range at sapropel tops indicate that returning to non-sapropel conditions was gradual rather than abrupt and differ in subbasins of the Aegean Sea. The age of Nisyros ash layer is calculated to be between 53.8–57.6 ka and disagrees with the previously published age. In addition, the ash layer identified as X1 in North Ikaria Basin must be further analysed in order to make an accurate identification.
- Large oxygen isotope fractionations (as much as 3.8‰) particularly during MIS5/4 and MIS2/1 transitions are similar to those observed in the eastern Mediterranean which indicate the occurrence of significant environmental modifications across the Aegean Sea.
- Interpretation of downcore planktonic foraminifera assemblage distributions allowed the identification of four major biozones. The distributional patterns of the most significant taxa exhibit the same trends at all core sites, which suggests that major oceanographic changes occurred rather synchronously across the Aegean Sea.
- The faunal contrast between the most recent sapropel and older sapropels shows

that the latter sapropels were deposited under similar hydrographic conditions during which a distinct deep chlorophyll maximum (DCM) layer was established, indicating a stratified water column and increased export production. On the other hand, sapropel S1 was deposited in the absence of a DCM layer, during which the water column lacked a deep phytoplankton assemblage. During deposition of sapropels S3, S4 and S5 the modifications in the hydrographic conditions leading to sapropel formation were initiated several thousand years before the sapropel onset.

- The appearance of *N. dutertrei* at sapropels S3, S4 and S5 is interpreted to represent maximum shoaling of the pycnocline and highest level of export productivity.
- Sea surface temperatures obtained both from transfer functions and Mg/Ca equation are in good agreement supporting the applicability of transfer functions. Calculations show that sapropels S3, S4 and S5 were deposited under cooler surface temperatures ($\sim 17^{\circ}\text{C}$) than those during the most recent sapropel S1 ($\sim 20^{\circ}\text{C}$).
- Primary productivity calculations based on two equations revealed two different scenarios: 1) surface productivities range mainly from $120\text{--}360\text{ g C m}^{-2}\text{ yr}^{-1}$ which are comparable to most productive coastal regions, 2) surface productivities were similar to those in the present implying that the export production was sourced from the establishment of a distinct DCM layer. Nonetheless, productivity calculations showed that the Aegean Sea was in fact eutrophic during times of

sapropel depositions.

- Elevated export productivities appear to be the primary factor causing the deposition of sapropels containing 1–3% TOC, however, bottom water stagnation is rather essential for the accumulation of sediments with very high TOC contents (9–12.6%) detected in sapropels S4 and S5.
- Marine and terrestrial organic matter comprised equally important fractions of sapropels S3, S4 and S5. The organic carbon isotope values in the Aegean Sea are 1–2‰ more depleted than those from their eastern Mediterranean Sea counterparts, denoting a stronger terrestrial contribution, hence, enhanced riverine input.
- All the sapropels interpreted to have been deposited under normal marine conditions with temporary establishment of semi-euxinic bottom water conditions.

APPENDIX A

Varimax assemblage description matrix (F)

Species	Tropical-	Low-		
	Subtropical	Transitiona	Salinity	Subpolar
<i>Globorotalia inflata</i>	-0.193	0.811	0.170	-0.320
<i>G. scitula</i>	-0.001	0.007	0.004	0.033
<i>G. truncatulinoides</i> (dextral)	-0.002	0.006	-0.001	0.006
<i>G. truncatulinoides</i> (sinistral)	-0.033	0.246	-0.045	-0.049
<i>Globigerinoides conglobatus</i>	0.000	0.000	0.006	-0.001
<i>G. ruber</i>	0.967	0.096	0.019	-0.142
<i>G. sacculifer</i>	0.059	0.021	0.063	-0.103
<i>G. tenellus</i>	0.023	0.007	-0.003	-0.007
<i>Globigerina bulloides</i>	0.134	0.483	0.028	0.666
<i>G. calida</i>	0.006	0.001	0.002	0.003
<i>G. digitata</i>	0.020	0.006	0.009	-0.017
<i>G. falconensis</i>	0.032	0.040	0.004	0.089
<i>G. quinqueloba</i>	-0.001	-0.011	0.003	0.193
<i>G. rubescens</i>	0.024	0.005	-0.002	0.005
<i>Neogloboquadrina dutertrei</i>	0.006	-0.142	0.973	-0.024
<i>N. pachyderma</i> (dextral)	-0.019	-0.059	0.089	0.584
<i>N. pachyderma</i> (sinistral)	-0.002	-0.010	-0.014	0.090
<i>Globigerinella aequilateralis</i>	0.045	0.028	-0.001	-0.020
<i>Globigerinita glutinata</i>	0.012	0.011	0.094	0.150
<i>Hastigerina pelagica</i>	0.003	0.000	0.000	-0.002
<i>Orbulina universa</i>	0.022	0.108	-0.009	-0.048

Regression Coefficients and intercepts for Mediterranean transfer function equations

	Coefficients		
	Ts	Tw	S
Tropical-Subtropical	9.360	6.923	2.747
Transitional	5.918	-	-
Low Salinity	7.479	-	3.196
Subpolar	-10.04	-7.471	-
Trap.-Subtrop. x Transitional	-	-4.725	-
Trop. - Subtrop. x Low Salinity	-10.04	-	-
Trap.-Subtrop. x Subpolar	-	-	-
Transitional x Low Salinity	-	-	-
Transitional x Subpolar	10.669	12.518	-
Low Salinity x Subpolar	17.111	10.421	-
Tropical-Subtropical, squared	-	-	-
Transitional, squared	-	4.269	-
Low Salinity, squared	-	-	-8.001
Subpolar, squared	-1.860	-	-

Intercept	15.275	9.180	35.793
Multiple correlation coefficient	0.897	0.806	0.904
Standard error of the estimate	0.99 °C	1.20 °C	0.72 ‰
80% Confidence interval	1.64 °C	1.99 °C	1.20 ‰



